The Dissertation Committee for James Harold Stephenson III
certifies that this is the approved version of the following dissertation:

Extraction of Blade-Vortex Interactions from Helicopter Transient Maneuvering Noise.

Committee:

Charles E. Tinney, Supervisor

Jayant Sirohi

David B. Goldstein

Mark F. Hamilton

Kenneth S. Brentner

Extraction of Blade-Vortex Interactions from Helicopter Transient Maneuvering Noise.

by

James Harold Stephenson III, B.S.; M.S.E.

DISSERTATION

Presented to the Faculty of the Graduate School of

The University of Texas at Austin

in Partial Fulfillment

of the Requirements

for the Degree of

DOCTOR OF PHILOSOPHY

THE UNIVERSITY OF TEXAS AT AUSTIN

May 2014

For Lindsey.

Always and Forever.

Acknowledgments

The research presented here could not have been completed without the support of so very, very many people. To quote Sir Isaac Newton, "If I have seen further, it is only by standing on the shoulders of giants."

I owe an amount of gratitude to my academic adviser, Professor Charles E. Tinney, for his research guidance and urging to seek outside funding. Without him, I would never have received the SMART fellowship which provided me with the contacts and data that made this analysis possible. Further, his advice has started me down a path to a promising career as a researcher with the U.S. Army. My sincerest appreciation is extended to the other committee members, Dr. Jayant Sirohi, Dr. David B. Goldstein, Dr. Mark F. Hamilton, and Dr. Kenneth S. Brentner. Their interest in my research and specifically their recommendations proved incredibly useful. This dissertation is certainly better for having their expert advice.

Another personal expression of gratitude is extended towards all of the team members from Bell Helicopters, the U.S. Army, and NASA who made this research project possible. Most especially I would like to thank Dr. Eric Greenwood for his helpful discussions and quiet confidence in my work. Further thanks is due to David Conner, of the U.S. Army, as well as Mike Watts, Dr. Casey Burley, and Stuart Pope from NASA-LaRC.

My time at The University of Texas at Austin has been marked most pleasurably by those I have had the chance to interact with. I have worked alongside some amazing fellow graduate students, several of whom have come to be close friends of mine. Thank you all, not only for the occasional research discussions, but also for the stress relieving, non-work related activities.

Throughout my career here at UT, I have had the pleasure of interacting with some amazing staff who work for the Department of Aerospace Engineering

and Engineering Mechanics department. The two staff members who provided the most amazing and friendly support are machinist, Joseph Pokluda, and electronics expert, Pablo Cortez. Administrative support was kindly provided by Donna Soward and David Crittenden. I will forever fondly remember David, may he rest in peace, for our car discussions.

As a final note, I would like to thank my friends and family who have supported me throughout these years in Austin. The graduate student lifestyle is not for everybody, and it was your loving support that helped get me through these trying times. To the friends I have made here in Austin, you will always be dear in my heart. I pray we will remain in touch, despite the distance that will soon separate us. Last, and by far the most important, I cannot thank my parents, nor my wife, Lindsey, enough for their encouragement and support. Truly, without you, I would have failed so very long ago. Thank you, and I love you.

Extraction of Blade-Vortex Interactions from Helicopter Transient Maneuvering Noise.

James Harold Stephenson III, Ph.D.
The University of Texas at Austin, 2014

Supervisor: Charles E. Tinney

Time-frequency analysis techniques are proposed as a necessary tool for the analysis of acoustics generated by helicopter transient maneuvering flight. Such techniques are necessary as the acoustic signals related to transient maneuvers are inherently unsteady. The wavelet transform is proposed as an appropriate tool, and it is compared to the more standard short-time Fourier transform technique through an investigation using several appropriately sized interrogation windows. It is shown that the wavelet transform provides a consistent spectral representation, regardless of employed window size. The short-time Fourier transform, however, provides spectral amplitudes that are highly dependent on the size of the interrogation window, and so is not an appropriate tool for this situation.

An extraction method is also proposed to investigate blade-vortex interaction noise emitted during helicopter transient maneuvering flight. The extraction method allows for the investigation of blade-vortex interactions independent of other sound sources. The method is based on filtering the spectral data calculated through the wavelet transform technique. The filter identifies blade-vortex interactions through their high amplitude, high frequency impulsive content. The filtered wavelet coefficients are then inverse transformed to create a pressure signature solely related to blade-vortex interactions.

This extraction technique, along with a prescribed wake model, is applied to experimental data extracted from three separate flight maneuvers performed

by a Bell 430 helicopter. The maneuvers investigated include a steady level flight, fast- and medium-speed advancing side roll maneuvers. A sensitivity analysis is performed in order to determine the optimal tuning parameters employed by the filtering technique. For the cases studied, the optimized tuning parameters were shown to be frequencies above 7 main rotor harmonics, and amplitudes stronger than 25% (−6 dB) of the energy in the main rotor harmonic. Further, it is shown that blade-vortex interactions can be accurately extracted so long as the blade-vortex interaction peak energy signal is greater or equal to the energy in the main rotor harmonic.

An in-depth investigation of the changes in the blade-vortex interaction signal during transient advancing side roll maneuvers is then conducted. It is shown that the sound pressure level related to blade-vortex interactions, shifts from the advancing side, to the retreating side of the vehicle during roll entry. This shift is predicted adequately by the prescribed wake model. However, the prescribed wake model is shown to be inadequate for the prediction of blade-vortex interaction miss distance, as it does not respond to the roll rate of the vehicle. It is further shown that the sound pressure levels are positively linked to the roll rate of the vehicle. Similar sound pressure level directivities and amplitudes can be seen when vehicle roll rates are comparable.

The extraction method is shown to perform admirably throughout each maneuver. One limitation with the technique is identified, and a proposal to mitigate its effects is made. The limitation occurs when the main rotor harmonic energy drops below an arbitrary threshold. When this happens, a decreased spectral amplitude is required for filtering; which leads to the extraction of high frequency noise unrelated to blade-vortex interactions. It is shown, however, that this occurs only when there are no blade-vortex interactions present. Further, the resulting sound pressure level is identifiable as it is significantly less than the peak blade-vortex interaction sound pressure level. Thus the effects of this limitation are shown to be negligible.

Table of Contents

Nomenclature

Acronyms

AR	Advancing side Roll maneuver
BVISPL	Blade-Vortex Interaction Sound Pressure Level
DGPS	Differential Global Positioning System
DNW	German-Dutch Windtunnel
FW-H	Ffowcs Williams - Hawkings
HART	HHC Aeroacoustic Rotor Test
HELENA	HELicopter Environmental Noise Analysis
HHC	Higher Harmonic pitch Control
MR	Main Rotor
OASPL	Overall Sound Pressure Level [ref: 20μPa]
RNM	Rotorcraft Noise Model
RSPL	Residual Sound Pressure Level
SLF	Steady Level Flight maneuver
SPL	Sound Pressure Level
STFT	Short-time Fourier Transform
TPP	Tip-Path Plane
TR	Tail Rotor
WPS	Wavelet Power Spectrum
WT	Wavelet Transform

Greek Symbols

α	Tip-path plane angle of attack

β	Mach angle ($= \sin^{-1}(1/M_{tr})$)
χ	Wake skew angle ($= \tan^{-1}(\mu_x/\lambda)$)
δ	Dirac delta functional
γ	Flight path angle
γ_v	Blade-vortex interaction angle
Λ	Modified Beddoes' wake inflow
λ	Inflow
μ	Advance ratio ($= V_\infty/(\Omega R)$)
μ_x	Advance ratio in x_H direction ($= \mu\ \cos(\alpha)$)
μ_z	Advance ratio in z_H direction ($= \mu\ \sin(\alpha)$)
Ω	Rotation rate
ω	Angular frequency
ω_ψ	Non-dimensional Morlet frequency
ϕ	Bank angle
ψ	Blade azimuth angle
ψ_D	Derivative of Gaussian wavelet
ψ_M	Morlet wavelet
ψ_w	Mother wavelet
ρ	Air density
σ	Rotor solidity
θ	Elevation

Other Symbols

$\Box^2$	Wave operator
$\overline{\partial}$	Distributional derivative
$\widehat{(\bullet)}$	Fourier transform of $(\bullet)$

$\widetilde{(\bullet)}$	Wavelet coefficients of $(\bullet)$
f-	Fast speed maneuver
m-	Medium speed maneuver

Roman Symbols

(X, Y, Z)	Inertial coordinate system
(x, y, z)	Local coordinate system
$\overline{\alpha}$	Atmospheric absorption length scale
A	Rotor area
$a_{(\bullet)}$	Acceleration force in $(\bullet)_H$ direction
c	Main rotor chord length (0.34 m)
$C(\eta)$	Shannon entropy cost function
c_0	Speed of sound
C_T	Thrust coefficient $(= T/(\rho A(\Omega R)^2))$
C_ψ	Wavelet admissibility factor
C_{d_0}	Zero-lift drag coefficient
D	Vehicle drag
E	Wavelet power spectrum
E_ψ	Mother wavelet energy
f_e	Flat plate drag area
f_{MR}	Main rotor harmonic frequency (23.2 Hz)
f_{surf}	Blade surface coordinate system
H	Heaviside functional
H_d	Rotor drag force
l	Wavelet scale
l_i	Local force normal to the surface

M_{tr}	trace Mach number
N	Number of samples
n	Order for derivative of Gaussian wavelet ($n \in \mathbb{N}$)
p	Time history of microphone pressure signal
p_{ref}	Reference pressure (20 μPa/$\sqrt{Hz}$)
R	Rotor radius
r	Non-dimensionalized rotor radius ($= \sqrt{x_H^2 + y_H^2}/R$)
T	Thrust
T_{ij}	Lighthill stress tensor
V	Velocity
v_n	Local velocity normal to the surface
v_r	Velocity through rotor
W	Vehicle weight

Subscripts

$(\bullet)_H$	Helicopter centered coordinate system
∞	Free-stream condition
i,j,k	Einstein notation of coordinate direction

List of Tables

List of Figures

Chapter 1

Introduction

Understanding helicopter transient maneuvering acoustics is the next great hurdle to overcome in the world of helicopter acoustics. While there is still much work to be done across the width and breadth of the helicopter acoustics field, insight into transient maneuvering acoustics is still lacking [18]. The effects of these maneuvers are of special importance to the military as maneuvering is known to impact vehicle acoustics, and therefore vehicle detection. Civilian impacts are also important, as vehicle maneuvers can impact community annoyance levels.

Unfortunately, experimental helicopter acoustics are predominantly relegated to expensive, full-scale flight tests or scaled ($\approx 1/7^{th}$) wind tunnel tests [110, 113]. This results in relatively few experiments, with which numerical results can be validated against. The primary necessity of having full-scale experiments comes from scaling issues involved with matching the full-scale hover tip Mach number [9]. Recent advances in model scale ($\approx 1/15^{th}$) technology have made reaching full-scale tip Mach numbers much easier, but it is still questionable if the scaling parameters can hold at this size [83, 92, 102]. It is possible that viscous effects due to lower Reynold's numbers, flow separation, aeroelastic effects, etc. will limit the usefulness of model scale investigations, especially when replicating transient maneuvers [92].

Transient maneuvering acoustics faces another challenge, caused by the very nature of its transitory signature. The selection of an appropriate analysis tool for characterizing sound intensity and spectral content of a transient signal is non-trivial. In the case of stationary systems, statistical properties can be generated through ensemble averages over long data sets. Because transient signals are non-stationary, the temporal component of the signal must be preserved, and

ensemble averages are no longer possible. Hence, a persistent difficulty in the statistical modeling of transient phenomena is determining the suitability of the analysis technique [3].

This work simultaneously pursues a suitable analysis technique and attempts to extract signals related to blade-vortex interactions associated with transient maneuvering acoustics. This will shed light on how transient maneuvers affect the noise footprint of a helicopter, while also providing a way to isolate the effects such maneuvers have on the impulsive blade-vortex interaction noise. A review of helicopter acoustics is provided in § 1.1, where a detailed breakdown of the known acoustic phenomena is provided. This is followed by a review of time-frequency analysis techniques in § 2, focusing primarily on wavelet transforms. The experimental description is provided in § 3, followed by initial results obtained through the wavelet transforms in § 4. The discussion continues with the development of a blade-vortex interaction extraction method description in § 5. The method is first applied to synthetic data in order to determine its strengths and potential weaknesses. Then, the blade-vortex interaction extraction method is applied to full-scale, experimentally acquired Bell 430 acoustic data in § 6. § 6 will demonstrate clearly how transient maneuvers effect both the overall radiated noise patterns and noise associated with blade-vortex interactions. Finally, a review of the pertinent findings is provided in § 7.

1.1 Review of Helicopter Aeroacoustics

The fundamentals of helicopter noise are now described. For the purposes of this discussion the subject of helicopter aeroacoustics has been divided into five categories. Thickness and loading noise mechanisms will be discussed together in § 1.1.1, while blade-vortex interactions are discussed in § 1.1.2. Broadband noise mechanisms are discussed in § 1.1.3, followed by a brief discussion on quadrupole noise sources in § 1.1.4. The review of helicopter acoustics will end in § 1.1.5 with a discussion looking into the current understanding of transient maneuvering noise. A sketch of these noise sources and their general directivities are given in figure

1.1 and is based off an illustration provided in Greenwood (2011) [53]. A brief

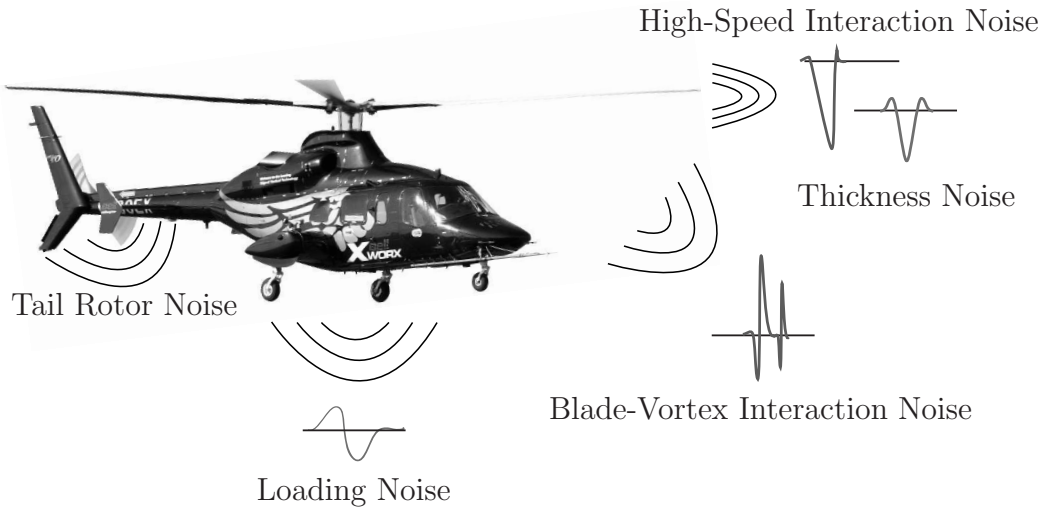

Figure 1.1: Typical pressure signal and approximate directivity pattern for the main vehicle noise sources.

review of the status of rotor wake predictions will follow in § 1.2.

The state of helicopter noise experiments and predictions have advanced greatly, since the early works of Gutin (1948) [57] and Garrick and Watkins (1954) [45]. Specifically, great progress has been made over the past several decades using the acoustic analogy put forth by Lighthill (1952) [70]. Lighthill's acoustic analogy used the method of distributions to rework the compressible Navier-Stokes equation into the form of an inhomogeneous wave equation. Lighthill's acoustic analogy led to the development of the Ffowcs Williams - Hawkings (FW-H) equation [43], given as,

$$\Box^2 p(\mathbf{x},t) = \overbrace{\frac{\overline{\partial}}{\partial t}[\rho_\infty v_n \delta(f_{surf})]}^{\text{Monopole}} - \underbrace{\frac{\overline{\partial}}{\partial x_i}[l_i \delta(f_{surf})]}_{\text{Dipole}} + \overbrace{\frac{\overline{\partial}^2}{\partial x_i \partial x_j}[T_{ij} H(f_{surf})]}^{\text{Quadrupole}}. \qquad (1.1)$$

Here, $\Box^2$ is the d'Alambert (wave) operator, with p representing the acoustic pressure signature. ρ is the density of air, v_n is the local velocity normal to the surface of the rotor blade (f_{surf}) and δ is the Dirac delta function. T_{ij} is the Lighthill stress tensor, H is the Heaviside functional and l_i is the local force acting on the rotor blade in the i'th direction. The right-hand side of the FW-H equation

are aerodynamic forcing terms of the acoustic wave equation represented by the left-hand side. The aerodynamics result in forcing terms that act as monopole, dipole, and quadrupole noise sources.

To date, the physical mechanisms responsible for the generation of discrete frequency noise from helicopters are fairly well understood. Brentner and Farassat (1994, 2003) [14, 15] provide an extensive overview of the current prediction capabilities of the five distinct noise mechanisms identified as thickness noise, loading noise, blade-vortex interaction noise, high speed impulsive noise and broadband noise. Brentner and Farassat also identify the parameters necessary for predicting each noise mechanism [14]. Thickness noise is caused by the physical presence of the blade disturbing the fluid, and is represented by the monopole (first) term in the FW-H equation. Thickness noise propagates primarily in the plane of the rotor, while loading noise, represented by the second, dipole term in the FW-H equation, propagates primarily beneath the vehicle [88]. High speed impulsive noise is predicted by the quadrupole (third) term in the FW-H equation [14]. This noise source also propagates in the plane of the rotor, as shown in figure 1.1. However, this noise source is not of great concern to modern commercial helicopters as it is easily avoided by decreasing the hover tip Mach number and employing slower advance speeds.

Blade-vortex interaction noise and broadband noise are both included in the dipole term of the FW-H equation, but are caused by distinctly different sources than what is typically referred to as loading noise [14]. A sample time history extracted from the current experiment is provided in figure 1.2, where thickness and loading noise together are identified as main rotor lower harmonic noise. Blade-vortex interaction noise, also identified in the sample time pressure history in figure 1.2, will be discussed in depth in § 1.1.2. Blade-vortex interaction noise is typically seen in the higher harmonics and affects the dipole term by creating an impulsive aerodynamic load on the rotor blades [77]. Broadband noise, discussed in § 1.1.3, is also represented in the dipole term [14]. Figure 1.2 includes the tail rotor signature which is typically ignored or modeled independently from the main rotor [14], although main-tail rotor interactions do occur [44].

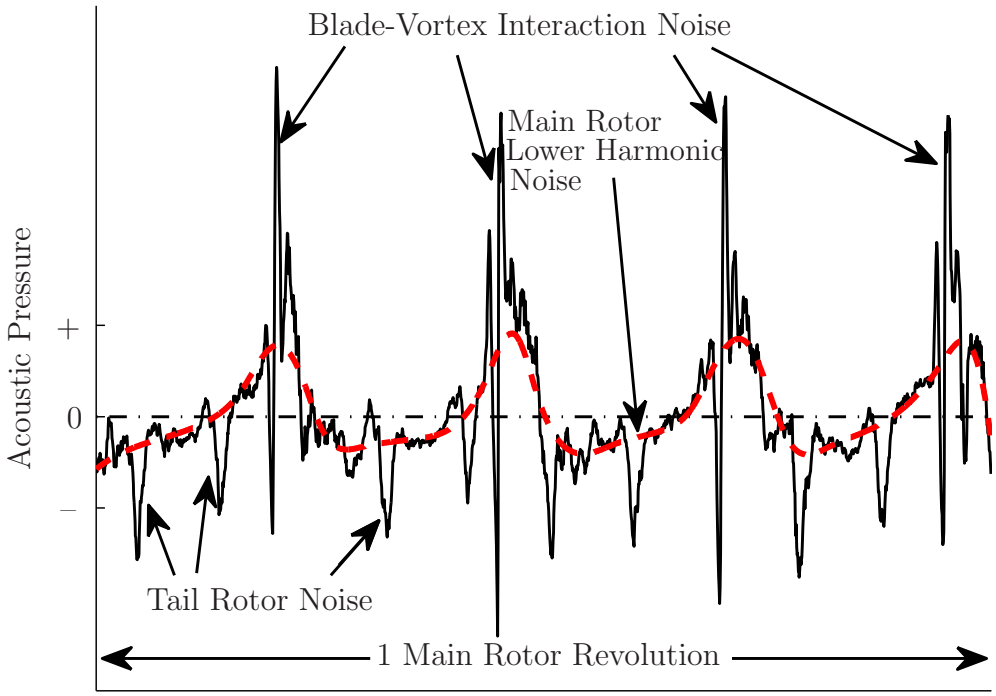

Figure 1.2: Acoustic pressure time history of a full rotor revolution identifying the main rotor lower harmonic noise, tail rotor noise, and blade-vortex interaction signatures. The lower harmonic noise signature provided is for reference only.

Several formulations of the FW-H equation have been developed to predict helicopter noise [36, 37, 40]. Computational codes such as WOPWOP are now available that can predict the acoustic footprint of a helicopter under steady flight regimes. WOPWOP was first developed at NASA by Brentner (1986) [11], and works by utilizing the Ffowcs Williams - Hawkings equation coupled with input blade loading and flow field information to predict the resulting acoustic signal of the vehicle [12].

Computational codes based on experimental data have also been developed to predict the acoustic footprint of a helicopter, including the Rotorcraft Noise Model (RNM) and the European Helicopter Environmental Noise Analysis (HELENA). RNM and HELENA, predict the acoustic footprint of a vehicle by matching each segment of a planned flight path, through an interpolation scheme, to a previously captured acoustic hemisphere [48, 75]. The signals that comprise

that acoustic hemisphere is then propagated to the ground plane and adjusted for atmospheric attenuation and ground effects. These codes rely on having access to a substantial database of acoustic hemispheres for multiple vehicles undergoing various steady flight maneuvers. WOPWOP does not rely on such a database, but it requires inputs about blade loading and the rotor flow field that are typically only available through coupling with a high-fidelity computational fluid dynamics flow solver and a computational structural dynamics solver [19, 22] or through experimentally acquired data [108].

1.1.1 Thickness and Loading Noise

Initial investigations into predicting helicopter noise focused on the thickness and lower harmonic loading noise components [60, 105]. The thickness noise term requires knowledge of blade geometry and motion, while the loading noise term also requires knowledge of the time dependent loads on the blades [14]. Dahan and Gratieux (1981) [32] worked analytically to show that loading noise dominates beneath the rotor system while thickness noise was the dominant source mechanism elsewhere. While Glegg (1987) [49] worked to further understand thickness noise by extending application of the FW-H equation to include unsteady gusts.

Initial work into determining the acoustic sensitivity to WOPWOP's input parameters was provided by Brentner, Burley and Marcolini (1991) [13]. Using pressure data acquired in the German-Dutch Windtunnel (DNW), Brentner *et al.* (1991) showed that acoustic emissions along the tip-path plane were highly susceptible to input errors, including variations in blade loading and blade motions. However, outside of this region the predicted acoustic emissions were less sensitive to input errors. Thus, quicker quality acoustic predictions could be obtained, outside of the tip-path plane, by making judicious use of engineering approximations.

Farassat and Brentner (1998) [39] investigated the comparison between WOPWOP prediction code, Euler analysis, and experimental measurements from

a UH-1H model rotor in hover. The comparison between WOPWOP and experiment are depicted in figure 1.3 alongside the prediction of the various noise

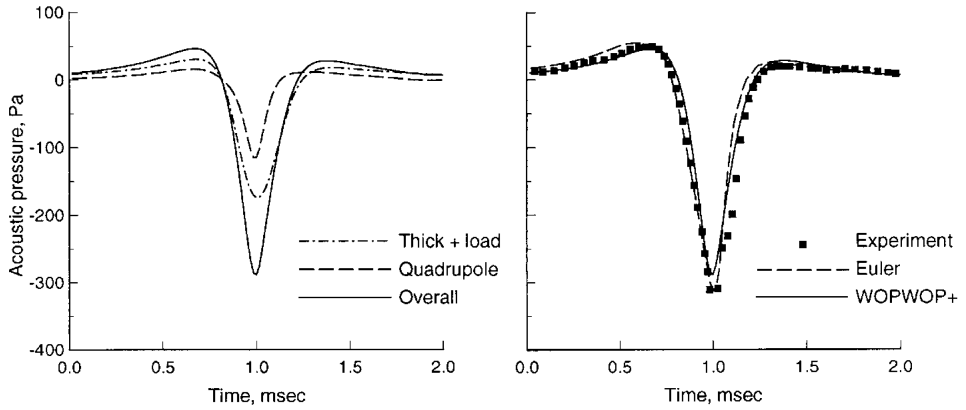

Figure 1.3: Comparison of WOPWOP+ prediction code with UH-1H model rotor experimental data at a tip Mach number of 0.88 [39].

sources identified by the FW-H equation. The right-hand side of figure 1.3 shows the comparison of WOPWOP with the experimental data as well as calculations obtained directly from the Euler equations [39]. Farassat and Brentner showed the relative importance of the quadrupole noise source for the model rotor with a tip Mach number of 0.88.

Overall, the prediction of main rotor lower harmonic noise is well understood, but relies almost entirely on having accurate blade loading and blade motion inputs [14]. Due to advances in computational power and formulations, accurate predictions for main rotor lower harmonic noise in steady-forward flight, are currently available directly through computational fluid dynamics, as demonstrated recently by Sim *et al.* (2010) [96]. Computational fluid dynamics have been used before, including Baeder's (1991) [4] work on non-lifting, hovering rotor blades, to predict helicopter acoustics. Sim *et al.* (2010) demonstrated that computational power and formulations have advanced sufficiently enough to model helicopters undergoing realistic flight conditions.

1.1.2 Blade-Vortex Interaction Noise

Of great and continuing importance to the helicopter acoustics field, is the prediction of blade-vortex interactions. Blade-vortex interactions occur when a blade passes in close proximity to the tip vortex generated by a preceding blade. Noise from such interactions is predictable, but requires high-fidelity pressure data from the surface of the blades [14]. A great deal of experimental and theoretical research has focused on blade-vortex interactions due to the severity of the noise produced by this process. A review of the research into blade-vortex interactions was provided by Schmitz and Yu (1983, 1986) [88, 89], where it was shown that blade-vortex interaction noise propagates predominantly forward and below the vehicle.

Several experimental programs are of note, especially the pioneering work of Schmitz and Boxwell (1976) [82] who used an OV-1C airplane to fly in front of a UH-1H helicopter, shown in figure 1.4, to capture the directivity pattern

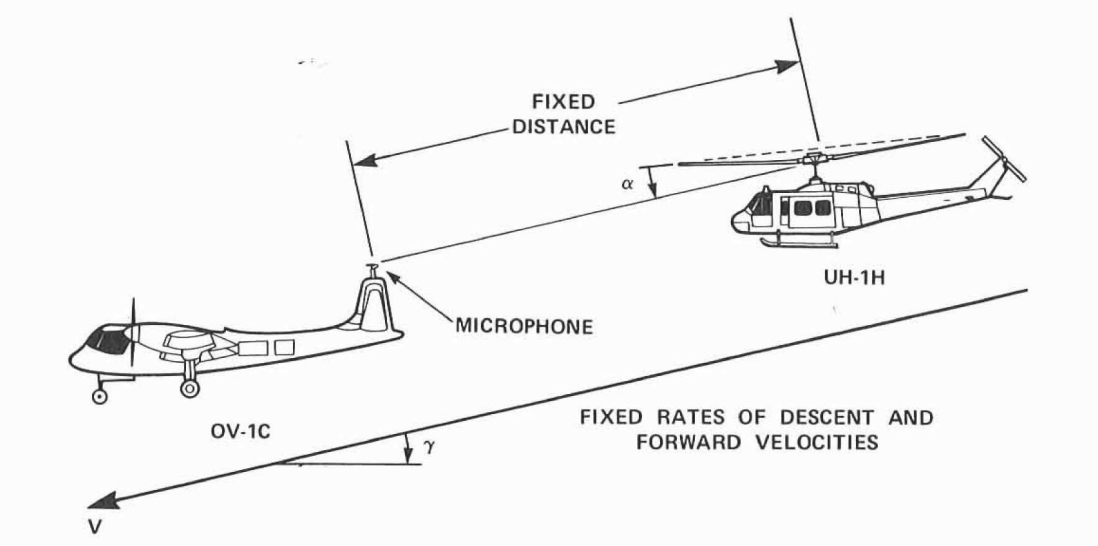

Figure 1.4: Schematic of in-flight far-field measurement technique from Schmitz and Boxwell [82].

of impulsive noise during descent flight conditions. In figure 1.4, γ is the angle of the flight path, and α represents the elevation angle relative to the vehicle. Other notable experimental investigations include the works of Brooks, Jolly and

Marcolini (1988) [20] who investigated a 40% scaled BO-105 helicopter main rotor in the anechoic German-Dutch Windtunnel. Through the use of various noise metrics, Brooks *et al.* (1988) showed that blade-vortex interaction noise was the dominant source mechanism during moderate descent flight conditions. During steady level flight and ascent conditions, they saw a new phenomenon become important, which they called blade-wake interaction noise. At high rates of ascent, Brooks *et al.* (1988) noticed that a new acoustic mechanism they called "rotor self noise" became significant.

Later experiments conducted in the DNW showed that blade-vortex interactions could also occur in some forward flight operations [73]. A single scaled model main rotor was investigated by Schmitz *et al.* (2000) [84], in both the DNW and French CEPRA-19 wind tunnel. They showed that good acoustic agreement could be made between facilities when measurements from the blade mounted pressure transducers were matched. However, they also showed that agreement between scaled rotors and full-scale systems was good for low advance ratios, but was less accurate at moderate and high advance ratios [84].

It has been shown by Hubbard and Leighton (1984) [63], that blade-vortex interactions on the retreating side of the rotor disk can be of greater intensity than those seen on the advancing side. Meanwhile, data from a $1/7^{th}$ scale model rotor in the DNW and a full scale flight test similar to that of Schmitz and Boxwell (1976) [82] were compared by Splettstoesser *et al.* (1984) [101]. They used this data to develop scaling parameters for matching model scale to full scale data. Figure 1.5 shows the comparison between model-scale (M/S) and full-scale (F/S) signatures where blade-vortex interaction is shown predominantly directed below the rotor. In figure 1.5, the advancing side tip Mach number (M_{AT}), advance ratio (μ), thrust coefficient (C_T) and rotor disc angle of attack (α_{TPP}) are provided. Rate of descent (R/D) and wind tunnel velocities (V_T) are also given along with the elevation (ϕ) and azimuthal (θ) angle of each microphone. Splettstoesser *et al.* (1984) showed that four non-dimensional parameters greatly influence blade-vortex interaction noise characteristics and directivity [101]. These are: hover tip Mach number, advance ratio, inflow ratio, and the coefficient of thrust.

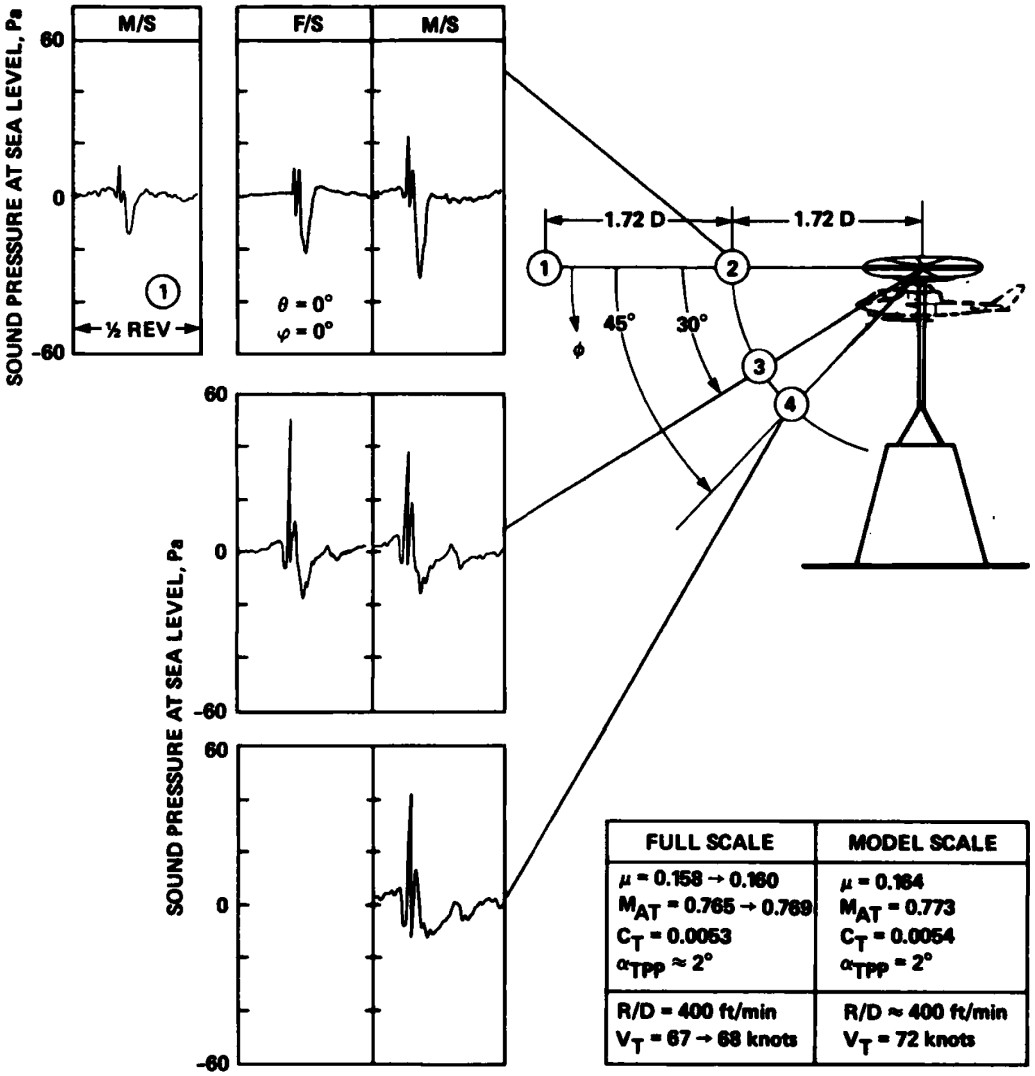

Figure 1.5: Comparison of model- to full-scale acoustic signals focusing on longitudinal directivity of blade-vortex interactions [101].

It was further identified by Hardin and Lamkin (1986) [58], that the incoming vortex strength, span over which the vortex interaction occurs, local blade lift during the interaction, and the miss distance of the vortex are all vital parameters in determining the noise produced during a blade-vortex interaction event. The four parameters identified by Hardin and Lamkin are equivalent to those identified by Splettstoesser *et al.* (1984), as each parameter set can be determined from the other. It has also been shown by Widnall and Wolf (1980) [112], that the

distribution of vorticity inside of the tip-vortex can impact the intensity of the acoustic signal related to blade-vortex interaction events.

1.1.2.1 Determination of Acoustic Directivity

It is now known that blade-vortex interactions do not always result in noise signatures that propagate into the far-field. Instead, certain physical conditions have to be met in order for the interaction to result in an acoustically radiating noise that propagates in a preferred direction.

The physical mechanisms relating to the noise propagation of blade-vortex interactions were investigated early on by Lyrintzis and George (1989) [76]. Lyrintzis and George (1989) used a Kirchoff based numerical method to verify the postulate of Widnall (1971) that blade-vortex interaction noise propagates along the Mach angle defined by the trace Mach number (M_{tr}). The trace Mach number is defined as,

$$M_{tr} = \frac{(\Omega R)\ r + V_\infty\ \sin(\psi)}{c_0\ \sin(\gamma_v)}, \tag{1.2}$$

where Ω is the rotor rotation rate and R is the rotor radius. The non-dimensional position along the rotor radius is represented by r. V_∞ is the velocity of the vehicle relative to the wind and c_0 is the speed of sound. ψ and γ_v are the azimuthal angle of the rotor blade and the angle between the rotor blade and vortex path, respectively. Figure 1.6 shows the trace Mach number, blade-vortex interaction

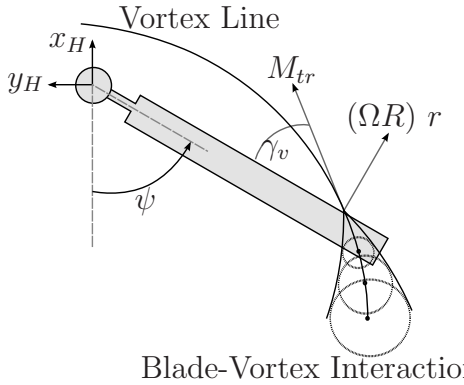

Figure 1.6: Sketch of an oblique blade-vortex interaction with trace Mach number identified. Relevant blade-vortex interaction angles are also identified.

sound waves and relevant angles.

When the collocation of a blade and tip vortex result in a supersonic trace Mach number, then the acoustic wave fronts sum in phase along the sonic cone [87, 111]. This creates a strong and impulsive noise that propagates along the Mach angle ($\beta = \sin^{-1}(1/M_{tr})$) [74]. If a tip vortex is perpendicular to the leading edge of a rotor blade during a blade-vortex interaction, then the trace Mach number is zero and the Mach angle is parallel with the blade. For a tip vortex that is parallel with the rotor blade, the trace Mach number is infinity and the acoustics propagate perpendicular to the leading edge of the rotor blade.

This trace Mach number analysis technique was later expanded on by Schmitz and Sim (2001) [87], who used simplified mathematical models of blade-vortex interactions. They showed that noise amplitudes relating to oblique blade-vortex interactions had a strong dependence on the trace Mach number. This leads to the fact that parallel blade-vortex interactions tend to be the most acoustically important event, when they occur.

1.1.2.2 Noise Mitigation Techniques

Over the years efforts to damp the noise generated by blade-vortex interactions have been proposed. Of those, the most promising have been based on differing designs of the blade tip shape, and actively controlling the rotor blades themselves [113]. A device to drastically increase vehicle drag during landing maneuvers was proposed by Schmitz, Gopalan and Sim (2002) [85]. The effect of such a device would force the rotor to entrain more air, thereby increasing the miss-distance of the vortex and reducing blade-vortex interaction during landing procedures. Blade tip design changes have proven successful in reducing blade-vortex interaction noise [113], but along with the drag-type device proposed by Schmitz *et al.* (2002) [85], they come at the cost of rotor performance characteristics.

An extensive experiment to investigate higher harmonic pitch control (HHC) was undertaken by the US Army in collaboration with NASA Langley, the DNW, France and Germany [100]. Higher harmonic pitch control superimposes a vi-

bration on the swashplate, completely independent of the standard swashplate inputs, at a frequency higher than once per revolution. The HHC Aeroacoustic Rotor Test (HART) experiment captured rotor acoustics, aerodynamics and performance characteristics while tracking the blade motion and deflections of a model BO-105 main rotor. This experimental database was made available for code validation and has lead to a multitude of papers [107, 113, 114]. Brooks *et al.* (2000) [19] combined a rotor wake and blade loads calculator with WOPWOP in order to predict the blade-vortex interaction noise generated during the HART test cases. A sample of their results is shown in figure 1.7, for the minimum vibra-

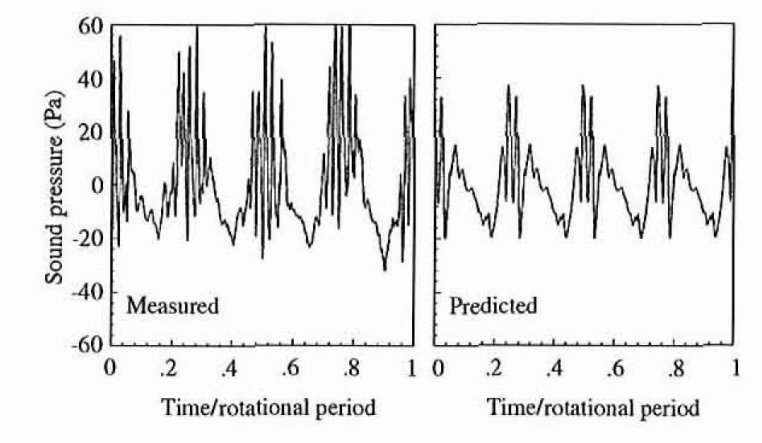

Figure 1.7: Measured and predicted noise signature extracted from the HART data set for the HHC test case that resulted in minimum vibration [19].

tion case of the HART data set. It is seen that their method under-predicts the impacts of blade-vortex interaction noise. This under-prediction is attributed to their rotor wake model, which was based on vortex roll-up models for fixed wing vehicles.

One key finding of the HART test was that HHC could change the vortex trajectory in such a way that parallel blade-vortex interactions are avoided. These types of interactions are particularly powerful as the trace Mach number is exceptionally high and so the process is acoustically efficient. This result lead to van der Wall's (2000) [107] work in expanding Beddoes' prescribed wake model to be able to account for the effects of HHC on the rotor inflow.

Concurrently, Caradonna *et al.* (2000) [23] performed an extensive comparison between available aeroacoustic methods designed to predict blade-vortex interaction noise. Using data acquired from an experimental arrangement with a scaled rotor in the NASA Ames 80 by 120 foot wind tunnel, they determined that the acoustics are well predicted when the aerodynamics around each blade are well defined. Specifically, the characteristics of the interacting tip vortex must be accurately known. Tip vortex characteristics were controlled in the experimental portion of the project as the interacting vortex was generated by a fixed wing mounted upstream of the rotor system, and not generated by the rotor itself.

The HART project was followed by another collaborative effort between the US Army, NASA Langley, France, Netherlands and Germany, entitled HART-II [115]. HART-II was conducted in the DNW with a 40% geometric and aeroelastically scaled BO-105 main rotor system. The HART-II project focused on understanding the flow physics resulting from HHC inputs, and the effect that had on rotor noise and vibration [115]. Blade surface pressures, blade deformations, rotor acoustics and rotor flow field were all examined to better understand the resulting physics.

Boyd (2009) [10] was later able to predict the acoustics for multiple cases investigated in the HART-II project, by using a coupled computational fluid dynamics and structural dynamics method. Other researchers also investigated coupling computational fluid dynamics and structural dynamics codes together in order to predict blade-vortex interaction noise [64, 71, 95]. Each found predicted noise amplitudes that compared favorably with the HART-II data set. The effects that aeroelastic modeling of the rotor blades has on blade-vortex interaction noise prediction was investigated by Bernardini *et al.* (2006) [7]. They showed that proper modeling of the blade deformations was important for accurate noise prediction as deflections, especially of the blade tips, affects the vertical miss distance of the tip vortex during blade-vortex interactions.

The HART and HART-II projects demonstrated reduction in the blade-vortex interaction noise through HHC inputs. However, this noise reduction oc-

curred simultaneously with an increase in the vibration experienced by the rotor hub [114, 115]. This lead to the computational work of Liu, Patt and Friedmann (2004) [72] who showed that simultaneous vibration and noise reduction could be achieved with a dual active flap operating on each rotor blade, working in conjunction with HHC. Therefore, blade-vortex interaction noise can be reduced but currently implemented methods come at the cost of rotor performance.

1.1.3 Broadband Noise

Broadband noise requires extensive knowledge of the flow field around the blades, and is also predicted through the dipole term in equation (1.1) [14, 79]. Broadband noise is generated through various mechanisms including turbulence ingestion from the atmosphere, blade self-noise through turbulence generated in the boundary layer of the blade itself, and turbulence associated with a tip-vortex interacting with the rotor system [14]. Each mechanism that results in broadband noise requires separate modeling techniques, and so advancement in predicting this noise source is still necessary. High speed impulsive noise, on the other hand, is well known and is generated when the helicopter blades experience transonic flow, which results in non-linear acoustic effects caused by shocks and other phenomena [90]. Predicting high speed impulsive noise requires extensive knowledge of the flow field around the blade [14].

The effects of turbulence ingestion through a 0.76 meter diameter rotor stand underneath various inflow conditions were investigated by Paterson and Amiet (1979) [79]. It was seen that atmospheric turbulence noise and steady loading noise were the two dominant noise sources in hover conditions. They also determined that broadband noise due to turbulence ingestion was directly proportional to the number of rotor blades, but insensitive to changes in pitch of the rotor blades. Later, George and Chou (1984) [47] investigated several broadband noise mechanisms and identified their associated frequency bands. George and Chou discovered that inflow turbulence noise produced strong low frequency content, while noise due to the trailing edge of the blade and tip vortex generation were found to produce higher frequency sounds.

A similar experiment as George and Chou was performed by Brooks, Marcolini and Pope (1987) [21] in the DNW. They were able to identify the blade-wake interaction noise mechanism and showed it was dominant in the mid-frequency range (approximately 15^{th} to 85^{th} blade passage harmonics) when blade-vortex interactions were not dominant. Brooks *et al.* (1987) also showed that this noise mechanism was very sensitive to changes in the tip-path plane orientation and the vehicle advance ratio. Research into blade-wake interactions was continued by Glegg (1991) [50], who showed it was associated with blade-vortex interactions occurring in the forward section of the rotor system. Later, Zhou and Joseph (2006) [116] developed a method to predict the rotor self-noise mechanism. Their frequency-domain method showed that rotor self-noise was directed predominantly along the rotor axis.

1.1.4 Quadrupole-Term Noise

Quadrupole-term noise sources require significant knowledge of the aerodynamic flow-field near the rotating blades. Due to computational limitations, this term was neglected in early research. The significance of quadrupole sources on rotorcraft acoustics was investigated by Farassat and Brentner (1991) [38]. They found that noise from volume and shock surfaces can have substantial effects on the noise propagated in the plane of the rotor. Thus, they showed that quadrupole source terms contained in Lighthill's stress tensor must be retained in the FW-H equation for high-speed rotor systems. Later, in Farassat and Brentner (1998) [39], they compared data from the WOPWOP acoustic prediction code with an Euler method and a UH-1H model rotor in hover. Figure 1.8 shows the comparison for a case where the hover tip Mach number was 0.95. At this tip speed, they showed that the quadrupole source term is incredibly important as shocks have formed on the rotor blades.

1.1.5 Transient Maneuvering Flight Noise

The studies described so far have been focused on the acoustics generated by helicopters in steady state flight conditions. However, the effects of transient

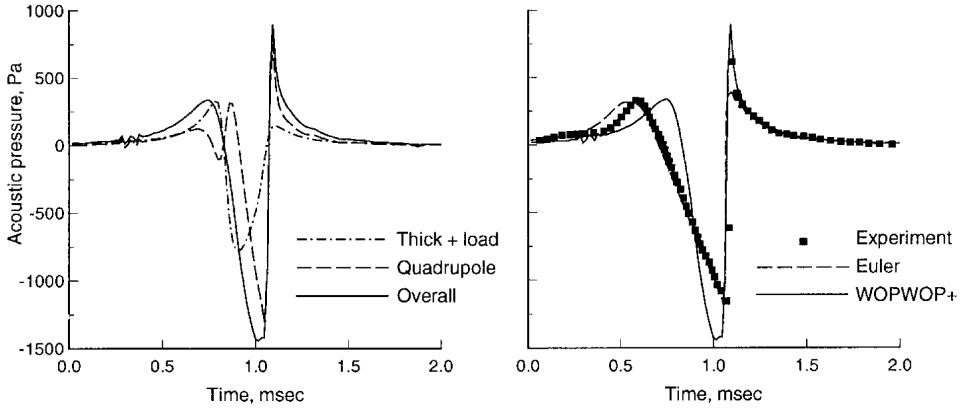

Figure 1.8: Comparison of WOPWOP+ prediction code with UH-1H model rotor experimental data at a tip Mach number of 0.95 [39].

maneuvers can have substantial impacts on the noise emitted by a helicopter. To date, the noise generated by maneuvering flight has been predominantly focused on steady maneuvers including steady turns and ascent/descents. The effects of transient maneuvers, where a vehicle transitions from one steady maneuver into another, has only recently been investigated. Research into the prediction of acoustics resulting from transient maneuvers was initiated by Brentner and Jones (2000) [16] who used numerical simulations to investigate an arrested descent flight condition. Full-scale experiments into transient maneuvers was initiated by Spiegel *et al.* (2005) [99], followed closely by Schmitz *et al.* (2007) [86], and later by Watts *et al.* (2012) [110]. Understanding and predicting the acoustic effects of transient maneuvers can be used to reduce community annoyance levels near heliports as well as detection distances for helicopters in flight.

The PSU-WOPWOP code developed by Brentner *et al.* (2002) [18] and more thoroughly described in Bres *et al.* (2004), expands greatly on the original WOPWOP code to allow for the investigation of transient flight maneuvers. The PSU-WOPWOP code was coupled with GENHEL and used by Brentner *et al.* (2003) [17] to investigate a transient roll maneuver. GENHEL is a vehicle dynamics modeling code that provides blade motions and loading. Brentner *et al.* (2003) concluded that acoustic amplitude is affected during a transient roll maneuver.

The GENHEL-PSU-WOPWOP code was also used by Chen *et al.* (2004) [26] to investigate a flight maneuver that included an ascending portion, two steady level sections and a coordinated turn. In this study, they attempted to investigate changes solely due to the transient maneuver noise by numerically predicting the acoustic signal on a sphere surrounding the helicopter at 30 rotor radii away. They then projected this data onto a Cartesian grid based on azimuthal (ψ) and elevation (θ) coordinates. This technique is shown in figure 1.9 where the azimuthal coordinate is centered on the rotor hub and starts along the

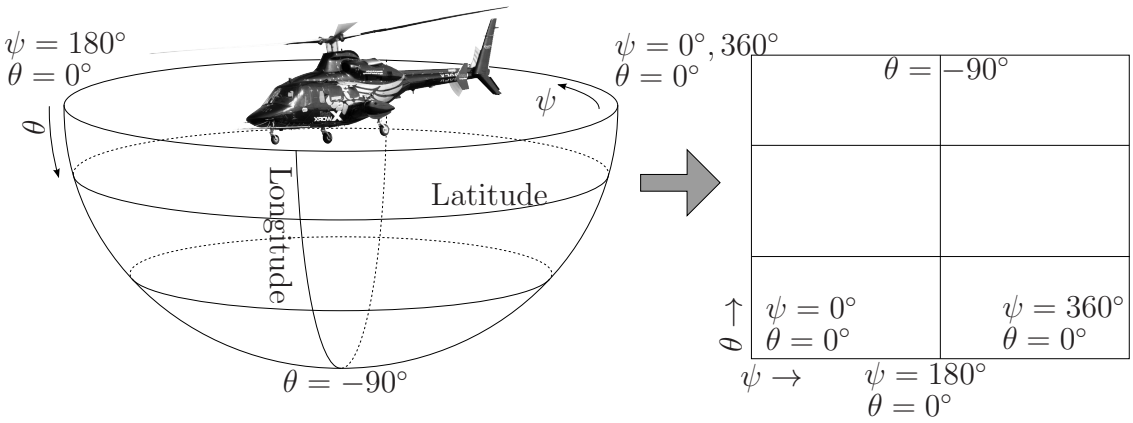

Figure 1.9: Spherical, helicopter centered grid to Cartesian transform.

tail. Azimuth increases counterclockwise with the rotor when seen from above, so that $\psi < 180°$ is on the advancing (right) side of the vehicle and $\psi > 180°$ indicates the retreating (left) side of the rotor disc. The elevation coordinate begins at $\theta = 0°$ in the plane of the rotor and decreases until $\theta = -90°$ directly beneath the rotor hub. While blade-vortex interactions were not included in this investigation, Chen *et al.* (2004) showed that acoustic directivity along with amplitude, is affected during a transient maneuver [26]. The change in noise was shown to correspond well with an associated change in directivity and amplitude of the loading noise mechanism.

Later, the PSU-WOPWOP code was coupled to a free wake vortex method to investigate "pop-up", "pop-down" and arrested descent flight conditions by Hennes *et al.* (2004) [59]. The "pop-up" condition is a flight maneuver where a vehicle in hover rapidly rises to a new altitude and holds. The "pop-down"

maneuver is the inverse situation, and an arrested descent is where a vehicle in forward flight descends rapidly to a new altitude and then holds at that altitude. Comparing to the works of Brentner *et al.* (2002), Hennes *et al.* (2004) suggests that a more accurate free wake model is necessary for predicting acoustics during transient maneuvers [17, 59]. Hennes *et al.* concluded that the simplified blade loading information provided by GENHEL is insufficient for accurately predicting the blade-vortex interactions.

A competing noise computation algorithm was described by Perez and Costes (2004) [80], and was based on the European codes HOST - MINT - MENTHE - ARHIS and MANEUVER PARIS. Essentially, Perez and Costes used a newly developed free wake code (MINT) coupled with a FW-H solver (MANEUVER PARIS). They investigated an advancing side roll maneuver and saw a 10 dB increase in noise level immediately upon initiation of the roll maneuver. This increase in noise was determined to be caused by an increase in blade-vortex interaction noise due to a decrease in miss distance on the advancing side of the rotor.

Advancing side transient roll maneuvers were also numerically investigated by Chen, Brentner, and Shirey (2005) [28], although they used the PSU-WOPWOP program chain described in Hennes *et al.* (2004) [59]. The aggressive dynamic advancing side roll maneuver investigated, lead to the advancing side vortices bundling together before interacting with the rotor. Chen *et al.* (2006) [27] and Chen *et al.* (2008) [25] continued research into this "super"-blade-vortex interaction phenomenon. The interaction itself occurs because of the very aggressive roll rate, which reaches a maximum of 40 degrees per second. The roll they investigated was established in a period of approximately one second, and this interaction helped lead to the conclusion that a free wake vortex method, and fully transient analysis, is needed for the investigation of transient maneuvers [25]. However, this situation is only possible for highly maneuverable military vehicles, and is not likely to be experienced under normal operating conditions.

Currently, only a few flight tests exist that include transient maneuvers

[86, 93, 99, 110]. Spiegel, Buchholz, and Pott-Pollenske (2005) [99] investigated the noise footprint of two helicopters during transient roll maneuvers and ascent/descent flight patterns. They used a heavily instrumented BO-105 vehicle whose main rotor system was equipped with strain gauges, used for the calculation of blade motion, and on-blade pressure sensors. A differential Global Positioning System was used on both the BO-105 vehicle and the EC135-FHS, and 43 microphones were deployed on the ground to capture the acoustic footprint of the vehicle during maneuvers. They showed that the BO-105 vehicle was louder than the EC135-FHS vehicle, except during steep descents. They also showed that noise directivity patterns were different between advancing side and retreating side roll conditions.

Another experimental investigation using a Bell 206B vehicle with a crop dusting boom attached that was modified to hold microphones for in-flight measurements was conducted by Schmitz *et al.* (2007) [86]. The published data from this experiment has focused on steady and accelerating descents where it was shown that accelerating during a descent could reduce the overall sound pressure level. Schmitz *et al.* (2007) projected their acoustic hemisphere data onto a Lambert projection. No 2-D map projection of a sphere, shown in figure 1.10, can

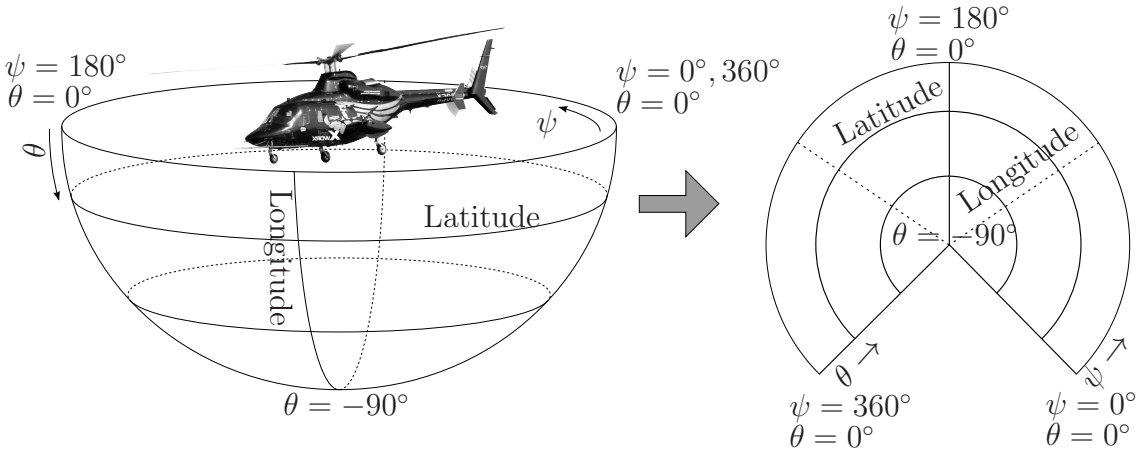

Figure 1.10: Lambert projection transform of a spherical, helicopter centered grid.

be free of distortion, but the Lambert projection is conformal and comes close to being equal-area when only half of a sphere is used [98]. Particular attention was also paid to a steady advancing side roll, where an increase in the noise was

seen to be louder, and shifted compared to the steady level flight condition. This increase in noise was attributed to the increase in thrust required by the tail rotor, in order to compensate for the increase in thrust on the main rotor. The origin of the shift in the noise directivity is difficult to determine, as a horizon-fixed coordinate system was used, and so the roll attitude of the vehicle was not accounted for.

A later test by Sickenberger, Gopalan and Schmitz (2011) [93] was conducted with a 'clean' Bell 206B vehicle and 5 ground based microphones. This flight test focused on several pull-up maneuvers, and employed a rigid wake model to predict blade-vortex interaction locations and subsequently the noise contributed to that signal. A time domain method for extracting the blade-vortex interaction noise was developed, and a detection algorithm was used to identify changes in detection distances during each maneuver. The described extraction method is based on removing the impulsive nature of the blade-vortex interaction noise from the original signal, and then interpolating and smoothing into place a new acoustic signal derived from the harmonic information located temporally around the removed signal. An example of this method is provided in figure 1.11. Using this method, Sickenberger *et al.* (2011) showed that the blade-vortex in-

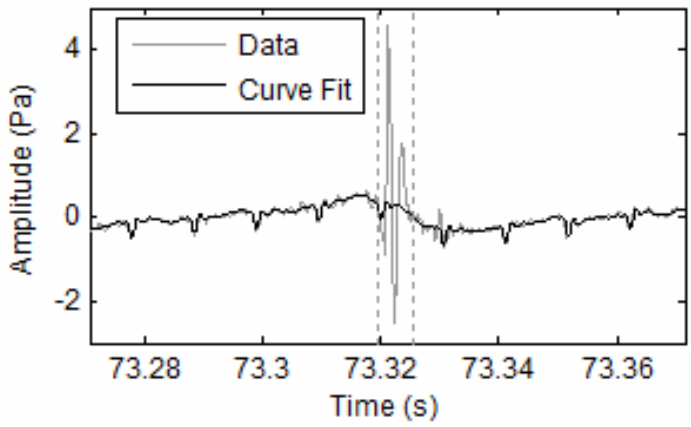

Figure 1.11: Blade-vortex interaction extraction method developed by Sickenberger *et al.* (2011) [93], implemented on data acquired from a Bell 206B vehicle.

teraction signal contributed up to 16 dB of the blade-vortex interaction sound

pressure level. The experiment also showed that blade-vortex interaction noise for transient pull up maneuvers are predominantly forward and centered on the vehicle. Their technique for identifying blade-vortex interactions, however, was not discussed.

The Schmitz *et al.* (2007) data set was also used to help develop a semi-empirical model to predict rotorcraft noise during maneuvering flight [56]. Greenwood, Schmitz, and Sickenberger (2012) [56] confirmed the conclusion of Sickenberger *et al.* (2011), that transient pitch up maneuvers exhibited blade-vortex interaction noise predominantly forward and centered on the vehicle. However, transient advancing side rolls showed blade-vortex interaction noise predominantly forward and to the retreating side of the vehicle. Greenwood *et al.* (2012) also developed a prescribed wake model based on Beddoes' method, that allows for changes in the inflow as a function of time. They used this method to show that the amplitude change in the blade-vortex interaction signal was primarily a function of the miss distance of the tip vortex during each maneuver.

In the present study, a time-frequency analysis of the sound produced by a Bell 430 helicopter during transient flight will be investigated. Data was acquired during a recent test campaign conducted by NASA, in conjunction with Bell Helicopters and the US Army [110]. The NASA, Bell and US Army experiment investigated both steady and transient flight maneuvers, acquiring a total of 410 data points. Instrumentation and experimental details are described more completely in chapter 3. Preliminary results by Watts *et al.* (2012) [110] showed a particularly large increase in noise for maneuvers controlled through cyclic inputs alone [110].

1.2 Rotor Wake Prediction

Central to the ability to fully predict rotor acoustics is the ability to predict the wake of the vehicle. Helicopter wakes are dominated by the shed tip vortices, which can interact with the rotor causing blade-vortex interactions and ultimately blade-vortex interaction noise. Thus, in order to predict the blade-

vortex interaction noise that was discussed in § 1.1.2, it is essential to be able to predict the rotor wake itself. Predicting the location of blade-vortex interactions, and thereby their acoustic directivity will better enhance our ability to capture such phenomenon during experimental investigations.

The seminal work into rotor wake prediction and vehicle performance was conducted by Landgrebe (1972) [67] who provided a simple formula for the slip stream boundary as a function of wake age and vehicle parameters. Later, Beddoes (1985) [6] proposed a prescribed wake model where the location of the tip vortex could be determined. Beddoes' method, shown in figure 1.12 prescribes the direction a tip vortex will travel and the velocity flowing through the rotor disk, known as inflow. The vertical displacement of the vortex can be determined by integrating the velocity through the rotor, experienced along the vortex path. Such prescribed wake methods rely on knowing the inflow through the rotor and the forward advance ratio of the vehicle. Prescribed wake models are based on steady flight conditions, but the inflow models can be tailored to include deformation caused by non-steady effects [66, 107]. Van der Wall (2000) [107] modified Beddoes' prescribed wake model by adding Drees' lateral asymmetries to the inflow. Van der Wall also developed an approximate method to account for the effects that higher harmonic control and individual blade control have on the rotor wake [107]. Krothapalli, Prasad and Peters (2001) [66] developed a dynamic inflow model that could account for effects seen in maneuvering flight, especially during pitch-up maneuvers.

Free wake models are a computationally more intensive method, than prescribed wake methods, for determining the position of a tip vortex. Although free wake models are still less intensive than full computational fluid dynamics analysis which solves the governing fluid dynamics equations on a large enough grid. Where a prescribed wake method defines the vortex trajectory and inflow through the rotor, a free wake method allows the tip vortices to develop in a more natural way, by determining induced velocities through successive use of the Biot-Savart law. A review of some free vortex methods is provided in Leishman, Bhagwat and Bagai (2002) [68]. Bagai, Leishman and Park (1999) [5] employed a

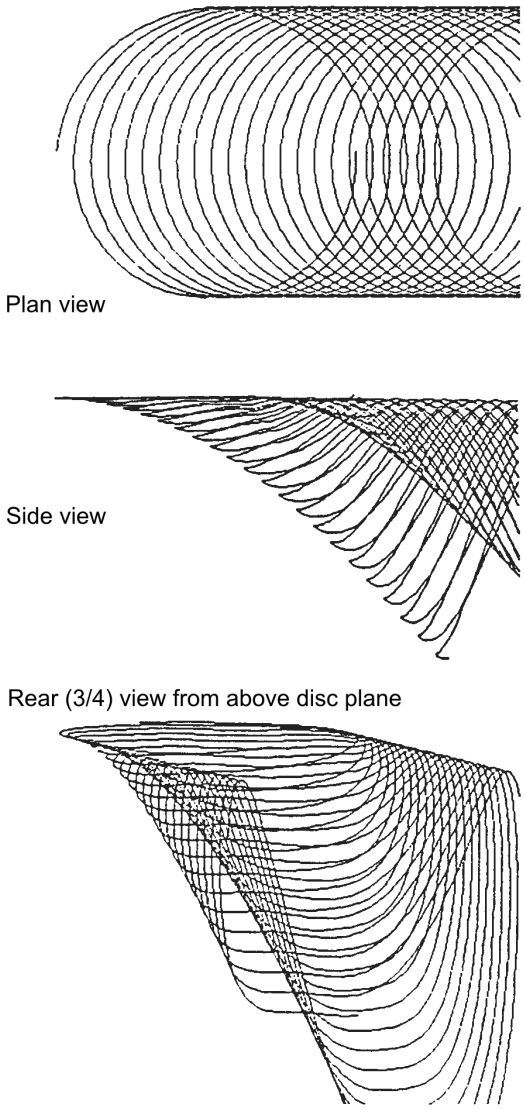

Figure 1.12: Beddoes' wake geometry for a 4 bladed rotor with a blade loading of 0.08 and advance ratio of 0.07 [6].

free wake model to predict the helicopter wake during steady maneuvering flight conditions. Bagai *et al.* (2002) showed that maneuvering flight results in changes to the inflow condition and distortions in the vortical wake structure. In order to provide a more accurate prediction of the rotor wake, however, their technique requires coupling with rotor dynamics solver and flight mechanics analysis techniques [5]. Ananthan and Leishman (2003) [2] used a free wake vortex method to investigate the wake response to transient blade pitch inputs. They saw that

large control inputs could easily result in vortex rings forming below the rotor and that certain flight maneuvers may cause these vortex rings to be re-ingested by the main rotor. Such a situation is what was described in Chen *et al.* (2006) [27] as "super"-blade-vortex interactions.

Ribera and Celi (2004) [81] investigated time accurate free wake method and showed that the time accurate method produced lower inflow than the more typical relaxation type method. A comparison of a relaxation based free wake method versus the time accurate method is shown in figure 1.13 extracted 15 ro-

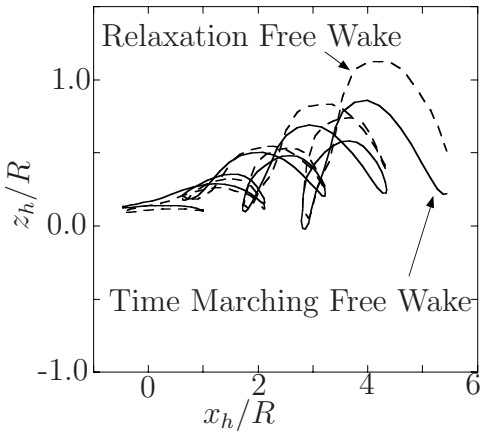

Figure 1.13: Comparison of relaxation and time accurate free wake methods during a roll reversal maneuver [81].

tor revolutions into a roll reversal maneuver. The lower inflow found for the time accurate method resulted in a greater contribution to the vehicle roll moments, creating a more accurate roll response on the vehicle. Overall, free wake methods can provide more accurate predictions of the vehicle wake especially during transient maneuvering flight. However, their calculations come at the expense of higher computational time, and so the benefits of a more accurate prediction must be weighed against this cost. A prescribed wake model may be sufficient for the determination of microphone placement during full scale flight experiments. However, the free wake methods, or even full computational fluid dynamics methods are necessary for the accurate numerical prediction of helicopter acoustics during transient maneuvers.

1.3 Objective

It is the purpose of this dissertation to develop a method for the extraction of blade-vortex interaction signals from acquired acoustic data. Such a method would enhance the understanding of blade-vortex interactions by isolating the phenomenon in experimental studies for further investigation. The method developed is robust, easily implementable, and applicable across a wide range of helicopter arrangements and maneuver profiles. It comes with few 'tuning' parameters, and those are based on physical processes related to the signal of interest. Further the process developed can be modified to extract any impulsive, high amplitude noise source of interest.

The dissertation will develop such a process and then apply this technique to further improve on the understanding of blade-vortex interactions, especially as they are affected by transient maneuvers. As discussed in § 1.1.5, analysis of experimental data sets, which include transient maneuvers, have focused predominantly on pitch-up maneuvers. As of yet, little experimental attention has been paid to transient roll maneuvers.

The discussion will begin with a description of time-frequency analysis techniques in chapter 2. A description of the experiment and the flight maneuvers investigated follows that in § 3. The experiment investigated here was conducted by the US Army in conjunction with NASA and Bell Helicopters [110]. It comprised 410 vehicle flights, of which the focus was on transient maneuvers. Only a subset of the flights will be used for the development of the extraction technique.

A discussion of three different vehicle maneuvers and their preliminary wavelet analysis results follows in § 4. It is shown how the acoustic signal changes as a function of time for a stationary microphone even in the steady level flight maneuver. Further, a comparison between the maneuvers is made, and it is seen that blade-vortex interactions have a significant impact on the overall sound pressure level.

A method for the prediction of blade-vortex interaction locations and acoustic directivities is discussed in § 5, followed by the development of the ex-

traction method itself. The extraction technique will first be applied to synthetic data to determine its strengths and weaknesses. A sensitivity analysis will then be conducted on the acquired test data, to determine the best fit tuning parameters for the extraction technique. Finally, an evaluation of the blade-vortex interaction extraction method and prescribed wake prediction will be conducted in § 6. Each maneuver from will be re-evaluated to determine the contribution that blade-vortex interactions have towards the overall sound pressure level.

§ 6 constitutes the first complete analysis of transient advancing side roll maneuvers, of various speeds, captured via experimental methods. The directivity associated with blade-vortex interactions that occur during these maneuvers are extracted and investigated independently. It will be shown that blade-vortex interaction directivity varies only slightly throughout the maneuver, when a coordinate frame that accounts for vehicle attitude is employed. Further, it will be shown that the sound pressure levels are directly related to the rate at which the vehicle is rolling, and not the vehicle attitude.

Further analysis is conducted to determine the applicability of a quasi-steady prescribed wake method in predicting the location of blade-vortex interaction noise. A prescribed wake method could be used in the future to determine the optimal location of microphones for capturing the acoustic emissions of blade-vortex interactions during transient maneuvering flight. The discussion will conclude in § 7 with a brief review of the work that was conducted and suggestions for future development.

Chapter 2

Time-Frequency Analysis Techniques

As discussed in § 1.1.2, blade-vortex interactions are highly impulsive acoustic events that, when present, comprise a large portion of the acoustic energy. Investigating impulsive events such as blade-vortex interactions, and transient events such as those present during unsteady maneuvers, is a non-trivial task as standard statistical methods are no longer applicable. Therefore, a methodology capable of handling transient phenomenon is required if one is interested in the spectral properties of the signal.

Time-frequency analysis methods employ basis functions that are non-zero over a finite time interval thus making them compactly supported. This differs from the standard Fourier transform technique, which uses trigonometric basis functions and relies on three basic assumptions. The Fourier transform assumes the signal is steady, periodic, and Lipschitz continuous [51]. The steady and periodic assumptions are invalidated for transient maneuvers, as well as instances where blade-vortex interactions occur. Thus, time-frequency methods must be employed for the analysis of such signals.

However, time-frequency techniques have their own drawbacks. An inherent difficulty to any time-frequency analysis is the trade-off between frequency and temporal resolution [33, 78]. The Heisenberg box, named after the Heisenberg uncertainty principle, is the maximum resolution a given time-frequency analysis is capable of [1]. Essentially, the principle states that as the resolution in one space (time, frequency) is increased the resolution in the opposing space (frequency, time) is subsequently decreased. Thus, a compromise must be reached for every application of time-frequency analysis techniques.

2.1 Time-frequency Analysis of Helicopter Acoustics

Time-frequency analysis techniques were introduced to the world of helicopter acoustics by Siegert, Nouals and Damongeot (1993) [94]. Siegert *et al.* (1993) showed that the time-frequency representation of a helicopter signal could greatly improve understanding of the physics, over either a time or frequency depiction alone. Constantine *et al.* (1995) [31] was simultaneously working on using the discrete wavelet transform to investigate blade-vortex interaction noise measured during a full-scale flight test. The discrete wavelet transform is a discrete representation of the wavelet transform, and is based on orthogonal bases that result in a non-redundant representation of the signal [1, 41].

The work of Constantine *et al.* (1995) was continued in Davis, Pezeshki, and Mosher (1997) [34] where a discrete wavelet transform utilizing five orthogonally spaced octave bands was used to locate and extract the blade-vortex interaction signal. Careful spacing of the sub-bands was necessary for the isolation of blade-vortex interaction noise, and the signals investigated, shown in figure 2.1 were dominated by blade-vortex interactions. The tail rotor and other sources of higher frequency content is not noticeably present in their signal. Further, blade-vortex interactions fell almost entirely into a singular sub-band, shown in figure 2.1. It is questionable how well their described technique would work in cases where significant higher frequency content, not caused by blade-vortex interactions, is present or when blade-vortex interactions occur in different frequency ranges.

Celi (2001) [24] further investigated various time-frequency techniques as applied to helicopter acoustics. He utilized four time frequency techniques to visualize a helicopter's acoustic signal. Those techniques included the wavelet transform, Choi-Williams distribution, short-time Fourier Transform, and Wigner-Ville distribution. Celi concluded that no technique was better than the others, each had their own advantages depending on what specifically was being investigated.

Stephenson and Tinney (2013) [103] successfully applied continuous wavelet transforms to investigate the transient nature of advancing side roll maneuvers. They identified the Morlet wavelet as the 'best' wavelet for use with helicopter

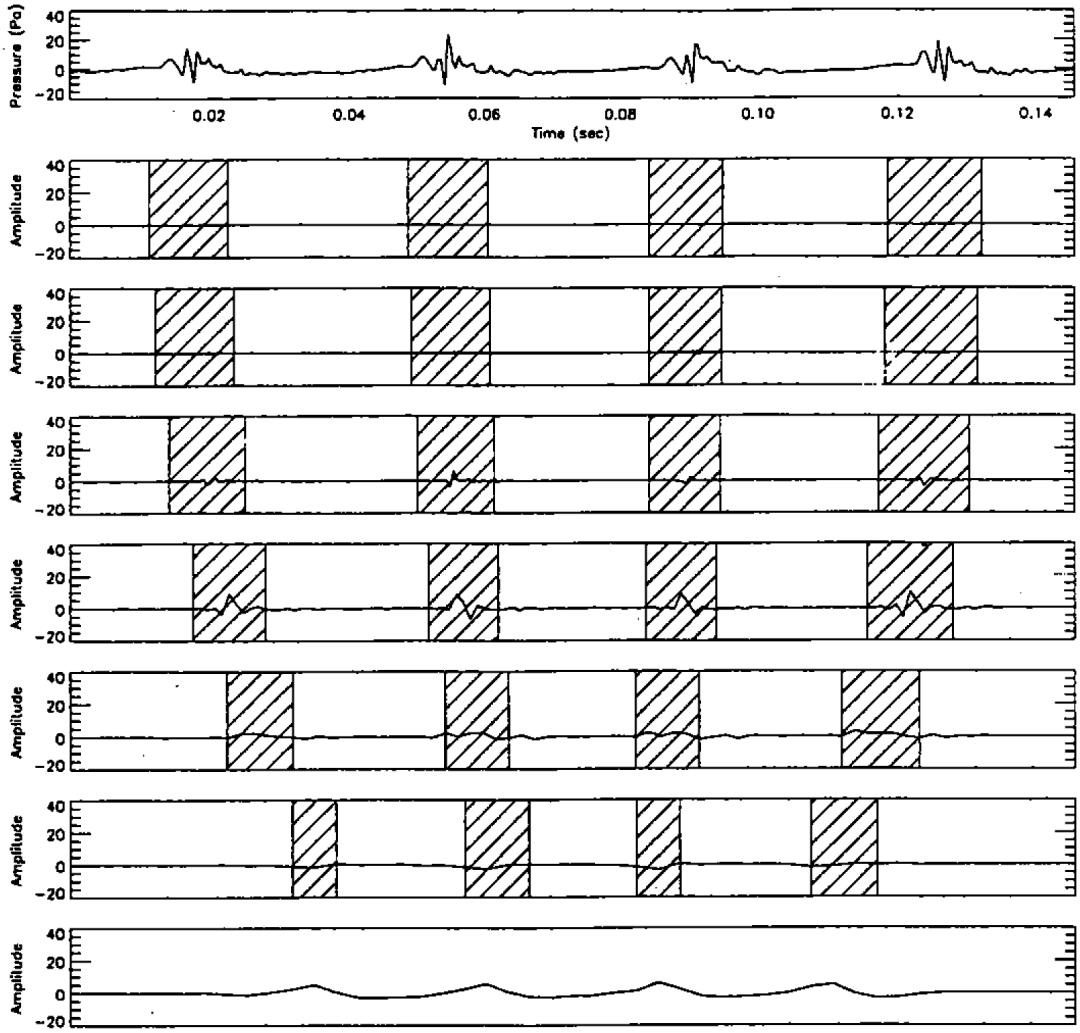

Figure 2.1: Original signal from Davis *et al.* (1997) shown at top, with cross-hatched blade-vortex interaction signal depicted below [34]. At each step down, the sub-band increases in frequency, and so the highest frequency components are at the bottom.

acoustic signals, regardless of flight condition. This work was continued in Stephenson *et al.* (2014) [104] where it was shown that the signature related to blade-vortex interactions was influenced greatly by changing flow through the rotor system. Increase in the overall sound pressure level throughout an advancing side roll maneuver was seen to occur coincident with decreasing flow through the rotor in the vicinity of known blade-vortex interactions. It was inferred that this decrease in local inflow resulted in a decrease in the vortex miss distance and thereby increase

in the overall sound pressure levels.

2.2 Wavelet Transforms

The methodology employed here to investigate the spectral content of the acoustic signals as a function of time, follows that of Stephenson and Tinney (2013), and is called wavelet transforms. The interested reader is referred to the work of others for an in-depth discussion on this technique [1, 29, 41, 69]. Wavelet transforms are only one of many techniques that fall underneath the time-scale analysis category.

Wavelet transforms temporally convolve an *a priori* known function (the 'mother' wavelet (ψ_w)) with a signal in order to reveal its time varying spectral content. In doing so, the spectral characteristics of localized bursts are preserved. The convolution comprises various scales (l) that decompose the signal into time-scale space, and is determined as,

$$\tilde{p}(l,t) = \frac{1}{\sqrt{l}} \int_{-\infty}^{\infty} p(t') \; \psi_w^*(\frac{t'-t}{l})dt. \tag{2.1}$$

where $\tilde{p}(l,t)$ are the wavelet coefficients. In general, small scales represent high frequency content in the signal, while large scales represent low frequency content. Wavelets do not, however, need to have a one to one correspondence between scale and frequency [41].

Wavelets may be any combination of real or imaginary, and the resulting wavelet coefficients are given in the same number set as the wavelet themselves. For example, complex wavelets result in wavelet coefficients that are complex valued, and so preserve both spectral amplitude and phase information. Real valued wavelets result in only real valued wavelet coefficients, and so phase information cannot be preserved.

Every wavelet must satisfy the admissibility criterion ($C_\psi < \infty$), defined as

$$C_\psi = \int_l \frac{|\hat{\psi_w}(l')|^2}{|l'|} dl' < \infty [1]. \tag{2.2}$$

According to Farge (1992) [41], this criterion weakly implies that the average of the wavelet must be zero and so $\hat{\psi_w}(0) = 0$. The wavelet must also have finite energy, to ensure that artificial energy is not created in the convolution process. Thus, the wavelet must also satisfy the following,

$$E_\psi = \int_{-\infty}^{\infty} |\psi_w(t)|^2 \, dt < \infty. \tag{2.3}$$

Complex wavelets have one additional criterion. The Fourier transform of a complex wavelet must be real valued and must vanish for negative frequencies [1]. Thus, only single-sided spectral characteristics are possible with the wavelet transform.

The inverse wavelet transform can be used to recreate the original signal, or any portion thereof. The inverse wavelet transform is given as,

$$p(t) = \frac{1}{C_\psi} \int_{-\infty}^{\infty} \int_l \frac{1}{\sqrt{l'}} \, \tilde{p}(l', t) \, \psi_w(\frac{t' - t}{l'}) \frac{dl' \, dt}{l'^2}. \tag{2.4}$$

Perfect reconstruction of the signal is possible when the scale space integral is performed across all decomposed scales. However, wavelet transforms can be used to filter signals by performing the scale space integral across a subset of scales. This technique is typically applied to remove noise from signals by recreating the signal using only the lower frequency (high scale) content [1].

The scale-normalized energy density $E(l, t)$ is given as

$$E(l, t) = \frac{1}{C_\psi} \frac{|\tilde{p}(l, t)|^2}{l^2} \tag{2.5}$$

and is known as the wavelet power spectrum (WPS). The admissibility factor (C_ψ) is included in equation (2.5), so that the total energy can be recovered as follows

$$\|E\| = \int_l \left(\frac{1}{T} \int E(l, t) dt \right) dl. \tag{2.6}$$

For the wavelets investigated here, a simple transformation from scale to frequency is performed, such that $E(l_j, t_i) \rightarrow E(f_j, t_i)$. The wavelet power spectrum is directly analogous to the power spectral density obtained through the Fourier transform, and so calculation of sound pressure levels can be determined

in an equivalent manner. Sound pressure levels (SPL) as a function of time can be determined as,

$$SPL(t) = 10\ \log_{10}\left(\frac{\int_f E(f,t)df}{p_{ref}^2}\right), \tag{2.7}$$

where p_{ref} is the reference pressure. An introduction into interpreting wavelet power spectra is provided for the benefit of the reader in appendix A.

2.3 Short-time Fourier Transform Comparison

A comparison between the more standard short-time Fourier transform (STFT), and an averaged wavelet power spectrum is now undertaken. The short-time Fourier transform is an application of the Fourier transform over a windowed portion of the overall data. Using a windowing function, whether it be a Hanning filter, box filter, or otherwise, imposes an external time-scale on the data. The time-scale imposed does not necessarily relate to a physical process. Further, as the window in time is increased, the Fourier transform distributes the signal's energy over a greater range of frequencies. This leads to a fluctuation in the energy at any given frequency, depending on the size of the time window chosen. All things being equal, the energy in a given frequency should be independent of the size of the interrogation window investigated. Thus, we will investigate the Fourier transform spectrum through several window sizes, and compare that with the values obtained through the averaged wavelet power spectrum for the same window.

The raw pressure signal used in this comparison is extracted from a medium, advancing side roll maneuver that will be described in detail later. For the purposes of this discussion, the raw pressure signal used to generate the power spectral densities will be shown below each figure while the wavelet power spectra is averaged across each window to provide a more direct comparison with the short-time Fourier transform. Three different windows in time are used, and the first window, figure 2.2, encompasses a 200 [ms] span in time. This integration window is chosen specifically as it represents the aural integration time of a human ear for low frequency sounds [52]. Given the rotation speed of the Bell 430 helicopter

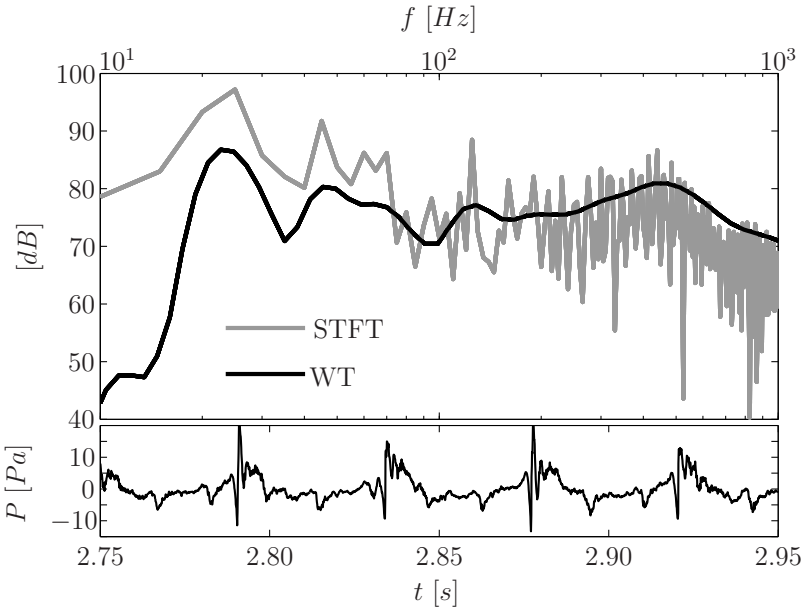

Figure 2.2: Estimates of power spectral density extracted from the medium advancing side roll maneuver computed using the STFT and a window averaged wavelet transform performed over a 200 [ms] window of data. Raw pressure time histories are shown below.

main rotor, this comprises approximately one complete revolution of the rotor, and so four bursts, each corresponding to a blade passage and blade-vortex interaction event, are captured and displayed. With this window size, the short-time Fourier transform over-predicts the energy of the first few rotor harmonics by a full 10 dB, which is an order of magnitude in energy, when compared to the wavelet power spectrum. This over-prediction is attributed to a redistribution of energy from the unresolved portions of the spectra. Likewise, higher frequencies are under predicted by the short-time Fourier transform, compared to the wavelet transform, as the impulsive nature of the high frequency blade-vortex interaction components are smeared by the averaging process.

In figure 2.3, a 50 [ms] interrogation window is used, so only one blade passage is retained. It is shown here how shorter windows are more appropriate for the higher frequency components as their energies are more realistically estimated using short-time Fourier transform when compared to the wavelet power spectrum. The aural integration time for the human ear is also shorter, for higher frequency

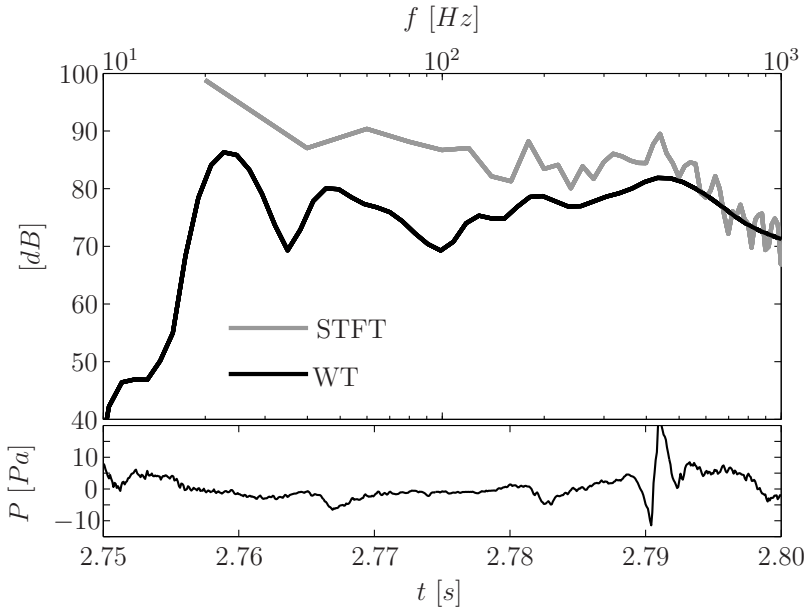

Figure 2.3: Estimates of power spectral density extracted from the medium advancing side roll maneuver computed using the STFT and a window averaged wavelet transform performed over a 50 [ms] window of data. Raw pressure time histories are shown below.

sounds [52]. This shorter window in time, however, leads to an even larger over-prediction in the lower frequencies with the short-time Fourier transform. The energy in the main rotor harmonic (23.2 [Hz]) has increased by 1.2 [dB], compared to a decrease of 0.5 [dB] in the wavelet power spectrum. This means the short-time Fourier transform is now almost 13 [dB] higher than what is seen in the wavelet power spectrum. Changes in the second main rotor harmonic (46.4 [Hz]) are even greater, with a 7 [dB] decrease being seen in the short-time Fourier transform, compared with only a 0.1 [dB] decrease in the wavelet power spectrum. The subtle changes in the wavelet power spectrum are likely due to changes in the energy spectrum averaged over a time window one-fourth the previous size.

The typical interrogation window that is chosen in helicopter acoustics spans 0.5 seconds of time, and is shown in figure 2.4, Comparing the 500 [ms] window in time, to the 200 [ms] window, the short-time Fourier transform provides a more consistent result, within 0.5 [dB], for each of the first three main rotor harmonics. However, the spectra between each of the harmonics fluctuates quite

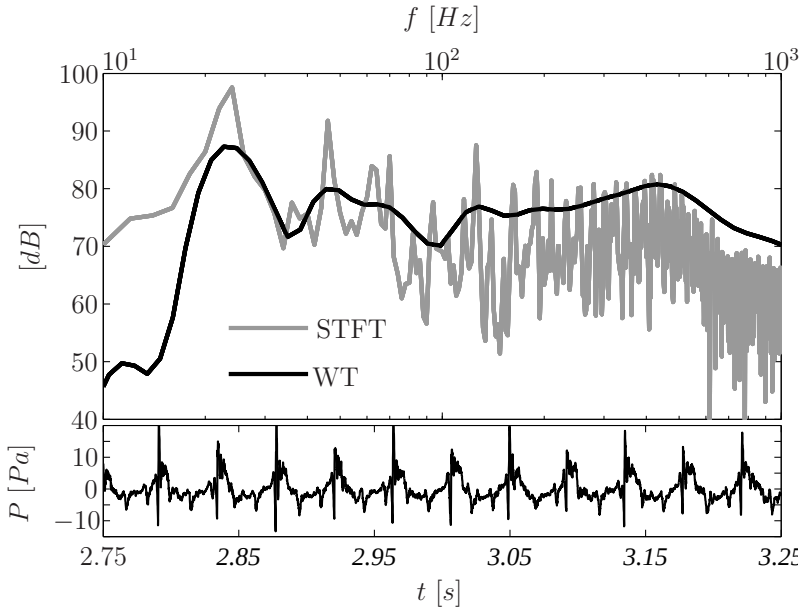

Figure 2.4: Estimates of power spectral density extracted from the medium advancing side roll maneuver computed using the STFT and a window averaged wavelet transform performed over a 0.5 [s] window of data. Raw pressure time histories are shown below.

drastically, and energy in the higher frequencies can fluctuate by 20 [dB] depending on how the transform partitions the energy.

Meanwhile, figure 2.5, provides an overlay of the wavelet transform spectra for each of the window sizes. It shows the energy distribution for any given frequency in the wavelet transform is within ±1 [dB] when comparing the 500 [ms] to 200 [ms] windows, and ±3 [dB] for the 50 [ms] to 200 [ms] windows. The Fourier transform clearly has a better frequency resolution at this window scale, however the dependence on the window size hampers interpretation of the spectrum for scales more appropriate to the transient phenomenon of interest.

In summary, the wavelet transform provides a consistent spectral energy distribution that is independent of the interrogation window. The short-time Fourier transform, however, is dependent on the size of the interrogation window, and requires fairly large window sizes in order to provide a more consistent energy spectrum. Further, if one is to use a windowed transform to develop a method to extract transient phenomenon, then the window should be on the same time

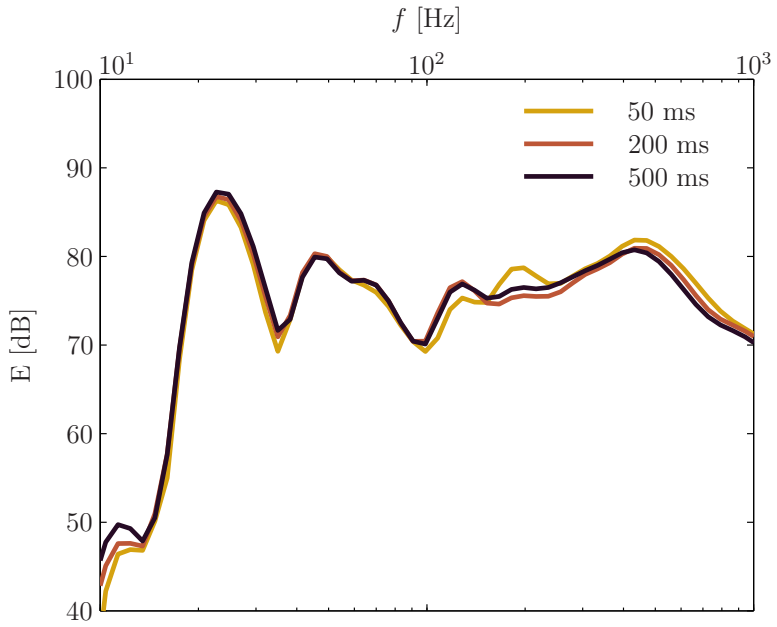

Figure 2.5: Wavelet power spectra averaged over each of the three previously investigated window sizes.

scale as the phenomenon itself. Figure 2.3 shows that blade-vortex interactions occur on the order of milliseconds, which is too small of a window for consistent results from the short-time Fourier transform. Therefore techniques that do not require windowing of the data, like wavelet transforms, are a better choice for this situation.

2.4 Morlet Wavelet

There are an infinite number of mother wavelets one could develop. Only a select few of these wavelets will be used for analysis, here. One of the more common wavelets in use today, is the Morlet wavelet (ψ_M), the shape of which is shown in figure 2.6. When compared to other wavelets, the Morlet wavelet offers a good frequency and temporal resolution, and is constructed by modulating a sinusoidal plane wave by way of a Gaussian function [1]. Applications of the Morlet wavelet to transient signals range from atmospheric modeling [106] to shock-wave boundary layer interactions [3]. The frequency domain representation of the Morlet wavelet is shown in figure 2.6 (right), and is defined by Torrence

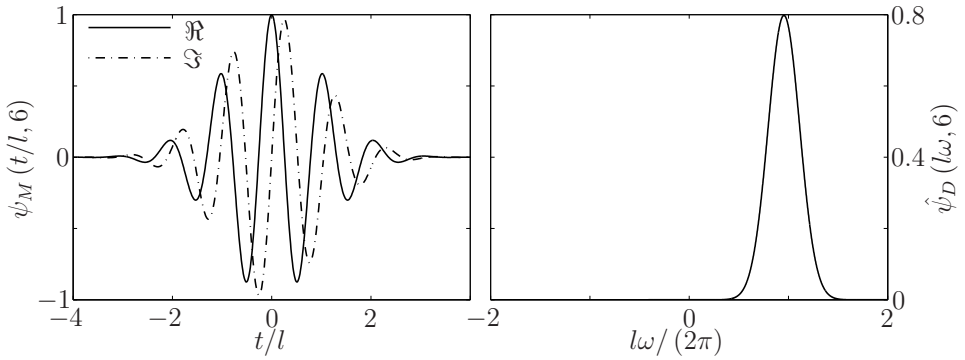

Figure 2.6: (left) Time domain and (right) frequency domain representations of the Morlet wavelet ($\psi_M(t/l, \omega_\psi) \in \mathbb{C}$).

and Compo (1998) [106] as,

$$\hat{\psi}_M(l\ \omega, \omega_\psi) = \sqrt{2\pi l\ \frac{f_s}{N}}\ \pi^{-1/4}\ H(\omega)\ e^{-(l\omega-\omega_\psi)^2/2}. \tag{2.8}$$

Here, N is the number of samples in the data set and f_s is the sampling rate. ω_ψ is a non-dimensional frequency which can be chosen to optimize frequency or time resolution. A higher value of ω_ψ results in more oscillations in the time domain. This typically yields better frequency resolution, but too high of a value can quickly lead to instabilities.

2.5 Derivative of Gaussian Wavelet

As an alternative to the Morlet wavelet, the derivative of Gaussian wavelet is also considered. Depending on the derivative, the derivative of Gaussian can be tailored to achieve better frequency or temporal resolution. The 4-th derivative of Gaussian wavelet is shown in figure 2.7. However, unlike the Morlet wavelet, the derivative of Gaussian wavelet has the disadvantage of being purely real (for even derivatives) and purely imaginary (for odd derivatives). This results in the loss of phase information, which is otherwise preserved in the Morlet wavelet. It is common practice that only even derivatives be used. The Fourier transform of the n-th DOG wavelet is expressed as ,

$$\hat{\psi}_D(l\ \omega, n) = \sqrt{2\pi l\ \frac{f_s}{N}}\ \frac{i^n}{\sqrt{\Gamma(n+1/2)}}\ (l\ \omega)^n\ e^{-(l\ \omega)^2/2}\ \ \text{[106]}. \tag{2.9}$$

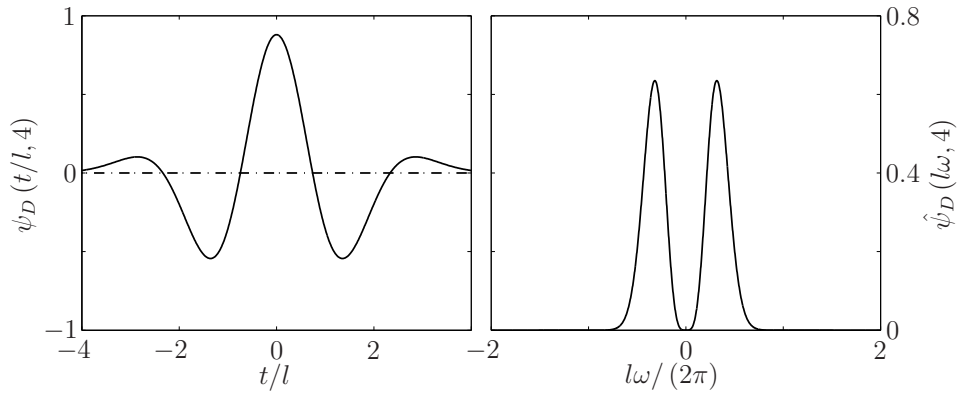

Figure 2.7: (left) Time domain and (right) frequency domain representations of the derivative of Gaussian wavelet.

The second-derivative of Gaussian is commonly referred to as the Mexican Hat, or more appropriately, the Maar wavelet; it is known to have poor frequency resolution relative to the Morlet wavelet [42]. It is possible to employ higher order derivative of Gaussian wavelets in order to better resolve the higher frequency content.

2.6 Shannon Entropy Cost Function

Determining the optimal parameter for use in the wavelet transform is an often overlooked, but non-trivial task [30, 35, 61, 78]. Each wavelet comes with its own tuning parameter that can influence the time and frequency resolution of the resulting spectra. In the case of the Morlet wavelet this is ω_ψ, the non-dimensional frequency, and for the derivative of a Gaussian wavelet the parameter is the order of the derivative (n). Rules of thumb have been developed for the commonly used wavelets, and are often applied without regards to the effect such a choice has on the results. The Morlet wavelet is typically used with a non-dimensional frequency of 6, while only even derivatives are investigated in the derivative of Gaussian wavelet, and of those the second derivative is the most commonly chosen order [1].

In order to determine what wavelet to choose and what analysis parameter best fits the data, a non-arbitrary method must be employed. Coifman and

Wickerhauser (1992) [30] proposed using the Shannon entropy cost function as a method for determining the optimal wavelet parameter. A normalized version of the one proposed by Coifman and Wickerhauser will be discussed here. The cost function proposed by Shannon (1946) [91] is given in its normalized form as,

$$C(\eta) = \frac{1}{\log(I\ J)} \sum_{i}^{I} \sum_{j}^{J} \frac{E(f_j, t_i)}{\|E\|} \log\left(\frac{E(f_j, t_i)}{\|E\|}\right), \tag{2.10}$$

and is a measure of how energy is distributed in a data set. In the cost function, η represents the analysis parameter to be varied. For the Morlet and derivative of Gaussian wavelets, this would be ω_ψ and n, respectively. 'J' represents the maximum number of scales (frequencies) and 'I' is the maximum number of time steps in a given data set.

The cost function is bounded between zero and one, which makes it particularly useful at comparing the appropriateness of various wavelets. If all energy is concentrated into a single scale at a single point in time, then $C(\eta)$ is identically equal to zero. Likewise, if the system's energy is evenly distributed across all scales and time, then $C(\eta) \equiv 1$. Therefore, the wavelet that represents the signal in the fewest scales and the least number of time steps can be found at the minima of $C(\eta)$. The wavelet and corresponding wavelet parameter at the minimum of the Shannon entropy cost function is deemed to be the 'best' wavelet for that particular data set.

Stephenson and Tinney (2013) [103] successfully applied the Shannon cost analysis to several steady level flight and advancing side roll maneuvers of various speeds to determine the best wavelet for helicopter acoustics. They employed both derivative of Gaussian wavelets and Morlet wavelets, investigating a range of derivatives and non-dimensional frequencies. The results from this cost analysis are shown in figure 2.8. It is interesting to note that regardless of the maneuver investigated, the same cost trend is identical within a given mother wavelet. Therefore, it is comfortable to assume that results from this technique will probably be applicable to any helicopter acoustics problem.

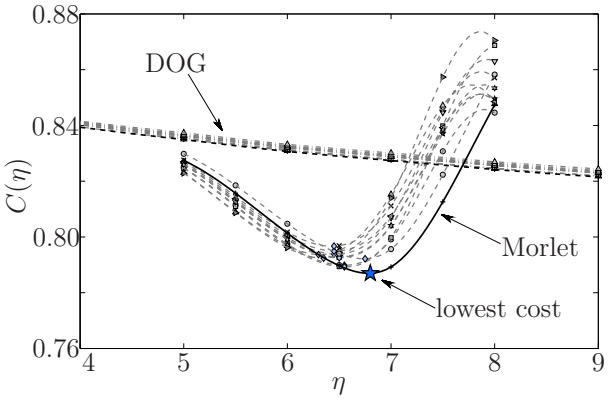

Figure 2.8: Shannon entropy cost function applied to multiple steady level flights and advancing side roll maneuvers of various rates.

Since the best wavelet has been defined as the wavelet that represents the signal in the least number of scales and time steps, then the best wavelet will be found at the minimum of the cost function. The work of Stephenson and Tinney (2013) [103] showed that the Morlet wavelet is preferred over the derivative of Gaussian wavelet for the data studied, and that ω_ψ between 6 and 7 oscillations in the Morlet wavelet yields the smallest cost. The Morlet wavelet transform with $\omega_\psi = 6$ possesses a smaller variance in cost value across each maneuver studied, and it comes at a comparable overall cost to the $\omega_\psi = 7$ wavelet. Thus the Morlet wavelet transform with $\omega_\psi = 6$ alone, will be used to extract the spectral content of the data studied herein.

Chapter 3

Experimental Setup

3.1 Experimental Overview

Measurements of a full-scale Bell 430 helicopter undergoing various flight maneuvers were conducted at Eglin Air Force Base during the summer of 2011. The test vehicle is shown in figure 3.1, and a full description of this test campaign

Figure 3.1: Bell model 430 in flight during testing.

is provided in Watts *et al.* [110] with relevant details being described herein. The full ten day campaign acquired 410 test points including steady flight, transient and steady maneuvering flight, as well as landing profiles.

3.2 Bell 430 Helicopter Description

Technical specifications concerning this standard model Bell 430 helicopter are provided in table 3.1. The Bell model 430 is a ten seat vehicle with a twin Allison 250-C40B turboshaft turbine engine. This helicopter was outfitted with a Differential Global Positioning System (DGPS), an inertial navigation unit and a

Empty Weight	10.7	[kN]
Maximum Gross Take-Off Weight	18.7	[kN]
Maximum Speed	73.5	[m/s]
Fuel Capacity	711	[L]

Table 3.1: Bell 430 vehicle specifications

measurement system for recording the Tip-Path-Plane (TPP) of the main rotor. The Bell 430 helicopter's relevant main and tail rotor specifications are found in table 3.2. The main rotor system is a 4-bladed system with a split tip-path plane,

	Main Rotor	Tail Rotor	
Number of Blades	4	2	
Radius (R)	6.4	1	[m]
Chord (c)	0.34		[m]
Rotation Rate	348.6	1880.7	[RPM]
Blade Pass Frequency	23.2	62.7	[cycles/s]

Table 3.2: Bell 430 rotor specifications

shown in figure 3.2, so one pair of opposing blades sits at a slightly higher elevation

Figure 3.2: Main rotor split tip-path plane.

than the other pair. When the main rotor system is tracked, this separation

distance is maintained [54].

The DGPS recorded aircraft position (±1.5 m) at a sampling rate of 5 Hz while providing real-time path guidance to the pilot. The inertial navigation unit sampled at 125 Hz and provides pitch and roll attitudes (±0.3 deg) as well as pitch and roll rates (±0.01 deg/s) as functions of time. The inertial navigation unit also provides yaw rate, true heading, and accelerations measured in the longitudinal, lateral, and vertical directions.

The DGPS and inertial navigation unit system are synchronized with microphone and weather station data using Coordinated Universal Time. The tip-path-plane measurement device uses a laser imaging system and reflective tabs on the tip of each blade, both are shown in figure 3.3. Measurements from the

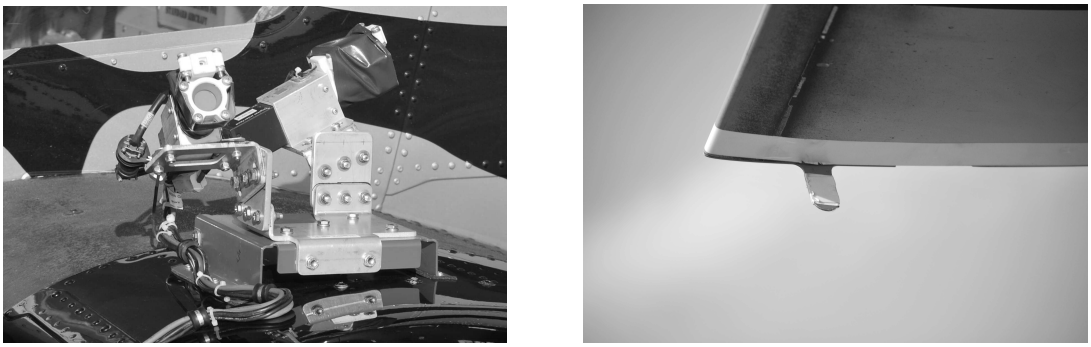

(a) (b)

Figure 3.3: The TPP measuring system complete with (a) laser imaging system, and (b) laser reflective tabs.

TPP imaging system showed the maximum deviation from the fuselage angle of attack, for any direction, was 0.2° during any given maneuver [109]. Therefore, the fuselage angle of attack will be used in subsequent analysis.

3.3 Data Acquisition Description

Acoustic data was acquired using 21 ground based microphones that are operated wirelessly from the control center, shown in figure 3.4. 1/2 inch B&K type 4189 free-field microphones were used with their diaphragms inverted 6.35 mm above a 381 mm round ground board, shown in figure 3.5a. Each microphone

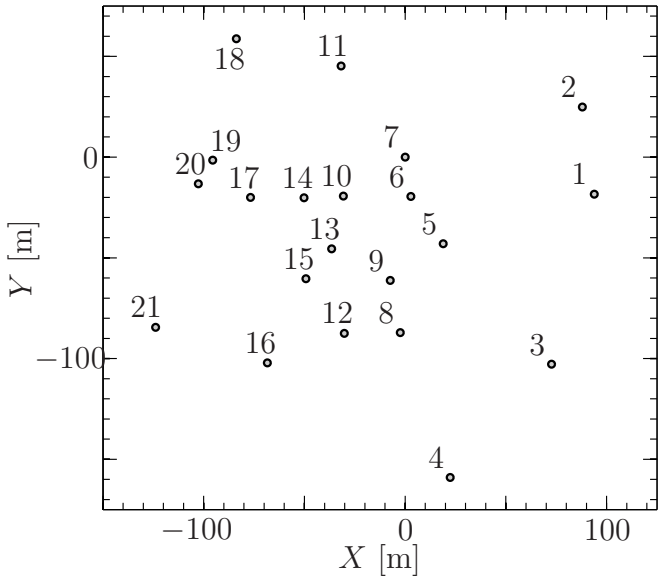

(a)

(b)

Figure 3.4: Microphone (a) ground position and (b) control center.

has a frequency range from 20 Hz to 20 kHz with a dynamic range from 16.5 dB up to 134 dB. The microphones have been numbered in figure 3.4a for decreasing 'X', consistent with previous literature [109], for ease of reference later in the manuscript.

Every wireless acoustic microphone system was outfitted with a DGPS receiver for accurate positioning relative to the vehicle. All microphone channels were sampled simultaneously and uninterrupted at (f_s) 25 kHz with 16 bit resolution. Acoustic pressure time series were transformed from time of observation

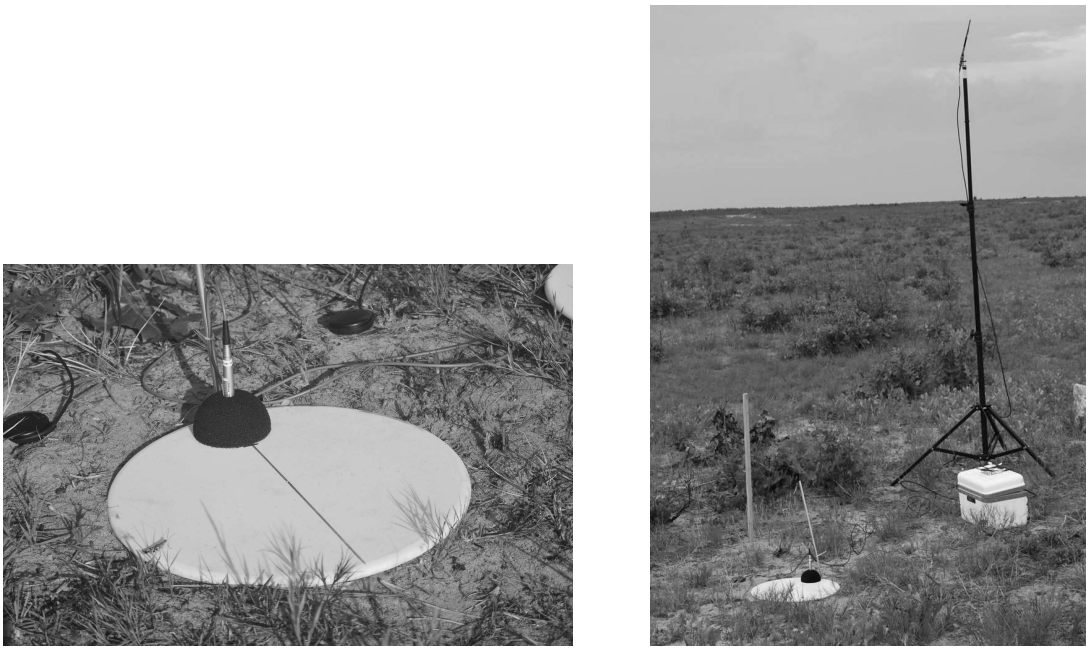

(a) (b)

Figure 3.5: Microphone setup with (a) microphone inverted over a ground board and (b) full system with wireless box, DGPS receiver and microphone.

to time of emission using a time domain de-Dopplerization algorithm developed by Greenwood and Schmitz [55]. The de-Dopplerization algorithm uses a linear interpolation scheme to adjust the pressure at time of reception to time of emission by accounting for the distance between the vehicle and microphone, as well as the speed of sound. Pressure amplitudes are subsequently scaled to adjust for spherical spreading losses, so that the microphone pressure signatures are scaled uniformly to 100 meters from the vehicle.

The time dependent de-Dopplerization scheme is based on similar work developed for fixed wing aircraft [62]. Due to the nature of the time dependent transformation from time of observation to time of emission, the de-Dopplerized signal is no longer sampled uniformly. Howell *et al.* (1986) [62] used this process in an investigation of the signal to noise ratio for a Doppler-shifted, band-limited random noise after de-Dopplerization. They showed that when the initial:final sampling rate was 2:1, then the signal to noise ratio after de-Dopplerization was 35 dB for linear interpolation and only 18 dB if the signal was resampled using

a "nearest neighbor" approach. Thus, a linear interpolation scheme is used to resample the resulting randomly sampled, de-Dopplerized signal at a lower sampling rate. The resulting sampling rate is 12 kHz, instead of the original 25 kHz. While this technique would affect the higher frequency components the original signal is sufficiently oversampled, and the final linear resampling corrects many of the negative effects. Further, since the acoustics of interest in this study occur below 1 kHz, the resampling process should have very little affect on the resulting analysis. No other post-processing of the pressure signatures are performed.

3.4 Helicopter Maneuver Description

Three distinct flight maneuvers executed at various speeds are investigated. They comprise medium (m-) and fast (f-) advancing side roll (AR) maneuvers, as well as a steady level flight (SLF) shown in figure 3.6. Each transient maneuver

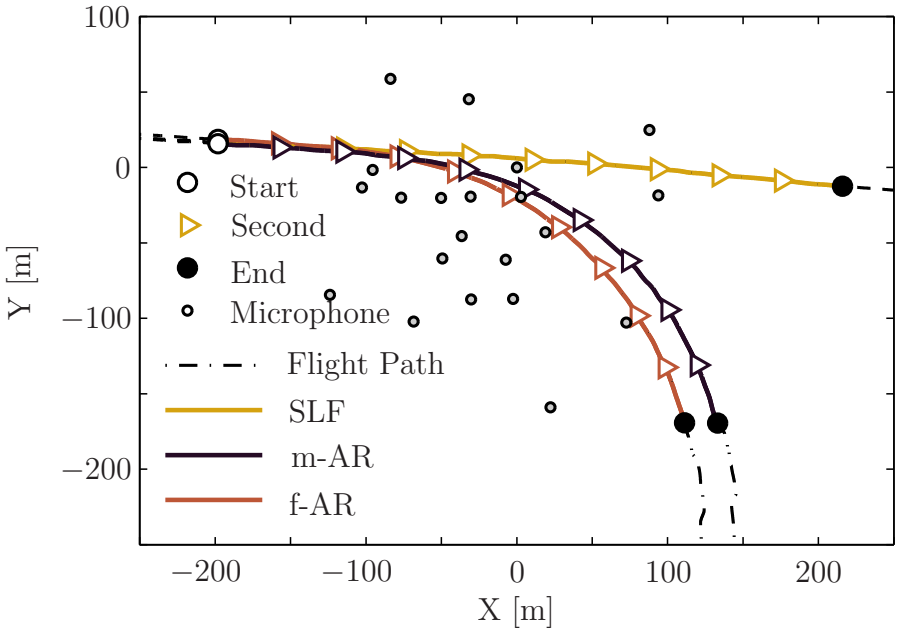

Figure 3.6: Ground track of each maneuver across the microphone array.

was initiated at approximately (X=25, Y=-125), 2 seconds into the 10 second *path of interest*. Relevant flight parameters are given in table 3.3. De-Dopplerized pressure signatures extracted from throughout the steady level flight profile are

	SLF	m–AR	f–AR	
Ground Speed [m/s]	41.5	39.4	41.5	
Median Height [m]	54.1	45.6	41.5	
Gross Weight [kN]	38.7	38.4	38.7	[±0.2]

Table 3.3: Averaged flight parameters and gross vehicle weight during each maneuver. Gross weight measurement is bounded by the limits of the measurement device.

provided in figure 3.7. It can be seen that the blade-vortex interaction signal,

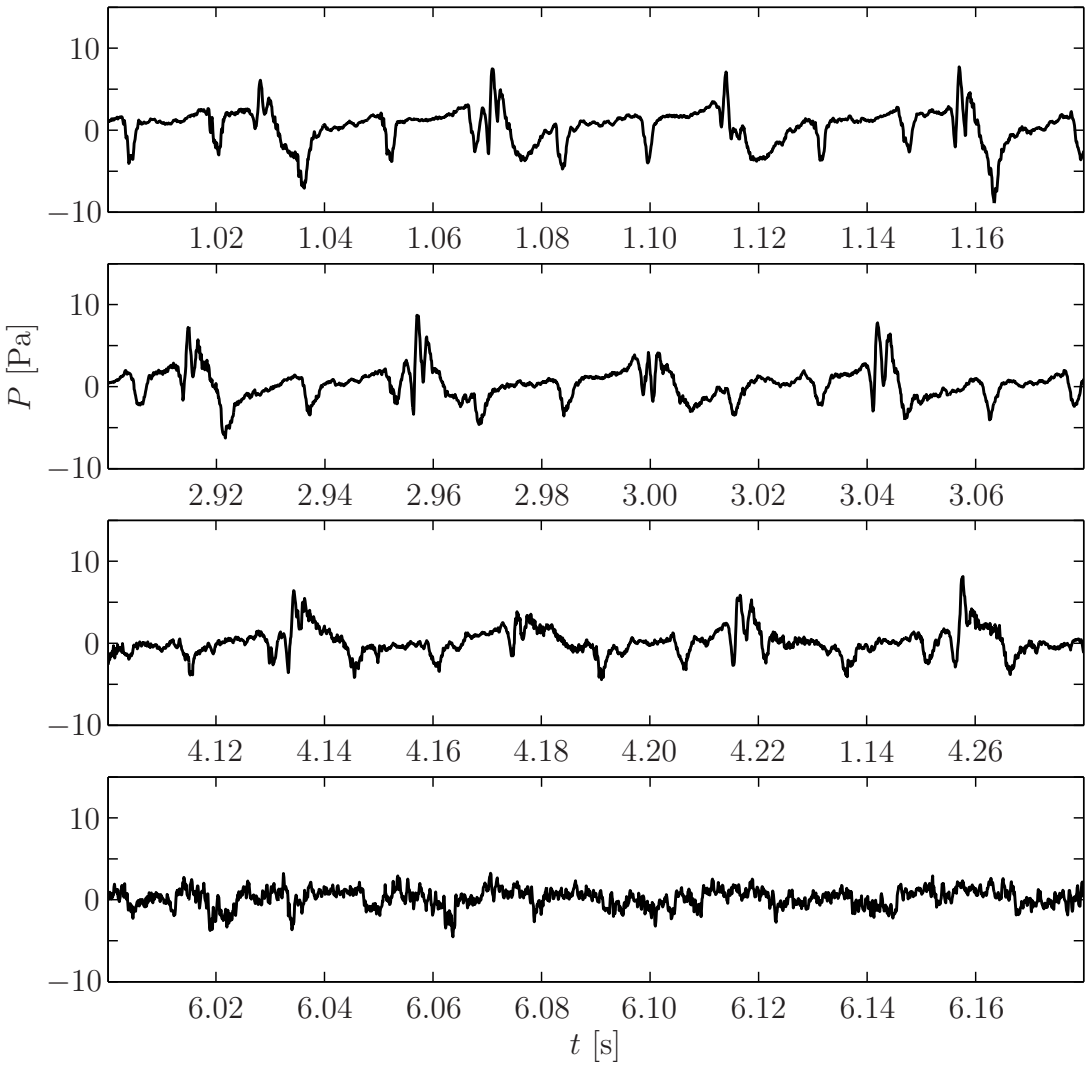

Figure 3.7: Pressure signatures extracted from microphone 7 during the steady level flight case at various instances in time.

originally identified in figure 1.2, begins quite strong and then decreases over time. Further, the tail rotor signal broadens and decreases with time as well. Since this signal is extracted from the steady level flight maneuver, any changes in pressure seen are due solely to changes in directivity related to the microphone used here. Overall, it is clear that the pressure signature changes drastically throughout the maneuver further necessitating the need for time-frequency analysis techniques.

The relevant vehicle parameters for pitch and roll attitudes and rates of change for each maneuver can be found in figure 3.8. The attitudes and rates of change for both pitch and roll confirm that each maneuver initiated approximately 2 seconds into the 10 second *path of interest*. Each dynamic maneuver was designed to focus on a single pilot input, and so the two roll rate maneuvers show very little pitch attitude or pitch rate of change. The medium roll rate maneuver does, however, show a small pitch up near the end of the flight path and is probably due to the vehicle flying at a slightly lower altitude on that run.

The medium roll rate maneuver enters into the roll slower than the fast roll rate maneuver, shown in figure 3.8d, but reaches a similar peak roll rate. The peak roll rate achieved for either maneuver never exceeds 18 degrees per second, and the transient portion of the fast maneuver takes a duration of approximately 3 seconds. This is in stark contrast to the very aggressive maneuver investigated by Chen *et al.* [25], who modeled an advancing side roll maneuver which reached a roll rate of 40 [°/s].

The load factor, defined here as the ratio of the vehicle thrust to average thrust during the steady level flight, is shown in figure 3.9. The increase in thrust can be determined through the accelerations measured by the inertial navigation unit or can be determined through the flight path as measured by the DGPS. The load factor provides relative thrust magnitudes between each of the maneuvers. The thrust experienced by the vehicle affects the inflow through the rotor as well as the blade loading. Thus, changes in the load factor can indicate changes in both the lower harmonic noise and impulsive noise due to blade-vortex interactions, as discussed in sections 1.1.1 and 1.1.2.

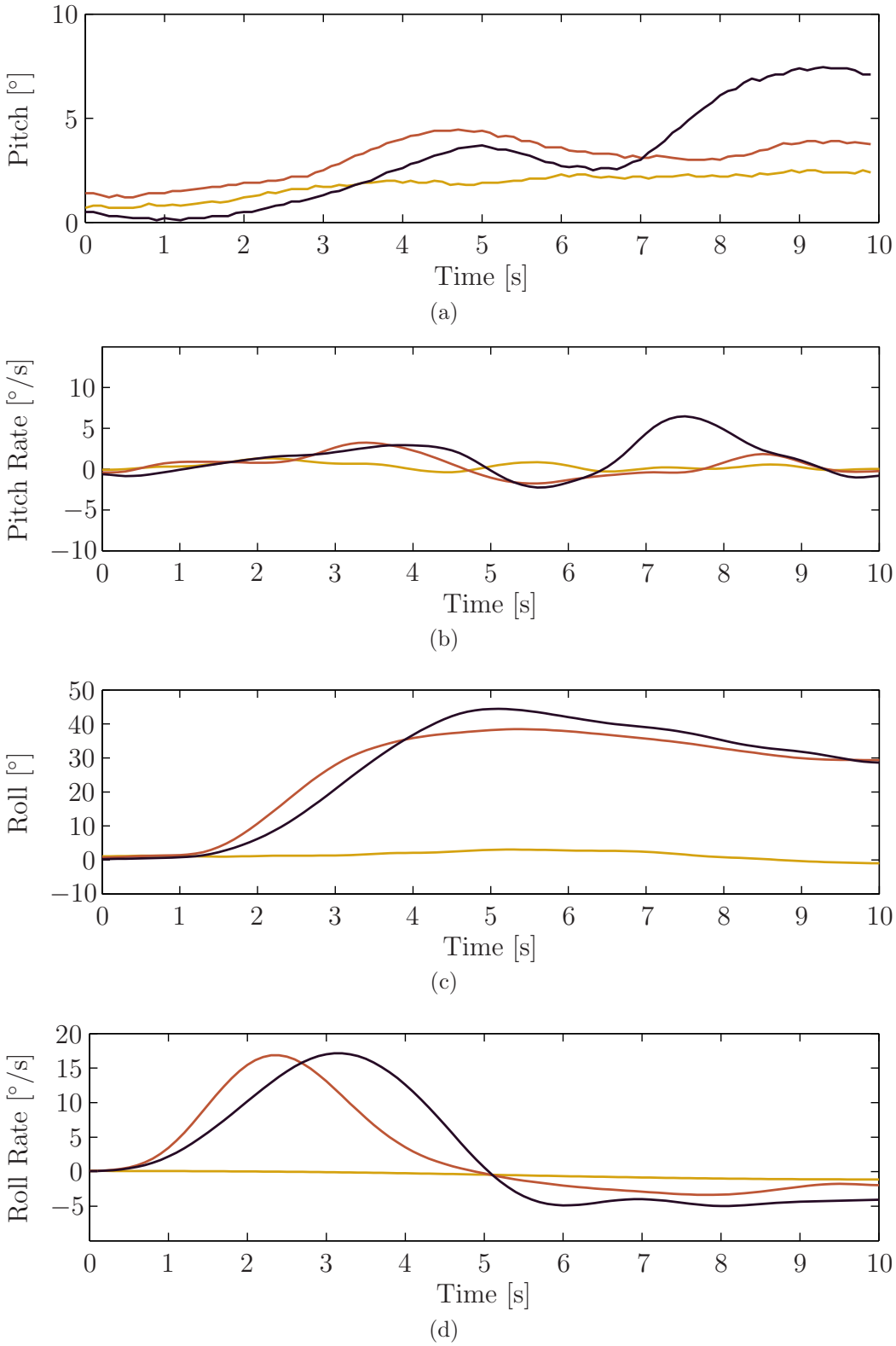

Figure 3.8: Vehicle (a) pitch attitude, (b) pitch rate, (c) roll attitude, and (d) roll rate throughout each maneuver. Legend provided in figure 3.6.

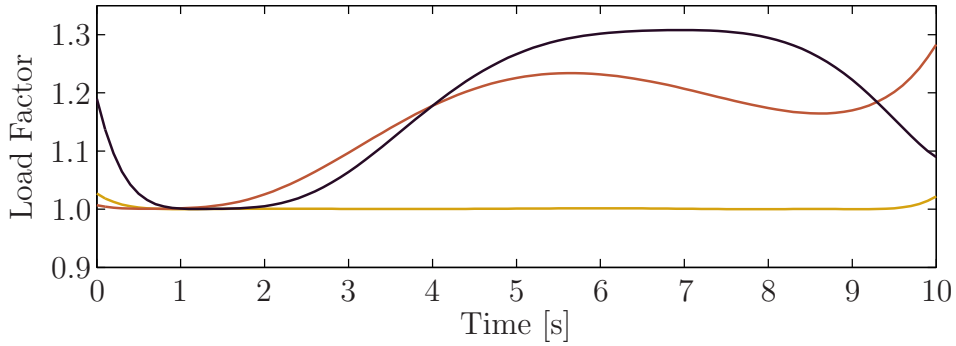

Figure 3.9: Load factor experienced by the vehicle during each maneuver. Legend provided in figure 3.6.

The forward speed of the vehicle was held fairly constant for the steady level flight and roll-right maneuvers, as shown in figure 3.10. The advance ratio

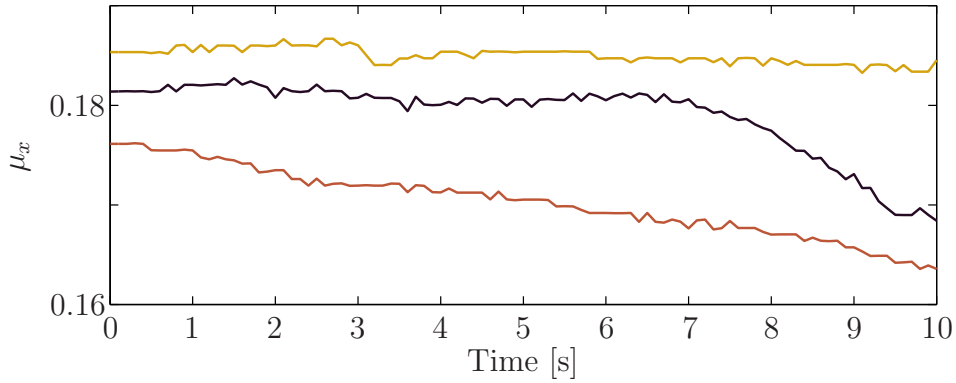

Figure 3.10: Forward advance ratio of the vehicle during each maneuver. Legend provided in figure 3.6.

is the speed of the vehicle non-dimensionalized by the rotor tip speed in hover ($\Omega\ R$). The maneuvers were designed to isolate given pilot inputs, and so the roll maneuvers see some decrease in the forward advance ratio as the pilot would have to otherwise change characteristics of the vehicle in order to maintain a given speed. With decreasing advance ratio, the vortex has more time to convect through the rotor inflow and so a subsequent increase in the vortex miss distance, and therefore decrease in blade-vortex interaction noise, is anticipated.

A weather balloon was deployed each day, shown in figure 3.11, and continuously profiled atmosphere conditions from 0 m to 91 m. The weather balloon provided atmospheric conditions such as wind speed and direction, temperature,

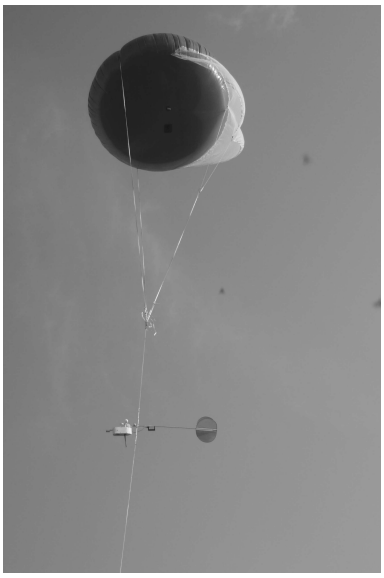

Figure 3.11: Weather balloon

pressure and relative humidity. Averaged atmospheric properties profiled during each maneuver are displayed in table 3.4 for the flyover conditions studied. It

	SLF	m–AR	f–AR	
Wind Speed [m/s]	1.6	2.6	2.9	[±2.7]
Temperature [°C]	23.76	24.32	24.70	[±0.05]
Pressure [kPa]	100.6	100.5	100.4	[±1.1]
Rel. Hum. [%]	98.18	93.37	89.24	[±0.01]

Table 3.4: Atmospheric conditions for each maneuver are averaged between 7 m and 46 m. Bounds on the data are provided by the maximum and minimum readings during each maneuver.

should be noted that wind speeds are relatively low for each maneuver, and the temperature and relative humidity are fairly consistent.

Attenuation due to atmospheric absorption is unaccounted for in the present study. However, figure 3.12 contains the calculated atmospheric absorption length scale ($\overline{\alpha}$) for several frequencies. Classical atmospheric absorption length scales are determined through the equations provided in appendix B of Blackstock (2000) [8], and are functions of atmospheric pressure, temperature, and relative humid-

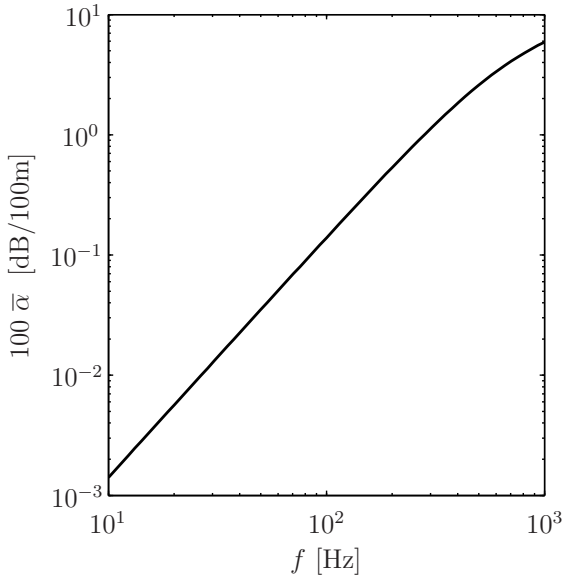

Figure 3.12: Calculated atmospheric attenuation rates as a function of frequency for the average atmospheric conditions provided in table 3.4.

ity. Classical absorption coefficients (α) are provided in units of nepers per unit distance, where neper is a unitless unit. These have been converted to units of dB per 100 meters as follows,

$$100\ \overline{\alpha}(f) = 100 \times 20 \log_{10}(e)\ \alpha(f) = 100 \times 8.686\ \alpha(f). \tag{3.1}$$

Distances in the present study are on the order of 100 meters, and so atmospheric conditions are not expected to affect the primary main rotor harmonics, but would slightly increase the energy in the higher frequencies of interest.

Chapter 4

Wavelet Transforms of Transient Maneuvering Acoustics

The wavelet transform is applied to each of the maneuvers investigated. A sample wavelet spectra is provided in figure 4.1, and the figure format is now explained. Three columns have been added to the left side of each wavelet power spectra to identify from left to right, the main rotor harmonics, tail rotor harmonics, and summed combinations of the two. The columns identify only where in frequency space the harmonics lie, and do not imply amplitude of the signal. Harmonic combinations less than 250 Hz are provided in table 4.1. The wavelet

$(\alpha_{MR}, \alpha_{TR})$	$f_{(\alpha_{MR},\alpha_{TR})}$	$(\alpha_{MR}, \alpha_{TR})$	$f_{(\alpha_{MR},\alpha_{TR})}$	$(\alpha_{MR}, \alpha_{TR})$	$f_{(\alpha_{MR},\alpha_{TR})}$
(1,0)	23.2	(6,0)	139.2	(9,0)	208.8
(2,0)	46.4	(1,2)	148.6	(1,3)	211.3
(0,1)	62.7	(4,1)	155.5	(4,2)	218.2
(3,0)	69.6	(7,0)	162.4	(7,1)	225.1
(1,1)	69.6	(2,2)	171.8	(10,0)	232.0
(4,0)	92.8	(5,1)	178.7	(2,3)	234.5
(2,1)	109.1	(8,0)	185.6	(5,2)	241.4
(5,0)	116.0	(0,3)	188.1	(8,1)	248.3
(0,2)	125.4	(3,2)	195.0		
(3,1)	132.3	(6,1)	201.9		

Table 4.1: Combinations of Bell 430 harmonics under 250 Hz. Frequencies are expressed in Hz.

power spectra in figure 4.1 has frequency on the vertical axis, with time on the horizontal axis. The Morgenstemning color map is employed in the wavelet power spectra as it provides a distinct color profile regardless of colorblindness, and has

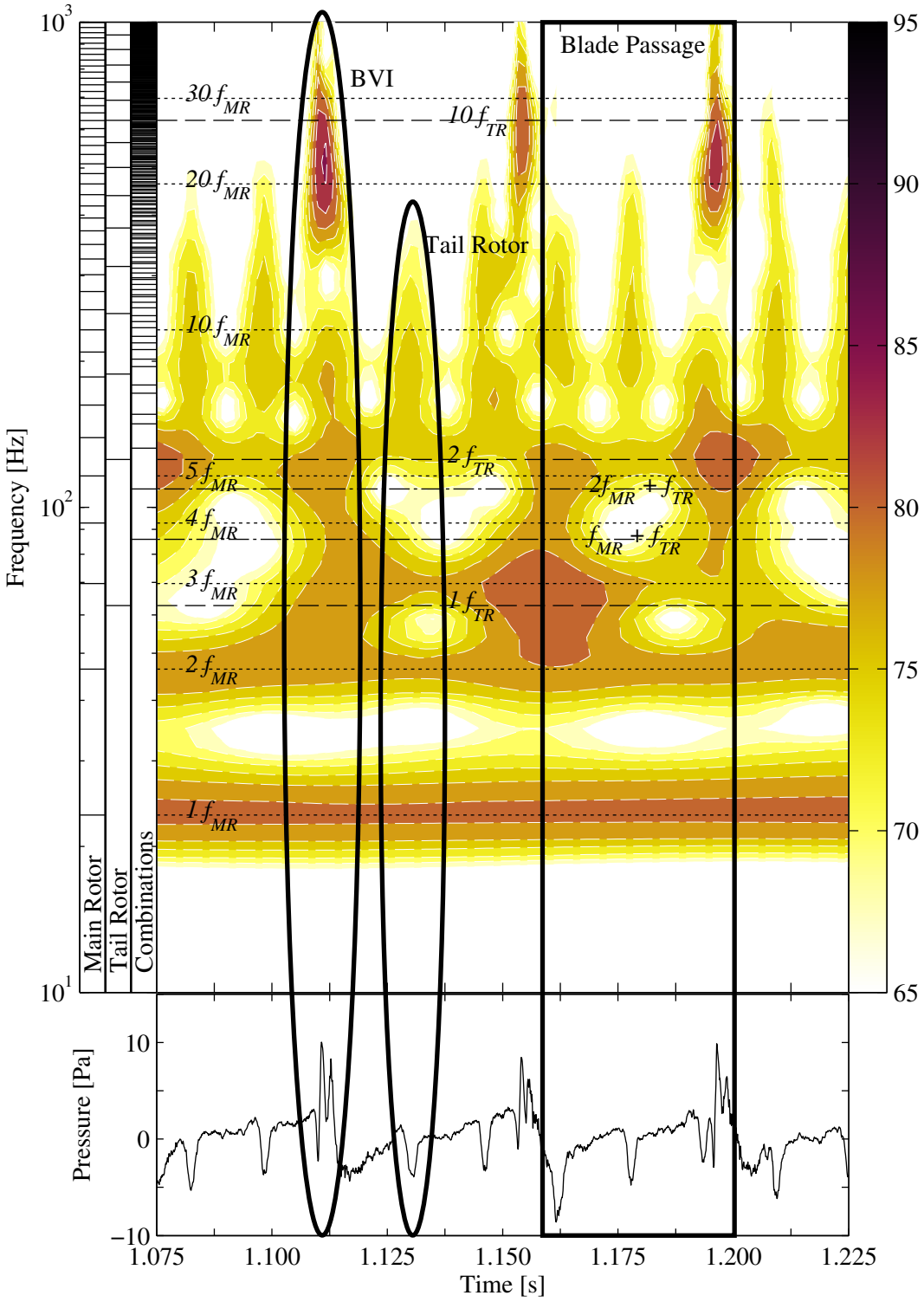

Figure 4.1: Sample wavelet power spectra with key features identified.

a monotonically increasing intensity for proper gray-scale printing [46]. Underneath the wavelet power spectra is the corresponding pressure signature in the time domain. Several main rotor, tail rotor, and combinations thereof have been further defined by dashed horizontal lines in the wavelet power spectra.

Figure 4.1 is certainly rich with information, and so key signatures have been identified. The key features relate to the full blade passage, tail rotor and blade-vortex interaction phenomemon, in conjunction with figure 1.2, from before. The tail rotor signature can be identified by the spectral pulse between the second tail rotor harmonic and the twentieth main rotor harmonic. Blade-vortex interactions, however, show a strong peak in energy between the tenth main rotor harmonic and 1 kHz. A method for extracting the blade-vortex interaction signal from the overall acoustic signal is possible due to the strong spectral content inherent in the phenomenon. Such a method will be developed in § 5.

4.1 Steady Level Flight Analysis

A single microphone, microphone 7 in figure 3.4a, is chosen from the available microphones for further investigation. The location of this microphone relative to the helicopter is shown in figure 4.2, plotted on a Lambert projection

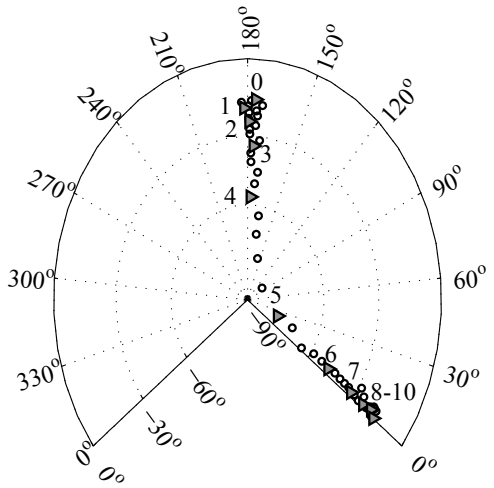

Figure 4.2: A single microphone directivity is shown with position denoted every fifth of a second by a circle and triangle symbols indicate each second. The second value identified by each triangle, throughout the *path of interest*, is also identified.

described in figure 1.10. Wavelet power spectra for the steady level flight is shown in figure 4.3, for the 10-second *path of interest* in figure 3.6. In order to investigate the spectra in more detail, subsamples of the WPS have been extracted and are shown in figures 4.4.

The first few seconds of the maneuver covers the approach of the vehicle and a rich spectra is seen, with lots of energy in the higher harmonics. The energy in the higher harmonics comes from the blade-vortex interaction signal present within the signal. Blade-vortex interactions are clearly seen in figure 4.4, where sharp pressure spikes at each blade passage are present. The sharp pressure spikes directly correspond with the strong spikes in the higher harmonics of the wavelet power spectra, as was shown in figure 4.1. The blade-vortex interactions appearing predominantly in the higher harmonics is in accord with the work of Widnall (1971) [111], as well as Martin and Hardin (1988) [77].

Close inspection of the pressure time series reveals an alternating strength in the blade-vortex interaction signature, where a strong event is followed by a slightly weaker event. This is also seen in the pressure signatures provided in figure 4.3a where the peak pressures are alternating between slightly higher and lower values. This alternating blade-vortex interaction signature is a manifestation of the split tip path plane of the vehicle main rotor system, previously shown in figure 3.2. Since each opposing set of blades are at differing heights, the miss distances of the blade-vortex interactions are alternating between slightly further away and slightly closer.

It is trivial to state that the steady level flight maneuver does not undergo any drastic changes to the aerodynamics experienced by the vehicle, yet a clear change in the spectra can be seen in figure 4.3, starting at 3.5 seconds into the maneuver. Since the microphone pressure signature has been normalized to a common distance, this means that changes in the spectra are a direct result of changes in the directivity seen by the microphone.

From 3.5 to 6 seconds, the vehicle passes directly over the microphone, and so loading, discussed in § 1.1, becomes predominant. This mechanism does not

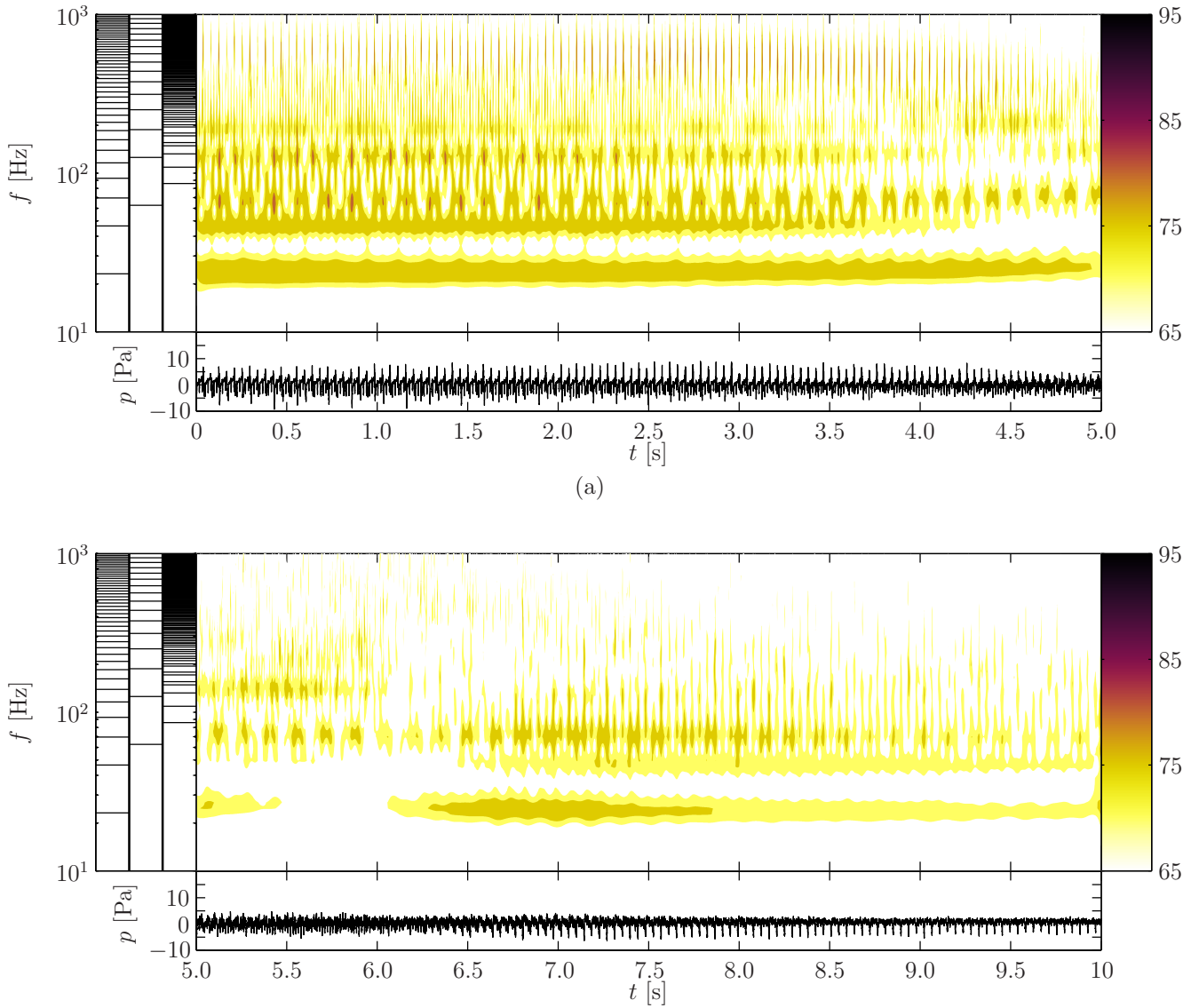

Figure 4.3: Wavelet power spectra for one microphone during the steady level flight maneuver, for the (a) first five and (b) last five seconds of the path of interest. The associated pressure signal is shown immediately below each spectra.

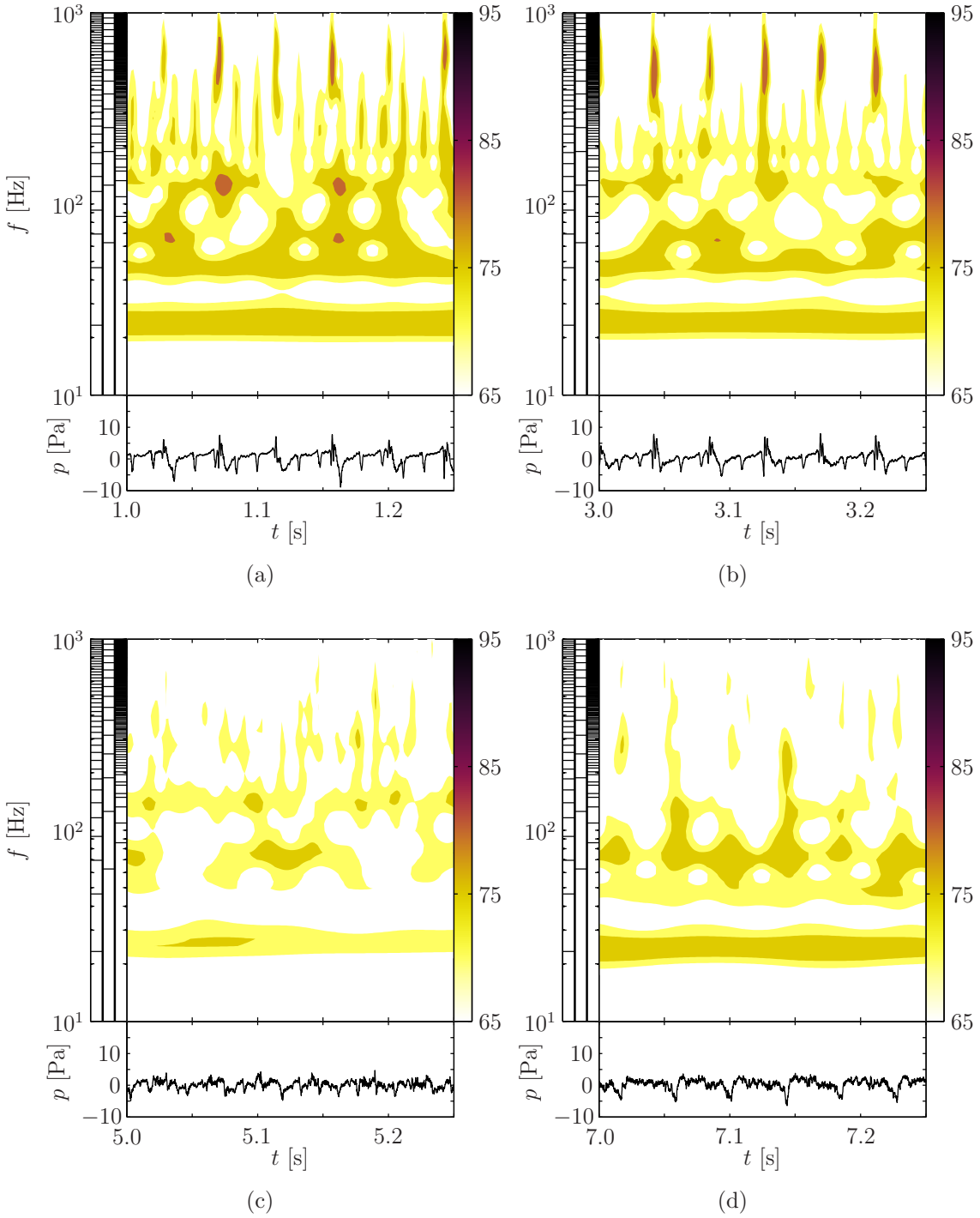

Figure 4.4: Subsamples of the wavelet power spectra extracted from the steady level flight maneuver, each containing a full rotor revolution. A subset of the spectra beginning at (a) one second, (b) three seconds, (c) five, and (d) seven seconds into the maneuver are included.

contain a lot of energy in the higher harmonics, therefore, the energy in the signal is relatively relegated to the first 7 main rotor harmonics. Starting at the 3.5 second mark, a decrease in the second main and second tail rotor harmonics can first be seen, followed then by a decrease in the first main rotor harmonic which starts at about 4.5 seconds and continues to decrease until almost the 6 second mark. A subsequent decrease in the higher harmonics can also be seen, except for the third main and first tail rotor harmonic which appears relatively unaffected until the 6 second mark. The reduction of energy across most harmonics implies that this area is marked by a lower overall sound pressure level, when distance to the vehicle is accounted for.

After the 6 second mark the vehicle then proceeds away from the microphone, and so the noise mechanisms seen by the microphone change yet again, and a strengthening of the harmonic signal begins. The main rotor harmonic strengthens almost to its previous magnitude, but then decreases again, while harmonics over 200 Hz fail to recover significantly. Figures 4.4c and 4.4d contains subsamples of the spectra from figure 4.3, pertaining to the substantially decreased spectra at the five second mark, and the slightly recovered spectra seen at seven seconds. After the vehicle has passed, the first three main rotor harmonics restrengthen and beginning at the 8 second mark, the spectra remains relatively constant. It is postulated that the overall weakening of the spectra beyond this point is a result of atmospheric attenuation acting over increasingly larger distances. The vehicle is now on the order of the atmospheric absorption length reported in table 3.12, and so atmospheric attenuation is expected to be relevant, although remains unaccounted for, at this time.

4.2 Advancing Side Roll Analysis

The advancing side roll maneuvers are investigated using the same microphone (microphone 7) as was used in the steady level flight maneuver. While the directivities of the microphone between the two roll maneuvers are very similar, seen in figure 4.5, the directivities are very different when compared to that of

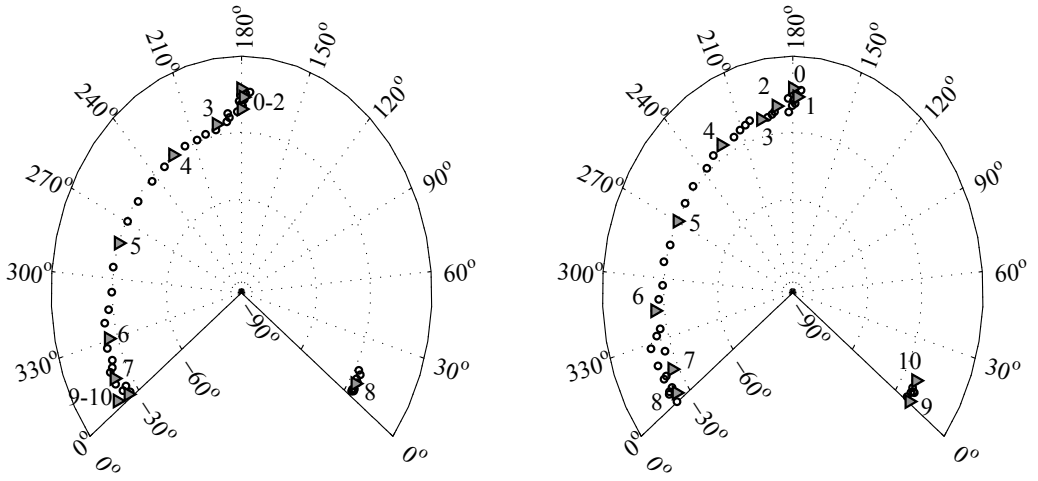

(a) (b)

Figure 4.5: Directivity paths for the (a) m-AR and (b) f-AR maneuvers for the microphone of interest. The second value identified by each triangle, throughout the *path of interest*, is also identified.

the SLF maneuver. This is because the roll angle changes the orientation of the microphone with respect to the vehicle. Since the roll angles, from figure 3.8c, and position of the vehicle, seen in figure 3.6, are similar between both roll maneuvers, then the microphone directivities are also similar.

4.2.1 Medium Advancing Side Roll Maneuver

Subsamples of the wavelet power spectra extracted throughout the medium advancing side roll maneuver can be seen in figure 4.6, while the full spectra from the microphone of interest is shown in figure 4.7. The spectra initially shares similarities with that of the steady level flight condition on approach, which showed a signal containing mild blade-vortex interactions. The commonalities between the two spectra in the first two seconds are expected, and is further confirmation that the medium advancing side roll maneuver is initiated after first attaining steady level flight.

As the vehicle enters into the roll, starting around the one second mark as seen in figure 3.8d, the overall energy in the signal begins to slowly increase. This increase in energy is due to the increase in the strength of the blade-vortex

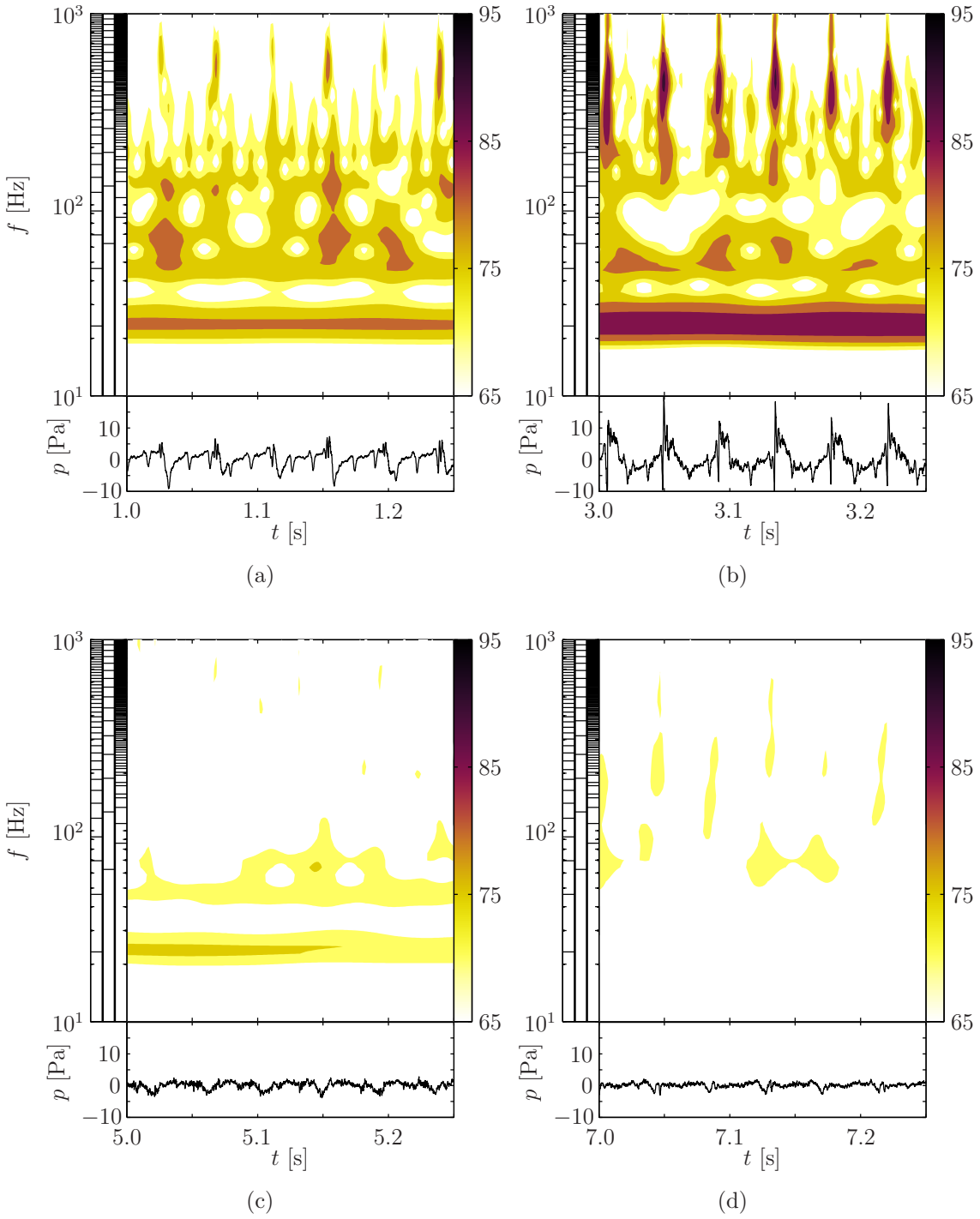

Figure 4.6: Subsamples of the wavelet power spectra extracted from the medium advancing side roll maneuver, each containing a full rotor revolution. A subset of the spectra beginning at (a) one second, (b) three seconds, (c) five, and (d) seven seconds into the maneuver are included.

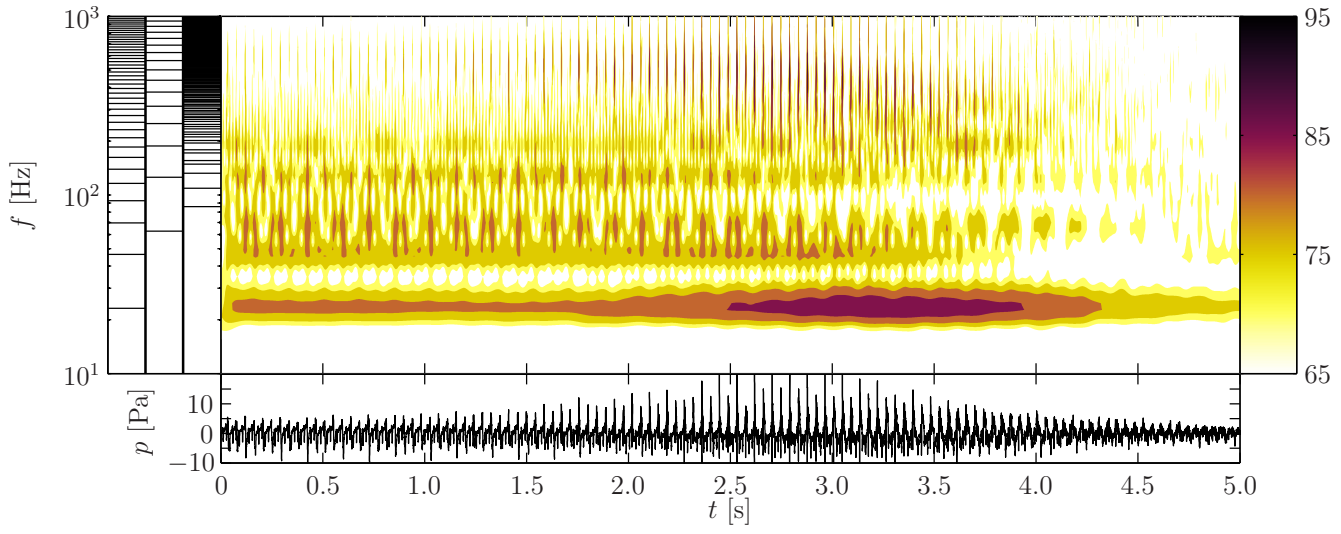

(a)

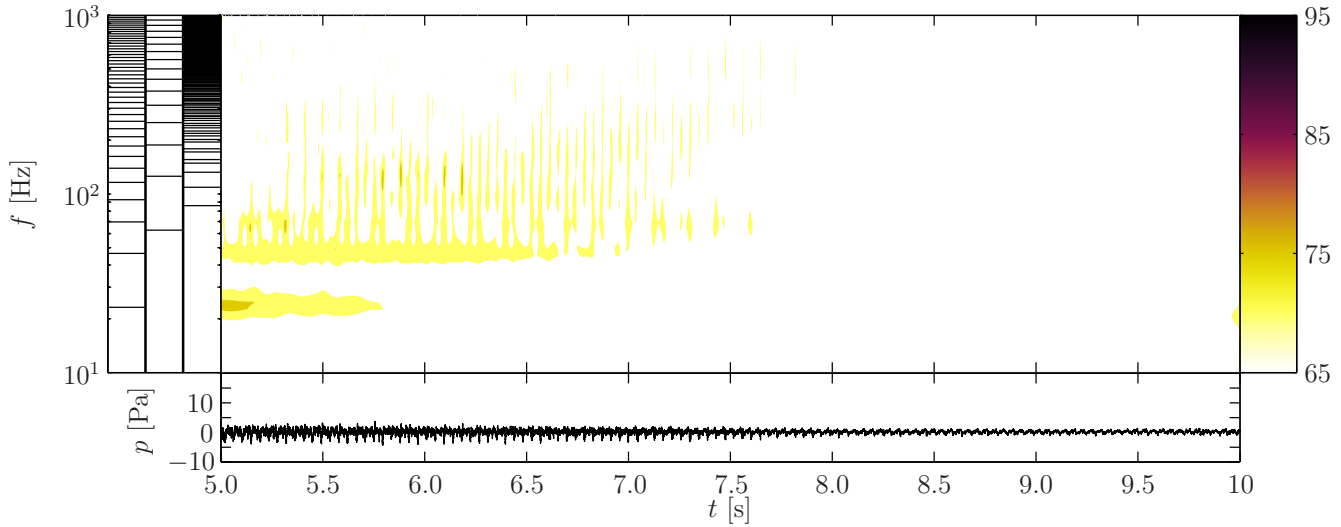

(b)

Figure 4.7: Wavelet power spectra for one microphone during the medium advancing side roll maneuver, for the (a) first five and (b) last five seconds of the path of interest. The associated pressure signal is shown immediately below each spectra.

interaction signature, as well as the increase in the lower harmonic noise signature. Figure 4.6a shows a rotor revolution extracted from the entrance into the maneuver, while figure 4.6b is an extraction of the WPS from near the peak roll rate of the maneuver.

The blade-vortex interaction signal appears to peak around the 2.75 second mark, just prior to figure 4.6b, a half second prior to the peak that occurs for the first main rotor harmonic. It is hard to isolate whether the peaks are due to the roll rate, seen previously, or due to the changing directivity pattern. This peak in blade-vortex interaction noise exists predominantly forward and to the retreating side of the vehicle (figure 4.5a), in accordance with the conclusions of Greenwood *et al.* [56] for blade-vortex interaction directivity during roll maneuvers. The lower harmonic noise increase is not likely caused by changes to loading noise, as that noise source is primarily focused below the rotor and the load factor on the vehicle has not changed substantially at the 3 second mark for this maneuver, seen in figure 3.9.

On departure, the medium advancing side roll maneuver shows significantly less energy then was seen for the SLF maneuver. Comparing figure 4.4c with figure 4.6c, shows the steady level flight possessed similar strengths for the main rotor harmonic, but contained more energy in the higher harmonics at the 5 second mark. The difference in these two is almost certainly caused by both the maneuver and difference in directivities.

At the 7 second mark, however, the steady level flight and medium advancing side roll maneuvers possessed very similar directivities, seen in figures 4.2 and 4.5a, respectively. Therefore, the differences in spectra between figures 4.4d and 4.6d are caused entirely by the maneuver. For the medium advancing side roll maneuver, the spectra is dominated by the tail rotor signature, while the main rotor and its harmonics are quite strong in the steady level flight. Assuming the tail rotor signature is simply masked by the strong third main rotor harmonic, this shows that the advancing side roll maneuver has significantly affected the noise signature related to the main rotor for this directivity.

4.2.2 Fast Advancing Side Roll Maneuver

Subsamples of the wavelet power spectra extracted from the fast advancing side roll maneuver are found in figures 4.8 and 4.9, while the full spectra is shown

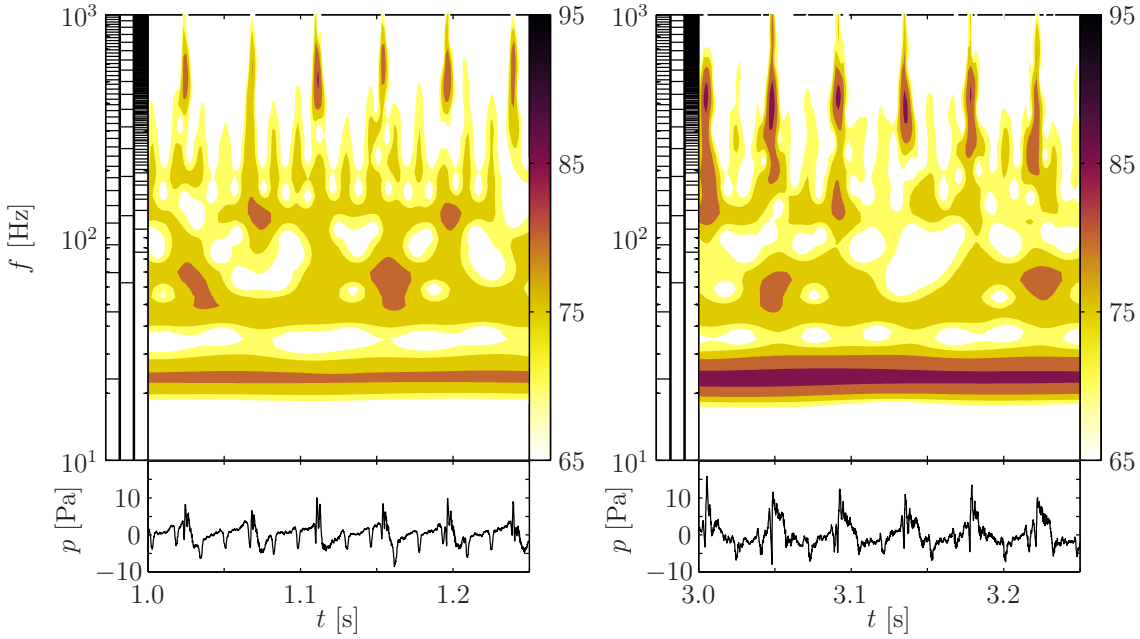

(a) (b)

Figure 4.8: Subsamples of the wavelet power spectra extracted from the fast advancing side roll maneuver, each containing a full rotor revolution. A subset of the spectra beginning at (a) one second and (b) three seconds into the maneuver are included.

in figure 4.10. The first two seconds of the fast advancing side roll spectra initially shares similarities with that of both the steady level flight and medium advancing side roll condition on approach, as expected.

Similar to the medium roll rate maneuver, the fast roll rate sees an increase in the signature associated with blade-vortex interactions, albeit the increase is noticeable sooner, at the 1.25 second mark. Since the roll rate peaks before that of the medium roll maneuver, seen in figure 3.8d, the increase in blade-vortex interaction is also expected to occur sooner. Also similar to the medium roll rate case, the energy in the main rotor harmonic peaks after the blade-vortex interaction signal, around the 2.75 second mark.

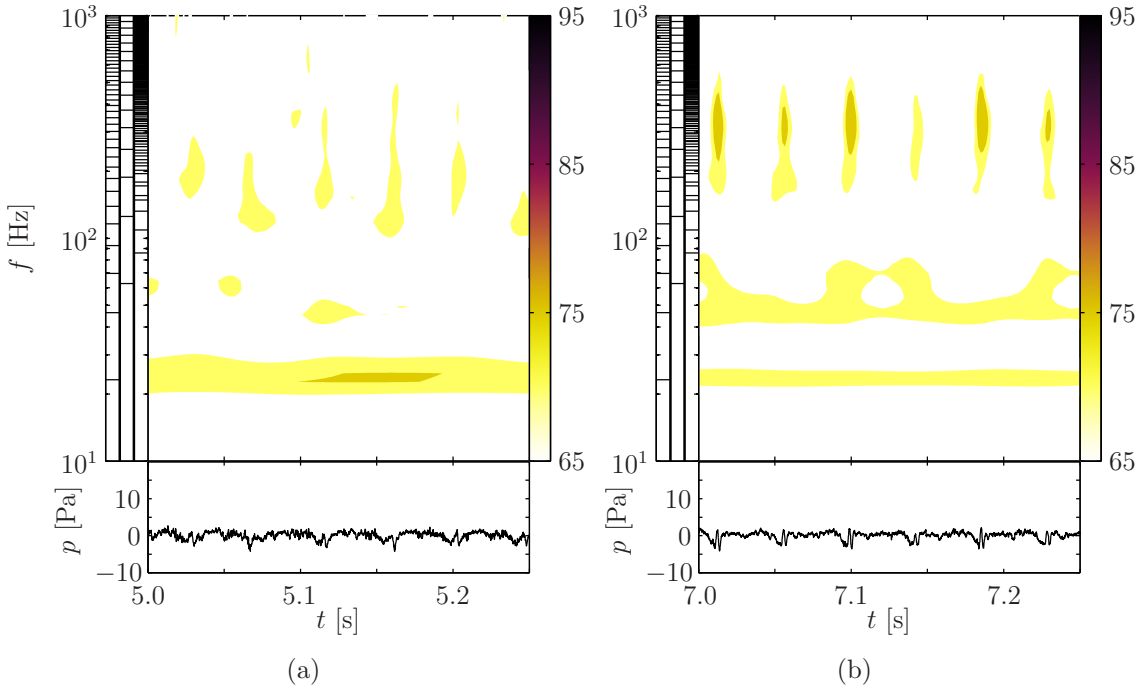

(a) (b)

Figure 4.9: Subsamples of the wavelet power spectra extracted from the fast advancing side roll maneuver, each containing a full rotor revolution. A subset of the spectra beginning at (c) five and (d) seven seconds into the maneuver are included.

Comparing figure 4.9a with figure 4.6c, it can be seen that the main rotor harmonic is similar in strength, although the fast maneuver has some higher harmonics present, but the second main rotor harmonic is not present as it is in the medium advancing side roll case. Further dissimilarities can be seen on departure when comparing figures 4.9b and 4.6d. The medium roll rate maneuver showed only mild higher harmonic information, associated with the first tail rotor harmonic. The fast roll rate maneuver, however, shows a distinct influence from the main rotor, and has also captured signal associated with a retreating side blade-vortex interaction.

At the 7 second mark, the roll rate is negligible, and the roll attitudes and pitch rate and attitudes between both maneuvers are similar, seen in figure 3.8. However, the load factor (figure 3.9) is less than that of the medium roll rate maneuver, and is decreasing while the load factor for the medium roll rate maneuver is holding constant. With a lower load factor, comes a lower inflow

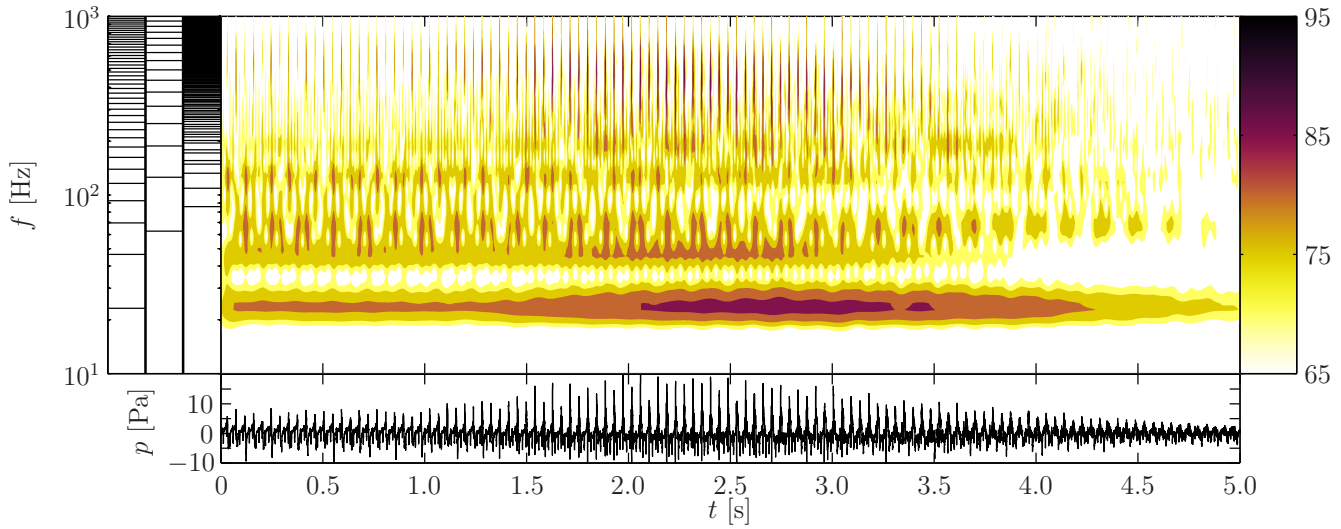

(a)

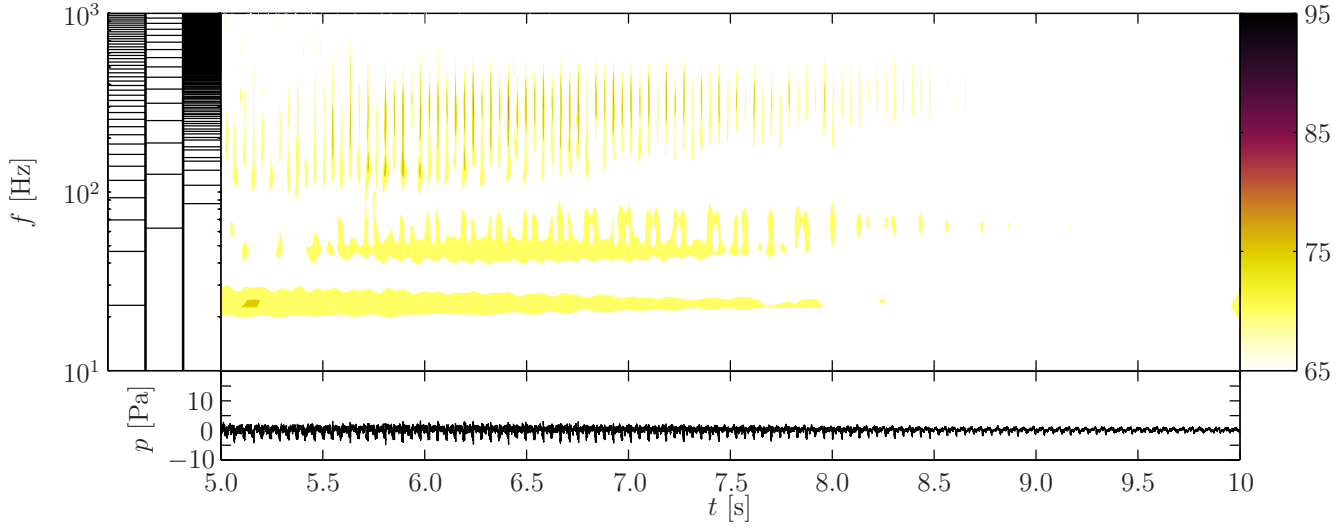

(b)

Figure 4.10: Wavelet power spectra for one microphone during the fast advancing side roll maneuver, for the (a) first five and (b) last five seconds of the path of interest. The associated pressure signal is shown immediately below each spectra.

through the rotor and so the miss distance that causes this retreating side blade-vortex interaction is expected to be less.

Further, it is noted that the spectral characteristics of the retreating side blade-vortex interaction are different from those of the advancing side interactions. Comparing figure 4.8b with figure 4.9b, one notices that the retreating side blade-vortex interactions exists at lower frequencies than the advancing side interactions. Advancing side interactions appear between 200 Hz and 1 kHz, while the retreating side blade-vortex interactions exist between 100 and 300 Hz. The shift in frequencies are partially due to Doppler affects, as the relative velocities experienced by the blades on the advancing and retreating sides are different. The de-Dopplerization algorithm discussed in § 3.3 only accounts for the vehicle velocity and not the velocity of the rotor blades. Some frequency shift and magnitude difference is also due to changes relating to the aerodynamics of the interaction, where the roll angle, roll rate, load factor, duration of the interaction, and trace Mach number are different for the two cases [58, 101, 111].

On close examination of the medium advancing side roll maneuver, in figure 4.6d, the pressure signature shows a very mild blade-vortex interaction at each blade passage, and so this retreating side blade-vortex interaction phenomenon is present in both signals, although it is of greater importance for the fast advancing side roll maneuver. This also shows that the energy in the main rotor harmonic is positively affected by the presence of blade-vortex interactions. Since the load factor for the fast roll rate maneuver is less, then it should stand to reason that the lower harmonic noise would also be less than that of the medium roll rate maneuver. With the presence of the blade-vortex interaction, however, the main rotor harmonic is strengthened.

Adjusting the wavelet power spectra shown in figure 4.8 for atmospheric attenuation (as discussed in § 3.4) yields figure 4.11. Comparing figure 4.11 with figure 4.8 shows that the atmospheric attenuation primarily affects the high frequency signatures related to blade-vortex interactions. Further, the signatures are only substantially affected in figure 4.11a, due to the larger distance from micro-

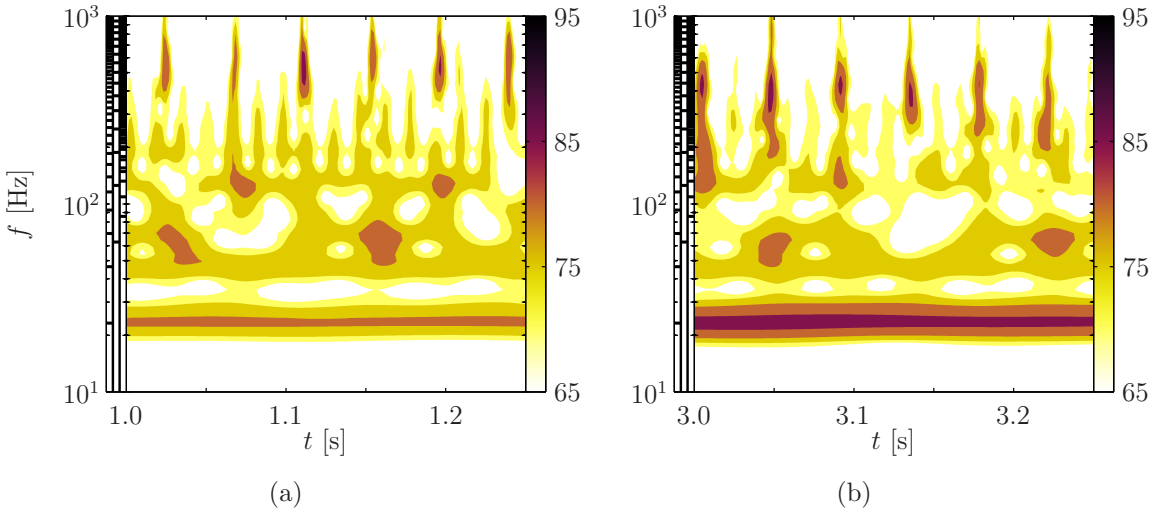

Figure 4.11: Subsamples of the wavelet power spectra extracted from the fast advancing side roll maneuver and adjusted for atmospheric attenuation. Each subset contains a full rotor revolution that begins at (a) one and (b) three seconds into the maneuver.

phone to vehicle at that time. This shows that atmospheric attenuation would have only a minor effect on the signal, and so will remain unaccounted for.

Chapter 5

Aerodynamic Analysis and Blade-Vortex Interaction Extraction Method

5.1 Rotorcraft Aerodynamics

Insight into the Ffowcs Williams - Hawkings equation (1.1) shows that the far-field acoustics are a result of the aerodynamics acting on the blade, and surrounding the blade. For modern helicopters, the quadrupole term of the FW-H equation can be ignored, and so the loading experienced by the helicopter blades, and the motion of the helicopter blades themselves, are necessary for the prediction of the resulting far-field acoustics [14]. Therefore, it is imperative that a basic understanding of helicopter aerodynamics is acquired. It is fundamental for the prediction of rotor acoustics and is the first step in each of the aeroacoustic prediction methods previously described in § 1.1. Further, this will allow us to relate the sound signatures registered in the far-field, to the physical mechanisms that act on and around the blades which generated the sound.

For any specified flight profile, the expected overall vehicle loads can be determined through a standard free-body diagram. A three degree-of-freedom trim analysis is shown in figure 5.1 where the longitudinal and lateral forces that act on the main rotor are identified. The orthogonal coordinate system (x_H, y_H, z_H) is centered on the helicopter's center of gravity with x_H aligned along the ground track of the flight path, z_H is oriented along the inertial Z direction, and y_H completes the system. Accelerations that act on the vehicle are identified and change throughout a given maneuver, depending directly on the specified flight path. The

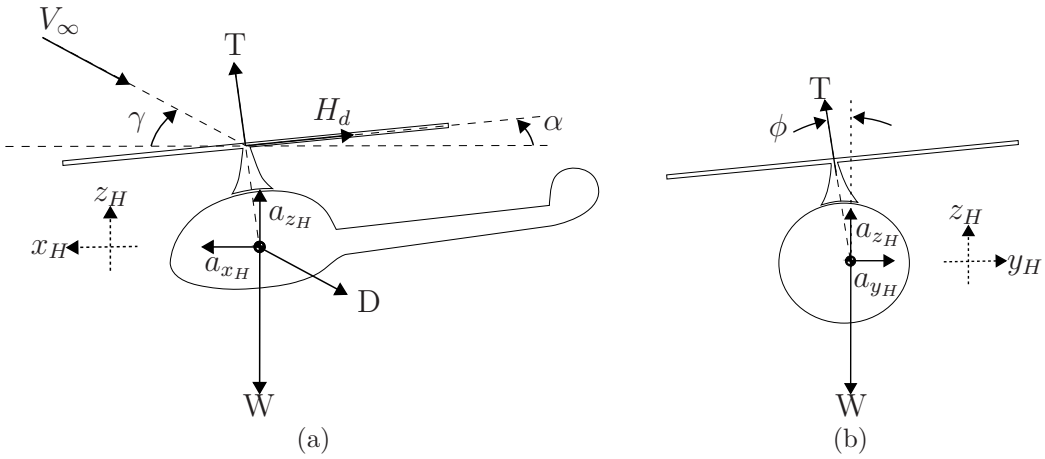

Figure 5.1: Helicopter (a) longitudinal and (b) lateral force balance.

complete transcendental equations of motion are described as follows

$$0 = T\cos(\alpha)\cos(\phi) - H_d\sin(\alpha) - D\sin(\gamma) - W(1 - a_z/g) \tag{5.1a}$$

$$0 = T\sin(\alpha)\cos(\phi) + H_d\cos(\alpha) - D\cos(\gamma) + W(a_x/g) \tag{5.1b}$$

$$0 = T\sin(\phi) + W(a_y/g), \tag{5.1c}$$

where rotor thrust (T), tip-path plane angle of attack (α), and bank angle (ϕ) are usually unknowns. The vehicle weight (W) is known, and accelerations ($a_{(\bullet)}$), flight path angle (γ), and vehicle velocity (V) can be determined from the specified flight path of the vehicle.

The vehicle velocity can be non-dimensionalized into a quantity called the advance ratio (μ) through the use of the rotation rate of the rotor (Ω) and rotor radius (R). Both the rotor drag force (H_d) and vehicle drag force (D) can be estimated using the following equations,

$$H_d/T = \frac{\sigma\ C_{d_0}\ \mu}{4} \tag{5.2a}$$

$$D/T = \frac{f_e\ \mu^2}{2A}, \tag{5.2b}$$

obtained from blade element momentum theory [65]. The zero-lift drag coefficient ($C_{d_0} = 0.008$) and flat plate drag area (f_e) are experimentally determined for the blades used on the rotor and the vehicle, respectively. Flat plate drag area is estimated to be 1.49 m^2, based on experiments from a similar vehicle design [54].

Rotor solidity (σ) is the planform area of the blades relative to the area of the rotor disk (A).

Thrust from the vehicle can also be non-dimensionalized by the rotor rotation rate, rotor radius, rotor area and density of the air (ρ). Once the tip-path plane angle of attack has been determined through equations (5.1) and (5.2), then the advance ratio can be broken into its forward (μ_x) and vertical components (μ_z). With the thrust coefficient (C_T) known, the non-dimensional flow through the rotor ($\lambda = v_r/(\Omega R)$) can be found from momentum theory using the following equation,

$$\lambda = \mu_x \tan(\alpha) + \frac{C_T}{2\sqrt{\mu_x^2 + \lambda^2}} + \mu_z. \tag{5.3}$$

The structure of the wake, and thereby the miss distance of the tip vortex during BVI, can be estimated through the Beddoes' prescribed wake method discussed in § 1.2. This work follows that of van der Wall's, where Beddoes' original inflow model [6] was modified by the inclusion of Drees' lateral asymmetries [107]. The resulting modified Beddoes inflow (Λ), given in equation (5.4a), is valid for the

$$\Lambda(1 \geq r > 0.3) = 1.2 + \frac{8}{15\pi} + \chi\left(-(x_H/R) - |(y_H/R)^3| + \overbrace{2\ \mu\ (y_H/R)}^{\text{Drees' Inflow}}\right) \tag{5.4a}$$

$$\Lambda(r \leq 0.3) = \chi\left(-(x_H/R) - |(y_H/R)^3| + 2\ \mu\ (y_H/R)\right) \tag{5.4b}$$

outer 70% of the rotor radius. The inside 30% of the rotor does not produce considerable thrust, and so the modified Beddoes' inflow in this portion is not affected by the average inflow through the rotor, as demonstrated in equation (5.4b).

Implementation of the Beddoes' wake model proceeds in 5 steps:

1. Initialize the blades at known locations and assume a tip-vortex is generated near the blade-tip.

2. Allow the blades to rotate to a new location (ψ_1), say 0.1 degrees from the previous location(ψ_0), and convect the previously generated tip vortex along its trajectory.

Assuming that the radial contraction is negligible for the wake directly underneath the rotor, then the tip vortex trajectory is aligned parallel with the x_h-direction and convects at a non-dimensional speed of μ_x.

3. Calculate new vertical position of tip vortex by integrating the inflow from the previous location and new location via equation (5.5) [6].

$$z_{H_1}/R = z_{H_0}/R + \mu_z(\psi_1 - \psi_0) - \frac{\lambda}{\mu_x}\int_{x_{H_0}/R}^{x_{H_1}/R} \Lambda \; d\frac{x_H}{R} \tag{5.5}$$

4. Identify and record the location and vertical displacement of all tip vortices which are in close proximity to rotor blades.

5. Repeat steps 2 through 4 until all blade-vortex interaction locations are determined.

The resulting wake structure for a nominal steady level flight ($\mu_x = 0.18, \lambda = 0.02, \Omega = 5$ [Hz]) can be seen in figure 5.2, for a 4 bladed rotor. The cyclic structure of a single tip vortex propagation path is shown in figure 5.2a. The vertical hump seen in the rear-view of the rotor wake, seen in figure 5.2b, shows the effect of neglecting the average inflow through the inner 30% of the rotor radius.

The locations, trace Mach number, and expected acoustic directivities of blade-vortex interactions, discussed originally in § 1.1.2.1 and shown in figure 1.6, can be identified directly from the Beddoes' wake model. This method can later be evaluated by examining the sound hemispheres extracted from measured data and ensuring that acoustically important blade-vortex interactions propagate in the expected direction. Further, the wake model can then identify miss distances of the important vortex interactions, which helps lead to an identification of the severity of the interaction. For instance, an oblique blade-vortex interaction is seen

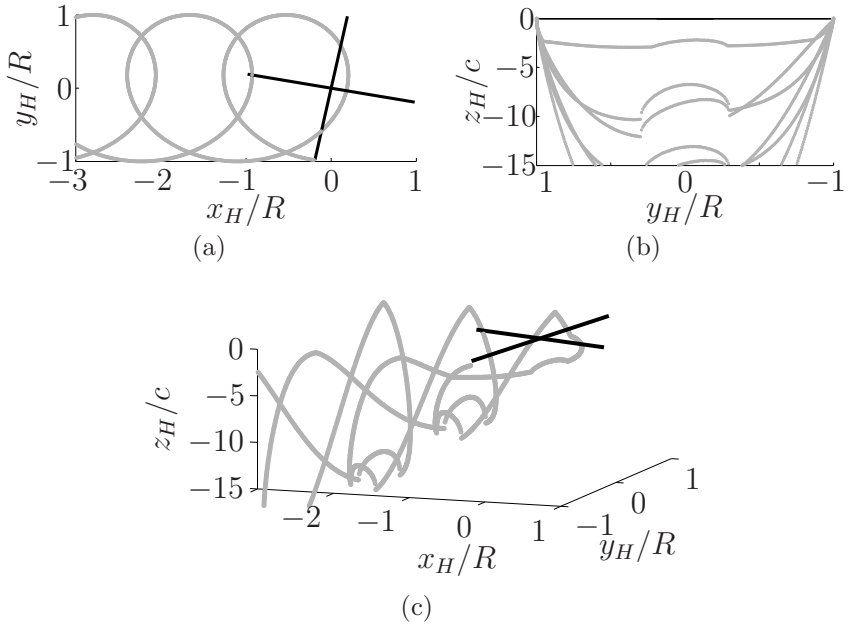

Figure 5.2: Rotor wake for steady level flight, as seen from (a) the top, (b) the rear, and (c) side.

occurring on the advancing side of the rotor at ($x_H/R \approx -0.1, y_H/R \approx -0.7$) in figure 5.2a. The miss distance of this interaction is approximately 3 chord lengths, shown in figure 5.2b. Successful implementation of this technique can prove useful in the planning of microphone locations for future transient maneuvering acoustic experiments.

Figure 5.3 shows the 8 vortex interactions, numbered 1 thru 8, possible for the nominal inflow condition used in figure 5.2. Here, the marker size is an indication of the miss distance, with larger symbols indicating small miss distances. Each symbol is color coded to indicate the trace Mach number of that location. Vectors pointing along the Mach cone angle, in the direction of sound propagation, are also provided for each acoustically important interaction. Thus, only two interactions are sonically important, and of those typically only one vortex interaction occurs in the direction of the predominant noise peak seen in chapter 4. The vortex interaction comprised almost entirely of supersonic trace Mach numbers is the oblique blade-vortex interaction shown in figure 5.2a [97].

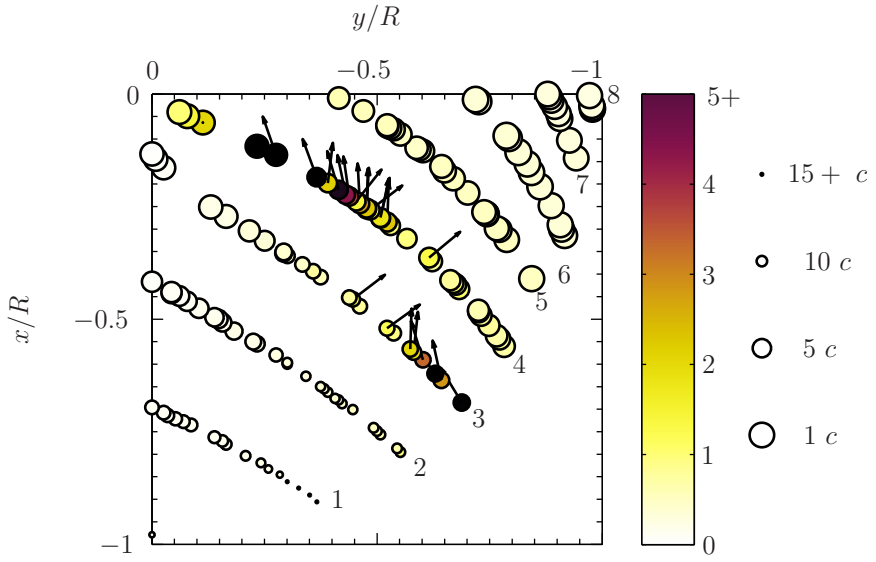

Figure 5.3: Blade-vortex interactions occurring within the first quadrant of the rotor. Symbol colors indicate trace Mach number, while marker size indicates vortex miss distances in chord length (c). Arrows point in the direction of acoustic propagation for relevant interactions.

5.2 Blade-Vortex Interaction Extraction Method

Methods to extract the noise signature related to the transient blade-vortex interaction phenomenon have proven difficult to develop. Davis *et al.* (1997) [34] first used a discrete wavelet transform to identify and extract the blade-vortex interaction noise from a relatively clean microphone pressure signature, seen in figure 2.1. This method worked well for the case where very little higher harmonic information, unrelated to blade-vortex interactions, was present in the original sound signature. The extraction technique developed here, will be an extension of the Davis *et al.* technique to continuous wavelet transforms. It will also provide a way to filter out higher harmonic energy that is unrelated to blade-vortex interactions.

Sickenberger *et al.* [93] also developed a method for extracting blade-vortex interaction signals from microphone data. They identified the blade-vortex interaction signature through an undocumented method and removed the entire signal from the time-history. They then used harmonic data from the surrounding, unmodified data to create a signal to fill in the 'missing' information. This method

is not employable in a larger data set, as the method for the identification of blade-vortex interactions is not described.

It has been shown analytically by Widnall (1971) [111] as well as Martin and Hardin (1988) [77], that the blade-vortex interaction signature exists predominantly in the higher harmonics of the pressure signature. The representation of blade-vortex interactions in the higher harmonics of the acoustic signal was confirmed in figure 4.1, using time-frequency analysis. Thus, a simple filtering algorithm can be developed using the continuous wavelet transform by identifying and extracting the blade-vortex interaction signature from the signal.

The method for filtering blade-vortex interactions will first be developed and implemented on a sample wavelet power spectrum in § 5.2.1. Then the method will be employed in § 5.2.2 on a synthetic set of data to determine whether or not the method can accurately recreate blade-vortex interactions from only their high amplitude, high frequency components. Afterwards, a sensitivity analysis will be employed in § 5.3, to determine the best tuning parameters for the removal of blade-vortex interaction noise during transient maneuvers.

5.2.1 Mathematical Description

Depending on the vehicle and the interaction investigated, the frequency associated with the blade-vortex interaction signature can change. Changes to the acoustic characteristics of blade-vortex interactions are expected during transient maneuvers, as the relevant aerodynamic parameters will change throughout the maneuver [58, 101]. A high-pass filter is not advised as higher frequency information, not associated with blade-vortex interactions, would also be extracted.

It was seen in § 4 that when blade-vortex interactions occur they are of similar strength as the main rotor harmonic. Therefore, a filtering method can be developed based off of the simultaneous occurrence of higher harmonic content that exceeds some amplitude threshold relative to the main rotor harmonic strength. As a reminder to the reader, the main rotor harmonic (f_{MR}) frequency is 23.2 Hz, provided in table 3.2.

The filtering method to remove the high frequency, high amplitude components of the blade-vortex interaction noise signal is described as follows,

$$\tilde{p}(f_j, t_i) = \begin{cases} \tilde{p}(f_j, t_i) & \text{if } f_j > f_{cut} \text{ and } E(f_j, t_i) > E(f_{MR}, t_i) - A_{cut} \\ 0 & \text{otherwise} \end{cases}. \quad (5.6)$$

Here $\tilde{p}(f_i, t_j)$ are the wavelet coefficients described in equation (2.1) for the corresponding wavelet scale (l_i). The frequency and amplitude cutoffs are f_{cut} and A_{cut}, respectively. This filtering method can easily be tailored to remove any high amplitude signal that falls within a given frequency range, and so has applications beyond the removal of blade-vortex interaction noise.

Figure 5.4 shows this filtering method working on an instantaneous slice of the wavelet power spectrum which contains a blade-vortex interaction. The interaction is identified by the filtering method and shown in the shaded region of figure 5.4a. The main rotor harmonic frequency is shown to peak just above 86 dB, and so the amplitude cutoff is slightly above 80 dB. Before the shaded region, there is a second peak that is related to the third main rotor harmonic and first tail rotor harmonic signal, at approximately 60 Hz. The wavelet coefficients ($\tilde{p}(l, t)$) that comprise the shaded spectral energy ($E(f, t)$) seen in figure 5.4b can be used to recreate the transient blade-vortex interactions via equation (2.4).

The wavelet coefficients extracted via this method can be reconstructed through equation (2.4) to create the signal directly associated with the blade-vortex interactions. Further, the wavelet coefficients extracted via this method can be used to directly determine the blade-vortex interaction sound pressure level (BVISPL) through equation (2.7). This should mark an improvement over the typical BVISPL metric, as it is directly associated with blade-vortex interactions, and not an integrated average of the sound pressure level over the anticipated frequency range of interest.

A schematic of the proposed extraction technique is shown in figure 5.5. The full process is shown, complete from transforming the original pressure signature through the use of the wavelet transform, filtering the transformed data

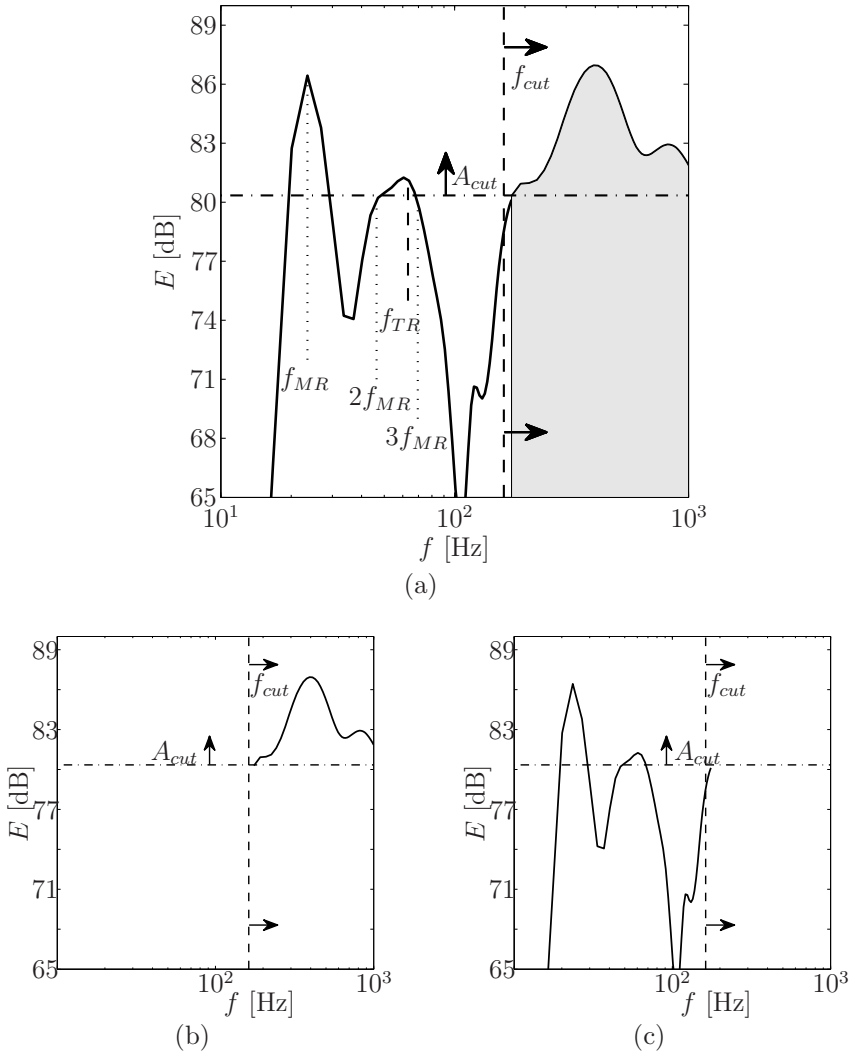

Figure 5.4: Demonstration of simultaneous frequency (f_{cut}) and amplitude cutoff (A_{cut}) for a signal containing blade-vortex interactions. The shaded portion of the spectra (a) is simultaneously above both the filter's frequency and amplitude cutoffs, and so is extracted and shown in (b). The first few main and tail rotor harmonics are also identified in (a). (c) Contains the residual signature.

via equation (5.6), and then inverse transforming the filtered data to create the associated pressure signatures.

A sample of the filtering method just described, is now presented from a pressure signature extracted during the fast advancing side roll maneuver. The tuning parameters selected for this pressure signature are frequencies above 7

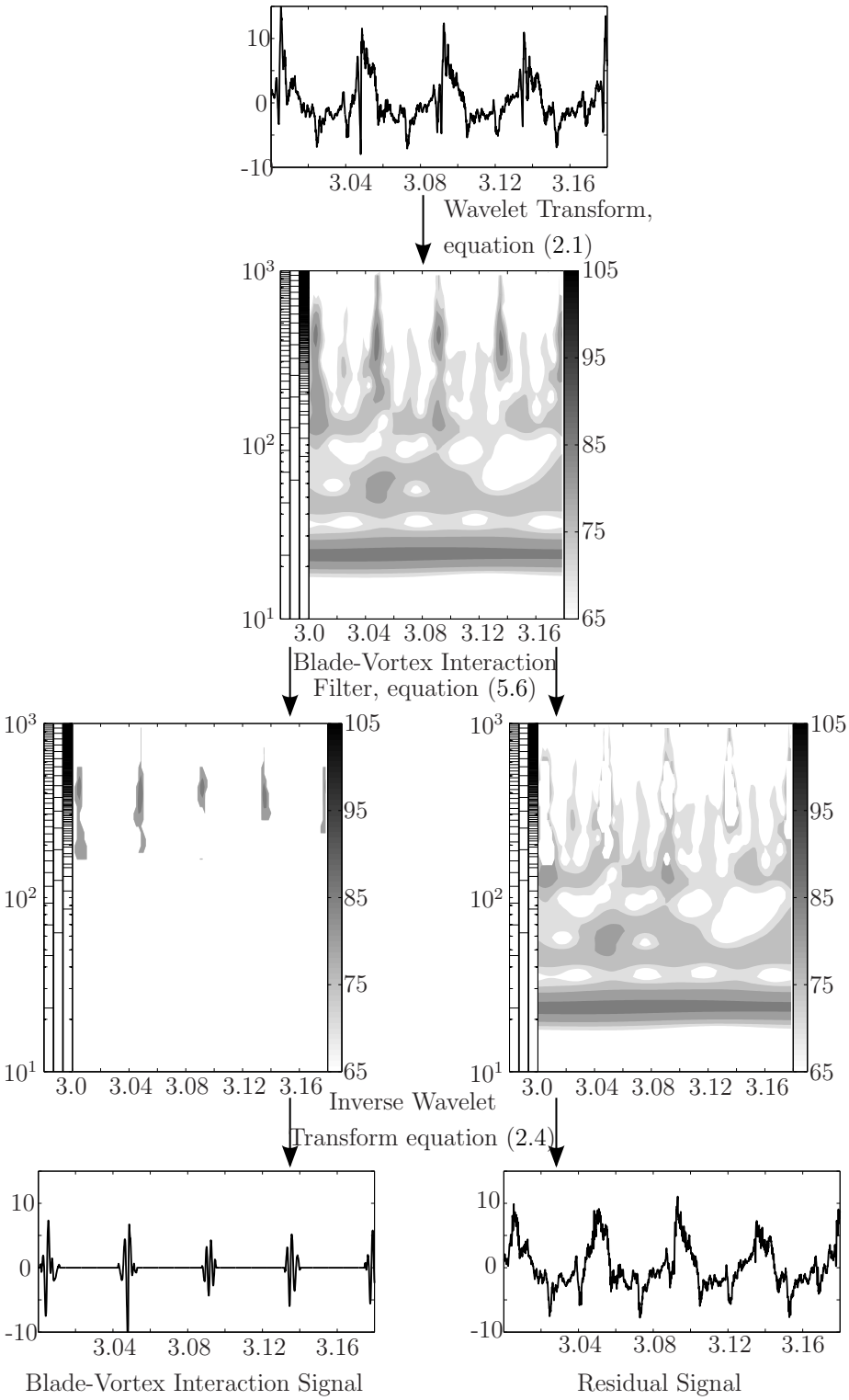

Figure 5.5: Schematic diagram of the full blade-vortex interaction extraction process, from original pressure signal through to the final, extracted signals.

blade passage frequencies, and amplitudes more powerful than 25% (−6 dB) of the main rotor harmonic. The original wavelet power spectra is shown in figure 5.6a, where the figure is identical to those seen in § 4. The signal investigated spans just over 1 complete rotor revolution and shows 4 predominant blade-vortex interactions as well as several negative pressure spikes associated with the tail rotor thickness noise. The wavelet power spectra shows a very strong main rotor harmonic with clear and well defined higher frequency spikes associated with the strong blade-vortex interactions.

Figure 5.6b shows the energy extracted from figure 5.6a with the reconstructed blade-vortex interaction pressure signature shown beneath. The recreated pressure signature for the blade-vortex interactions are fairly uniform across the rotor revolution. Some slight differences are seen between each of the signatures, due to the presence of the tail rotor signature that shifts in time, relative to each blade passage. The tail rotor also produces energy in the higher frequencies, and so a small portion of the tail rotor signature is also removed in the current implementation of the described filtering process.

The residual signature without blade-vortex interactions is given in figure 5.7. When comparing to the original signal in figure 5.6a, the overall shape of the pressure signature is preserved, with only the blade-vortex interaction signal removed. There is a small pressure rise at each blade passage that is slightly larger in magnitude than what one intuitively anticipates. This pressure rise is particularly evident in the first and third blade-vortex interaction events.

The pressure rise suggests that the full blade-vortex interaction signal is not represented entirely by its higher harmonic components, but also exists in some limited lower frequency content as well. This is anticipated, since the blade-vortex interactions can occur at every blade passage, so logically some energy associated with these interactions must be in the main blade pass frequency. This was also suggested by Martin and Hardin (1988) [77]. However, investigating the main rotor harmonic signature in either figures 5.6a or 5.7 shows that the energy within the first hundred hertz does not change during blade-vortex interaction

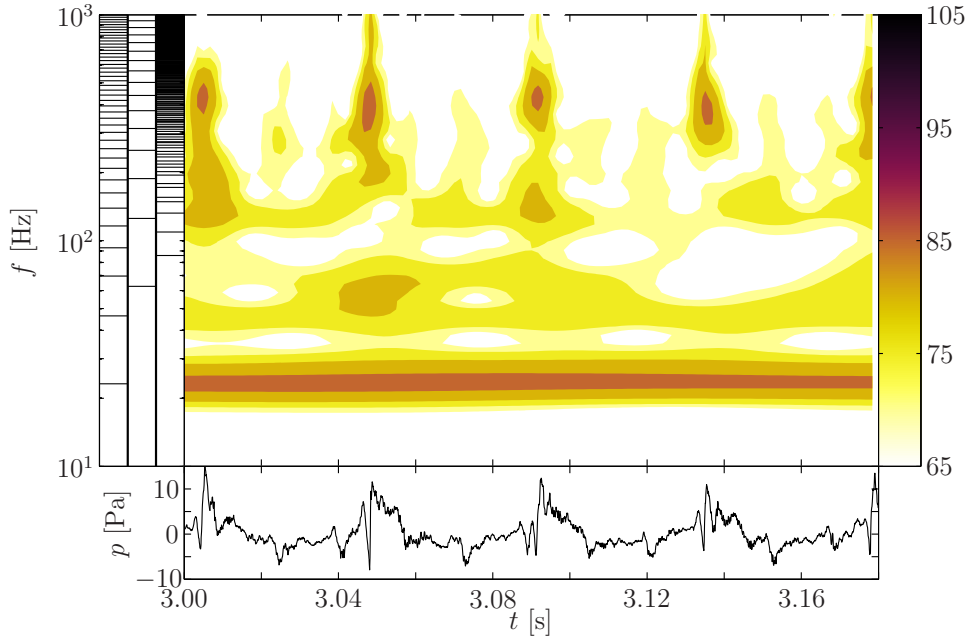

(a)

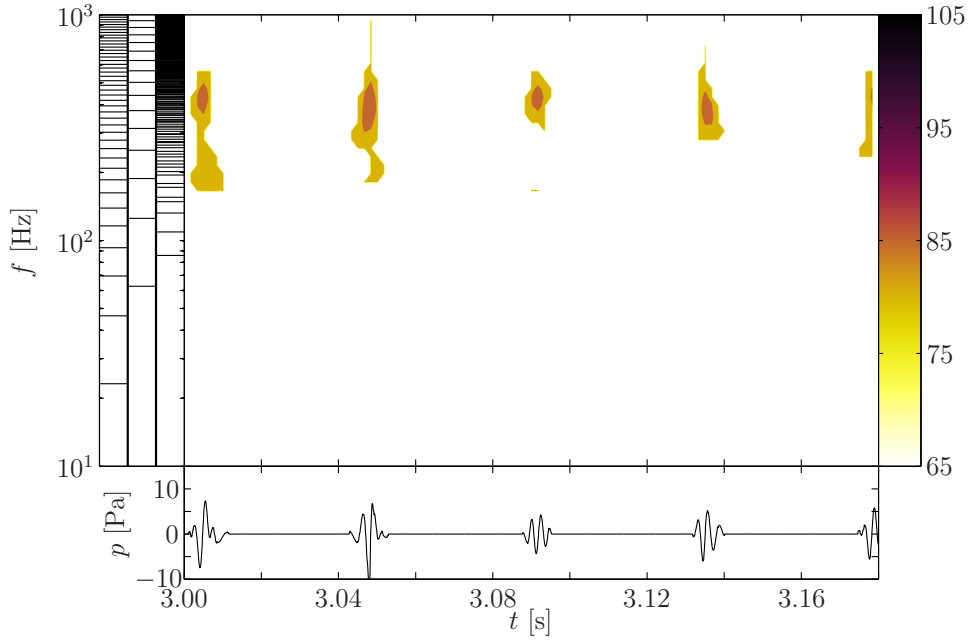

(b)

Figure 5.6: (a) Full wavelet power spectra from the fast advancing side roll maneuver showing strong presence of a blade-vortex interaction signal. (b) Extracted wavelet power spectra and associated pressure signature, related to the blade-vortex interaction during the fast advancing side roll maneuver.

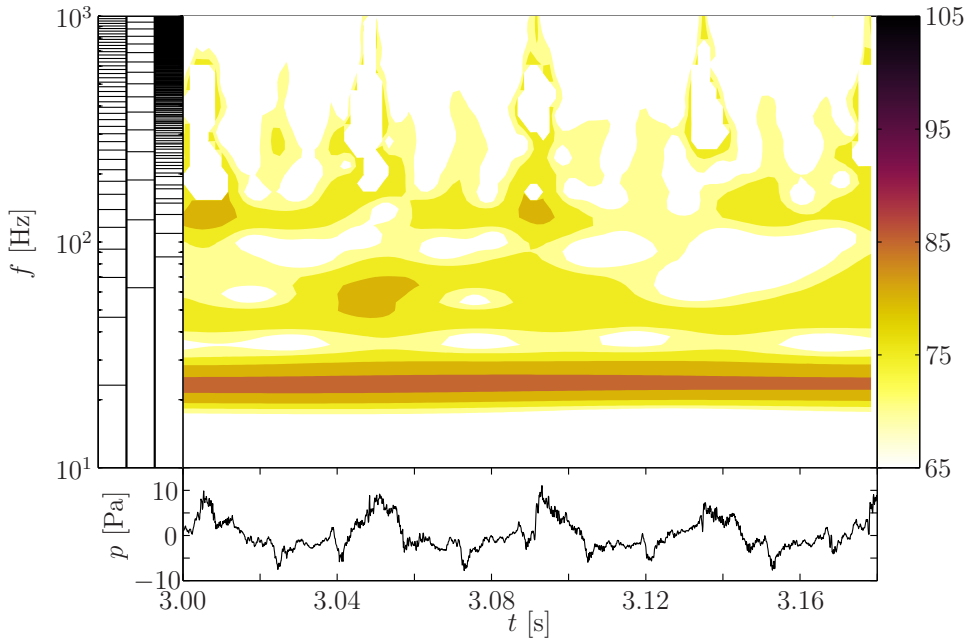

Figure 5.7: Residual wavelet power spectra and associated pressure signature, from the fast advancing side roll maneuver without blade-vortex interactions.

events. This prevents the lower harmonics from being removed from the wavelet power spectra by any wavelet based filtering technique, as the energy in the lower harmonics attributed to blade-vortex interactions are indistinguishable from the rest of the signal.

5.2.2 Synthetic Analysis

Now that the general technique has been developed in § 5.2.1, let us investigate a couple of signals to further understand the implicit assumptions made. First, a review of Sickenberger*et al.* 's (2011) spectral results will be investigated. Then, the blade-vortex interaction extraction method will be used to determine a 'typical' blade-vortex interaction. This interaction will be repeated at the blade passage frequency, to generate a signal containing only 'typical' blade-vortex interactions. This signal will be Fourier transformed, and that will be compared to the spectral representation provided by Sickenberger *et al.* (2011) [93]. That same signal will also be used to determine whether the blade-vortex interaction signal can be reconstructed adequately using only the high amplitude, higher harmonic

components.

Once that is complete, another 'typical' blade-vortex interaction will be generated. This process will be repeated, except now the main rotor harmonic signal will also be extracted. By extracting the main rotor harmonic signature separately, it allows us a way to vary the strength in the main rotor harmonic, while maintaining the same strength in the 'typical' blade-vortex interaction signal. This provides a way to determine what the affect of the main rotor harmonic strength is, on the reconstructed blade-vortex interaction signal. A method for extracting blade-vortex interactions through a high frequency filter of the Fourier transform will also be discussed. The Fourier method will be compared to the wavelet transform based method for the varying main rotor harmonic energy data. In the end, it will be shown that the wavelet based method provides a better extraction of the blade-vortex interaction signal than is possible for the Fourier transform based method.

Determining how the energy of a blade-vortex interaction is distributed in spectral space is a non-trivial task. Sickenberger *et al.* [93] performed a Fourier transform on a cropped blade-vortex interaction, a sample of which was shown in figure 1.11 and is provided again in figure 5.8a for convenience. Sickenberger's Fourier transform, shown in figure 5.8b, shows that the energy is distributed fairly evenly across all but the mid-frequency range. This is directly contrary to what is seen in the wavelet power spectra of figure 5.6a where the energy is focused primarily in the higher frequencies. The distribution of energy found by Sickenberger *et al.* is most likely tainted by the small interrogation window, and therefore large frequency bin size, necessary to investigate a blade-vortex interaction pulse in isolation.

To determine a more realistic energy distribution, a 'typical' blade-vortex interaction noise signature must be identified. Since the noise signature of a blade-vortex interaction is highly dependent on the aerodynamics surrounding each blade-vortex interaction, no 'typical' signature can truly be developed. Instead of attempting to develop a 'typical' signature, we will let the data provide

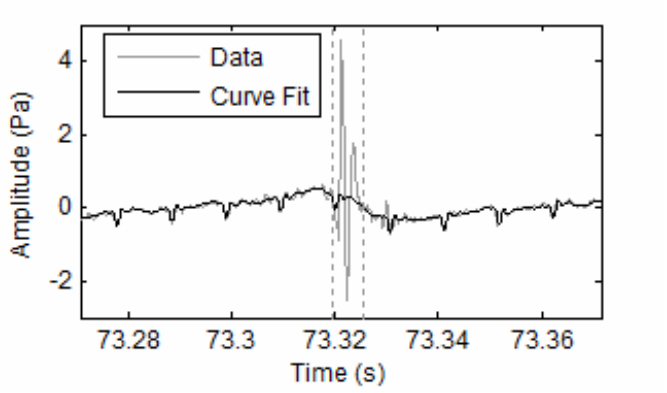

(a)

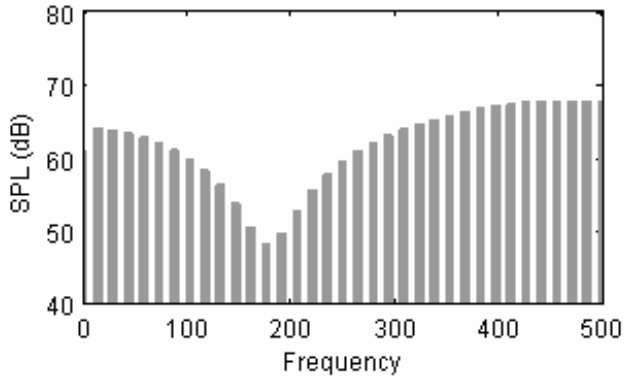

(b)

Figure 5.8: (a) Extracted blade-vortex interaction pressure signature and (b) associated Fourier transform produced in Sickenberger *et al.* (2011) [93].

one for the situation viewed in figure 5.6b. By time averaging the pressure signatures of the four full blade-vortex interactions shown in figure 5.6b, a 'typical' pressure signature can be determined. This pressure signature is passed through a Gaussian window to ensure zero acoustic pressure at the beginning and ending of the signature, and is shown in figure 5.9.

The 'typical' blade-vortex interaction signature can then be repeated at the blade passage frequency (f_{MR} = 23.2 Hz), to generate a pressure signature that contains only 'typical' blade-vortex interactions. Performing a wavelet transform on a string of such interactions, results in figure 5.10. This shows that the majority of the energy contained within a blade-vortex interaction is, indeed, located within the higher harmonics. A Fourier transform of the same data also provides the spectral representation of the signal. Figure 5.11 shows the Fourier transform of

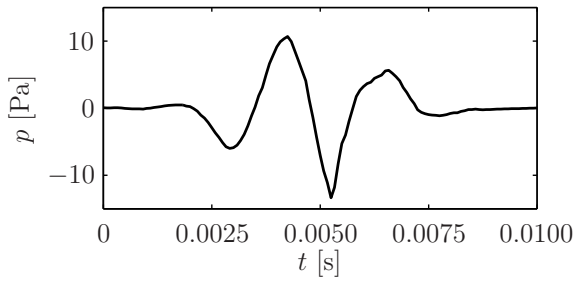

Figure 5.9: 'Typical' blade-vortex interaction pressure signature, calculated from the data provided in figure 5.6b.

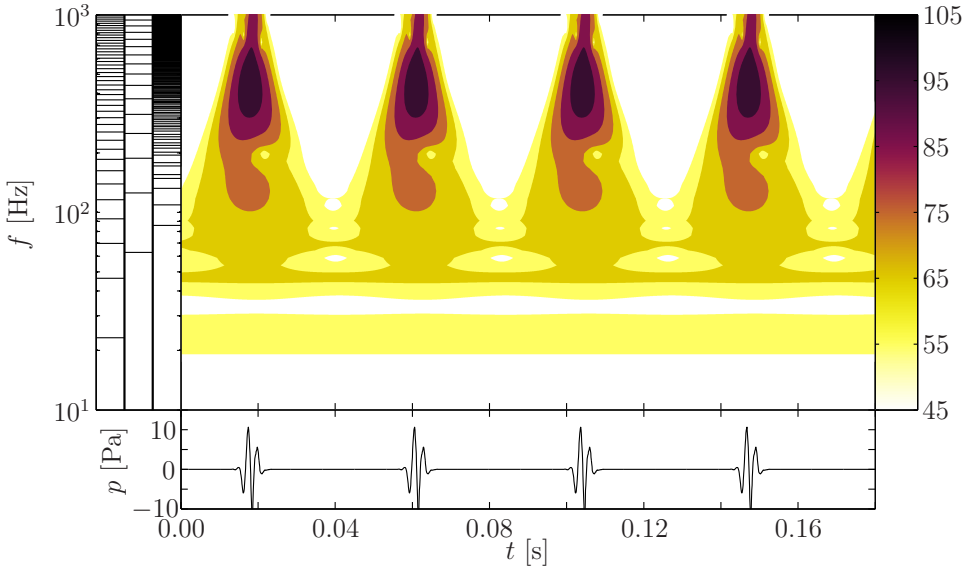

Figure 5.10: Wavelet power spectra of the 'typical' blade-vortex interaction pressure signature. Note the contour levels have changed so that the lower harmonic energy of the blade-vortex interactions can be seen.

the full 1 second blade-vortex interaction signal. The peaks in the spectra occur at each main rotor harmonic, and the energy is clearly focused in the high frequency region of the content. The full signal is used in the Fourier transform to ensure adequate frequency resolution and window size for correct energy determination.

Performing the blade vortex extraction technique on the generated signal results in figure 5.12. Since this is a synthetic signal without a strong main rotor harmonic to measure the amplitude cutoff from, an amplitude cutoff of 75 [dB] was used, while the frequency cutoff was kept at 7 main rotor harmonics (162.4 Hz). The subsequent pressure signal that was recreated from this new extracted power

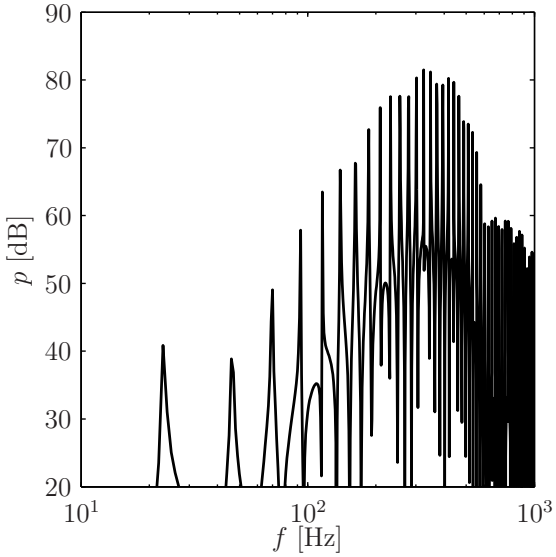

Figure 5.11: Fourier transform of the full 'typical' blade-vortex interaction pressure signature with main rotor harmonic of 23.2 Hz.

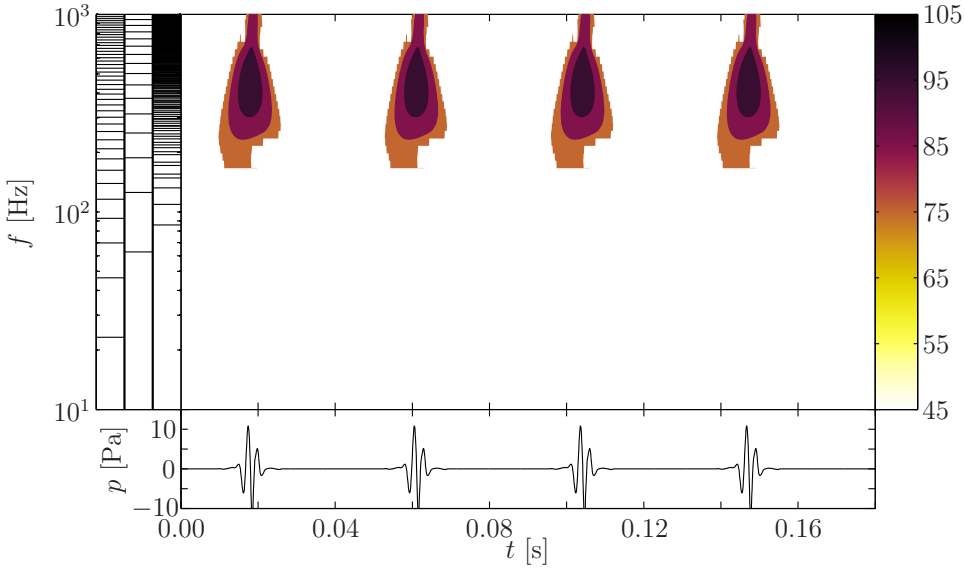

Figure 5.12: Extracted wavelet power spectra of the 'typical' blade-vortex interaction pressure signature.

spectra is shown beneath the wavelet power spectra in figure 5.12. Figure 5.13 compares one instance of the blade-vortex interaction extracted from the original 'typical' spectra, to the 'typical' blade-vortex interaction shown in figure 5.9. The small pressure difference between both pressure signatures demonstrates that the wavelet based extraction method of the higher harmonic blade-vortex interaction

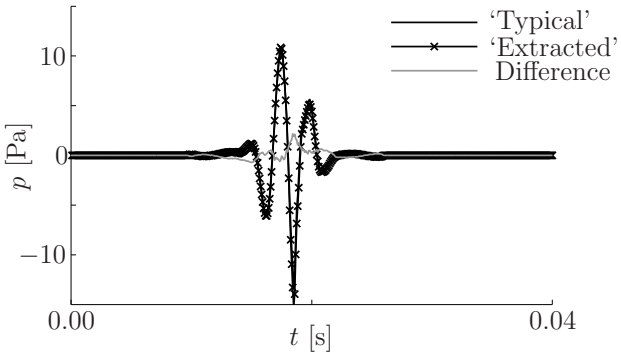

Figure 5.13: Comparison of 'typical' and extracted blade-vortex interaction pressure signature. The difference between both signatures is also provided.

signatures adequately captures the relevant physics of the situation.

A second 'typical' blade-vortex interaction can be generated from similar data. Figure 5.14 shows the signal from microphone 6 in figure 3.4a, extracted dur-

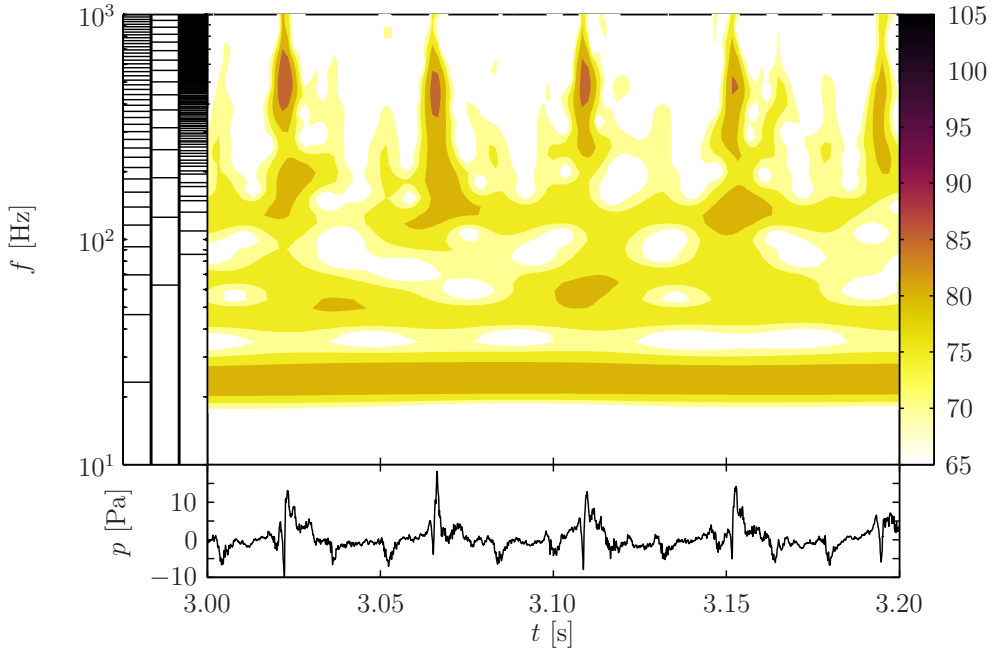

Figure 5.14: Wavelet power spectra and associated pressure signature, extracted from microphone 6 during the fast advancing side roll maneuver.

ing the fast advancing side roll maneuver at the same time as the previous signal. Following the same analysis as before, the blade-vortex interaction pressure signatures are identified, extracted, and then averaged together. The resulting 'typical'

blade-vortex interaction pressure signature and subsequent Fourier transform are provided in figure 5.15b.

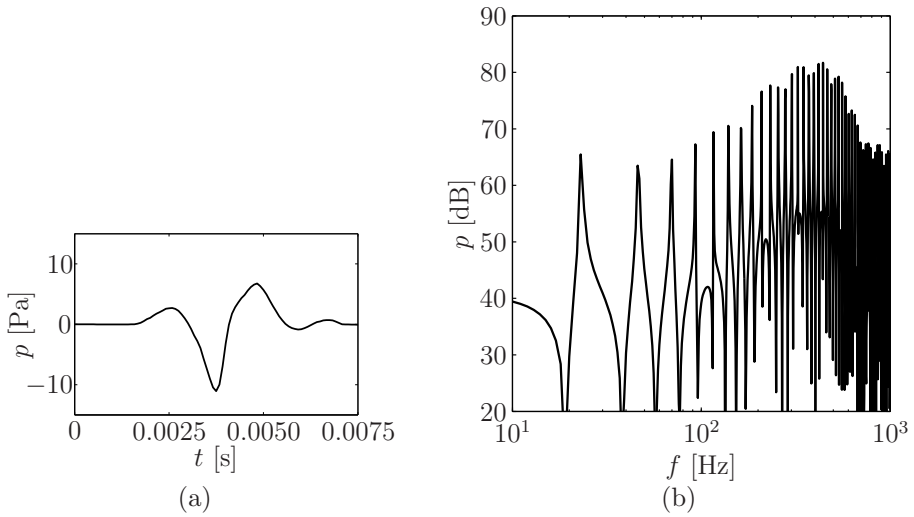

Figure 5.15: Second 'typical' blade-vortex interaction (a) pressure signal and (b) Fourier transform of the full 'typical' blade-vortex interaction pressure signature.

The pressure signature related to this 'typical' blade-vortex interaction (figure 5.15a) is from a slightly different directivity, and is shown to be dissimilar compared to the first 'typical' blade-vortex interaction signature (figure 5.9). This 'typical' blade-vortex interaction has only one primary pair of negative-positive pulses. Further, the spectrum provided in figure 5.15b, possesses more energy in the lower harmonics. However, the bulk of the energy is still in the higher frequencies.

Using wavelet transforms, the signature related to the main rotor harmonic can also be extracted. Extracting the main rotor harmonic by itself, allows the energy in the harmonic to be scaled independently of the strength of the blade-vortex interactions. Figure 5.16 shows a scaled main rotor harmonic signature superimposed with 'typical' blade-vortex interactions. In figure 5.16, the main rotor energy is scaled to be 3 dB greater than the peak blade-vortex interaction energy (Δ MRE = 3 dB). Varying the energy level of the main rotor harmonic, allows one to investigate how the main rotor harmonic strength affects the resulting extracted blade-vortex interaction signal.

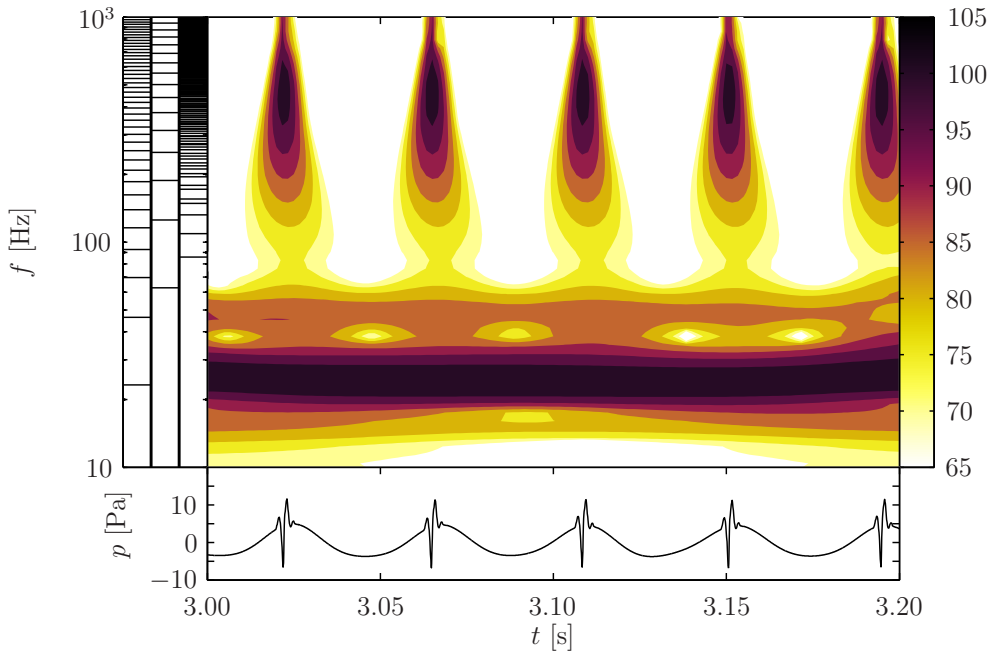

Figure 5.16: Extracted wavelet power spectra of the second 'typical' blade-vortex interaction pressure signature, superimposed on a scaled main rotor harmonic signature.

Signals representing various main rotor harmonic strengths are shown in figure 5.17. In each successive figure, the main rotor harmonic has been uniformly scaled to a higher energy value. The extraction technique with cutoffs of ($f_{cut} = 7f_{MR} = 162.4$ Hz, $A_{cut} = 6$ dB) is then applied to this artificial data.

The resulting extracted pressure signatures are shown in figure 5.18 where labels are consistent with figure 5.17. It can be seen that as the energy in the main rotor harmonic increases, relative to the blade-vortex interaction strength, then less and less of the blade-vortex interaction is extracted. Finally, when the energy in the main rotor harmonic is 5 dB or greater than the blade-vortex interaction energy, little to no signal is extracted. This is expected, as the amplitude cutoff for extracting blade-vortex interactions was set at 6 dB below the main rotor harmonic energy level.

The same signals are also filtered by way of the Fourier transform. A Fourier transform was applied to the signals shown in figure 5.17. Then, energy in frequencies below 7 blade rotor harmonics are set to zero. A sample of the

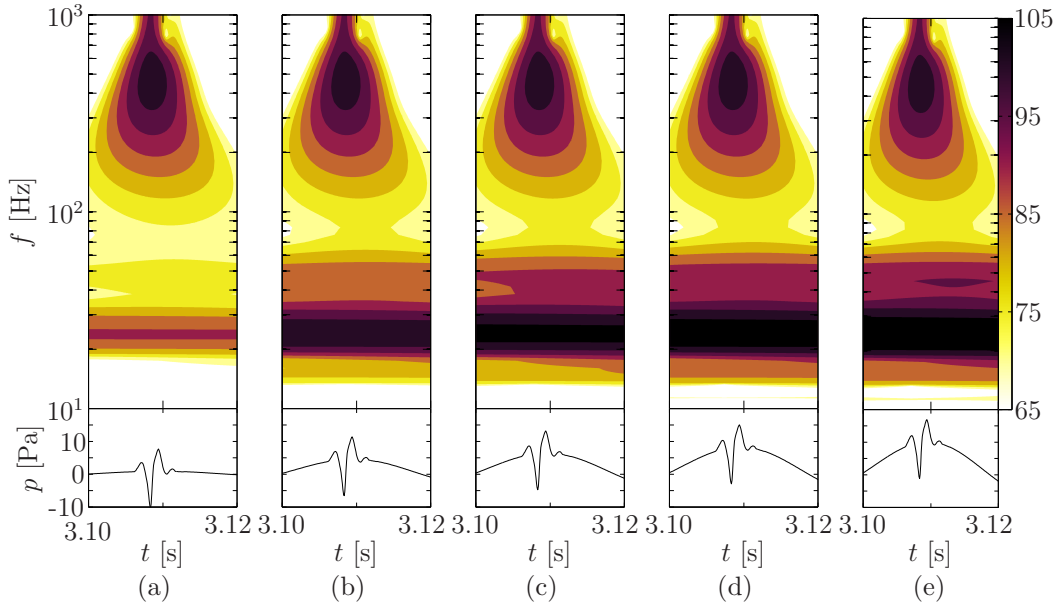

Figure 5.17: 'Typical' blade-vortex interactions superimposed onto a main rotor signature of varying strengths. Main rotor peak energy strengths relative to the peak blade-vortex interaction signature (Δ MRE) are (a) −13 (b) 0 (c) 3 (d) 5 (e) 7 dB.

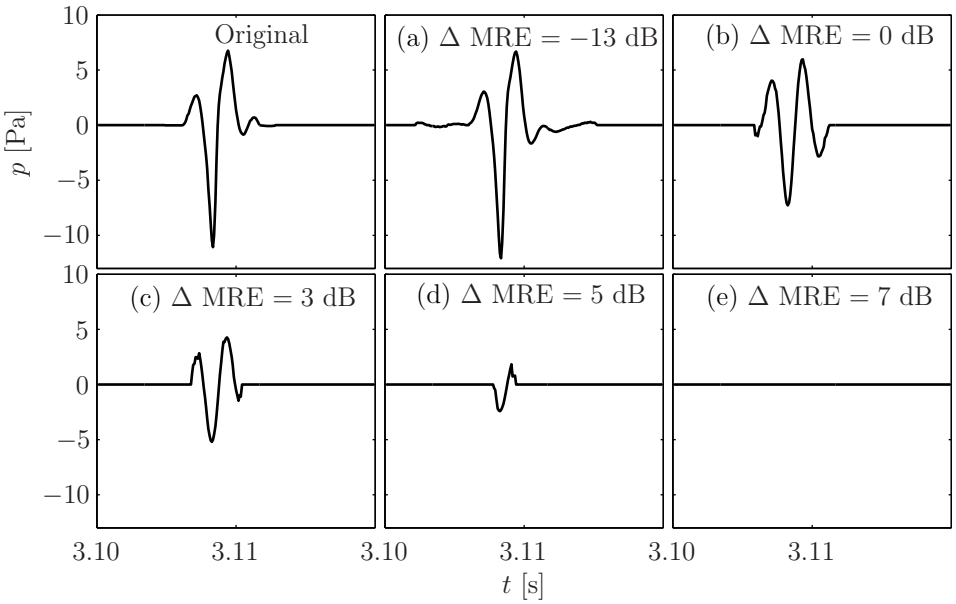

Figure 5.18: Blade-vortex interaction signature extracted from figure 5.17. Original, superimposed blade-vortex interaction signature, is also provided.

filtering technique is shown in figure 5.19. The main rotor harmonic is clearly the strongest frequency in the signal, peaking at close to 100 dB. However, the main

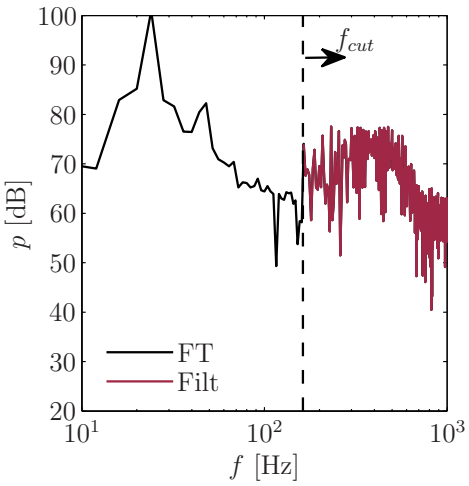

Figure 5.19: Fourier transform (FT) and filtered spectra (Filt) of the blade-vortex interaction signal with scaled main rotor energy. Δ MRE = 7 dB for the case shown.

rotor harmonic has seriously affected the energy in the higher frequencies as well. If we compare figure 5.19 with the original blade-vortex interaction spectra in figure 5.15b, it is obvious that the higher frequency components have more energy than before.

The presence of higher energy in the higher frequencies, is due to the way the Fourier transform distributes energy into it's full harmonic components. Previously, however, it was seen that changing the main rotor harmonic signal did not affect the amplitudes of the higher frequencies, when using the wavelet transform. The ability of the wavelet transform to properly localize a signal's frequency components is yet another reason why the wavelet transform should be employed, instead of the Fourier transform for instances were blade-vortex interactions are in the signal.

The filtered spectra, seen in figure 5.19, is then inverse transformed, and only the real component of the resulting pressure signal is retained. The resulting pressure signatures are shown in figure 5.20 where the lower harmonic energy is still clearly present in the filtered signals. This was expected, as the energy from the main rotor harmonic was distributed into the higher frequencies as well.

Analyzing the sound pressure level of the resulting extracted pressure sig-

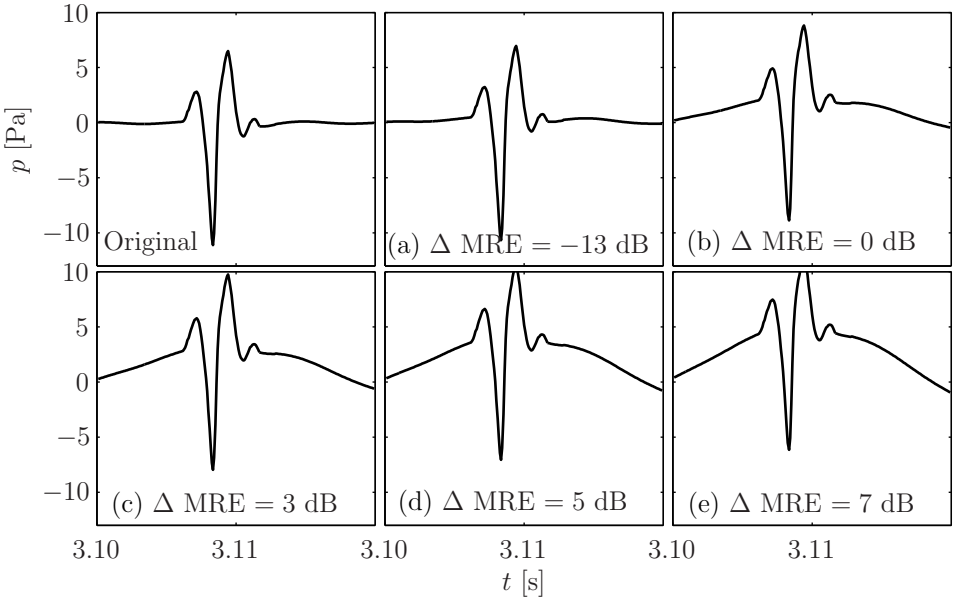

Figure 5.20: Blade-vortex interaction signature filtered through Fourier transform from figure 5.17. Original, superimposed blade-vortex interaction signature, is also provided.

natures, from both the wavelet transform and Fourier transform techniques, provides a means for quantifying the effect that the main rotor energy level has on the extracted signal. The sound pressure level, relative to the original 'typical' blade-vortex interaction signal, can be calculated as follows,

$$\Delta SPL = 20 \log_{10} \frac{P_{i_{RMS}}}{P_{o_{RMS}}}. \tag{5.7}$$

In equation (5.7) RMS stands for the root-mean-square, 'i' represents the i'th energy level of the main rotor harmonic, and 'o' is the value for the original, 'typical' blade-vortex interaction pressure signature.

The main rotor scaling process was performed for relative main rotor energies ranging from 35 dB below the peak blade-vortex interaction signature, to 7 dB above. It can be seen, in figure 5.21, that the Fourier transform extraction method requires the main rotor harmonic energy to be significantly below the peak blade-vortex interaction level, in order for proper reconstruction of the blade-vortex interaction signal. When the main rotor harmonic energy is half the strength of the peak blade-vortex interaction energy (Δ MRE = 3 dB), then the

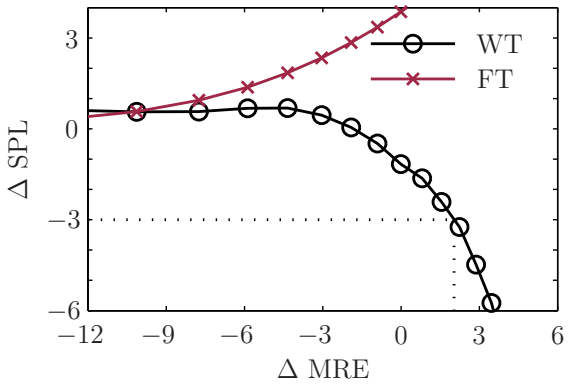

Figure 5.21: Sound pressure level comparison of extracted 'typical' blade-vortex interactions for varying main rotor harmonic energies. Comparison for both wavelet transform (WT) and Fourier transform (FT) are provided. Extraction of half the blade-vortex interaction energy is identified by dashed lines.

reconstructed signal is accurate within 2 dB. However, the metric used only investigates the fluctuating component of the signal, and does not properly take into account the slow, main rotor harmonic fluctuations that are still clearly visible in the extracted signal. Hence, a visual inspection of figure 5.20 shows a substantial portion of the lower main rotor noise remains in the extracted signal for Δ MRE = 3 dB.

Further, the accuracy of this technique is true only for the signal investigated, which was steady with identical blade-vortex interactions occurring at a fixed time interval. In a transient signal, like those exhibited by a transient maneuvering helicopter, the Fourier transform extraction method is expected to perform quite poorly in capturing and filtering individual blade-vortex interactions. This is due to the very small time windows over which blade-vortex interactions occur. It was shown previously, in § 2.3 that the Fourier transforms do not provide consistent spectra at such small window sizes, and so the filtering and reconstruction process will be severely affected by the necessary window size.

The wavelet transform extraction technique, however, shows that when blade-vortex interactions are as strong as (or more powerful than) the main rotor harmonic, the extracted signal is correct within 1 dB. When the main rotor harmonic energy is more powerful than the energy in the blade-vortex interactions,

especially 2 dB above the peak value, then the resulting wavelet transform extracted signal is no longer indicative of the 'true' blade-vortex interaction signal. Further, the extracted signal does not show any presence of the main rotor harmonic energy, as was seen in the Fourier transform case. Preliminary results from § 4 shows that when blade-vortex interactions occur their peak energies are, in general, more powerful than the main rotor harmonic energy. Thus, unless otherwise noted, it will be assumed with some confidence that blade-vortex interactions identified and extracted through this method represent the 'true' blade-vortex interaction signal.

5.3 Sensitivity Analysis

In an effort to determine how the filtering technique affects the full, transient system, two metrics will be investigated for the three signals shown in figures 5.6 and 5.7. The first metric, is the average overall sound pressure level, which is the wavelet power spectra averaged in time and integrated over all frequencies according to equation (2.7). The second metric is the blade-vortex interaction sound pressure level and is defined analogous to the overall sound pressure level, although for this helicopter the frequency range of integration is from 5^{th} to 60^{th} main rotor harmonics ($f_{MR} = 23.2$ Hz). Table 5.1 shows the comparison between

	Orig	BVI	Res	Orig-Res
OASPL	105.5	100.8	103.7	1.8
BVISPL	103.5	100.7	100.1	3.4

Table 5.1: Overall sound pressure level and blade-vortex interaction sound pressure level comparison for the original signal (Orig), extracted blade-vortex interaction signal (BVI), and residual signal (Res).

these two metrics for each of the three signals contained in figures 5.6 and 5.7. Since the energy removed for the blade-vortex interaction signal in figure 5.6b is 7 blade passage frequencies and above, there is little difference between its overall sound pressure level and the blade-vortex interaction sound pressure level.

It is interesting to see, in table 5.1, that removing the signature related to the blade-vortex interaction from the original signal reduced its OASPL and BVISPL by 1.8 and 3.4 dB, respectively. This is in stark contrast to the 16 dB reduction in BVISPL, seen by Sickenberger *et al.* (2011) [93]. It is important to recall, though, that a 3 dB reduction in noise level is still a removal of half the acoustic energy in the signal.

The BVISPL metric, however, provides a skewed version of what is happening with the blade-vortex interaction signal. The averaging process used in the standard BVISPL metric reduces the blade-vortex interaction signal measured, due to the large amounts of time between interactions where there is zero energy in the signal. Averaging across only the non-zero portions of the wavelet power spectra, shown in figure 5.6b, produces a sound pressure level of 107.3 dB. This is 6.5 dB stronger than what is reported in table 5.1, and is almost 4 dB higher than the anticipated BVISPL from the original signal.

Since the blade-vortex interactions are impulsive, it is more proper to investigate the sound pressure levels as functions of time. Figure 5.22 shows both the OASPL and BVISPL for the same time interval investigated in figures 5.6 and 5.7. It is seen that the sound pressure level associated with each blade-vortex interaction event has only one local maxima. That maxima comes in close proximity to the BVISPL for the original signal suggesting that the BVISPL metric does capture the energy content of the blade-vortex interaction. However, the non-zero BVISPL seen when the interactions are not occurring shows that the original metric alone is insufficient for capturing the full effects of this transient phenomenon. Further, the maximum BVISPL seen in figure 5.22b agrees much better with the previously calculated non-zero 'average' BVISPL of 107 dB. This agrees with the work of Davis *et al.* (1997) [34] who showed that the severity of blade-vortex interactions were well predicted by the peak amplitudes in the blade-vortex interaction subband.

To this point, the tuning parameters associated with the filter were chosen somewhat arbitrarily to be any content above 7 blade passage frequencies (162.4

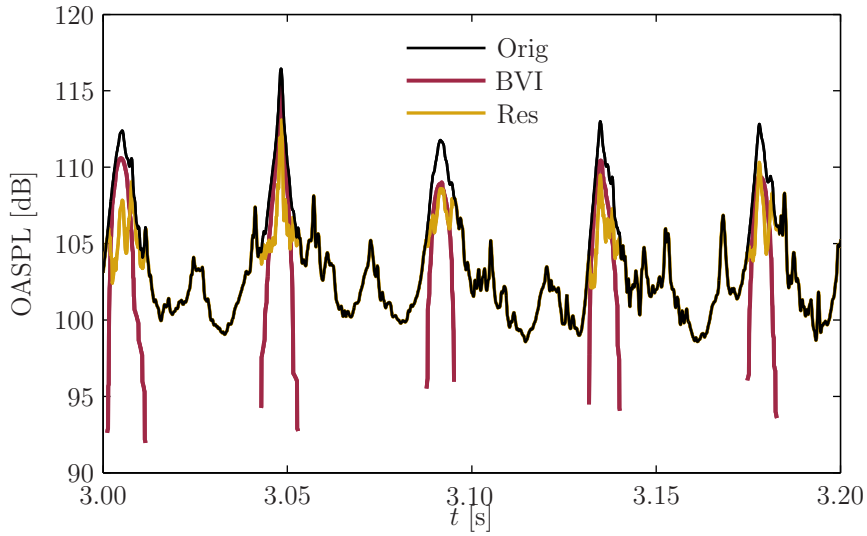

(a)

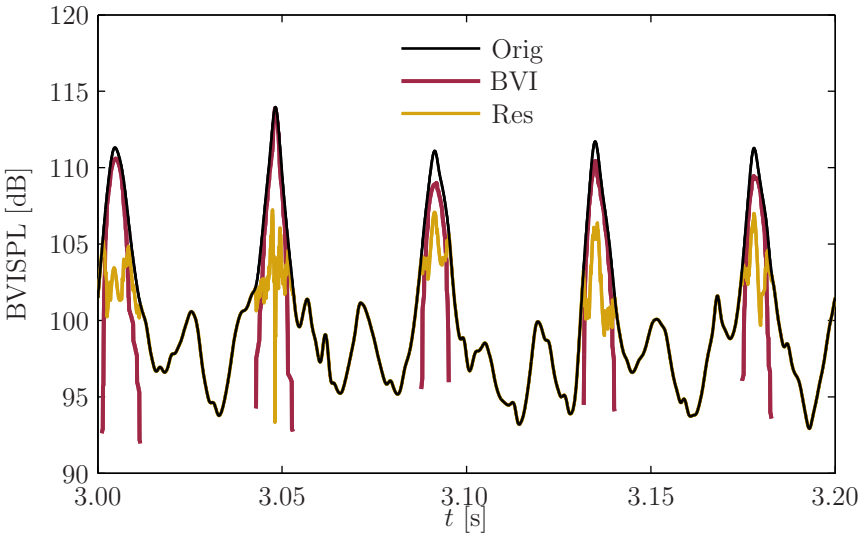

(b)

Figure 5.22: (a) OASPL and (b) BVISPL metrics from the original signal (Orig), extracted blade-vortex interaction signal (BVI), and residual signal (Res).

Hz) whose energy exceeds a magnitude of 6 dB less than the current power in the main rotor harmonic. This was shown to work well for the single instance in time investigated. However, a sensitivity analysis must be performed in order to determine what frequency and amplitude represents the best selection for the entire acoustic signal. A frequency range from one to 25 main rotor blade passage

frequencies is investigated at amplitudes ranging from 0 to −9 dB relative to the energy of the main rotor harmonic.

Figure 5.23 shows the same time instance as discussed before (figure 5.6a),

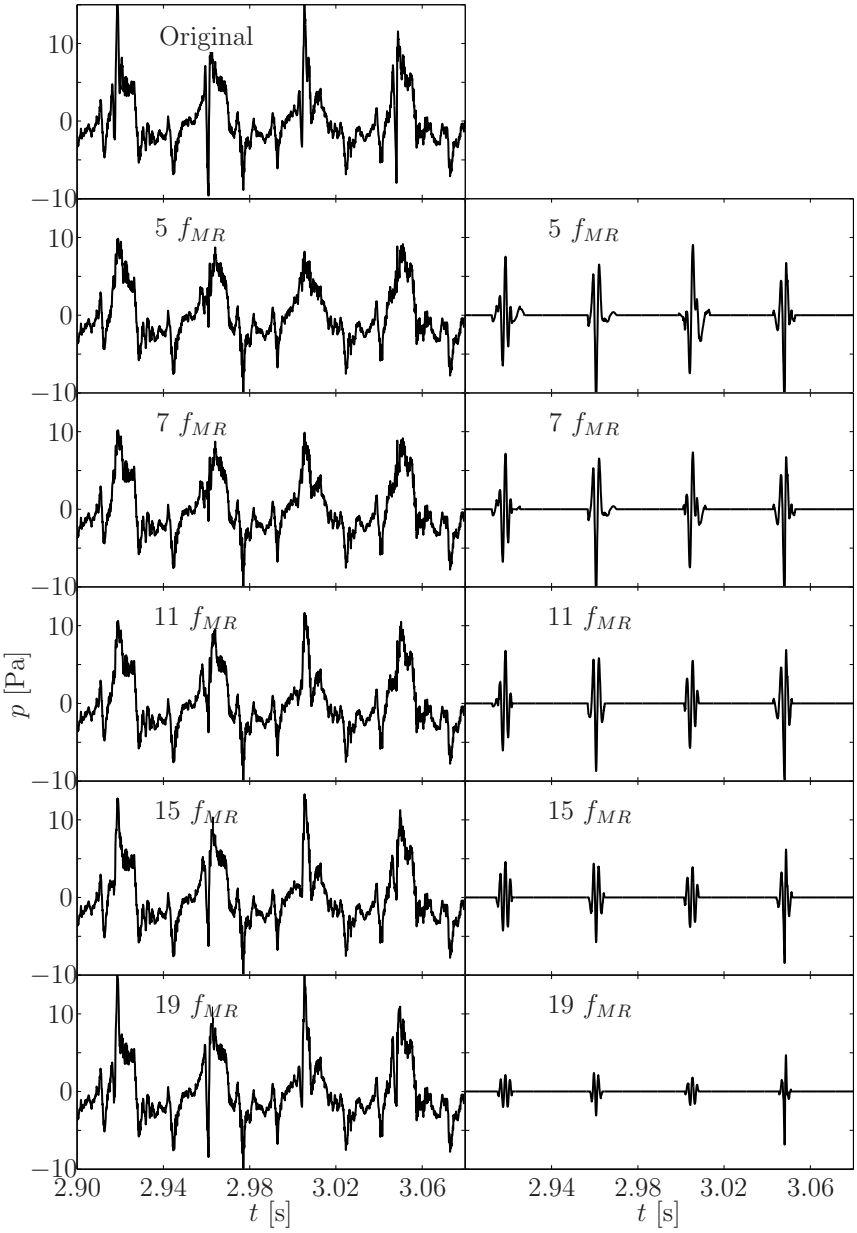

Figure 5.23: Frequency cutoff variation for a −6 dB amplitude cutoff of the fast advancing side roll maneuver beginning at $t = 2.9$ s. From top to bottom, the figures represent frequency cutoffs at 5, 7, 11, 15 and 19 main rotor harmonics (f_{MR}), with the original signal shown in the very top. Left side is the residual signal, while the right side is the extracted signal.

for the fast advancing side roll maneuver. Several different cutoff frequencies are investigated with a -6 dB amplitude limit, to investigate how the frequency cutoff affects the blade-vortex interaction extracted signal. The extracted blade-vortex interaction signals are shown next to the residual pressure signatures for each frequency cutoff. Showing them side-by-side allows for a better visualization as the extraction parameters are varied.

Viewing the 19 blade passage frequency cutoff in figure 5.23, the reconstructed signal (left) shows large amplitude spikes associated with blade-vortex interactions, suggesting the cutoff frequency should be lower than this. Indeed, these amplitude spikes decrease all the way to the lowest frequency cutoff shown, of 5 blade passage frequencies. Such a low cutoff frequency can lead to the extraction method removing the higher harmonics of the tail rotor signature, and not just the blade-vortex interaction signal. However, for this instance in time, the extraction method does not remove the tail rotor signature as indicated by the zero-valued extracted pressure signature between blade passages. If higher harmonics of the tail rotor were extracted, then some non-zero pressure signature would be recorded between each of the blade passages, at the frequency of the tail rotor.

If, instead, we look at an earlier instance in time for the same microphone (microphone 7) and flight condition, a different story unfolds. Figure 5.24 shows that lowering the frequency cutoff still removes more and more of the signal related to blade-vortex interactions. However, when the cutoff frequency falls below 11 blade passage frequencies, the tail rotor signature begins to appear in the extracted (right) signal.

Indeed, varying the amplitude range of interest for a chosen frequency cutoff can result in similar trend. Figure 5.25 demonstrates that a cutoff with low enough amplitude can begin to extract tail rotor information. When a higher energy amplitude cutoff is used, the lower energy from the tail rotor is not extracted from the signal by the filtering technique. And so, the -9 dB amplitude cutoff (energy above $1/8^{th}$ the magnitude of the main rotor harmonic) removes a

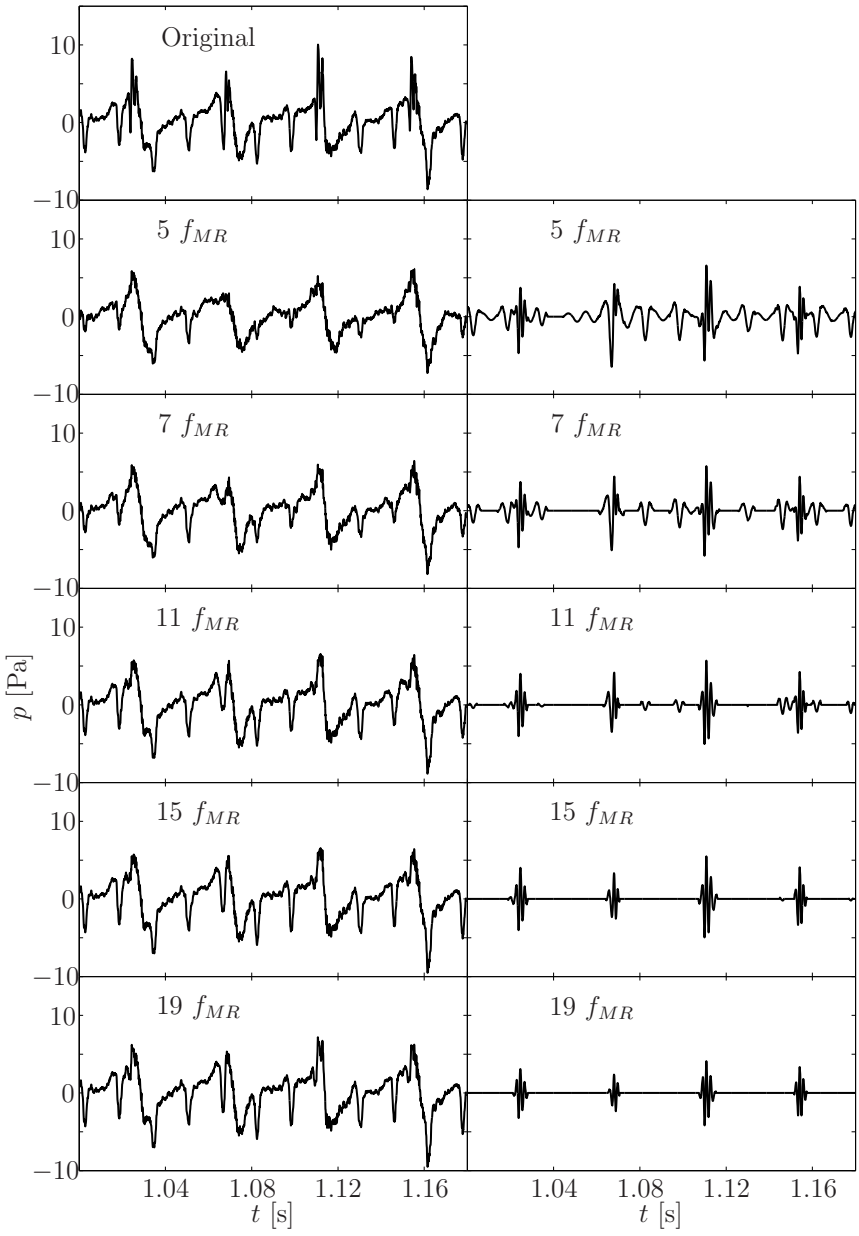

Figure 5.24: Frequency cutoff variation for a −6 dB amplitude cutoff of the fast advancing side roll maneuver beginning at $t = 1$ s. From top to bottom, the figures represent frequency cutoffs at 5, 7, 11, 15 and 19 main rotor harmonics (f_{MR}), with the original signal shown at the very top. Left side is the residual signal, while the right side is the extracted signal.

substantial amount of the tail rotor signature, along with some other higher harmonic content; meanwhile the -3 dB amplitude cutoff (energy above one half the magnitude of the main rotor harmonic) does not substantially affect the tail rotor

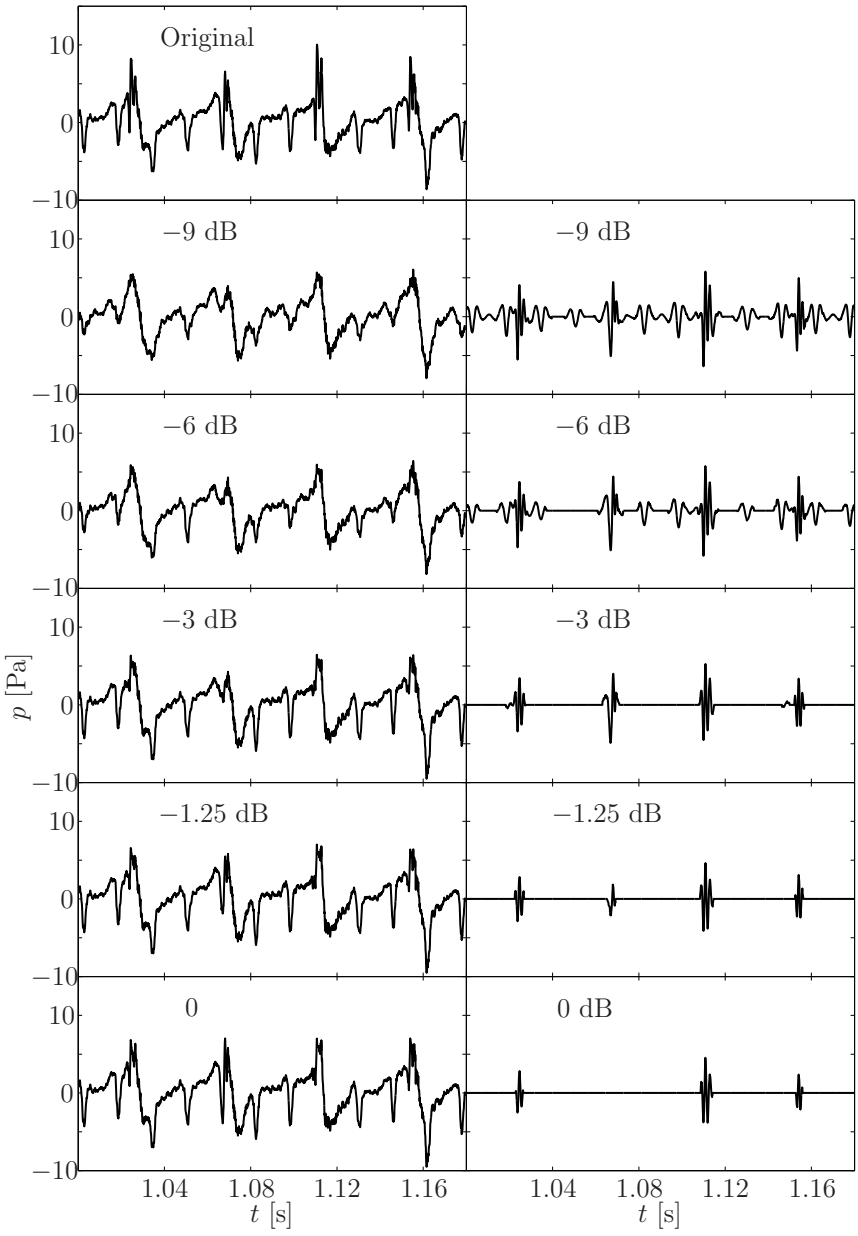

Figure 5.25: Amplitude cutoff variation for a single frequency cutoff of 7 main rotor harmonics. Samples extracted from the fast advancing side roll maneuver beginning at $t = 1$ s. From top to bottom, the figures represent -9, -6, -3, -1.25 and 0 dB amplitude cutoffs, with the original signal shown at the very top. Left side is the residual signal, while the right side is the extracted signal.

signature. Therefore, some method must be devised in order to determine the best cutoff frequency and amplitude for the extraction of blade-vortex interaction signals with minimal tail rotor and other higher harmonic content contamination.

5.3.1 Blade-Vortex Interaction Sound Pressure Level

The blade-vortex interaction sound pressure level, calculated as the sound pressure level of the extracted blade-vortex interaction signal, provides a plausible metric for testing the sensitivity of the filtering method to both tuning parameters. Investigating how the blade-vortex interaction sound pressure level changes with respect to changing amplitude or frequency cutoff can show where the cutoffs should be made. The ideal location for a frequency or amplitude cutoff would be the location where lowering either the amplitude or frequency cutoff results in a substantially larger blade-vortex interaction sound pressure level, but raising either parameter would change the blade-vortex interaction sound pressure level very little. This is ideal because it means the filtering method is capturing as much of the blade-vortex interaction signal, without removing a substantial portion of the tail rotor and lower main rotor harmonic signals. Removing more of the tail or lower main rotor harmonics would result in a higher sound pressure level for the extracted vortex interaction signal as that newly extracted energy would be included in the sound pressure level integral.

Recall figure 5.24 where it was shown that lowering the frequency but holding amplitude constant resulted in the removal of more tail rotor signal, while figure 5.25 showed that lowering amplitude cutoff but keeping frequency cutoff constant, also removed more tail rotor signal. Both of these figures also show that raising either quantity resulted in the removal of less blade-vortex interaction noise, and so the anticipated optimal solution will be at the point where lowering either frequency or amplitude cutoff results in an increase in the blade-vortex interaction sound pressure level. Figure 5.26 shows precisely this trend for the averaged BVISPL extracted from the fast advancing side roll maneuver starting at 1 second into the maneuver. Sound pressure levels calculated in the sensitivity analysis are averaged over one revolution. The ΔBVISPL shown is the increase in blade-vortex interaction sound pressure level measured, relative to the smallest value calculated at that time. Therefore, figure 5.26 shows the expected increase in blade-vortex interaction sound pressure level for decreasing frequency

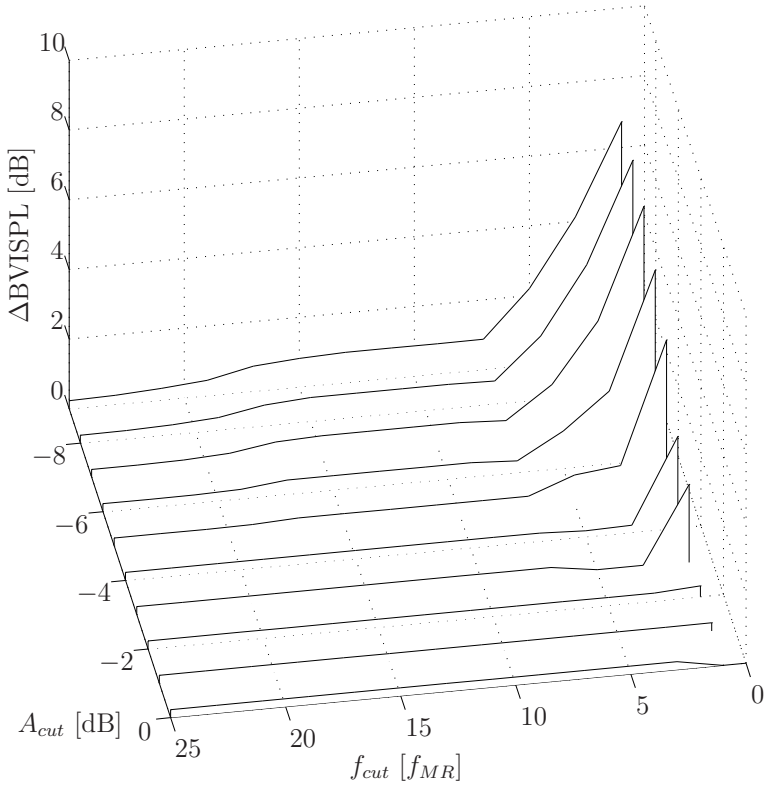

Figure 5.26: Amplitude (A_{cut}) and frequency (f_{cut}) cutoff sensitivity analysis taken from one second into the fast advancing side roll maneuver. ΔBVISPL is the change in the averaged overall sound pressure level of the blade-vortex interaction signal, such that ΔBVISPL = 0 represents the minimum calculated value.

and amplitude. The blade-vortex interaction sound pressure level appears relatively insensitive to changes outside of the low amplitude, low frequency region, for this instance in time.

The level region before the low frequency, low amplitude cutoff demonstrates the relative insensitivity of the blade-vortex interaction sound pressure level. Investigating the same signal, but beginning at 2.9 seconds into the maneuver, sheds some light onto whether or not this metric is insensitive to changes in tuning parameter. Figure 5.27a shows that the blade-vortex interaction sound pressure level can be sensitive outside of the low amplitude, low frequency region. Recalling figure 4.1, it was seen that a frequency at 25 blade passages bisects the higher harmonics related to advancing side blade-vortex interaction noise. Therefore, lowering the frequency cutoff from there would remove more and more of the

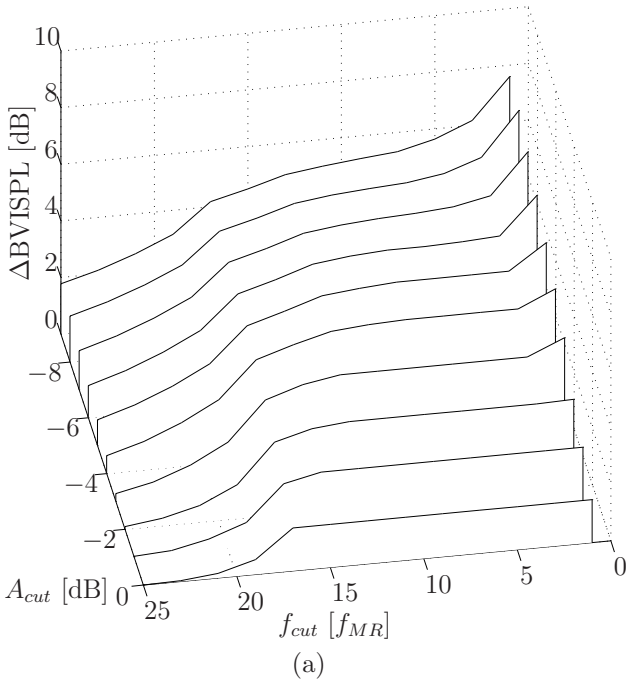

(a)

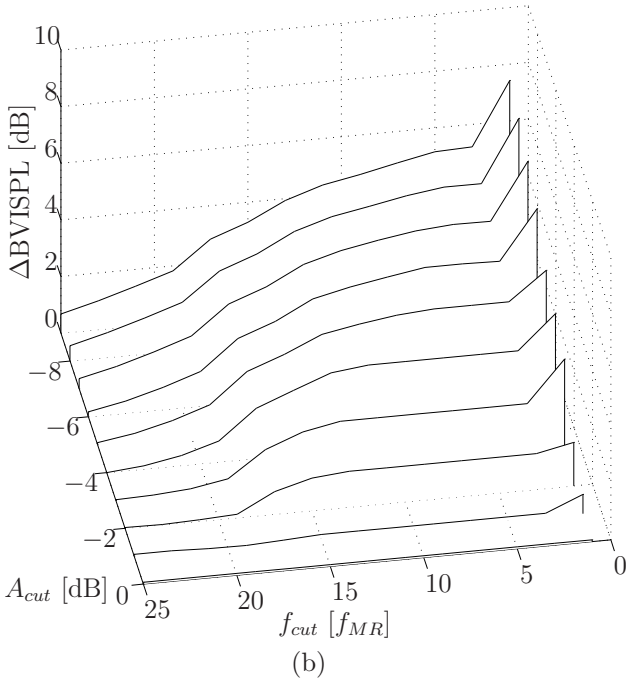

(b)

Figure 5.27: Amplitude (A_{cut}) and frequency (f_{cut}) cutoff sensitivity analysis taken from (a) 2.9 and (b) 4.1 seconds into the fast advancing side roll maneuver. ΔBVISPL is the change in the averaged overall sound pressure level of the blade-vortex interaction signal, such that ΔBVISPL = 0 represents the minimum calculated value.

signal related to blade-vortex interactions, increasing the ΔBVISPL metric seen in figure 5.27a. Eventually, around 15 blade passage frequencies, the blade-vortex interaction signal is almost entirely removed, and so the ΔBVISPL metric levels off into a plateau region. Continuing to lower the cutoff frequency eventually results in the removal of the tail rotor and lower main rotor harmonic signatures, and a subsequent increase in the ΔBVISPL metric is seen on the far right of figure 5.27a. This same pattern is seen in figure 5.27b, for the fast advancing side roll maneuver starting at 4.1 seconds into the maneuver.

While the pattern seen in figure 5.27 is intelligible, it does not provide the cleanest representation of where the tuning parameters should be chosen. The average sound pressure level of the blade-vortex interaction extracted signal is too sensitive to changes in the tuning parameters. The ideal metric would possess a flat plateau region bounded by steep sound pressure level slopes. Figure 5.28 provides the sound pressure level for the blade-vortex interaction extracted signal for both the steady level flight and medium roll right maneuvers. Figure 5.28 shows that the metric is useful for this microphone throughout the steady level flight maneuver, but is too sensitive for the transient roll maneuvers. Therefore, another metric must be sought that will provide more consistent and easier to interpret results.

5.3.2 Residual Sound Pressure Level

The residual sound pressure level provides a plausible metric for testing the sensitivity of the filtering method to both tuning parameters. The residual sound pressure level (RSPL) is defined here as the overall sound pressure level of the residual pressure signature after blade-vortex interactions have been removed. Investigating how the residual sound pressure level changes with respect to changing amplitude or frequency cutoff can show where the cutoffs should be made. The residual sound pressure level should provide a better metric as the sound pressure level is not significantly affected by the removal of blade-vortex interactions, as shown in table 5.1. It is expected that the RSPL will remain relatively steady

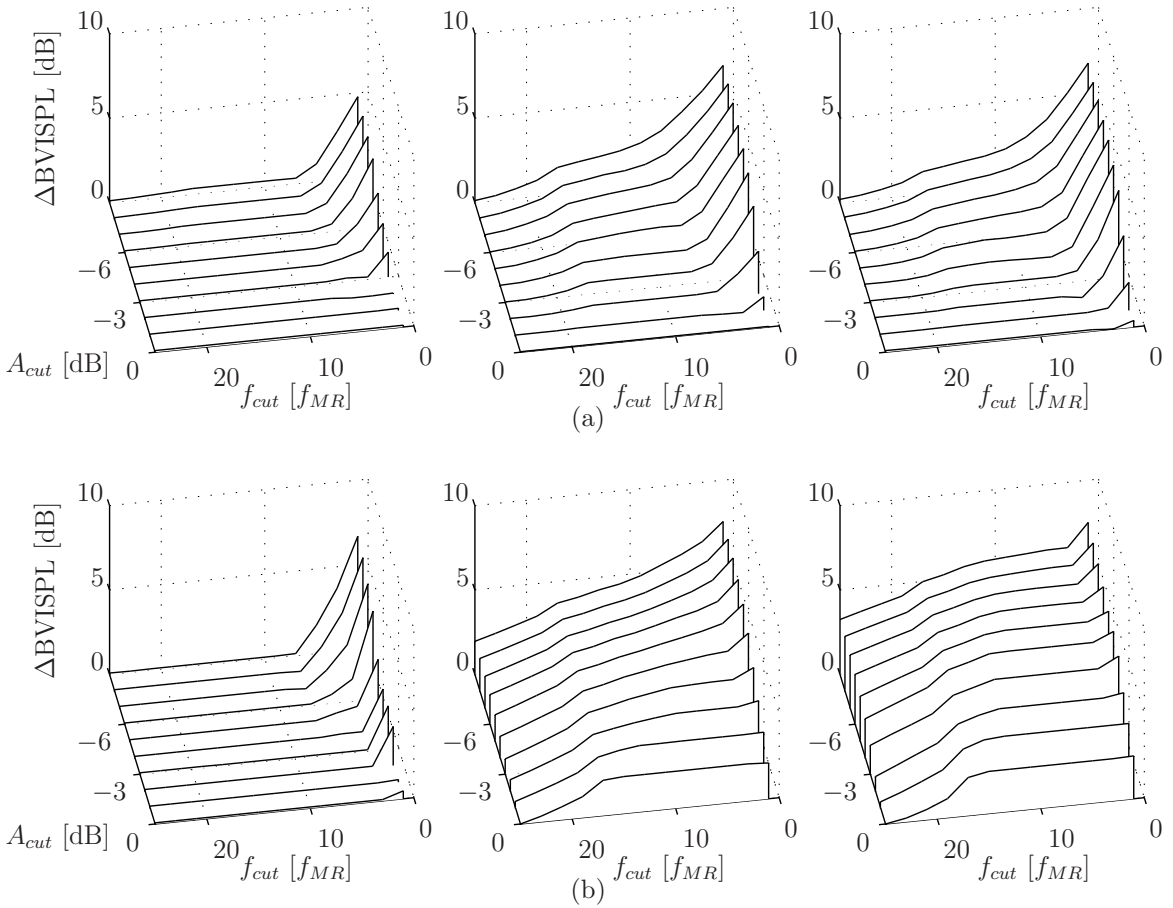

Figure 5.28: (a) Steady level flight and (b) medium advancing side roll maneuver averaged sound pressure levels of the extracted blade-vortex interaction signal. From left to right, in each figure, shows the sensitivity to changes in the tuning parameters for each maneuver beginning at (left) 1.0, (center) 2.9, and (right) 4.1 seconds, respectively.

until significant tail rotor and main rotor harmonics, unrelated to blade-vortex interactions, are removed.

It is anticipated that the optimal solution will be at the point where lowering either frequency or amplitude cutoff results in a decrease in the residual sound pressure level. Figure 5.29 shows precisely this trend for the average RSPL

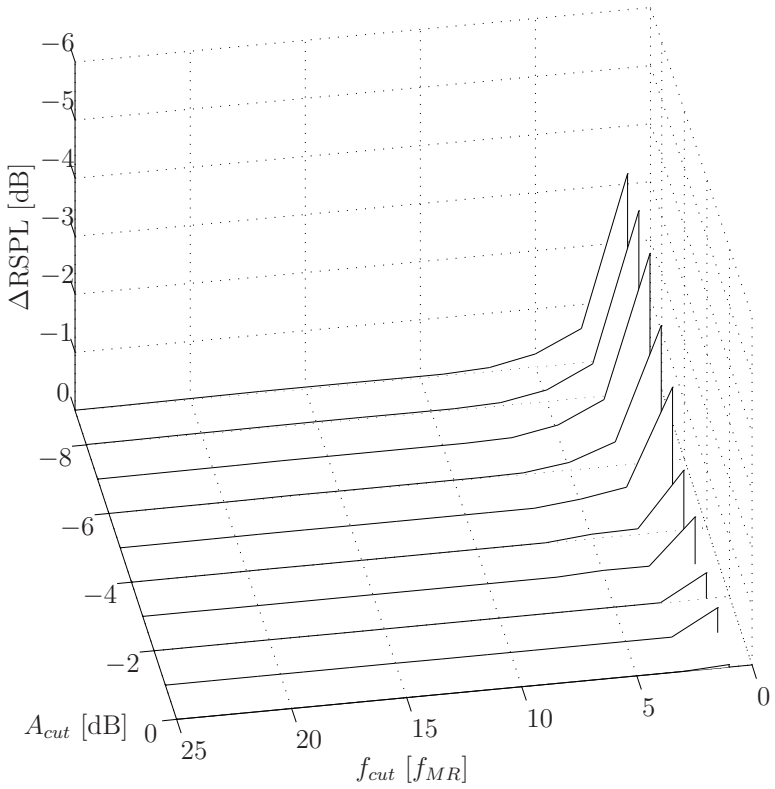

Figure 5.29: Amplitude (A_{cut}) and frequency (f_{cut}) cutoff sensitivity analysis taken from one second into the fast advancing side roll maneuver. ΔRSPL is the change in the averaged overall sound pressure level of the residual signal, such that ΔRSPL = 0 represents the maximum calculated value.

extracted from the fast advancing side roll maneuver starting at 1 second into the maneuver. Sound pressure levels calculated in the sensitivity analysis are averaged over one revolution. The ΔRSPL shown is the decrease in overall sound pressure level measured, relative to the largest value calculated at that time. Therefore, figure 5.29 shows the expected decrease in sound pressure level for decreasing frequency and amplitude. The residual sound pressure level appears relatively insensitive to changes outside of the low amplitude, low frequency region.

The level region before the low frequency, low amplitude cutoff demonstrates the relative insensitivity of the residual sound pressure level. Investigating the same signal, but beginning at 2.9 seconds into the maneuver, sheds some light onto whether or not the residual sound pressure level is insensitive or not. Figure 5.30 confirms that the residual sound pressure level is insensitive outside of the low amplitude, low frequency region, as desired.

Figure 5.31 includes residual pressure signatures extracted from the steady level flight and medium advancing side roll maneuver. This figure proves that the residual sound pressure level is in fact ideally insensitive to changes in the tuning parameter, regardless of maneuver, outside of the low frequency, low amplitude region. The optimal tuning parameter according to either the BVISPL or the RSPL metric exists along the line formed by the frequency and amplitude at the base of the respective sound pressure level spike. For figure 5.30 this would indicate a value of 3 to 4 blade pass frequencies for any amplitude cutoff. However, if the RSPL metric is used to guide the ideal frequency parameter, then the BVISPL metric can be used to determine the ideal amplitude. Looking at the third to fourth blade pass frequency in 5.27, an amplitude value of -6 dB becomes appropriate. Amplitudes higher than -6 dB produce lower ΔBVISPL values suggesting that the blade vortex signature is insufficiently captured. Meanwhile, amplitude values lower than -6 dB lose the anticipated level area in the mid-frequency range, suggesting that the tail rotor and lower harmonics of the main rotor are being removed due to the lower amplitude threshold.

So far, the sensitivity analysis has only been conducted on one microphone at various times during each maneuver. If a threshold is sought that is uniform across all maneuvers and microphones, then the ideal tuning parameters become -6 dB for amplitude, and 7 blade passage frequency for the lower frequency cutoff. The increase in frequency over what was suggested for the single microphone comes from the desire to limit the influence of higher tail rotor harmonics. The results shown in § 6 will use these tuning parameters for the extraction of blade-vortex interaction signals, regardless of microphone investigated. Appendix B contains a

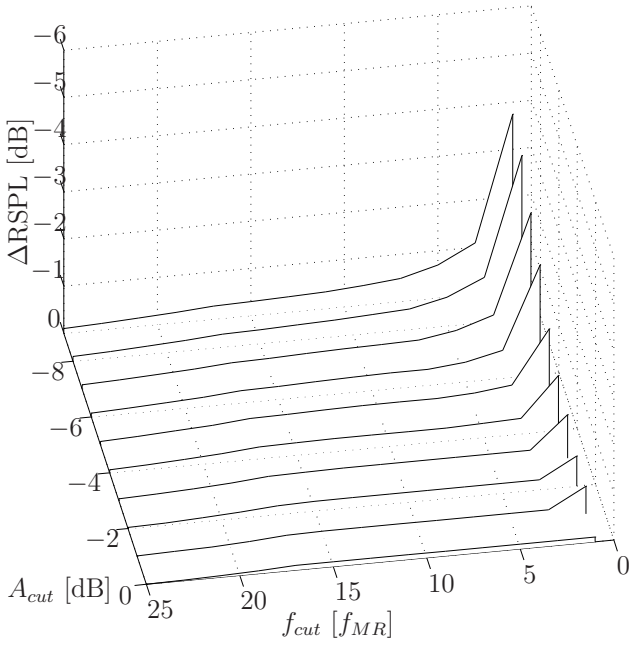

(a)

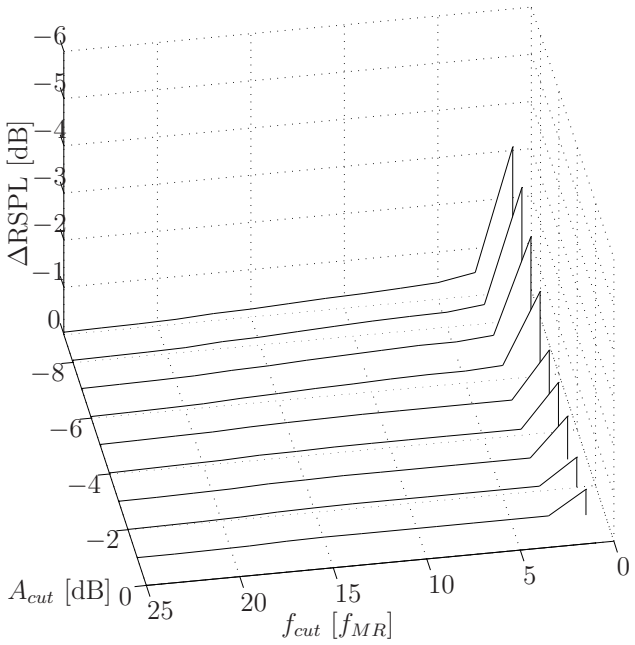

(b)

Figure 5.30: Amplitude (A_{cut}) and frequency (f_{cut}) cutoff sensitivity analysis taken from (a) 2.9 and (b) 4.1 seconds into the fast advancing side roll maneuver. ΔRSPL is the change in the averaged overall sound pressure level of the residual signal, such that ΔRSPL = 0 represents the maximum calculated value.

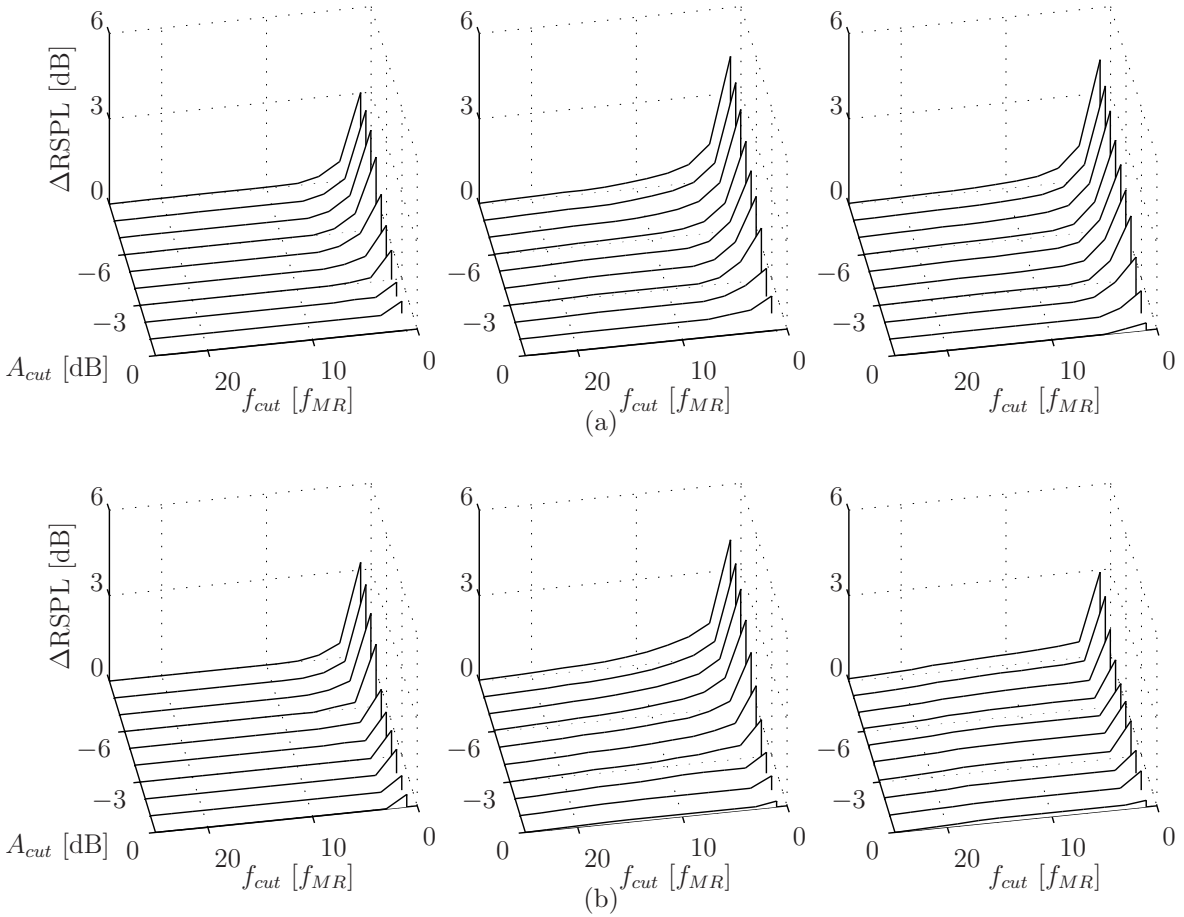

Figure 5.31: (a) Steady level flight and (b) medium advancing side roll maneuver averaged sound pressure levels of the residual signal. From left to right, in each figure, shows the sensitivity to changes in the tuning parameters for each maneuver beginning at (left) 1.0, (center) 2.9, and (right) 4.1 seconds, respectively.

limited set of the sensitivity analysis for various microphones and times throughout each of the maneuvers investigated.

5.3.3 Known Limitations

One particular drawback to this filtering method is the implicit requirement that the main rotor harmonic signature be the predominant noise in the spectra. This is not always the case, as was shown in figure 4.3, where the main rotor signature dropped substantially 5.5 seconds into the maneuver. Blade-vortex interactions were not noticeably present in the higher harmonics at that time, but the lower amplitude threshold due to the low main rotor harmonic signature results in the removal of high frequency noise unrelated to blade-vortex interaction events. The recreated signal for microphone 7 (used in figure 4.3) at several instances during the maneuver is shown in figure 5.32. This shows that when the main rotor harmonic signature is low, more of the high frequency noise, unrelated to blade-vortex interactions, is extracted and can falsely imply that blade-vortex interactions are occurring. Figure 5.33 shows that the sensitivity analysis can give clues that this is taking place. In figure 5.33b, there is no level region present in the mid-frequency range, which was previously seen in figure 5.28. That level region indicates the presence of blade-vortex interactions. In this figure, the ΔBVISPL rises almost linearly with decreasing cutoff frequency, suggesting that blade-vortex interactions are not present.

The limitation on the strength of the main rotor harmonic energy is not terribly restrictive, as the main rotor harmonic energy remains quite strong throughout approach, and is later strong during close departure of the vehicle. These times are ideal for investigating blade-vortex interactions that occur on the advancing and retreating side, respectively. As discussed in § 1.1.2, blade-vortex interactions propagate primarily at an elevation of $-30°$, and so blade-vortex interactions are not expected to be strong in the areas where the power of this filtering technique is diminished.

Therefore, while this filtering technique may have some drawbacks, it is

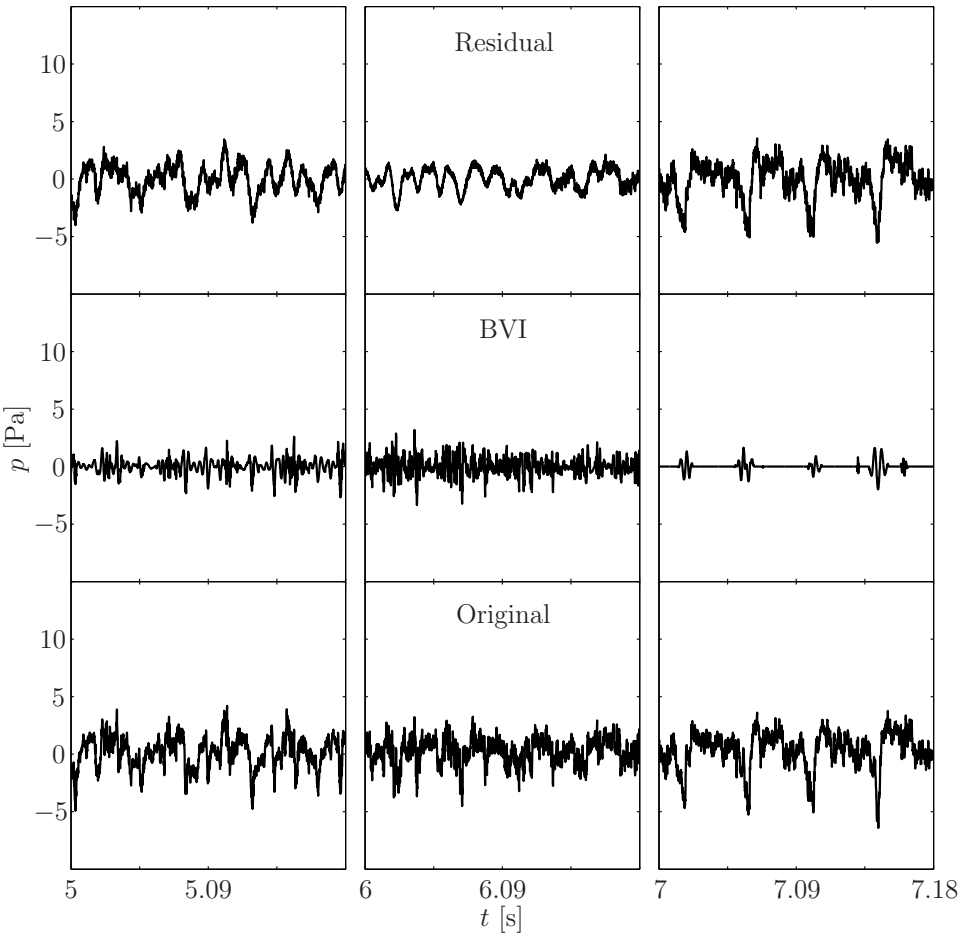

Figure 5.32: Sample pressure signatures from microphone 7 during the steady level flight maneuver. Top to bottom shows the (top) residual signal, (middle) blade-vortex interaction extracted signal, and (bottom) original signal.

quite powerful in the regions where blade-vortex interactions are expected to be intense and of interest. Further, the filter and reconstruction ideology is completely independent of the transform method employed. Therefore, one could adapt this process for use with short-time Fourier transforms, Choi-Williams distributions, Wigner-Ville distributions, or any other time-frequency analysis method. Depending on the design and sophistication of the filtering algorithm, a similar technique can be developed to extract any strong, impulsive signal based on its unique spectral representation. Thus, the implications for this technique range beyond its currently employed purpose.

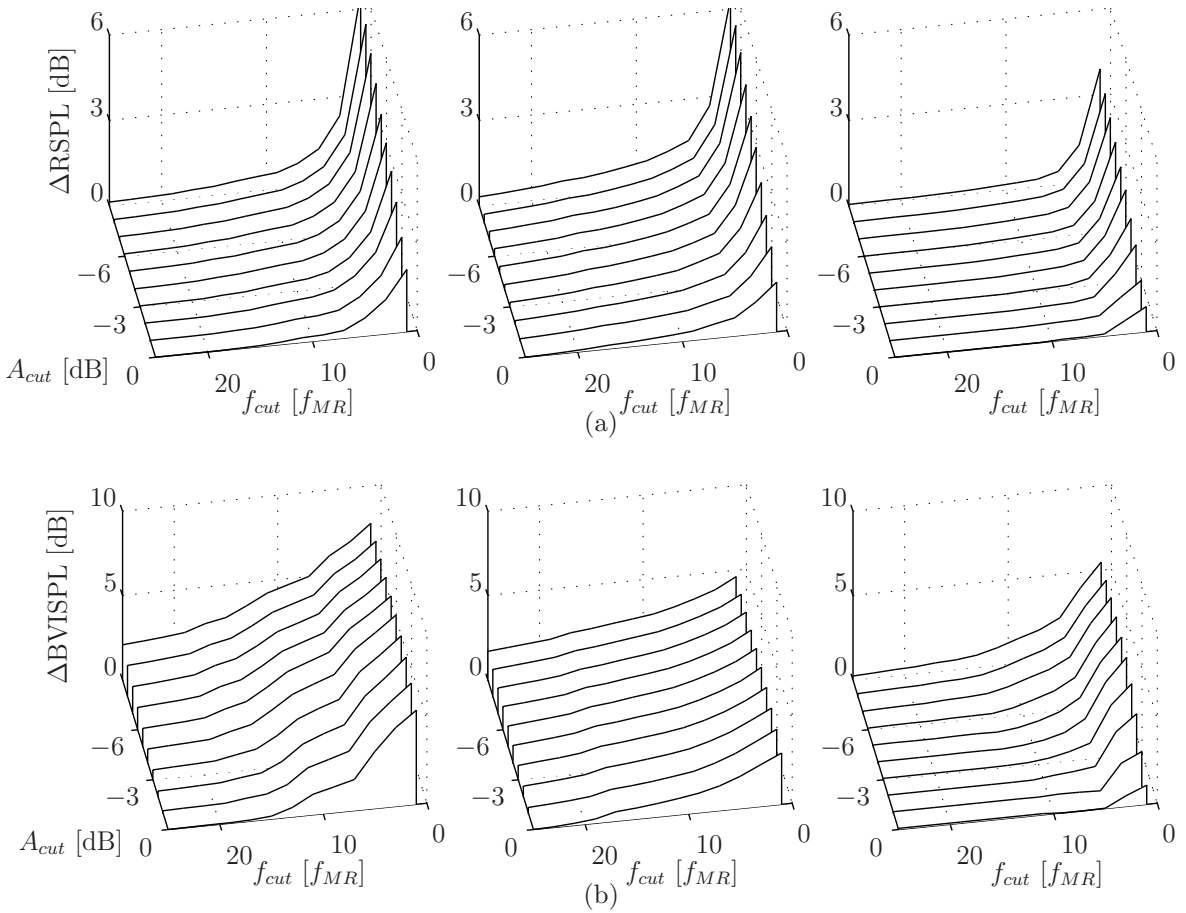

Figure 5.33: Steady level flight sensitivity analysis of the (a) residual and (b) blade-vortex interaction averaged sound pressure levels. From left to right, in each figure, shows the sensitivity to changes in the tuning parameters for each maneuver beginning at (left) 5.0, (center) 6.0, and (right) 7.0 seconds, respectively.

Chapter 6

Blade-Vortex Interaction Extraction Results

The blade-vortex interaction extraction method is applied to all microphones using the tuning parameters of frequencies above 7 main rotor harmonics ($f_{cut} = 7f_{MR} = 162.4$ Hz), and amplitudes greater than 25% of the energy in the main rotor harmonic ($A_{cut} = -6$ dB). The energy threshold is relative to the main rotor harmonic measured by each individual microphone at every point in time. Contour plots of the blade-vortex interaction extracted sound pressure levels, and overall sound pressure levels will be investigated through the use of a Cartesian projection of spherical space.

A similar Cartesian projection was previously described in figure 1.9 of § 1.1.5. The projection used here has the in-plane elevation ($\theta = 0°$) at the top of the graph, while below the rotor, indicated by $\theta = -90°$, is at the bottom of the graph. The azimuthal angle increases, starting at $\psi = 0°$ along the tail, counter clockwise with the main rotor rotation. Thus the right half of the vehicle is from 0° azimuth, to 180°; while the left half of the vehicle is from 180° azimuth to 360°. The Cartesian projection then, decreases in azimuth from 360° to 0°, such that the left half of the vehicle appears on the left half of the Cartesian projection, and the right half of the projection is dedicated to sound propagating to the right side of the vehicle. Figure 3.6 is reproduced as figure 6.1, for ease of reference. Azimuthal and elevation angles are calculated through a simple coordinate transform, described in Stephenson and Tinney (2013) [103], that takes into account the roll and pitch attitudes of the vehicle, along with it's position and trajectory. All sound pressure levels presented have been averaged over a quarter second interval, centered on the given time step, which encompasses at least one full rotor revolution.

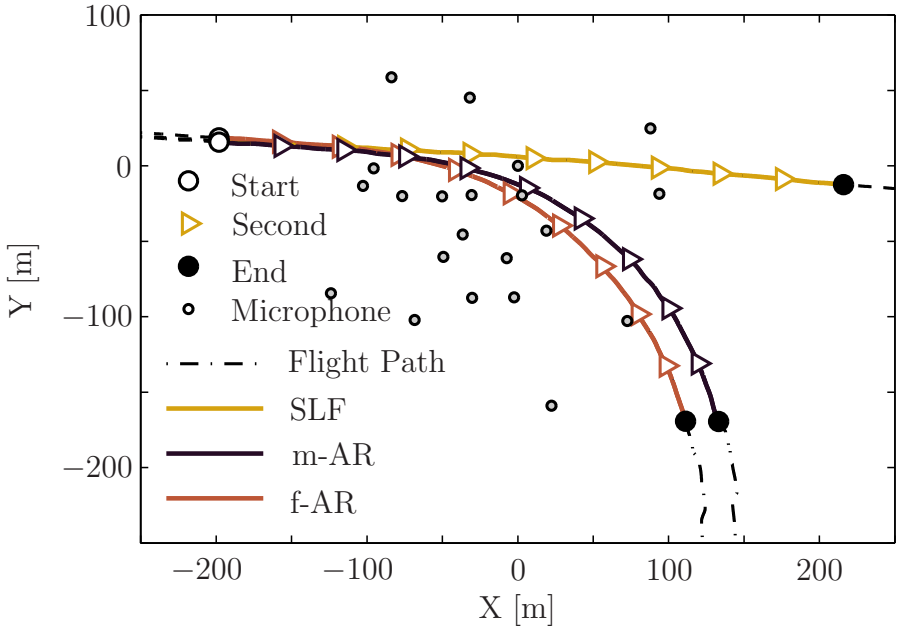

Figure 6.1: Ground track of each maneuver across the microphone array.

Information extracted from these contour plots will be used to evaluate the effectiveness of the Beddoes' wake model for predicting the location of blade-vortex interaction noise during transient maneuvering flight. The character of blade-vortex interaction noise is expected to change throughout the transient roll maneuvers, as the maneuver will modify the advance ratio, inflow, and thrust coefficient of the vehicle [101]. This will lead to the interactions occurring over various spans of the blade, which will affect the noise according to Hardin and Lamkin (1986) [58], and will also modify the trace Mach number of the interaction which will modify the emitted sound [87, 111].

6.1 Steady Level Flight Analysis

The steady level flight provides us with the basis of our analysis. Throughout the maneuver the rotor thrust and advance ratio should not vary drastically. This leads to a near constant uniform inflow, and should lead to consistent miss distances for blade-vortex interactions.

Beginning the analysis $t = 0.5$ seconds into the steady level flight maneuver,

figure 6.2 shows both the overall sound pressure level and the sound pressure level

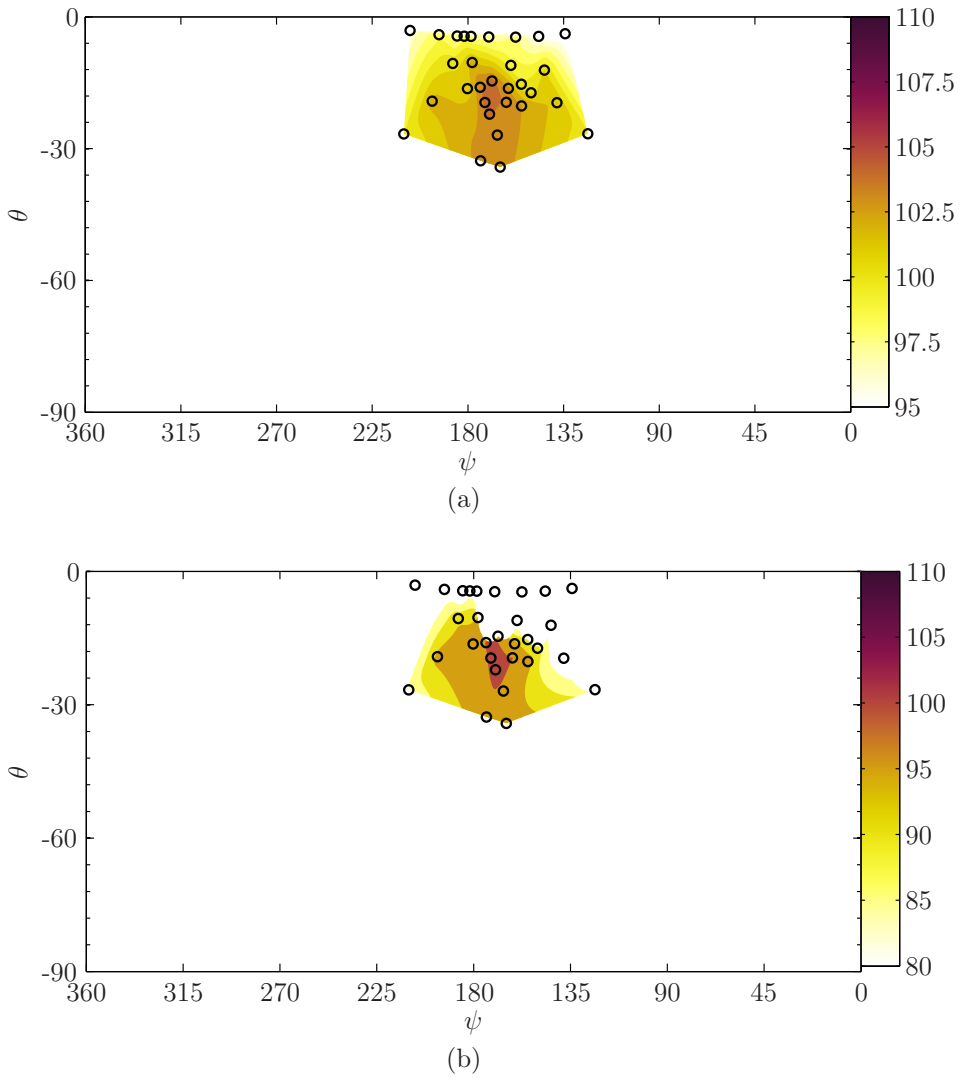

Figure 6.2: Contour plots of the (a) overall and (b) blade-vortex interaction extracted sound pressure levels extracted 0.5 seconds into the steady level flight maneuver.

associated with blade-vortex interactions. Note from figure 3.6, the vehicle is on approach and so all microphones are forward of the vehicle. The individual contour range for overall sound pressure level and blade-vortex interaction sound pressure level will be the same for all contour plots. The 15 dB contour range for overall sound pressure level and 30 dB range for blade-vortex interaction sound pressure level provides adequate resolution throughout all maneuvers. The maximum of

110 dB was kept constant between the overall sound pressure level contours and blade-vortex interaction contours to help aid in the comparison of both figures. For ease in interpretation, movies of each contour plot as a function of time throughout the maneuvers are available in appendix C.

Figure 6.2 shows peak overall sound pressure levels of around 105 dB, directly in front of the vehicle at an elevation of approximately $-20°$. Blade-vortex interactions are also noticeable, and peak in the same direction. Blade-vortex interactions are not seen in all microphones present, based on the extraction method, and so the contour map does not project a color to those areas. In the future, some microphones will have measurable blade-vortex interaction levels below the 80 dB cutoff range, and so they will also not have a projected color.

The blade-vortex interactions that are seen in figure 6.2b, agree with the expected directivity of such interactions, namely that they are forward and below the rotor, as discussed in § 1.1 and first investigated by Schmitz *et al.* [82]. Employing the aerodynamic analysis discussed in § 5.1, an estimate for the relevant rotor aerodynamics is provided in table 6.1. The relevant parameters for

λ	$0.86\ 10^{-2}$	
C_T	$4.59\ 10^{-3}$	
μ_x	0.185	
$\dot{\phi}$	0	[°/s]

Table 6.1: Calculated aerodynamic properties from the steady level flight at 0.5 seconds into the maneuver.

blade-vortex interactions occurring in this experiment are inflow (λ), coefficient of thrust (C_T), forward advance ratio (μ_x), and roll rate ($\dot{\phi}$). Each of these parameters contributes in some way to modifying the strength of the vortex, the miss distance of the vortex, or the location of the vortex interaction.

The resulting blade-vortex interactions determined through the prescribed Beddoes' wake method discussed in § 5.1 are shown in figure 6.3. The interactions shown in figure 6.3 have been color coded to emphasize their trace Mach number,

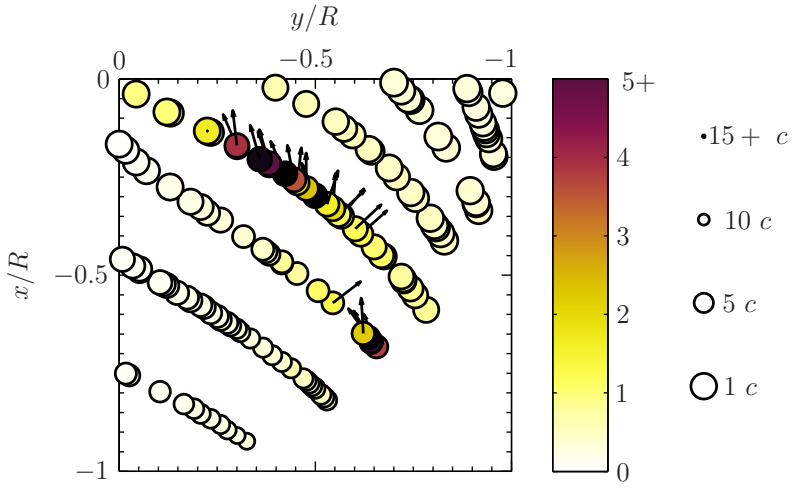

Figure 6.3: Blade-vortex interactions for the steady level flight extracted 0.5 seconds into the maneuver. Color scale indicates trace Mach number, while marker size indicates vortex miss distance in chord length (c). Vectors point in the direction of noise propagation determined by the Mach angle and vortex interaction angle.

and the size of the markers indicate how close the vortex is to the rotor disc. The vectors provided in figure 6.3 indicate the expected acoustic propagation direction for the affiliated, acoustically important interaction. Interactions occurring within the first 30% of the rotor radius are not provided vectors as they are likely to not produce much acoustics due to the limited lift provided by the blades in that region.

Figure 6.3 shows eight distinct blade-vortex interactions, with only two of them predicted to produce acoustic signals. One blade-vortex interaction event is particularly strong, and propagates predominantly forward and slightly to the right of the vehicle. This event is a parallel-type interaction, indicated by the fact that the Mach-trace number greatly exceeds 1 for a large duration of the interaction [87]. The second blade-vortex interaction occurs over a small region of the blade, but closer to the blade tip where a greater lift is expected to occur. This interaction also propagates predominantly forward of the vehicle, as indicated by the propagation arrows, although it is expected to be less powerful than the parallel interaction due to its shorter duration.

The overall sound pressure levels seen near the plane of the rotor ($\theta \approx 5°$) are a full 10 dB in strength below those seen at the peak of their propagation path. Figure 6.4 compares the pressure signatures associated with the peak microphone

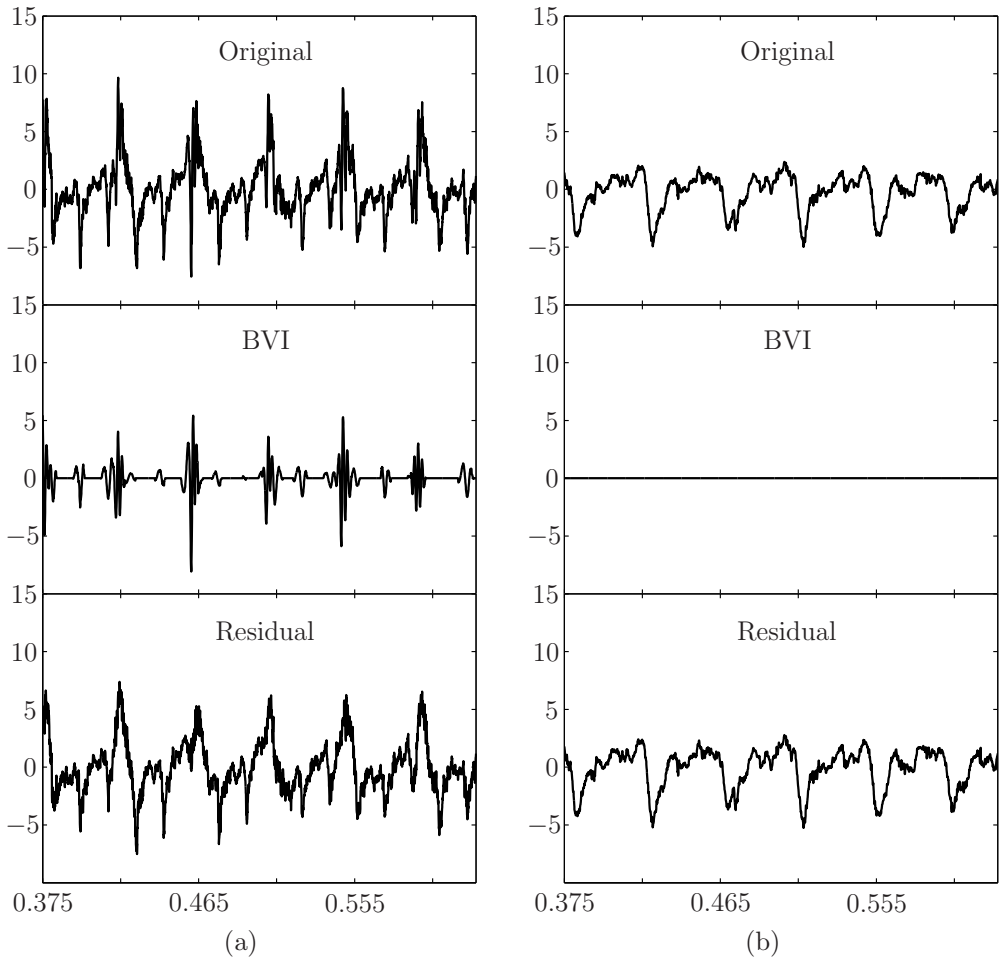

Figure 6.4: Pressure signatures extracted from 0.5 seconds into the steady level flight maneuver. Signatures extracted from (a) peak blade-vortex interaction microphone located at ($\psi = 174°, \theta = -33°$) and (b) an in-plane microphone located at ($134°, -4°$).

to that of the microphone in the top right of figure 6.2. The microphone with peak overall sound pressure level is shown in figure 6.4a. This microphone also has the peak blade-vortex interaction signature, which has been extracted and shown in said figure. The original pressure signature shows a very strong main rotor lower harmonic noise, as well as clear and powerful instances of blade-vortex interactions. The extraction method was able to identify these impulses, but has

also extracted some limited energy from the tail rotor signatures as well. This highlights a problem with the filtering technique, where a strong tail rotor signal can lead to the extraction of some tail rotor energy. However, the ability to extract blade-vortex interactions in general, is a powerful tool, and an improved filtering technique could eliminate tail rotor noise from the extracted signal.

The pressure signature extracted from the in-plane microphone (figure 6.4b), located at ($\psi = 134°, \theta = -4°$), shows a strong thickness noise signature associated with the main rotor. Recalling the discussion of § 1.1, the presence of thickness noise in this direction was anticipated. The original pressure signature does not contain noticeable blade-vortex interactions, and the tail rotor signature is negligible at this time. There are also no sharp negative pulses associated with high-speed impulsive noise, also as anticipated for a modern commercial helicopter. The extracted blade-vortex interaction signal seen for this instance is identically equal to zero, as the extraction method has no strong higher harmonic information to extract. Instead, the residual signal matches the original signal exactly, showing that the wavelet transformation method can recreate the original signal without significant aberrations.

The analysis jumps now, to the two second mark in the maneuver. Figure 6.5 shows the identical patten that was exhibited in figure 6.2. The overall sound pressure level peaks directly forward of the vehicle and at approximately 30° below the rotor tip-path plane. Blade-vortex interactions are now seen to peak at an elevation of 30° below the rotor, and slightly right of center at $\psi = 170°$.

Blade-vortex interactions are seen to be measurable as far below the rotor as $\theta = -66°$. Figure 6.6 shows the pressure signature at this time from the microphone located at 152° azimuth and −66° elevation. The original pressure signature seen in figure 6.6 presents a complicated image where there are intermittent blade-vortex interaction pulses visible. The tail rotor signature is also intermittent and can be quite strong, as seen by the pulse near 2.1 seconds.

The original pressure signature in figure 6.6, also shows a weaker main rotor lower harmonic noise presence than what was seen in figure 6.4. This weaker

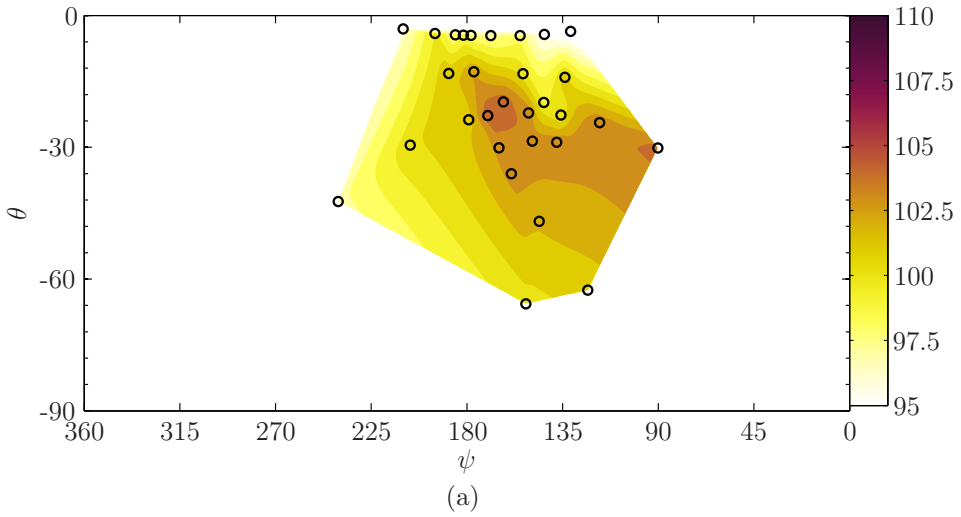

(a)

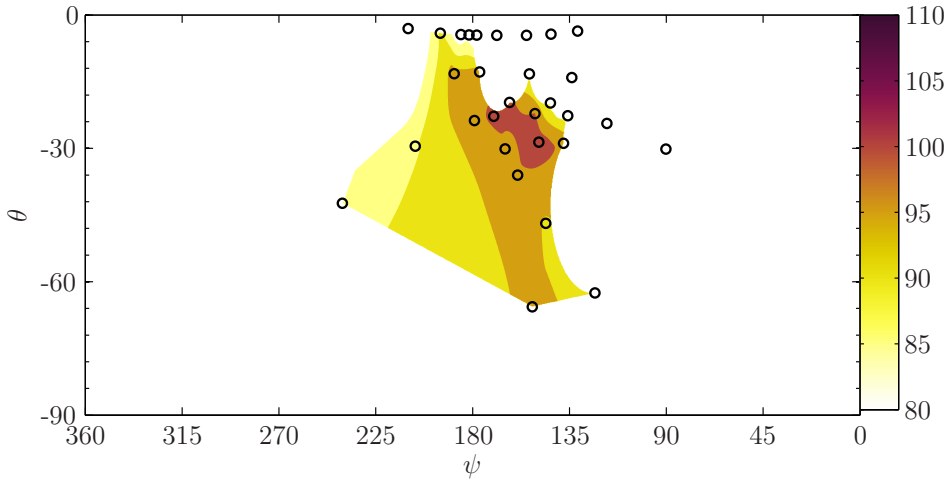

(b)

Figure 6.5: Contour plots of the (a) overall and (b) blade-vortex interaction extracted sound pressure levels extracted 2.0 seconds into the steady level flight maneuver.

presence suggests a lower energy in the main rotor harmonic. With this lower energy, the amplitude cutoff allows in noise from higher frequency sources outside of blade-vortex interactions. This is why there is significant activity in the extracted blade-vortex interaction signal. This is a known weakness with the filtering method. However, it has properly identified two blade-vortex interactions. The first is seen just after the start of the signal, while the second can be found near the 2.055 second tick-mark.

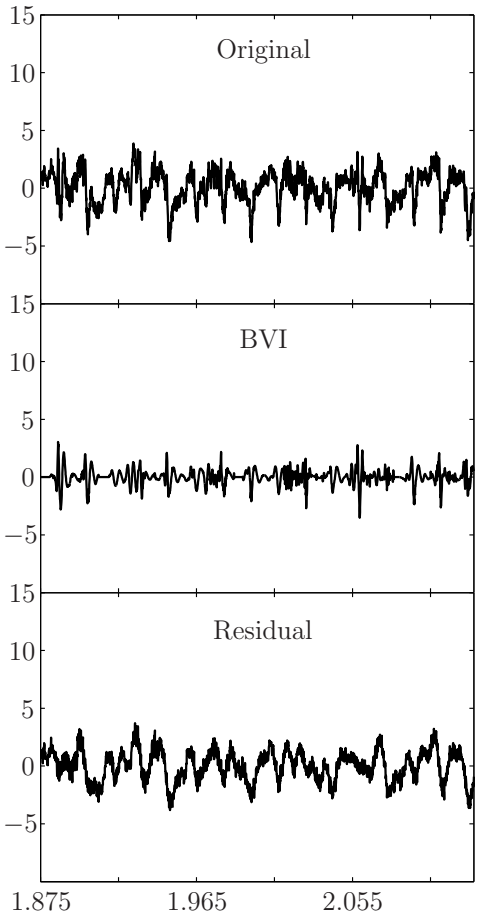

Figure 6.6: Pressure signature extracted from two seconds into the steady level flight maneuver. The microphone is located at an elevation of -66° below the rotor and now slightly left of center at $\psi = 152^\circ$.

Regardless of the filtering error, the calculated blade-vortex interaction sound pressure level shows that this phenomenon is only a partial contributor to the overall signal. Figure 6.5 shows that the overall sound pressure level in this direction is at 100 dB, while the extracted signal is 5 dB lower than that. This shows that the high amplitude, high frequency portion of the signal contributes only 30% to the overall signal, as opposed to half the energy as was seen in figure 6.2.

Figure 6.7 is extracted from the 4.5 seconds into the steady level flight, and shows significant rotor noise on the right side of the vehicle, but no discernible blade-vortex interactions are present. However, in the peak blade-vortex interac-

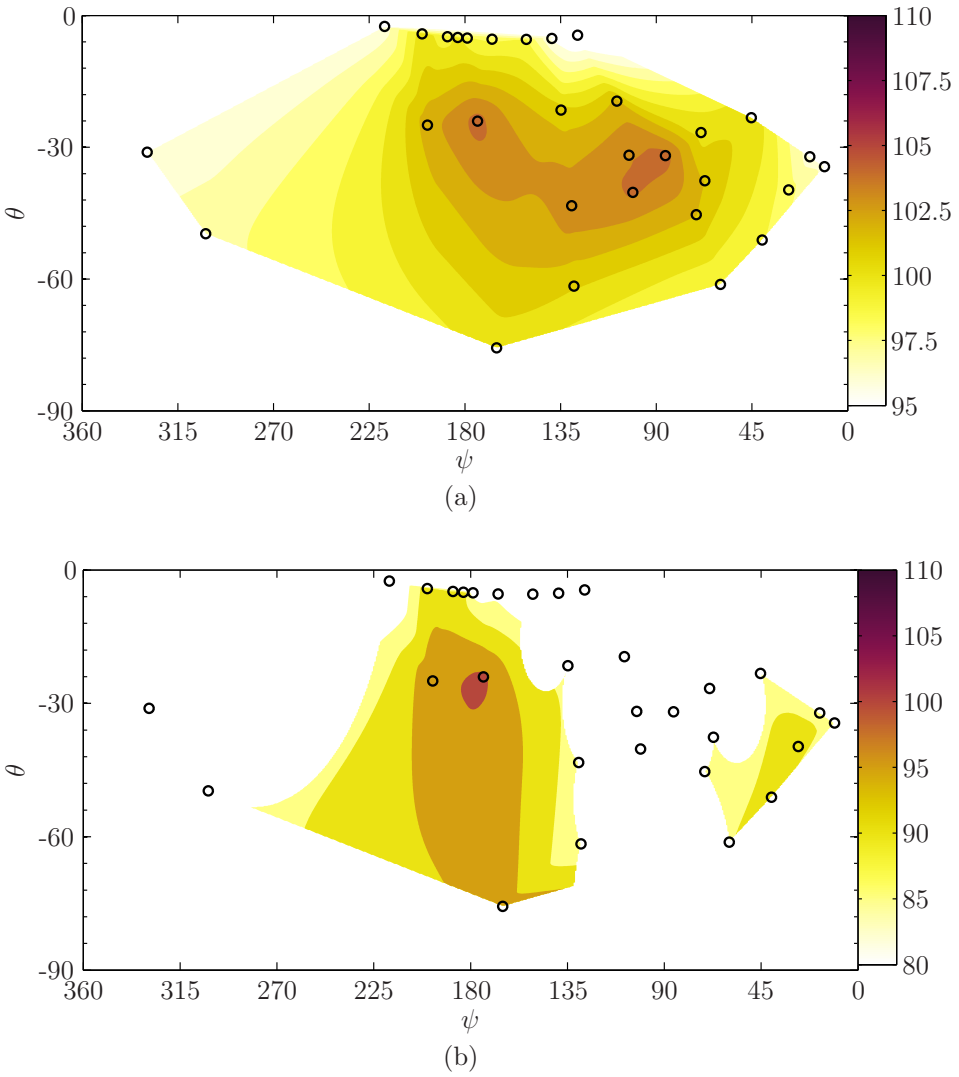

Figure 6.7: Contour plots of the (a) overall and (b) blade-vortex interaction extracted sound pressure levels extracted 4.5 seconds into the steady level flight maneuver.

tion direction, the blade-vortex interaction sound pressure level reaches 100 dB. Meanwhile, the overall sound pressure level is around 103 dB, showing that blade-vortex interactions can substantially increase the overall sound pressure level, even in steady level flight [93]. This is also consistent with what has been seen at each previously investigated time step.

Significant changes are not expected in the acoustic footprint of the vehicle during the steady level flight maneuver. In general, both the overall sound pressure

level and blade-vortex interaction sound pressure level directivity patterns have remained fairly constant. The only major difference between the contours have been due to the changing location of the microphones, which has allowed a greater extent of the directivity pattern to be investigated.

The aerodynamic parameters have also not changed significantly, as shown in table 6.2, which was extracted 4.5 seconds into the maneuver. All aerodynamic

λ	$1.18\ 10^{-2}$	
C_T	$4.58\ 10^{-3}$	
μ_x	0.186	
$\dot{\phi}$	0	[°/s]

Table 6.2: Calculated aerodynamic properties from the steady level flight at 4.5 seconds into the maneuver.

parameters reported stayed within 1%, except for the calculated inflow ratio, which varied substantially. The effect of the varying inflow can be seen in figure 6.8, where an increase in the miss distance is seen when compared to figure 6.3.

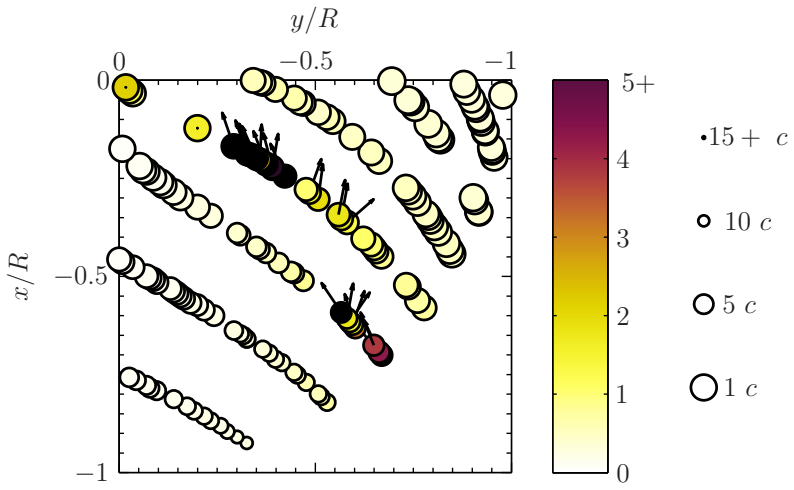

Figure 6.8: Blade-vortex interactions for the steady level flight extracted 4.5 seconds into the maneuver. Color scale indicates trace Mach number, while marker size indicates vortex miss distance in chord length (c). Vectors point in the direction of noise propagation determined by the Mach angle and vortex interaction angle.

This increase in calculated miss distance, however, did not have a significant

impact on the acoustics. The expected propagation direction is still identical to what was seen before, however, and is true to the directivity patterns indicated in the blade vortex extraction sound pressure level contours.

The original pressure signature from the microphone located at approximately 80° azimuth and −32° elevation is shown in figure 6.9. This direction

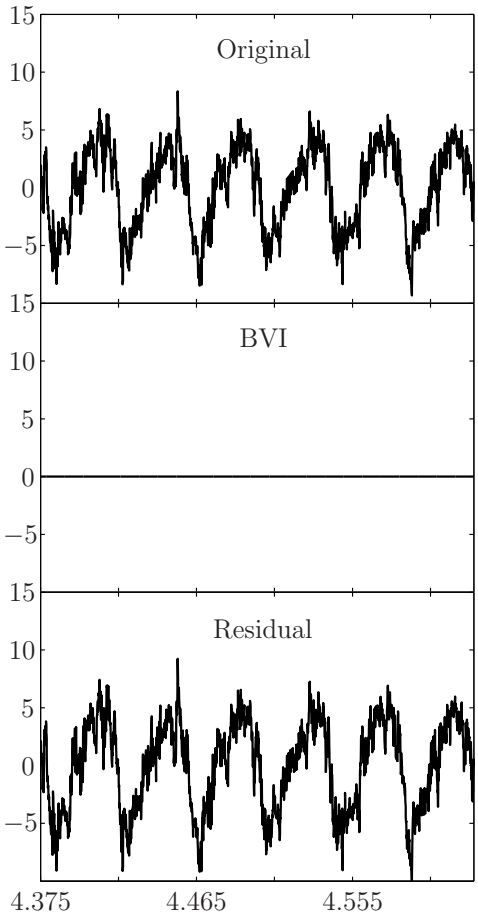

Figure 6.9: Pressure signature extracted from 4.5 seconds into the steady level flight maneuver. The microphone is located at approximately 86° azimuth and −32° elevation in figure 6.7.

shows a very strong overall sound pressure level, but no discernible blade-vortex interactions as seen in figure 6.7. The original pressure signature, seen at the top of figure 6.9 shows the very strong presence of lower main rotor harmonic noise. This mixture of loading and thickness sources does not include significant levels of blade-vortex interactions.

Two noticeable, but weak, blade-vortex interactions are seen in the first two blade passages of figure 6.9. These interactions are not extracted, however, because they are significantly weak when compared to the very strong energy in the main rotor harmonic. A lower amplitude threshold would have seen these interactions removed from the signal, but at the cost of removing non-related higher frequency noise as well. Again, a better filtering method could identify and remove this signature. Although the currently employed method does not show that blade-vortex interactions are present, it does adequately identify that they are insignificant in this direction.

6.2 Fast Advancing Side Roll Analysis

The fast advancing side roll maneuver is now analyzed using the blade-vortex interaction extraction method. Beginning at 0.5 seconds into the maneuver, the sound pressure level contours, shown in figure 6.10, show almost identical contours as was seen for the steady level flight maneuver at the same instant (figure 6.2). This is not unexpected, as the first one to two seconds of each maneuver are in established steady level flight.

The blade-vortex interaction sound pressure level contour map, however, does show some slight differences as the peak direction magnitude is slightly less than that seen in the steady level flight condition. The relevant aerodynamic parameters for the fast advancing side roll maneuver are provided in table 6.3, and

λ	$1.36\ 10^{-2}$
C_T	$4.58\ 10^{-3}$
μ_x	0.176
$\dot{\phi}$	1 [°/s]

Table 6.3: Calculated aerodynamic properties from 0.5 seconds into the fast advancing side roll maneuver.

shed some light on the decrease in sound pressure levels. Comparing table 6.3 with 6.1, it becomes apparent that the fast advancing side roll maneuver was advancing

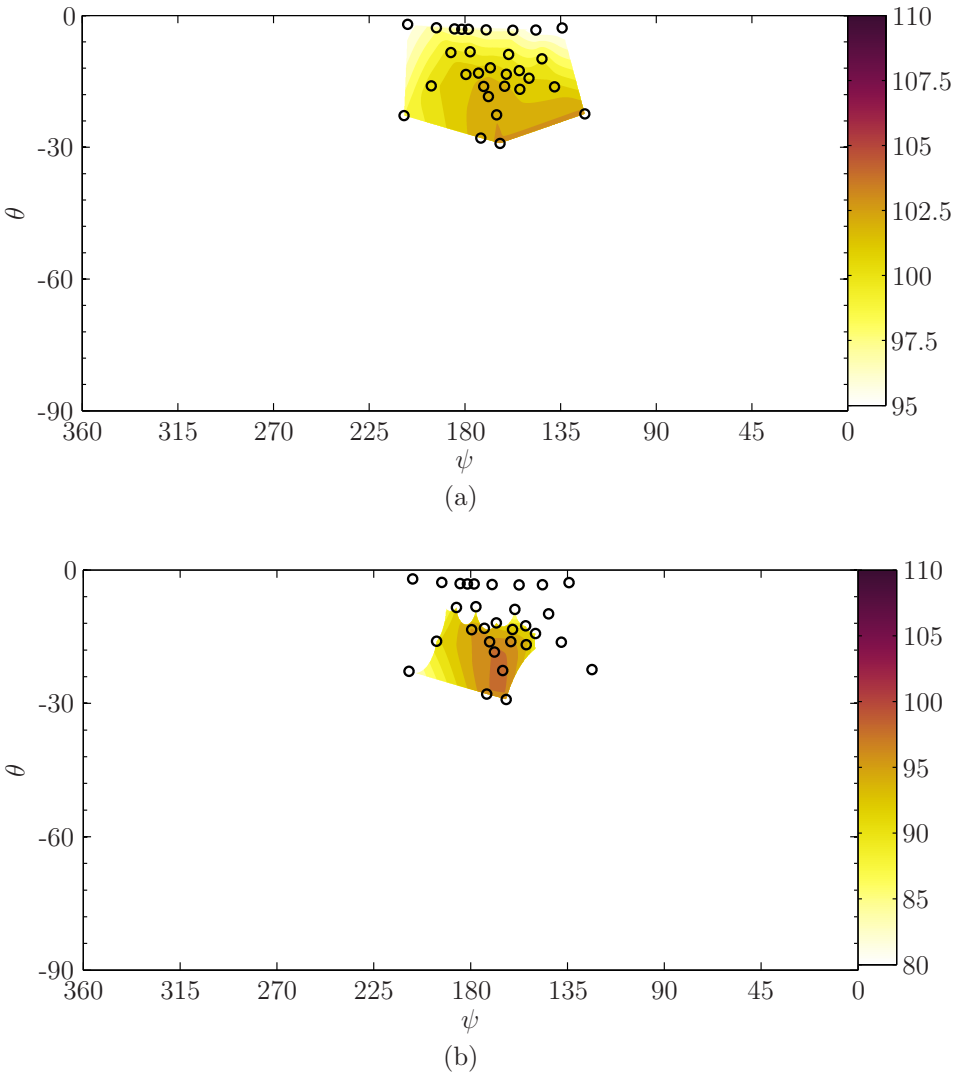

Figure 6.10: Contour plots of the (a) overall and (b) blade-vortex interaction extracted sound pressure levels extracted 0.5 seconds into the fast advancing side roll maneuver.

slower, and had a larger inflow than the steady level flight maneuver. Both of these should couple to increase the miss distance during the blade-vortex interactions, and thereby decrease the resulting sound pressure levels. Figure 6.11 shows the predicted blade-vortex interactions using Beddoes' prescribed wake model. Comparing with figure 6.3, it can be seen that the miss distances are indeed larger than what was previously seen. Further, the difference in the advance ratio resulted in interactions that occurred in a slightly different manner, and now 9 distinct

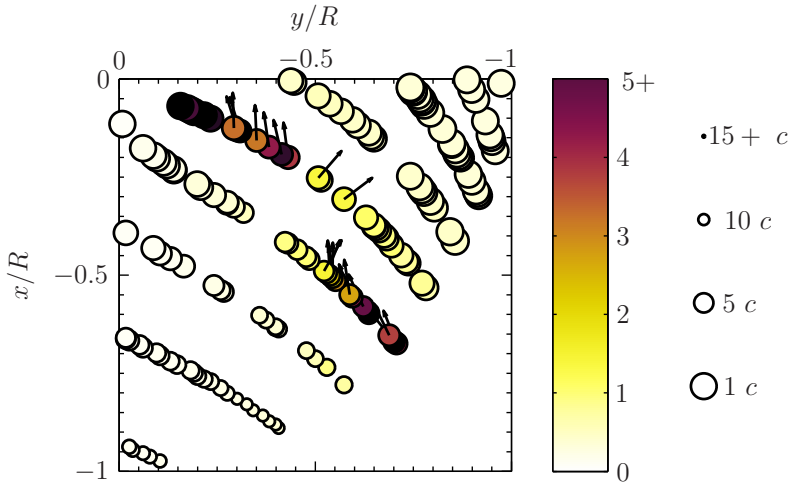

Figure 6.11: Blade-vortex interactions for the fast advancing side roll maneuver extracted at 0.5 seconds. Color scale indicates trace Mach number, while marker size indicates vortex miss distance in chord length (c). Vectors point in the direction of noise propagation determined by the Mach angle and vortex interaction angle.

vortex interactions are partially visible. Due to the change in the interaction, the trace Mach number for the predominant vortex interaction was markedly decreased, and the duration and trace Mach number of the secondary interaction was increased. Coupled together, this could explain the slightly broader and less powerful blade-vortex interaction signatures as seen in the sound pressure level contours.

Figure 6.12 is identical to figure 6.4, in that it provides the pressure signatures from the peak blade-vortex interaction noise direction, and an in-plane microphone. Comparing with the steady level flight condition from before, the blade-vortex interactions are indeed less powerful, as their peak to peak pressure changes are smaller [34]. However, the tail rotor signature is also less powerful for this signal, and so the higher harmonics of the tail rotor are no longer being extracted from the overall signal. Changes can also be seen in the in-plane microphone, where the signature associated with main rotor thickness noise, is also diminished.

Figure 6.13 are sound pressure levels extracted from 1.5 seconds into the

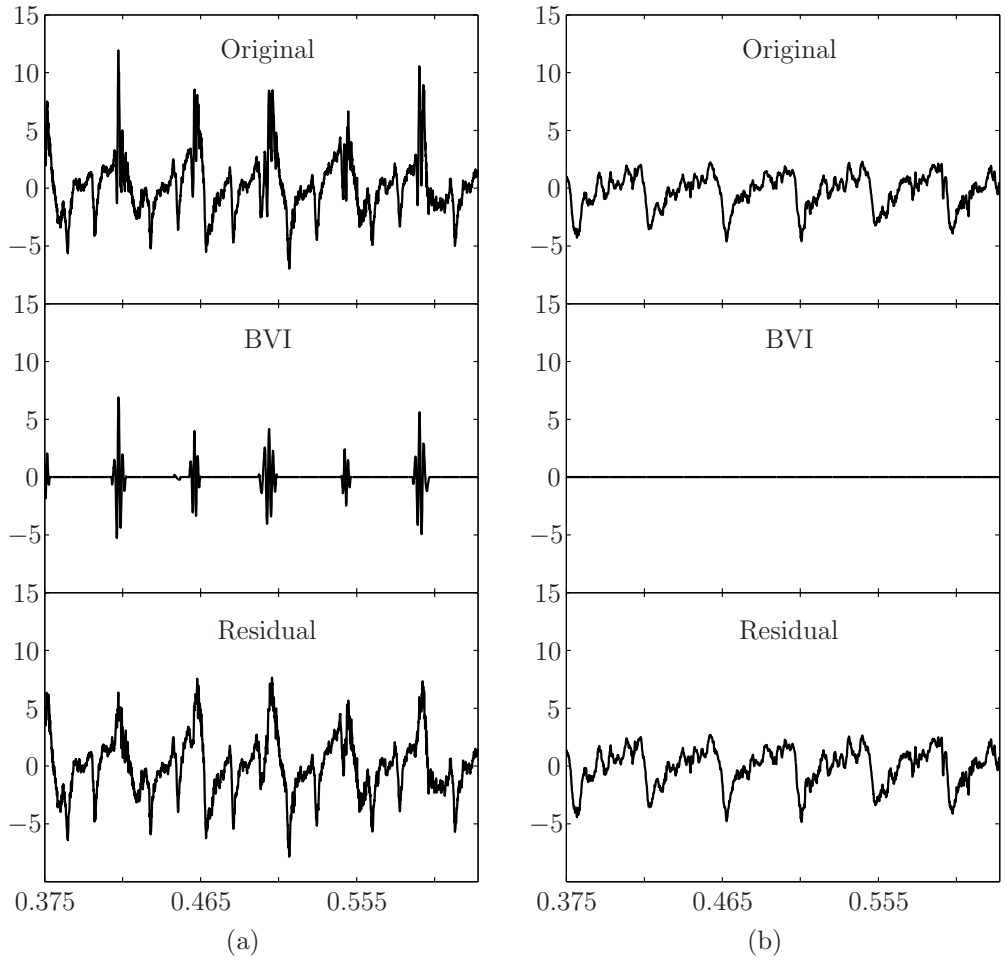

Figure 6.12: Pressure signatures extracted from 0.5 seconds into the fast advancing side roll maneuver. Signatures extracted from (a) peak BVI microphone located at ($\psi = 173°, \theta = -28°$) and (b) an in-plane microphone located at ($134°, -3°$).

fast advancing side roll maneuver. The vehicle has entered into its roll maneuver by this time, as indicated in figure 3.8d. Rolling towards the advancing side of the rotor disc reduces the miss distance of the vortices on that side, thereby increasing the noise associated with blade-vortex interactions. The contour plots shown in figure 6.13 show that the peak blade-vortex interaction sound pressure level is approximately 103 dB, where the overall sound pressure level is only 1 dB greater than that. This is a sizable jump, as previously the blade-vortex interaction sound pressure level was 3 dB less than the overall sound pressure level.

Schmitz *et al.* (2007) [86] demonstrated that the tail rotor noise contributed

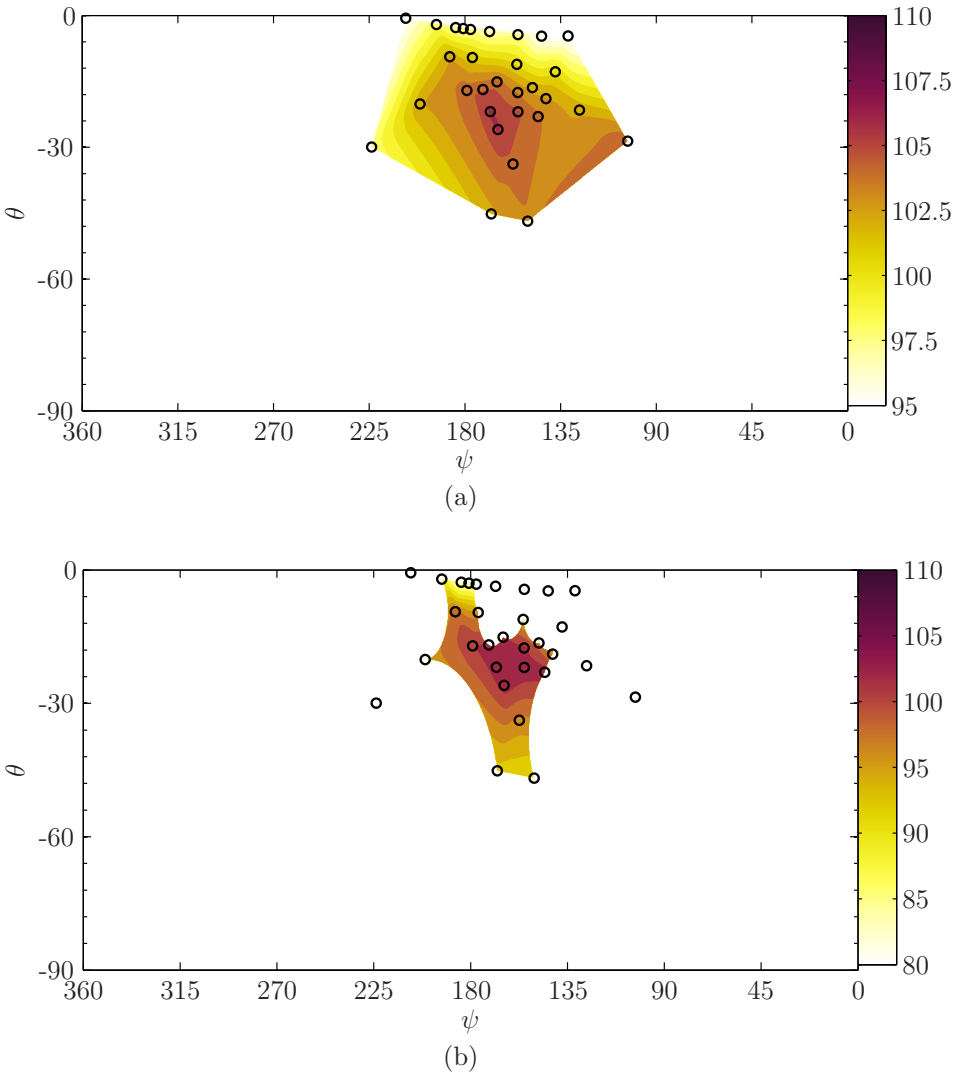

Figure 6.13: Contour plots of the (a) overall and (b) blade-vortex interaction extracted sound pressure levels extracted 1.5 seconds into the fast advancing side roll maneuver.

significantly to the increase in overall sound pressure level during steady turning flight. They postulated that the tail rotor noise signature increased due to the increase in thrust needed to maintain steady flight. This resulted in an increase in rotor torque and therefore tail rotor thrust. This is not that case in the current transient maneuver, however, as the thrust has not significantly changed as demonstrated in table 6.4. Here, the coefficient of thrust is less than 1% greater than it was for the 0.5 second, steady level flight portion of the maneuver. Figure

λ	$1.42\ 10^{-2}$	
C_T	$4.61\ 10^{-3}$	
μ_x	0.175	
$\dot{\phi}$	10	[°/s]

Table 6.4: Calculated aerodynamic properties from 1.5 seconds into the fast advancing side roll maneuver.

6.14 shows the pressure signature from the peak blade-vortex interaction direction

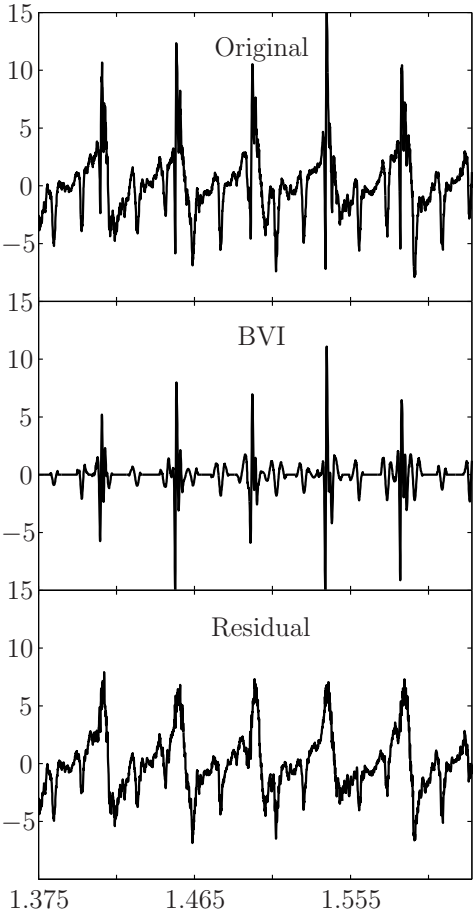

Figure 6.14: Pressure signatures extracted from 1.5 seconds into the fast advancing side roll maneuver. Extracted from the peak BVI microphone located at ($\psi = 179°, \theta = -17°$).

and further confirms that the increase in sound pressure level does not come from the tail rotor signature. Instead, strong blade-vortex interactions are present, and are greater in magnitude than was previously seen in figure 6.12a. While some

tail rotor noise is being extracted, the peak to peak magnitude is significantly less than that of the blade-vortex interactions, showing their negligible contribution to the sound pressure level [34].

Table 6.4 also shows that the roll rate is at 10 [°/s] and the vehicle has increased its inflow, while slowing slightly. Figure 6.15 shows the Beddoes' pre-

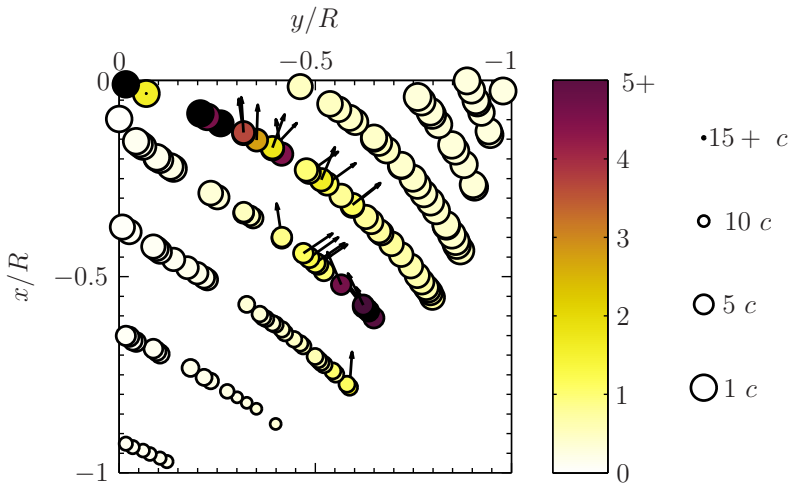

Figure 6.15: Blade-vortex interactions for the fast advancing side roll maneuver extracted at 1.5 seconds. Color scale indicates trace Mach number, while marker size indicates vortex miss distance in chord length (c). Vectors point in the direction of noise propagation determined by the Mach angle and vortex interaction angle.

scribed wake prediction for the blade-vortex interactions that would occur at this time. The prediction method suggests that the miss distance is slightly greater now, due to the increased inflow and slower advance ratio. This suggests that the blade-vortex interaction sound pressure level should have decreased. The Beddoes' wake model assumes a steady flight condition, however, and so it does not model the physical rolling of the vehicle towards the tip vortices [107]. The motion of the vehicle is easily enough to cause a decrease in the miss distance, and could thus explain why the blade-vortex interaction sound pressure level is seen to increase for this instance in time [56]. This helps to confirm the conclusion of Hennes *et al.* (2004) [59], that prescribed wake models and the resulting blade loads are insufficient for accurately modeling blade-vortex interactions during maneuvering

flight. The Beddoes' method does, however, show a broader range of directivities associated with the interactions, which is true to what can be seen in figure 6.13b.

Several other factors that can impact the strength of blade-vortex interaction noise include local inflow and local blade loading distribution. The current model employed provides only the average inflow across the rotor while the inflow varies during normal operating conditions, especially in the lateral direction during roll maneuvers. Changes in the local inflow will adjust the miss distance of the tip vortex during interactions. Further, increasing local blade loading increases the strength of the generated tip vortex. Stronger tip vortices will have a larger aerodynamic impact on the system due to the Biot-Savart law, and thus can produce stronger blade-vortex interaction noise. Neither the miss distance change due to variations in local inflow, nor the aerodynamic impacts from locally varying vortex strengths are accounted for in the current model, although they are known to impact the noise levels.

Slightly further into the maneuver, at 2.0 seconds, the overall sound pressure level has increased by another 2 dB, as seen in figure 6.16. So far, there has been an increase in the overall sound pressure level of close to 7 dB in the peak direction, when compared to the original steady level signature in figure 6.10. This increase in sound pressure level is close to the computational work of Perez and Costes (2004) [80], who saw a 10 dB increase in noise for an advancing side roll maneuver. Their maneuver, however, comprised multiple pilot inputs and a roll rate of approximately 7 [°/s], so a direct comparison of maneuvers is not possible.

The blade-vortex interaction sound pressure level has also increased, and the peak direction has shifted closer to the retreating side of the vehicle. This agrees with the flight tests of Spiegel *et al.* (2005) [99], who saw peak noise shift to the retreating side of the vehicle during a transient roll to the advancing side. This was contrary to the normally perceived noise pattern, which typically sees a peak on the advancing side of the vehicle during steady rolls towards the advancing side [99]. This increase in sound pressure level is directly associated with the increase in the roll rate of the vehicle, as seen in table 6.5. Spiegel *et al.* also noted that the

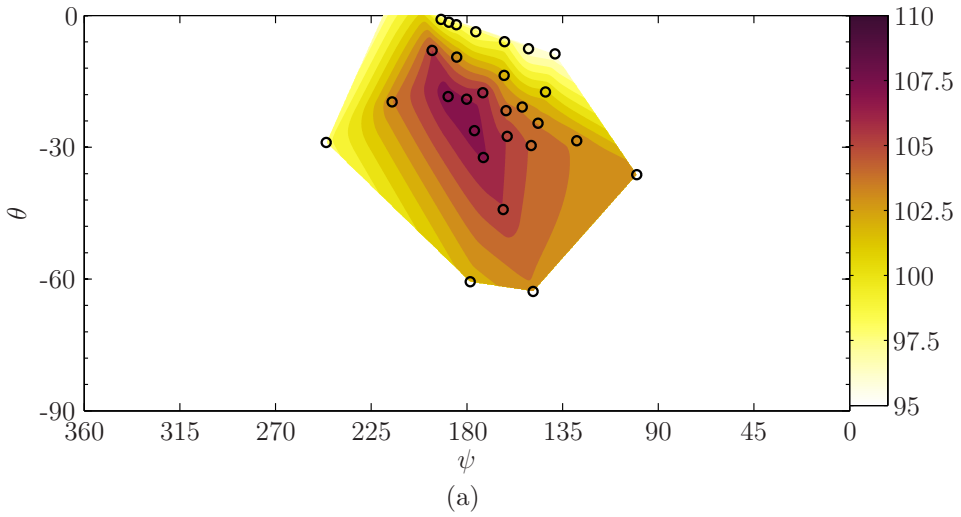

(a)

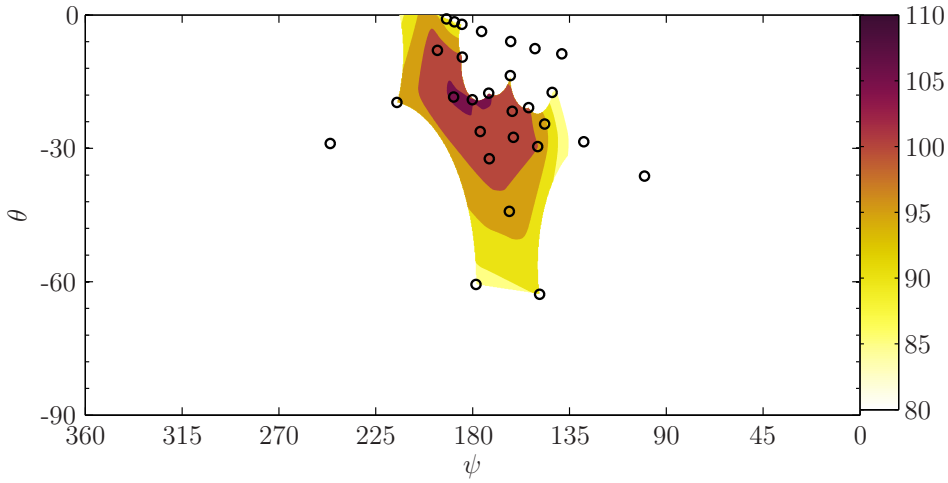

(b)

Figure 6.16: Contour plots of the (a) overall and (b) blade-vortex interaction extracted sound pressure levels extracted 2.0 seconds into the fast advancing side roll maneuver.

λ	$1.43\ 10^{-2}$	
C_T	$4.69\ 10^{-3}$	
μ_x	0.174	
$\dot{\phi}$	15	[°/s]

Table 6.5: Calculated aerodynamic properties from 2.0 seconds into the fast advancing side roll maneuver.

advancing side roll is less sensitive to roll rate than the retreating side transient roll maneuver [99]. So a future investigation into retreating side transient rolls using this analysis technique is warranted.

With the increase in roll rate, the advance ratio has further decreased, and the inflow and thrust coefficient are still increasing. These changing aerodynamic parameters, however, have not significantly affected the Beddoes' wake model. Seen in figure 6.17, the secondary interaction is slightly more powerful and directed

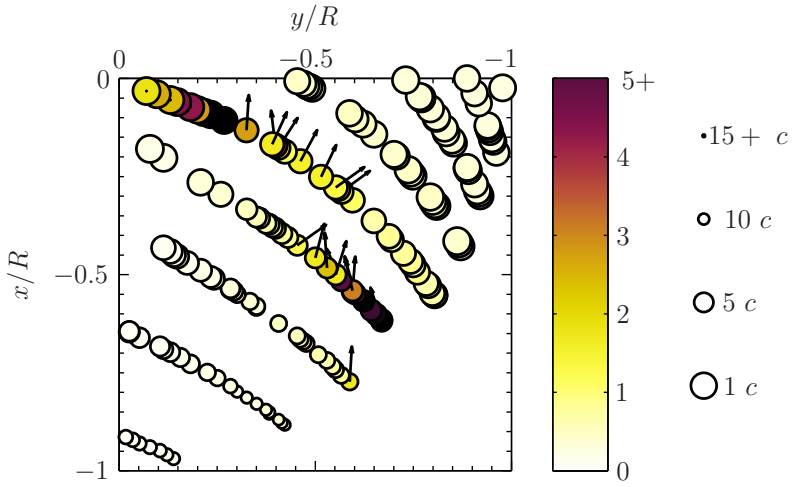

Figure 6.17: Blade-vortex interactions for the fast advancing side roll maneuver extracted at 2.0 seconds. Color scale indicates trace Mach number, while marker size indicates vortex miss distance in chord length (c). Vectors point in the direction of noise propagation determined by the Mach angle and vortex interaction angle.

closer towards the retreating side of the vehicle than before. However, according to the Beddoes' prescribed wake method, the miss distances have not changed dramatically due to the changes in the aerodynamic state of the helicopter.

The increase in thrust coefficient, and therefore the strength of the tip vortices is not significant enough to increase the magnitude of the sound pressure levels to the extent that has been seen thus far. Assuming the thrust coefficient is directly proportional to the strength of the blade-vortex interaction sound pressure level, then a change in thrust coefficient would result in a change in the blade-vortex interaction sound pressure level according to the following approximate

equation,

$$\Delta BVISPL = 20 \log_{10} \frac{C_{T_1}}{C_{T_2}}. \tag{6.1}$$

Thus, the expected increase in sound pressure level from 1.5 seconds to 2.0 seconds would be on the order of a tenth of a decibel. Therefore, the 2 dB increase in sound pressure level is more likely to be caused by a change in the miss distance of the tip vortices due to the transient rolling maneuver. This transient roll is not modeled in the prescribed wake method, and so the miss distances are not entirely accurate during the transient portion. However, the directivity changes observed do correspond fairly well with the perceived changes in the blade-vortex interaction signal.

Half a second later, at 2.5 seconds into the maneuver, the aerodynamic parameters have changed very little relative to the 2.0 second mark, as seen in table 6.6. This was not unexpected, as we are near the maximum roll rate of the

λ	$1.41\ 10^{-2}$	
C_T	$4.83\ 10^{-3}$	
μ_x	0.173	
$\dot{\phi}$	17	[°/s]

Table 6.6: Calculated aerodynamic properties from 2.5 seconds into the fast advancing side roll maneuver.

fast advancing side roll maneuver. The sound pressure contours, given in figure 6.18, are also very close in magnitude to what was seen in figure 6.16. However, the blade-vortex interaction sound pressure level contour map is more fully flushed out due to the change in the microphones relative to the vehicle. The blade-vortex interactions predicted by the Beddoes' prescribed wake model, shown in figure 6.19, are also very close to what was seen at the 2.0 second maneuver.

As was seen before, at the 2.0 second mark of the steady level flight maneuver, blade-vortex interactions are seemingly present and extend deep beneath the rotor. The pressure signature seen in figure 6.20 is similar to that seen previously, in that the extraction method has filtered out higher harmonic noise unrelated to

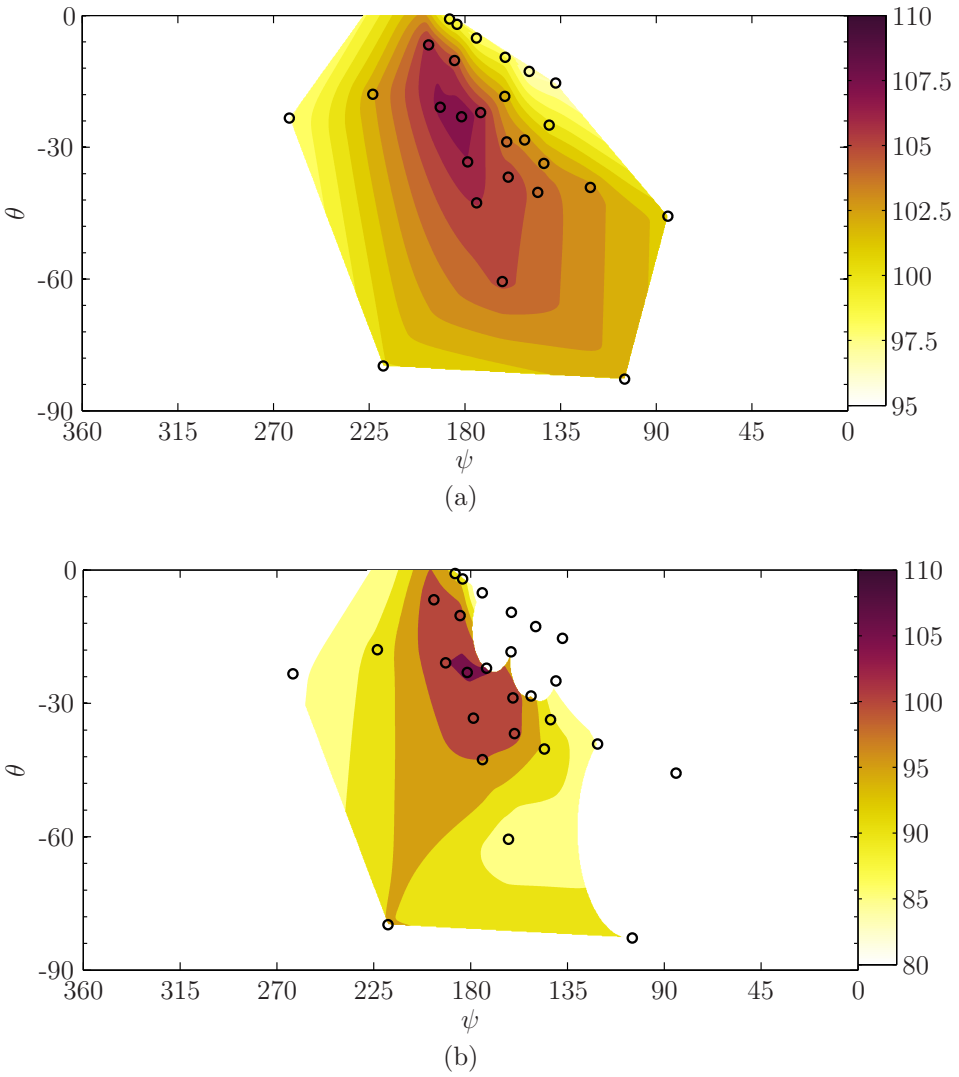

Figure 6.18: Contour plots of the (a) overall and (b) blade-vortex interaction extracted sound pressure levels extracted 2.5 seconds into the fast advancing side roll maneuver.

blade-vortex interactions. Indeed, there is no strong main rotor harmonic signal seen in this direction, as evidenced by the original pressure signature in figure 6.20, and so the amplitude cutoff has allowed for the removal of other higher frequency noise sources. However, the blade-vortex interaction sound pressure level for this direction is 9 dB lower than that seen for the peak direction. Thus, being only one-eighth the peak energy, the signal in this direction is easily negligible. Improving the cutoff amplitude criteria could result in a cleaner blade-vortex interaction

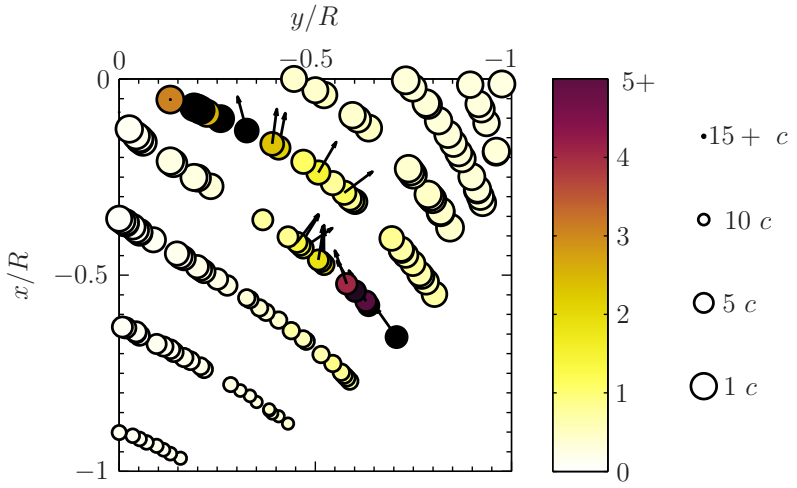

Figure 6.19: Blade-vortex interactions for the fast advancing side roll maneuver extracted at 2.5 seconds. Color scale indicates trace Mach number, while marker size indicates vortex miss distance in chord length (c). Vectors point in the direction of noise propagation determined by the Mach angle and vortex interaction angle.

signal. Applying a lower threshold to the main rotor harmonic energy signature, could be appropriate. However, the filtering method as described is currently independent of arbitrary vehicle specific cutoff limits, and a lower threshold on the main rotor harmonic would have to be vehicle and maneuver specific.

Three seconds into the fast advancing side roll maneuver, the peak blade-vortex interaction sound pressure level has shifted to nearly in-plane with the rotor and on the retreating side of the vehicle, as shown in figure 6.21. There is also some blade-vortex interactions extracted at the rear of the vehicle, close to 360° azimuth. Figure 6.22 shows a comparison between the peak blade-vortex interaction signal, and the microphone recording blade-vortex interactions at the rear of the vehicle. The microphone recording the noise propagating backwards has identified higher frequency noise unrelated to blade-vortex interactions. This was expected, as the magnitude of the sound pressure level was 9 dB less than the peak in the blade-vortex interaction signal, and was 5 dB less than the overall sound pressure level at that point.

The peak blade-vortex interaction signal, shown in figure 6.22a, however,

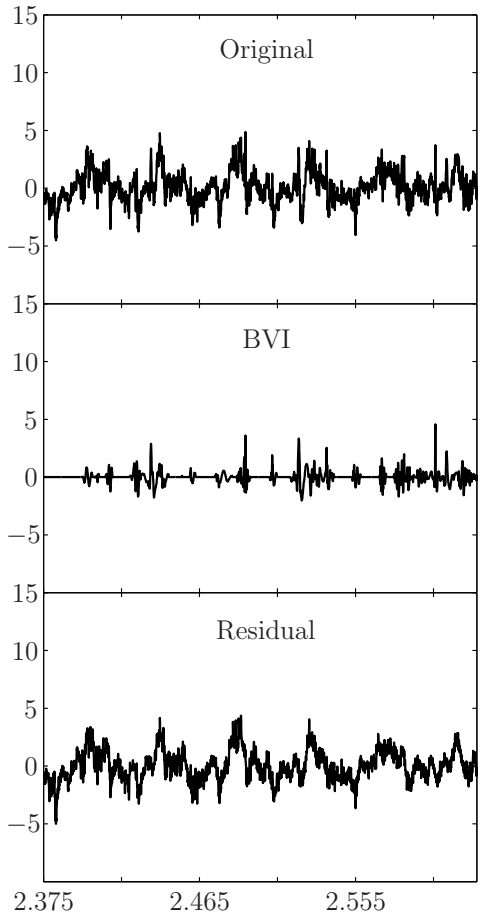

Figure 6.20: Pressure signature extracted from 2.5 seconds into the fast advancing side roll maneuver. The microphone is located at an elevation of $-80°$ below the rotor and now slightly left of center at $\psi = 218°$.

shows very strong blade-vortex interactions that were extracted quite cleanly. The original signal possesses a high presence of energy in the main rotor harmonic with a strong blade-vortex interaction signal, and so the filtering method worked quite well. The tail rotor signature is also quite strong, with higher harmonics clearly present by the sharpness of the signature. Previously, in figure 6.4a, the sharp presence of the tail rotor resulted in the extraction of some tail rotor energy. Here, however, this is avoided as the main rotor harmonic is strong enough such that the amplitude cutoff is above the strength of the tail rotor higher harmonics. However, the increase in the tail rotor signature does contribute some to the increase in the overall sound pressure level. Further, this increase was expected as the coefficient

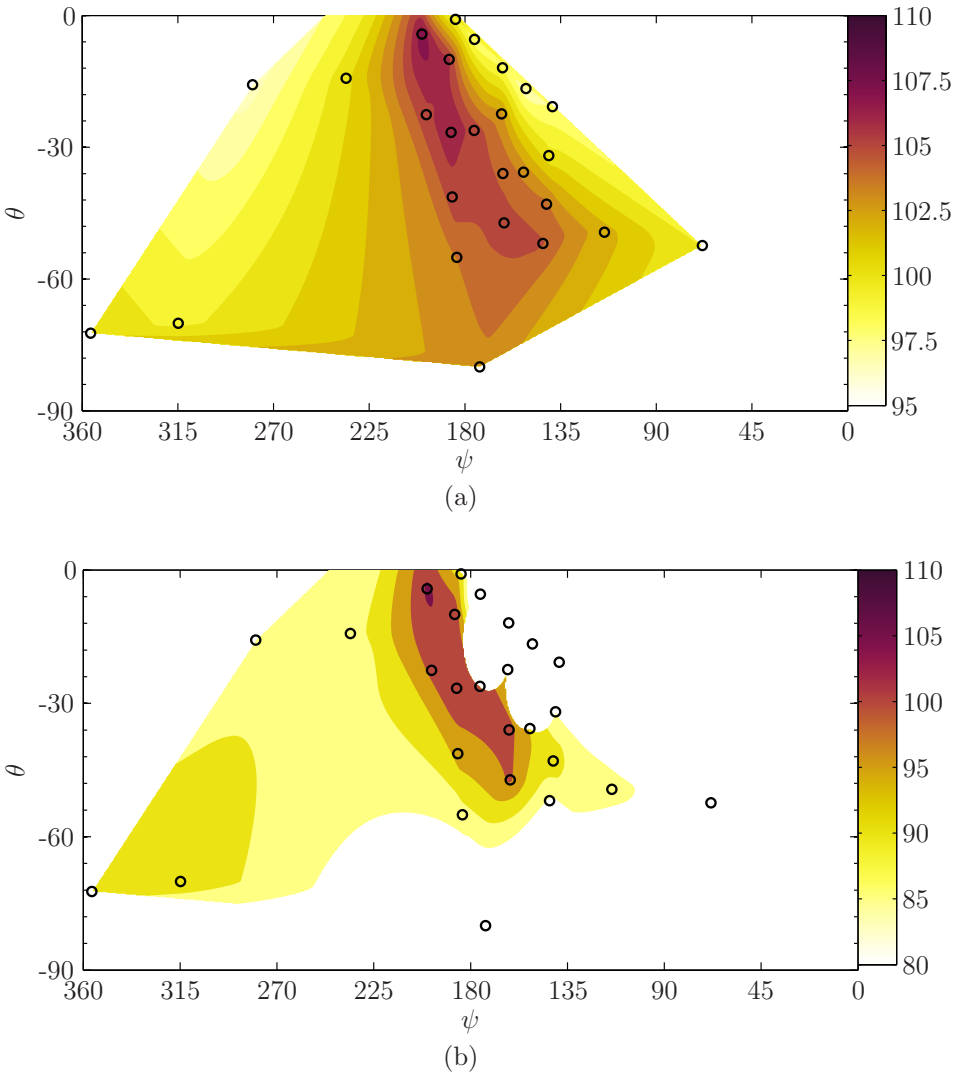

Figure 6.21: Contour plots of the (a) overall and (b) blade-vortex interaction extracted sound pressure levels extracted 3.0 seconds into the fast advancing side roll maneuver.

of thrust has increased 7% over the original thrust at 0.5 seconds, seen in table 6.3. This is consistent with the findings of Schmitz *et al.* (2007) [86], who showed that tail rotor noise would be a major contributor to the increase in overall sound pressure level for steady turning flight.

The overall sound pressure levels seen in figure 6.21 are slightly decreased from what was seen at the 2.5 second mark. This decrease in overall sound pressure level is partially due to the decreasing roll rate of the maneuver, as given in table

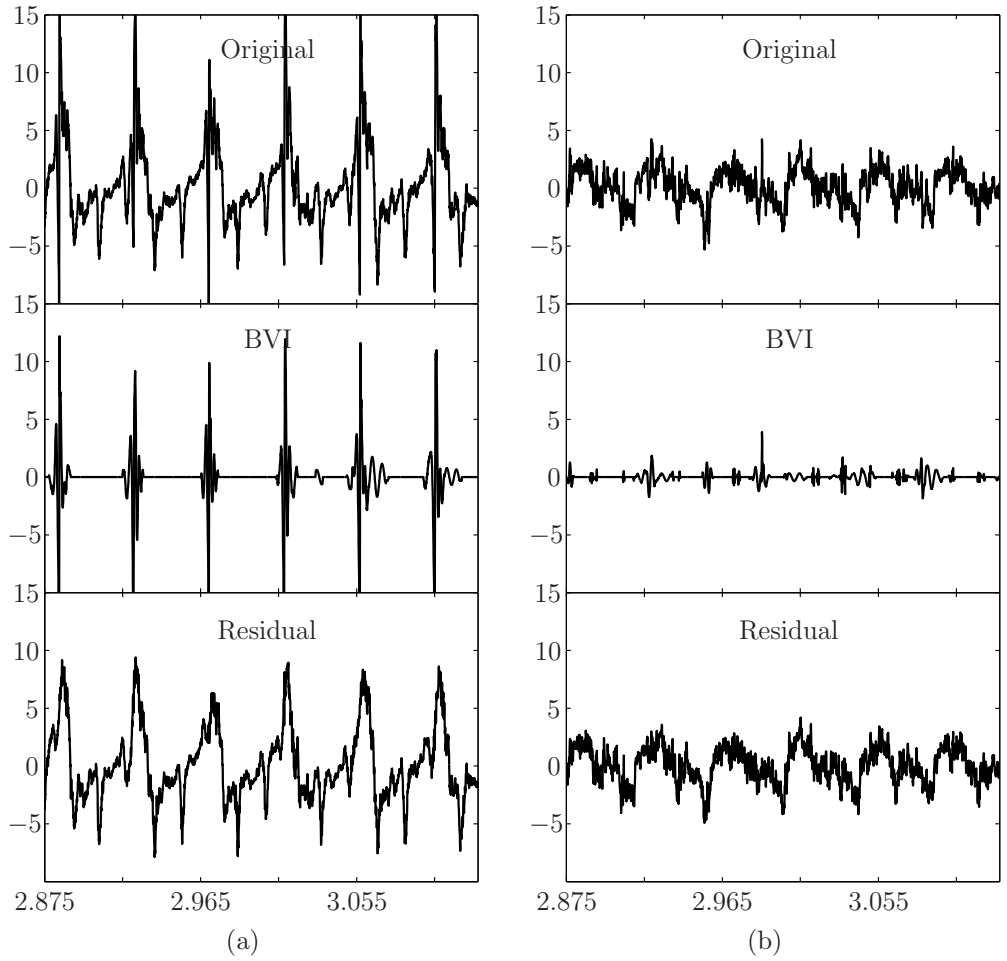

Figure 6.22: Pressure signatures extracted three seconds into the fast advancing side roll maneuver. Signatures are extracted from (b) peak blade-vortex interaction microphone located at ($\psi = 200°, \theta = -4°$) and (b) retreating directivity microphone located at ($356°, -72°$).

6.7. Having reached the maximum roll rate, the vehicle is approaching its desired

λ	$1.37\ 10^{-2}$	
C_T	$5.02\ 10^{-3}$	
μ_x	0.172	
$\dot{\phi}$	13	[°/s]

Table 6.7: Calculated aerodynamic properties from 3.0 seconds into the fast advancing side roll maneuver.

roll attitude. The inflow and thrust coefficient, however, are still increasing as the

centripetal forces on the vehicle are increasing.

The decreasing roll rate results in a slightly larger miss distance than what was experienced at the 2.5 second mark, although this is not reflected in the Beddoes' wake model in figure 6.23. The Beddoes' wake model does show a decreasing

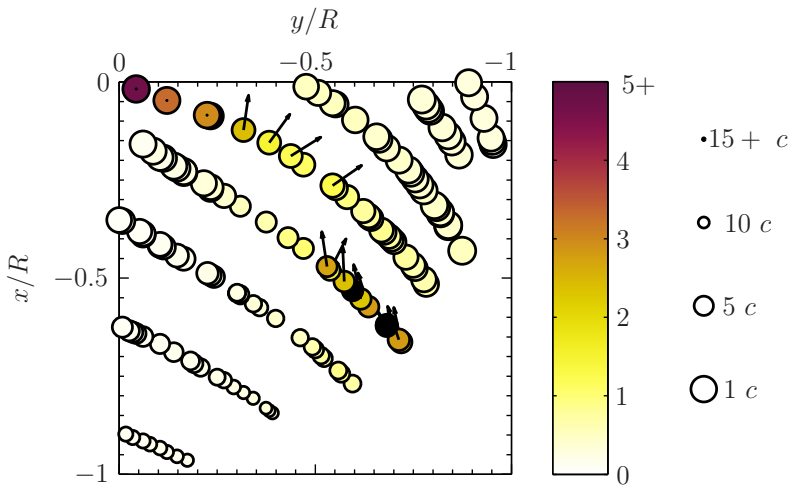

Figure 6.23: Blade-vortex interactions for the fast advancing side roll maneuver extracted at 3.0 seconds. Color scale indicates trace Mach number, while marker size indicates vortex miss distance in chord length (c). Vectors point in the direction of noise propagation determined by the Mach angle and vortex interaction angle.

trace Mach number, due to the decreasing forward advance ratio. However, the blade-vortex interaction sound pressure level has not altered dramatically, and so neither the change in roll rate or trace Mach number has resulted in significant acoustic implications. Instead, the decrease in the overall sound pressure level, without a subsequent decrease in the blade-vortex interaction sound pressure level, suggests that another mechanism is responsible for the changes. It is postulated that the change in overall sound pressure level is a result of changes in the loading noise mechanism as the vehicle roll rate is decreasing but centripetal forces are increasing the required vehicle thrust.

Skipping ahead to the 4.0 second mark, the sound pressure level contours in figure 6.24 are very close to those seen at the 3.0 second mark. The only significant difference is the lessening of the overall main rotor harmonic. The blade-vortex

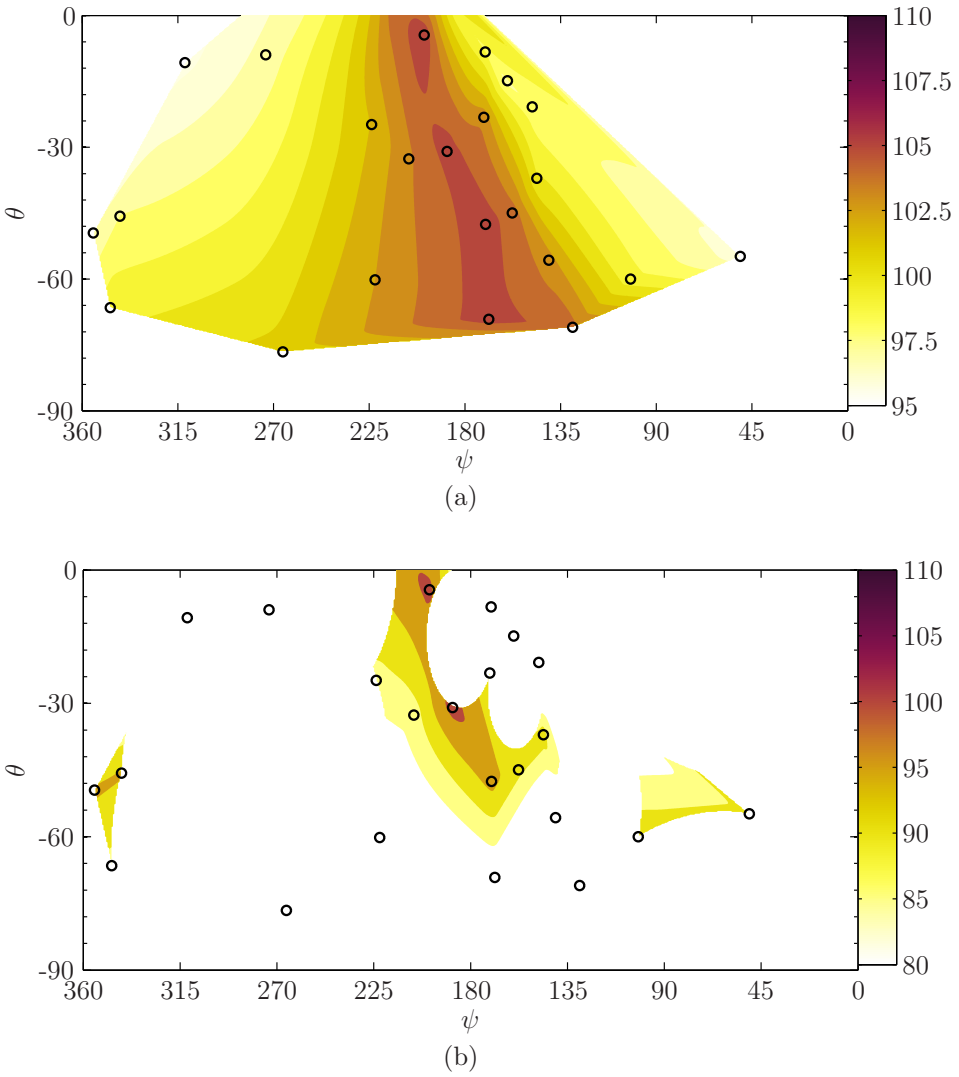

Figure 6.24: Contour plots of the (a) overall and (b) blade-vortex interaction extracted sound pressure levels extracted 4.0 seconds into the fast advancing side roll maneuver.

interaction sound pressure level is still strongly present, with the same core directivity as seen before. While the directivity pattern appears somewhat different than what was seen in figure 6.21, this is primarily caused by the interpolation scheme used and not due to a change in physics. The microphones located in the peak direction register very similar magnitudes; the differing contour grids are due to the change in relative microphone positions.

The aerodynamic parameters, provided in table 6.8, show that at the four

λ	$1.24\ 10^{-2}$	
C_T	$5.38\ 10^{-3}$	
μ_x	0.171	
$\dot{\phi}$	4	[°/s]

Table 6.8: Calculated aerodynamic properties from 4.0 seconds into the fast advancing side roll maneuver.

second mark, the vehicle roll rate has decreased significantly to only 4 [°/s]. The thrust has increased by 7% compared to the previous time step, while the inflow has reduced by almost 10%. The resulting Beddoes' wake model is shown in figure 6.25, where the primary vortex interaction has seen an increase in the trace Mach

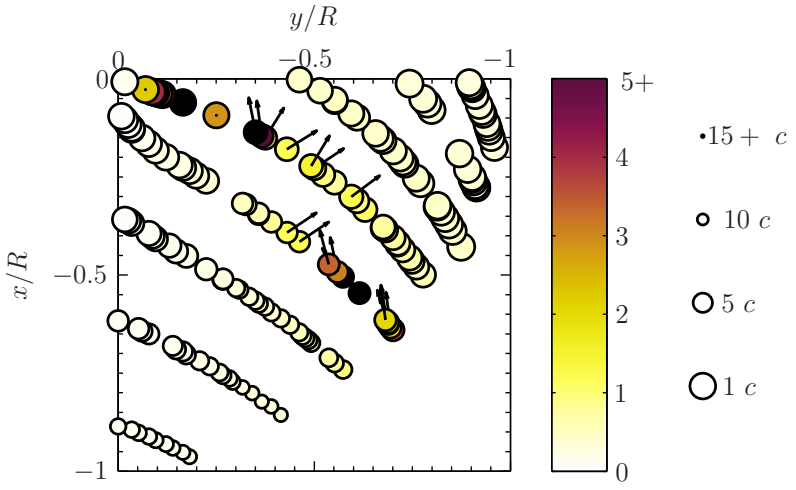

Figure 6.25: Blade-vortex interactions for the fast advancing side roll maneuver extracted at 4.0 seconds. Color scale indicates trace Mach number, while marker size indicates vortex miss distance in chord length (c). Vectors point in the direction of noise propagation determined by the Mach angle and vortex interaction angle.

number, and the secondary interaction has moved in-board slightly. Overall, the directivities determined through the Beddoes' wake model are identical to what was seen previously at the three second mark, and this is consistent with the blade-vortex interaction sound pressure level plots. The predicted miss distances have also not changed substantially, despite the change in every aerodynamic parameter. The decrease in advance ratio should have resulted in larger miss

distances, but with decreasing inflow ratio these two parameters canceled each other out in the prescribed wake method resulting in similar miss distances.

Seemingly anomalous blade-vortex interaction sound pressures are measured on the rear, advancing side of the rotor. The sound pressure levels measured in this area are quite small with a magnitude approximately 6 dB less than that seen in the peak direction. The low blade-vortex interaction level compared to the peak direction suggests that blade-vortex interactions are not present in the signal or are very weak. The pressure signatures shown in figure 6.26 confirms

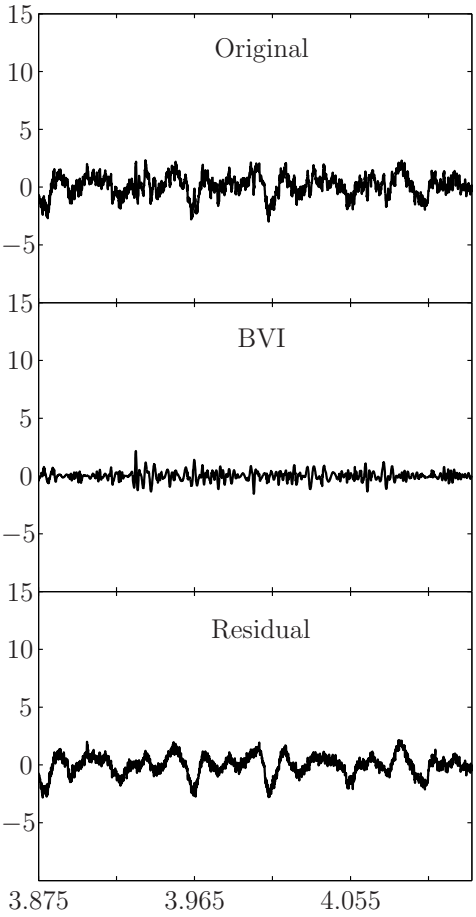

Figure 6.26: Pressure signature extracted from four seconds into the fast advancing side roll maneuver. The microphone is located at an elevation of $-55°$ below the rotor and to the right rear of the vehicle at $\psi = 50°$.

that blade-vortex interactions are not present. Instead, the filtering method has extracted higher frequency noise due to the low main rotor harmonic energy con-

tent.

It is apparent that the primary weakness in the employed filtering technique comes from the amplitude cutoff criteria. The higher harmonics of the tail rotor extend into the frequency range of interest for blade-vortex interactions, and so a single frequency cutoff will always intrude on the tail rotor signature. However, the amplitude cutoff fails whenever there are very strong higher tail rotor harmonics, or when the main rotor harmonic energy drops to lower levels. Fortunately, the instances when the extracted signal does not contain blade-vortex interactions are easily determined, as the sound pressure level in those areas are 25 percent or less of the energy in the peak amplitude direction. Even though the filtering method does not extract a clean signal in these situations, it is immediately evident through the sound pressure levels that blade-vortex interactions are not occurring.

6.3 Medium Advancing Side Roll Analysis

The medium advancing side roll maneuver is investigated in a similar manner as the fast advancing side roll maneuver. It will be shown that the sound pressure level contours are very similar for conditions where the roll rate of the vehicle are similar. Beginning half a second into the maneuver, when the vehicle is still in steady level flight, allows us to make a direct comparison to the previous two maneuvers.

The sound pressure levels, shown in figure 6.27, are close to the levels seen in the steady level flight (figure 6.2) and fast advancing side roll (figure 6.10) maneuvers. This was expected as the vehicle is still in steady level flight, and the aerodynamic parameters, provided in table 6.9, are very close to those seen previously.

The blade-vortex interaction level for the medium advancing side roll is slightly less than previously seen. This decrease in sound pressure level is adequately predicted by the Beddoes' wake model shown in figure 6.28. According to the Beddoes' wake model, the current vortex miss distance is slightly larger than was seen for the steady level flight maneuver, but on the same order as the fast

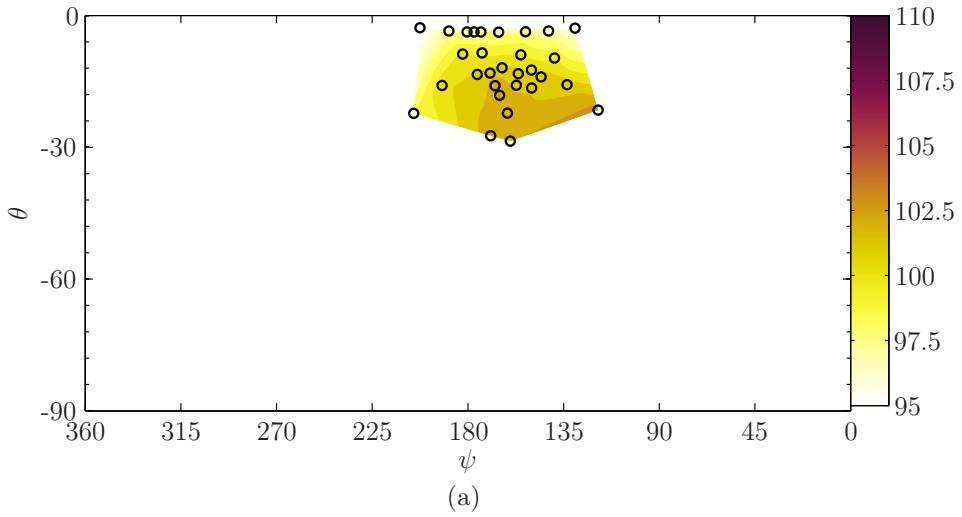

(a)

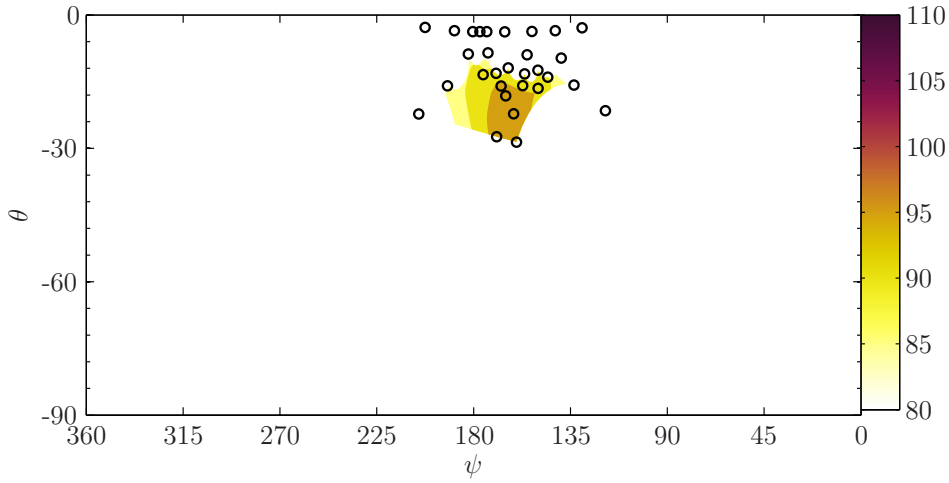

(b)

Figure 6.27: Contour plots of the (a) overall and (b) blade-vortex interaction extracted sound pressure levels extracted 0.5 seconds into the medium advancing side roll maneuver.

λ	$1.21\ 10^{-2}$	
C_T	$4.61\ 10^{-3}$	
μ_x	0.181	
$\dot{\phi}$	0	[°/s]

Table 6.9: Calculated aerodynamic properties from 0.5 seconds into the medium advancing side roll maneuver.

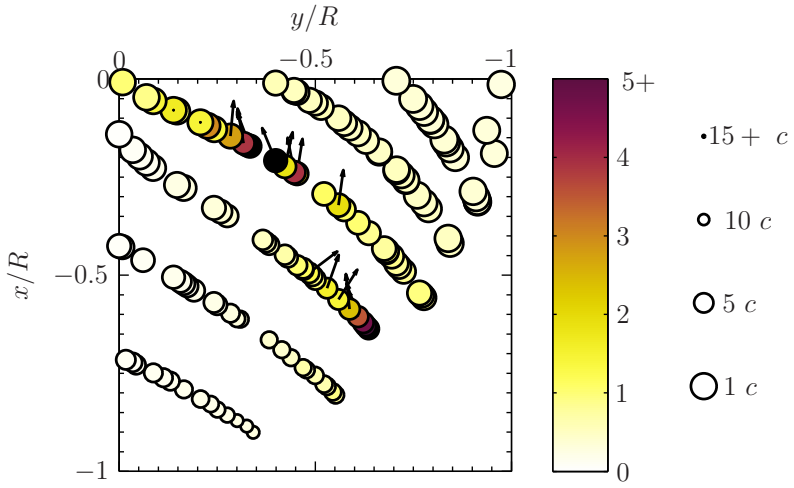

Figure 6.28: Blade-vortex interactions for the medium advancing side roll maneuver extracted at 0.5 seconds. Color scale indicates trace Mach number, while marker size indicates vortex miss distance in chord length (c). Vectors point in the direction of noise propagation determined by the Mach angle and vortex interaction angle.

advancing side roll maneuver. However, the trace Mach numbers are significantly lower for this maneuver, than was seen for either of the two previous maneuvers. This lower trace Mach number suggests that the acoustic wave fronts from the interaction are not coalescing as well, and so result in a lower blade-vortex interaction noise signature [111].

Advancing into the maneuver, the vehicle roll rate at the two second mark, provided in table 6.10, is very close to those seen at 1.5 seconds into the fast roll

λ	$1.18\ 10^{-2}$	
C_T	$4.57\ 10^{-3}$	
μ_x	0.181	
$\dot{\phi}$	10	[°/s]

Table 6.10: Calculated aerodynamic properties from 2.0 seconds into the medium advancing side roll maneuver.

maneuver. The resulting vortex interactions are shown in figure 6.29. Comparing figure 6.29 with figure 6.15, the Beddoes' wake model suggests that the trace Mach number is greater for the primary blade-vortex interaction on the medium speed

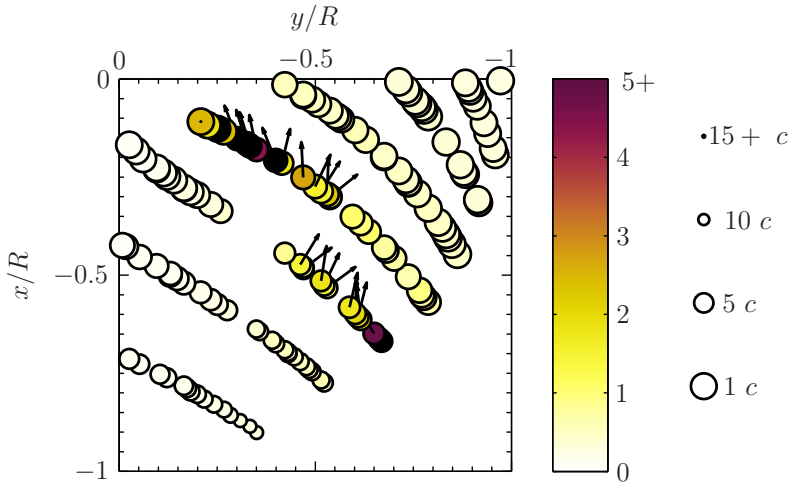

Figure 6.29: Blade-vortex interactions for the medium advancing side roll maneuver extracted at 2.0 seconds. Color scale indicates trace Mach number, while marker size indicates vortex miss distance in chord length (c). Vectors point in the direction of noise propagation determined by the Mach angle and vortex interaction angle.

roll maneuver. The vortex miss distance is also less for this maneuver, compared to the fast advancing side roll maneuver. Both of these suggests that the blade-vortex interaction sound pressure levels should be increased for the medium advancing side roll maneuver.

The sound pressure levels at 2.0 seconds into the medium advancing side roll maneuver are provided in figure 6.30. Comparing to figure 6.13, the blade-vortex interactions are slightly less severe in this maneuver then was seen in the fast roll maneuver. This confirms that the Beddoes' prescribed wake method is inadequate for predicting the severity of the blade-vortex interaction signal, as both metrics associated with its strength were incorrect for this time point in the maneuver. This is in further agreement with the finding of Hennes *et al.* (2004) [59] who found prescribed wake models to be insufficient for predicting blade-vortex interaction noise during transient maneuvers. However, the directivities associated with blade-vortex interactions and identified through the Beddoes' prescribed wake method are quite similar, as seen in both the sound pressure level contour maps and blade-vortex interaction plots. Therefore, this method is adequate for determining the appropriate placement of microphones for capturing blade-vortex

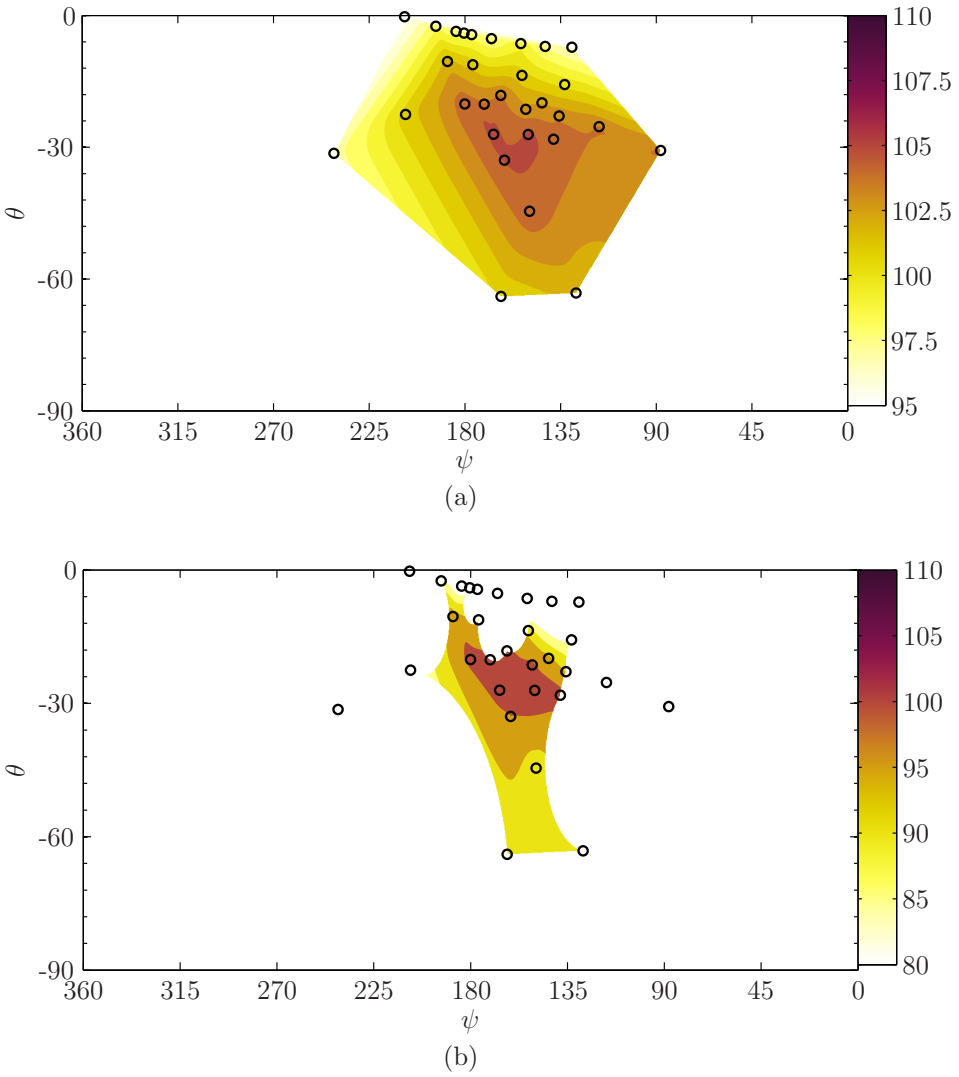

Figure 6.30: Contour plots of the (a) overall and (b) blade-vortex interaction extracted sound pressure levels extracted 2.0 seconds into the medium advancing side roll maneuver.

interactions during transient roll flight tests.

The roll rate 2.5 seconds into the medium advancing side maneuver, provided in table 6.11, is very close to the rate of 13 [°/s] seen at two seconds into the fast advancing side roll maneuver. At this point, the load factor between both roll maneuvers, as provided in figure 3.9, is just beginning to diverge. This will be seen in the changing thrust coefficient and should ultimately manifest itself in the overall sound pressure level as it will increase the loading noise on the main

λ	$1.22\ 10^{-2}$	
C_T	$4.66\ 10^{-3}$	
μ_x	0.182	
$\dot{\phi}$	15	[°/s]

Table 6.11: Calculated aerodynamic properties from 2.5 seconds into the medium advancing side roll maneuver.

rotor [14].

Figure 6.31 provides the sound pressure level contours for this instance in time. Comparing to figure 6.16, the sound pressure levels and directivities are almost identical. This strongly suggests that the roll rate of the vehicle is a principle factor in the maneuvering noise. The sound pressure level contours of figures 6.31 and 6.30 compare very favorably for similar roll rates during the fast advancing side roll maneuver. Once other factors have been accounted for, like changing directivity and distance to microphones, the sound pressure levels agree quite well.

An extraction of the microphone signature located at the peak blade-vortex interaction direction of (180°, −23°), is provided in figure 6.32. Very strong blade-vortex interactions are seen to occur at this time. Also, the tail rotor signature is quite strong with significant energy in the higher harmonics. This results in a larger portion of the tail rotor signature being extracted. The peak to peak extracted tail rotor pressure signature, however, is approximately one third or less the strength of the extracted blade-vortex interaction peak to peak pressures. Suggesting that while the some tail rotor thickness noise has been extracted, it comprises a small portion of the blade-vortex interaction sound pressure level [34].

The peak roll rate for the medium advancing side roll maneuver occurs three seconds into the maneuver. The aerodynamic parameters from this time are provided in table 6.12, where it can be seen that the peak roll rate is comparable to the peak roll rate of the fast advancing side roll maneuver. The fast roll maneuver peaked at a rate of 17 [°/s], 2.5 seconds into the fast roll maneuver. The thrust coefficients, provided in tables 6.7 and 6.12, are also very comparable.

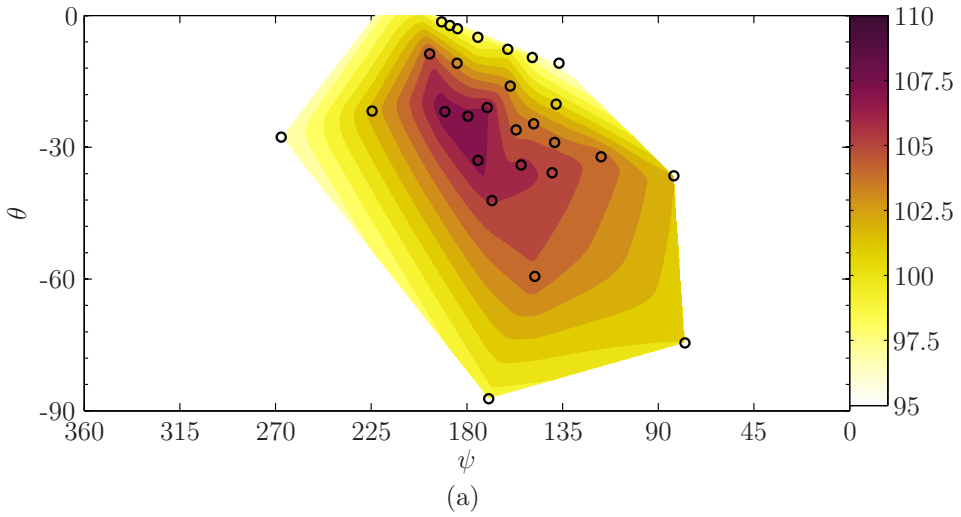

(a)

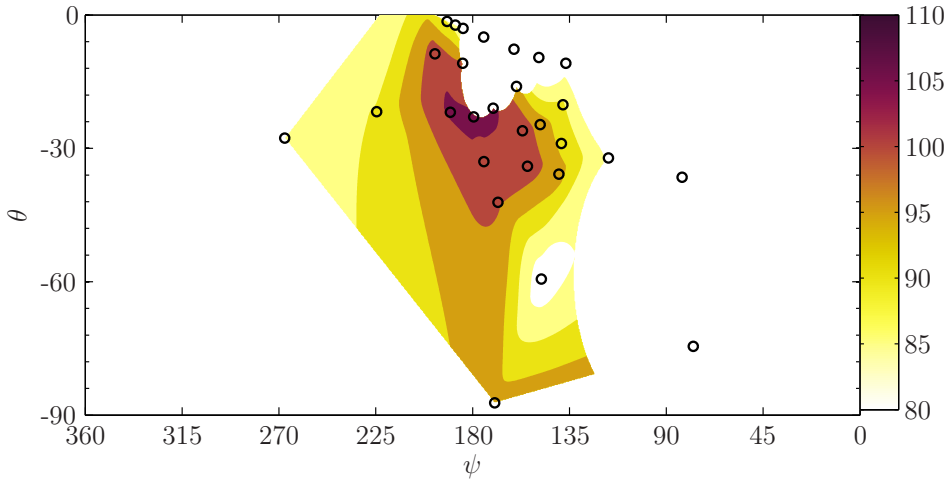

(b)

Figure 6.31: Contour plots of the (a) overall and (b) blade-vortex interaction extracted sound pressure levels extracted 2.5 seconds into the medium advancing side roll maneuver.

λ	$1.24\ 10^{-2}$	
C_T	$4.84\ 10^{-3}$	
μ_x	0.181	
$\dot{\phi}$	17	[°/s]

Table 6.12: Calculated aerodynamic properties from 3.0 seconds into the medium advancing side roll maneuver.

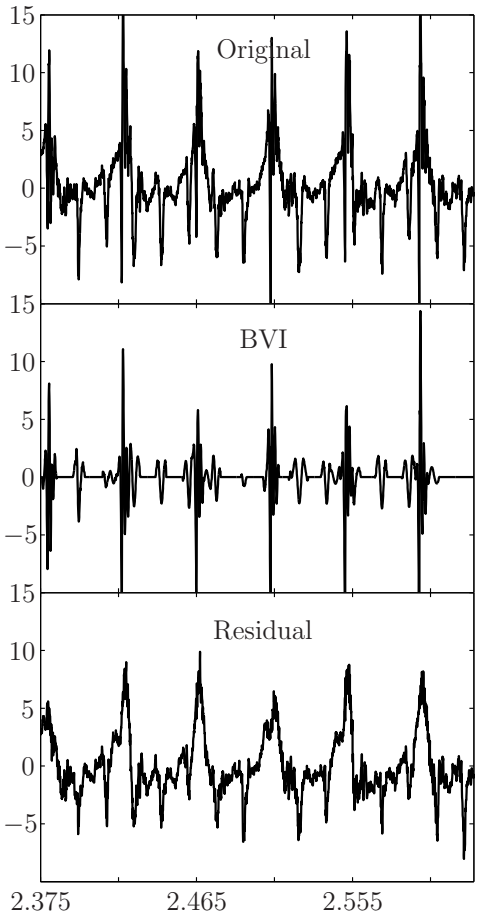

Figure 6.32: Pressure signature extracted from 2.5 seconds into the medium advancing side roll maneuver. The microphone is located at an elevation of $-23°$ below the rotor and to the right rear of the vehicle at $\psi = 180°$.

The Beddoes' wake blade-vortex interaction predictions are provided in figure 6.33. The directivities and miss distances for both maneuvers are consistent according to the Beddoes' wake model. Thus, the blade-vortex interaction signals should be of comparable levels and in similar directions for these times. The medium advancing side roll maneuver may possess higher blade-vortex interaction levels, however, due to the increased trace Mach number for the in-board portion of the primary blade-vortex interaction.

The sound pressure level contours for the three second mark of the medium advancing side roll maneuver are found in figure 6.34. When comparing with figure 6.18, the overall sound pressure levels are very similar. This was not entirely

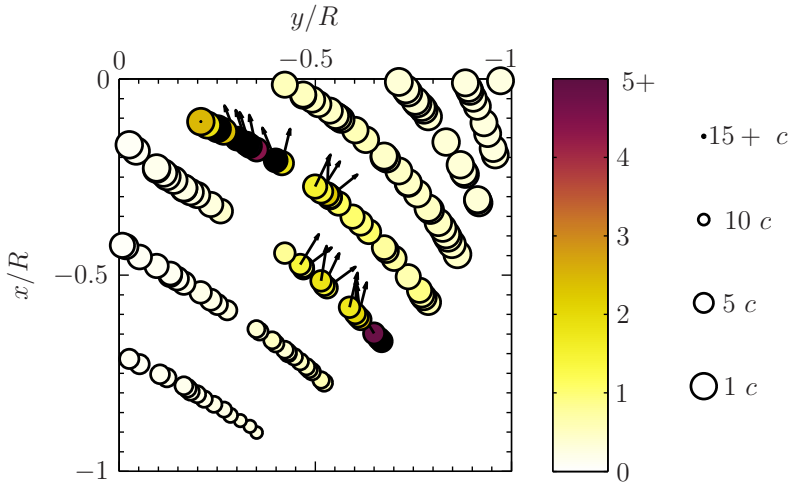

Figure 6.33: Blade-vortex interactions for the medium advancing side roll maneuver extracted at 3.0 seconds. Color scale indicates trace Mach number, while marker size indicates vortex miss distance in chord length (c). Vectors point in the direction of noise propagation determined by the Mach angle and vortex interaction angle.

unexpected, as the roll rates are identical and the thrust coefficients are very close together as well. The blade-vortex interaction sound pressure levels are also similar, although the medium advancing side roll maneuver shows a stronger peak amplitude in the same direction as seen before. This is likely due to the increased trace Mach number as noted in discussion of figure 6.33. Overall, however, we see very close agreement between the sound pressure levels for similar vehicle roll rates. The strong agreement that has been seen to this point suggests that it is not the attitude of the vehicle that affects transient roll maneuvering noise, but the rate at which the vehicle is rolling, in agreement with Chen *et al.* (2006) [27].

Continuing in the maneuver to the four second mark, the roll rate has begun to decrease, although at a slower rate than the fast advancing side roll maneuver. The aerodynamic parameters for this point in time are provided in table 6.13, where the roll rate is more similar to the two second mark in the fast advancing side roll maneuver, or 2.5 second mark for the medium roll maneuver. Figure 6.35 provides the sound pressure levels associated with this point in time.

Direct comparison cannot be made between the four second mark of the

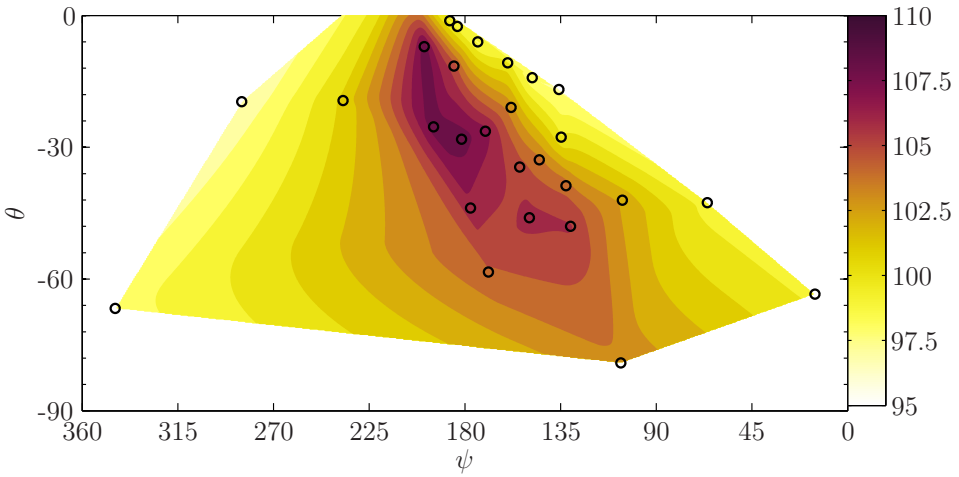

(a)

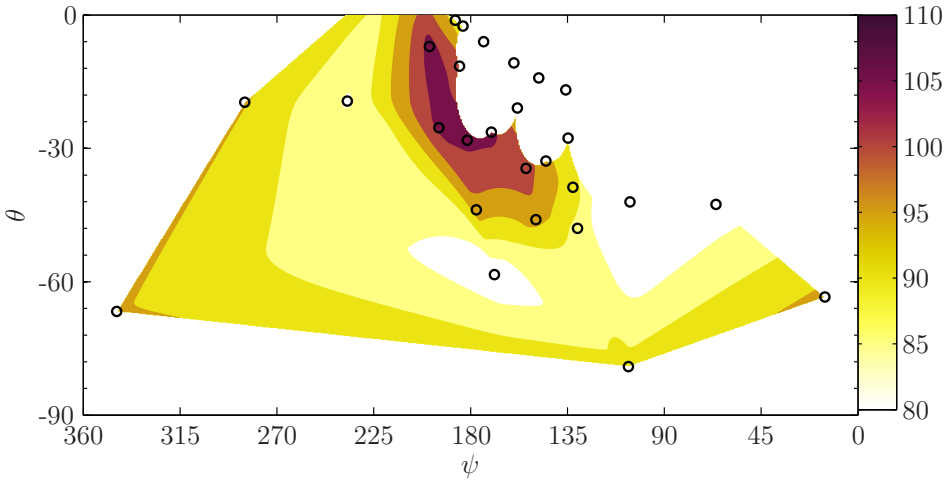

(b)

Figure 6.34: Contour plots of the (a) overall and (b) blade-vortex interaction extracted sound pressure levels extracted 3.0 seconds into the medium advancing side roll maneuver.

λ	$1.11\ 10^{-2}$	
C_T	$5.35\ 10^{-3}$	
μ_x	0.180	
$\dot{\phi}$	13	[°/s]

Table 6.13: Calculated aerodynamic properties from 4.0 seconds into the medium advancing side roll maneuver.

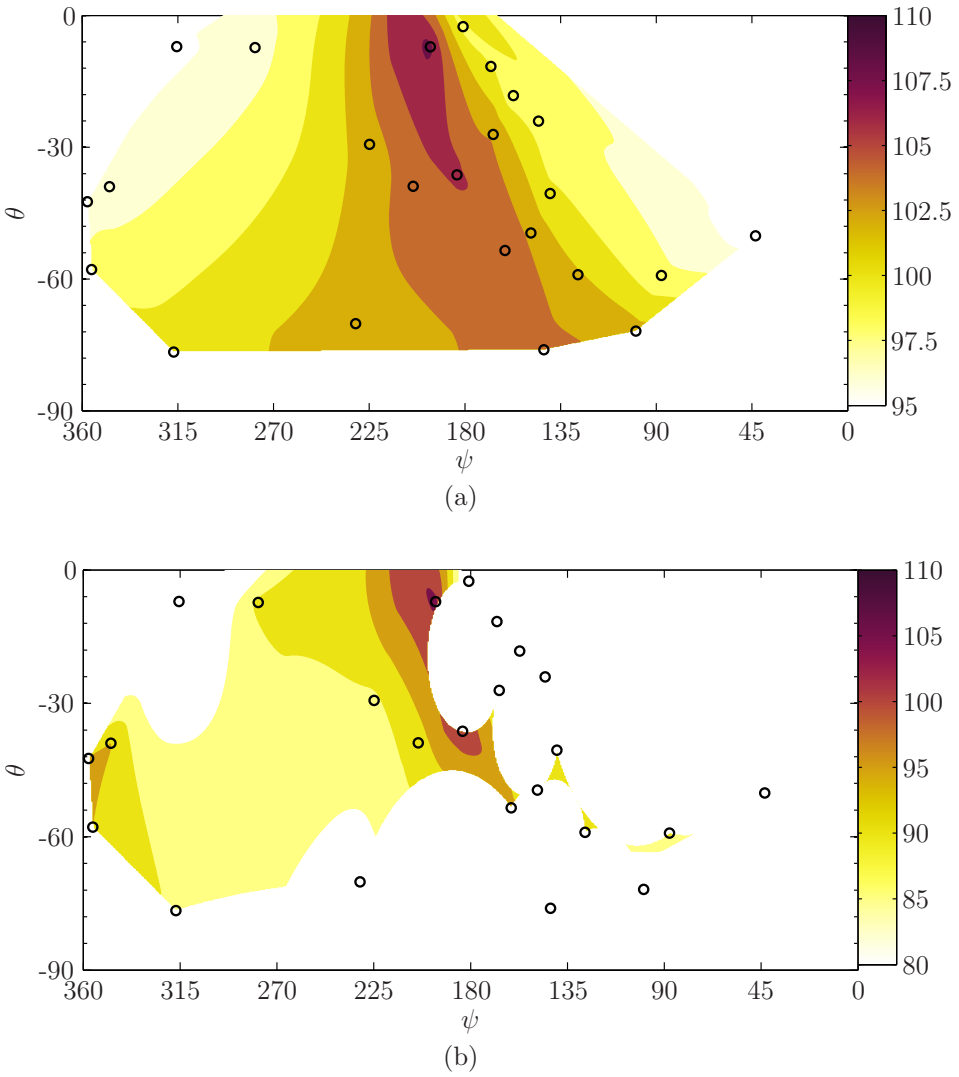

Figure 6.35: Contour plots of the (a) overall and (b) blade-vortex interaction extracted sound pressure levels extracted 4.0 seconds into the medium advancing side roll maneuver.

medium advancing side roll maneuver, and the 2.0 second mark of the fast advancing side roll maneuver shown in figure 6.18. This is due to the changing microphone directivities which resulted in significantly different contour interpolations. The same can be said for comparison to the 2.5 second mark of the medium advancing side roll rate, shown in figure 6.30. However, consistent with the rest of the findings, the peak blade-vortex interaction sound pressure level occurs slightly right of center on the vehicle, and at an elevation approximately 20°

below the tip-path plane. The peak interaction levels are similar to what was seen before, although there is no microphone directly located in the peak direction.

There are some blade-vortex interaction sound pressure levels measured on the rear of the vehicle. Pressure signatures extracted from (358°,−42°) are shown in figure 6.36. As was seen with the previous rearward microphone, in

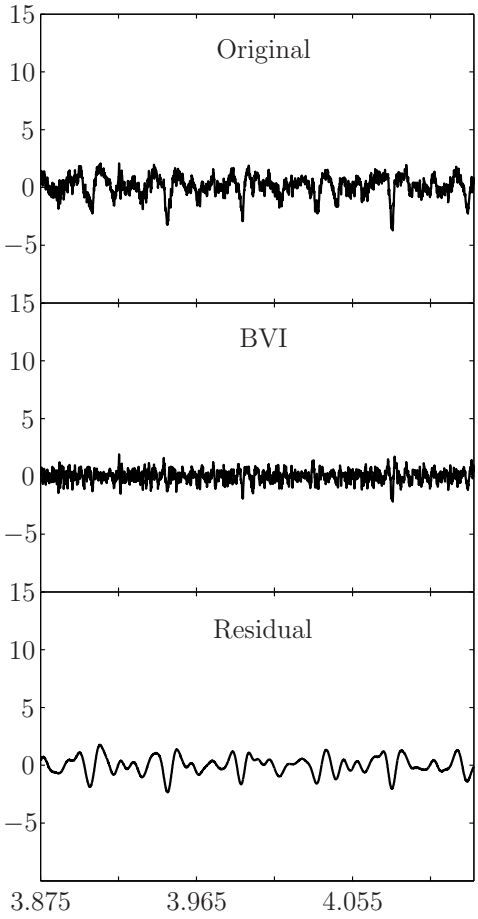

Figure 6.36: Pressure signature extracted from 4.0 seconds into the medium advancing side roll maneuver. The microphone is located at an elevation of −42° below the rotor and to the rear of the vehicle at $\psi = 358°$.

figure 6.26, only high frequency noise was extracted. The extraction of unrelated high frequency noise was again due to the amplitude cutoff coupled with a low main rotor harmonic energy.

Four primary conclusions can be made from the blade-vortex interaction extraction results provided in this section, and are itemized as follows,

- The wavelet transform based blade-vortex interaction extraction method provides the means for extracting the blade-vortex interaction signals during transient and steady state maneuvers. The filtering method works quite well in cases where the main rotor harmonic energy is strong. As seen in figures 4.8b and 6.22a, the presence of blade-vortex interactions occurs simultaneously with a strong main rotor harmonic energy. However, the reverse is not true, as demonstrated by figure 6.9, where energy associated with the main rotor signature is clearly very strong but no significant blade-vortex interactions are present.

- A need for a more complicated filtering method has been identified to prevent the extraction of high frequency noise. The current implementation of the filtering method removes relatively high amplitude, high frequency noise from the signal when the main rotor harmonic energy is weak. A method that employs a second amplitude criteria, such as a lower limit on the main rotor harmonic energy, is suggested.

- The Beddoes' prescribed wake model is insufficient for characterizing the vortex miss distance during transient roll maneuvers, in agreement with Hennes *et al.* (2004) [59]. However, the method did provide consistent results for the directivity associated with blade-vortex interactions, and this directivity did coincide with the peak in blade-vortex interaction noise. Thus, while the prescribed wake method is insufficient for the modeling of blade-vortex interaction noise, it is sufficient for determining the placement of microphones to adequately capture blade-vortex interactions during transient roll maneuver investigations.

- The sound radiated from a transient roll towards the advancing side of the vehicle results in blade-vortex interactions that peak forward and slightly to the left of the vehicle. This is in agreement with limited findings from a previous flight test by Speigel *et al.* (2005) [99]. Further, the overall sound pressure levels were seen to compare quite favorably for similar vehicle roll rates. Thus suggesting that the roll rate of the vehicle, and not roll attitude,

is a primary factor in determining the noise associated with a transient roll maneuver. Decreasing the roll rate magnitude of a maneuver, where possible, can decrease the associated vehicle sound footprint.

Chapter 7

Conclusions and Future Work

The summary of the work accomplished herein can be briefly itemized as follows,

- A blade-vortex interaction extraction technique was developed and implemented successfully using time-frequency analysis.
- An in-depth investigation of experimentally acquired acoustic data from transient advancing side roll maneuvers was conducted.
- It was experimentally shown that transient advancing side blade-vortex interaction noise is directly linked to the roll rate of the vehicle.
- Time-frequency analysis techniques were shown to be a powerful tool in analyzing the acoustic signature emitted by a helicopter during transient and steady state maneuvers.

A more complete discussion of the full results is broken into two separate parts, with suggestions for future work spread throughout. A review of the need and applicability of time-frequency analysis is provided in § 7.1. Meanwhile, § 7.2 includes a review on the development and application of the blade-vortex extraction method.

7.1 Time-Frequency Analysis

An experimental investigation of the acoustic signal emitted during advancing side transient roll maneuvers of a Bell model 430 helicopter was conducted. Overall, 410 vehicle flyovers were performed covering various steady and transient

maneuvers, with up to 31 microphones being deployed during any given flight. The current analysis focused on a steady level flight alongside both a fast, and medium advancing side roll maneuver. 21 microphones were investigated in an attempt to flush out the relevant physics that affected the noise characteristics throughout the transient roll maneuvers. This analysis constitutes the one of the first in-depth experimental investigations into the acoustic effects of transient advancing side roll maneuvers.

In order to investigate the transient maneuvering noise signals, a mathematically appropriate, time-frequency analysis method had to be identified and implemented. Wavelet transforms and the more commonly used short-time Fourier transform are two of several mathematically appropriate methods available. The wavelet transform was first compared with short-time Fourier transform for several window different sizes. Differing window sizes were employed to investigate the dependence of each analysis technique on the size of the interrogation window. The wavelet transform was shown to provide consistent spectral amplitudes, independent of the interrogation window size. However, the short-time Fourier transform was shown to provide spectra that was highly dependent on the size of the window investigated. Spectral magnitudes provided by the short-time Fourier transform were shown to fluctuate by up to 10 dB in the lower harmonics, and 20 dB for higher frequencies, depending on the window size. Contrary to this, the wavelet transform varied by only 3 dB over the window ranges investigated; and that fluctuation was linked to averaging the instantaneous spectra over larger window sizes.

The wavelet transform was then applied to a single microphone to investigate how the recorded acoustic pressure signal changed throughout each maneuver. Spectral representations of various noise sources were first identified. It was shown that the blade-vortex interaction signal resulted in a strong, high amplitude presence in the higher frequency portion of the spectra. This agreed well with the literature, which showed analytically that blade-vortex interaction noise is predominant in higher frequencies [77, 111]. A fairly strong signature was also seen

in the mid-frequency range, which was related directly to the tail rotor thickness noise.

An investigation of a single microphone in steady level flight revealed that transient acoustic phenomena is prevalent even in such a benign flight maneuver. The transient acoustics experienced by the stationary microphone were related to the changing directivity of the vehicle, relative to the microphone. It was noted that as the vehicle flew over the stationary microphone, the predominant noise mechanism evolved from thickness noise to loading noise. A decrease in the lower harmonic energy was seen coincident with the change in noise source, due to change in microphone directivity. After the vehicle passed by the microphone, thickness noise became dominant again, and the lower harmonic energy levels recovered to their previous values.

Two interesting features were noted in the steady level flight maneuver. The first, was that blade-vortex interactions could be seen in the data during the majority of the vehicle's approach. This showed that blade-vortex interactions existed forward of the vehicle to an elevation of almost $-45°$. While this is not exactly unexpected, it was originally anticipated that blade-vortex interactions would not be seen in the steady level flight maneuver. More important, though, was the alternating strengths of the blade-vortex interactions. Each blade-vortex interaction was paired, where one strong interaction was followed by a weaker version. This alternating in strengths was linked to the split tip-path plane of the vehicle main rotor, where one set of opposing blades sits at a higher altitude than the other pair. This modifies the miss distance of the blade-vortex interaction, resulting in interactions with a slightly smaller miss distance, followed by a greater miss distance.

The same microphone was then investigated for the two advancing side roll maneuvers. As the vehicle entered into the roll maneuvers, the signatures associated with blade-vortex interactions began to increase. This was subsequently followed by an increase in the main rotor harmonic energy. It was seen that the blade-vortex interaction energy peaked prior to the main rotor harmonic energy,

and peaked almost simultaneously with the roll rate. This pattern was consistent for both the medium and fast roll rate maneuvers. However, it was impossible to determine if the increase in noise was directly linked to the roll rate of the vehicle, or if it was due to the changing directivity of the microphone.

One particular detail of note was the spectral differences seen between the advancing side blade-vortex interactions, and the retreating side interaction. It was shown that the retreating side blade-vortex interactions occurred at lower frequencies than its advancing side counterpart. The amplitude of the interactions were also quite less, for the retreating side case. However, the differences between the two interactions were expected, as the aerodynamic characteristics surrounding each interaction, including interaction duration and trace Mach number, are different [58, 111].

7.2 Blade-Vortex Interaction Extraction Method

A method for the identification and extraction of blade-vortex interactions was then developed. The express purpose for such a method is the isolation and investigation of blade-vortex interactions independent of other acoustic phenomena. This allows for the determination of important aerodynamic parameters and their direct impact on the resulting blade-vortex interaction acoustic signal. Two other extraction techniques have been developed, and were discussed. One technique was seen to be inadequate, as a method for identifying blade-vortex interactions was not provided [93]. The second extraction technique was discussed and shown to be effectively a band-pass filter using discrete wavelet transforms [34].

The method developed here identifies and isolates high frequency, high amplitude pressure signatures based on physically relevant tuning parameters. The filter method was based on previous analytical research that showed blade-vortex interactions exist predominantly in the higher frequency range [77, 111]. This was further confirmed in the previous section, where it was also shown that blade-vortex interactions were quite powerful, relative to the overall pressure signal, when they were present. This method marks a significant improvement over the

Davis *et al.* technique, as it advances that technique into the realm of continuous wavelet transforms [34]. The developed technique also provides a way of removing only the content from blade-vortex interactions and not all content from a single frequency band.

The blade-vortex interaction extraction method was then implemented on a synthetic pressure signal comprised solely of 'typical' blade-vortex interactions. It was shown that the extraction method could adequately recreate the pressure signature of a blade-vortex interaction from only its high frequency, high amplitude wavelet coefficients. It was also discussed that this method marks an improvement for the calculation of blade-vortex interaction sound pressure levels over the traditional method of integrating over an arbitrary frequency range. Sound pressure levels can now be calculated based solely on the blade-vortex interaction pressure signature, and not an integrated average over the expected frequency range for such interactions.

A sensitivity analysis was then conducted to determine the proper tuning parameters for the extraction method. Two metrics, namely the sound pressure level of the blade-vortex interaction extracted signal, and the sound pressure level of the residual signal, were employed in the sensitivity analysis. It was shown that the sound pressure level related to blade-vortex interactions were sensitive to variations in both frequency cutoff and amplitude cutoff tuning parameters. The sound pressure level of the residual signal, however, proved to be insensitive to changes in tuning parameters outside of the low frequency, low amplitude region.

It was determined that a combination of both metrics was best in identifying the optimized tuning parameters. The insensitivity of the residual pressure signal provided a means for identifying the lower frequency cutoff tuning parameter. Below a given frequency, the lower main and tail rotor harmonic energies are extracted resulting in a sharp decrease in the residual sound pressure level. The sound pressure level of the extracted blade-vortex interaction signal, however, provided a better metric for determining the optimal amplitude cutoff. It was shown that as frequency was held constant, and amplitude cutoff was reduced,

then more and more of the noise unrelated to blade-vortex interactions were removed. Combining information from both metrics over all available microphones yielded the optimized frequency and amplitude cutoff parameters. The optimized parameters were determined to be frequencies above seven main rotor harmonics and amplitudes greater than 6 dB below the main rotor harmonic.

The extraction method using these two tuning parameters was then applied to all microphones throughout each of the three maneuvers investigated. Contour sound pressure levels from the overall sound pressure level and extracted blade-vortex interaction signal were investigated to determine the effects each maneuver had on noise directivity and amplitude. An aerodynamic analysis with accompanying prescribed wake model, based on Beddoes' method, was also used to help determine the cause of changes in the noise signature throughout each maneuver [6, 107].

The steady level flight analysis was used as a baseline for comparison. Blade-vortex interactions were seen forward of the vehicle and slightly to the advancing side, for the steady level flight maneuver. This directivity is fully consistent with previous research [82]. Further, the blade-vortex interaction directivity pattern was adequately predicted through Beddoes' prescribed wake model and the employed Mach-trace analysis technique [6, 111]. Two blade-vortex interactions were predicted for the steady level flight maneuver, with the primary blade-vortex interaction spanning the majority of the rotor blade and being comprised of high trace Mach numbers. The secondary interaction occurred over a shorter duration near the blade tip, and possessed lower trace Mach numbers than the primary interaction.

The blade-vortex interaction extraction method consistently identified, throughout the steady flight maneuver, the peak blade-vortex interaction direction to be forward of the vehicle at an elevation of approximately $-25°$. Pressure signatures from this direction showed the extracted signal was dominated by the removed blade-vortex interaction signature, but occasionally contained mild traces of the tail rotor noise.

The higher harmonics of the tail rotor occur at similar frequencies as the lower frequency portion of the blade-vortex interaction signal. Thus, a high frequency filter would either always remove a portion of the tail rotor signature, or would fail to remove the complete high amplitude, high frequency content of the blade-vortex interactions. On occasion, the tail rotor possesses high amplitude energy in the higher frequency portion of its signal, and it is on those occasions that portions of the tail rotor signature are also removed. With a higher amplitude cutoff, this would not occur. However, a higher amplitude cutoff would result in removing less of the blade-vortex interaction signal. The extraction of some tail rotor noise using this method is therefore inevitable. Although it is shown that the energy content the tail rotor contributes to the extracted signal is quite small, and does not contribute much to the sound pressure level of the extracted signal.

The advancing side roll maneuvers were also investigated using the blade-vortex interaction extraction method. It was shown that the overall sound pressure level increased by at least 7 dB in the peak direction, depending on the roll rate. This was comparable to the 10 dB increase in sound pressure level seen in computational work on a similar transient advancing side roll case [80].

Further, it was shown that the blade-vortex interaction peak direction shifts during transient advancing side roll maneuvers, to a direction slightly on the retreating side of the vehicle. This shift in direction is opposite of the originally anticipated direction, as steady advancing side turns see a peak noise direction on the advancing side of the vehicle. The directionality shift seen for the two maneuvers currently investigated was fully consistent with the limited findings of a similar experimental flight test which also included transient roll maneuvers [99].

One significant finding, was that the overall sound pressure level was positively linked to the roll rate of the vehicle. An investigation of the noise signatures at similar roll rates revealed that the sound pressure level amplitudes and directivities were highly similar. A future analysis of transient retreating side rolls was proposed, as Speigel *et al.* suggested that noise generated by retreating side

transient rolls were more dependent on vehicle roll rate than their advancing side counterparts [99].

An investigation into the Beddoes' prescribed wake model, and its ability to predict the location of blade-vortex interactions during transient maneuvers, was also undertaken. It was shown that the prescribed wake model was insufficient for accurately modeling miss distances of blade-vortex interactions during transient roll maneuvers, as the miss distances identified by the model was independent of roll rate. Previous research had shown that prescribed wake models were insufficient for the prediction of blade-vortex interactions, especially during transient maneuvering flight. However, the Beddoes' method did correctly identify the expected noise propagation path for blade-vortex interactions, and it was shown to shift in accordance with measured shifts in the blade-vortex interaction peak directivity. Thus, prescribed wake methods may be useful when planning the placement of microphones for transient maneuvering flight tests.

Most importantly, however, the blade-vortex interaction extraction method was shown to work exceptionally well. The method is easily implementable and has only two physically relevant parameters. The method correctly identified the direction of peak blade-vortex interactions and extracted minimal noise unrelated to blade-vortex interactions. There was one primary limitation to successful interpretation of the extraction results. The primary limitation of the technique comes in the form of the amplitude cutoff threshold. The implicit assumption in this method, is that the main rotor harmonic energy is always strong. However, as was discussed in § 7.1, this is not always true. When the main rotor harmonic energy drops, then the amplitude cutoff allows for the filtering of high frequency noise unrelated to blade-vortex interactions.

Fortunately, there is a strong connection between the simultaneous presence of blade-vortex interactions and high energy in the main rotor harmonic. When blade-vortex interactions are present, energy in the main rotor harmonic and blade-vortex interaction frequency range are the most energetic features in the signal. This is true regardless of the main rotor noise mechanism that is causing

the energy in the main rotor harmonic (thickness or loading noise). However, the reverse of this is not always true. When the energy in the main rotor harmonic is strong, this does not imply that blade-vortex interactions are present.

The extraction method will correctly remove blade-vortex interactions, if present, when the energy in the main rotor harmonic is sufficiently strong. It was shown, however, that when the main rotor energy is not sufficiently strong, then high frequency noise unrelated to blade-vortex interactions will be removed. When this occurred, the resulting sound pressure level was significantly (6 dB or more) below the amplitude in the peak blade-vortex interaction direction. Thus, with judicious use of engineering judgment, this limitation can easily be mitigated as this lower amplitude sound pressure level immediately suggests that blade-vortex interactions are not truly present in the signal.

A further criteria was proposed for the filtering technique. Due to the requirement for a strong main rotor harmonic energy, and the fact that blade-vortex interactions occur in conjunction with a strong main rotor harmonic energy, then a third parameter can be established. This parameter would require that the energy in the main rotor harmonic be above some predetermined threshold for the filter to be invoked. However, this threshold would likely need to be specific to the individual vehicle and maneuver.

It was also discussed that the basis of this filtering technique has applications beyond its currently employed use. Depending on the filter developed, this technique could be used to remove any high amplitude impulsive signal. It should even be possible that a version of this technique could be used to remove the tail rotor signature from an experimentally recorded acoustic signal, thereby reducing the remaining acoustic information to almost solely main rotor noise.

Appendices

Appendix A

Wavelet Transforms of Known Signals

Wavelet transforms, described in § 2, are an excellent way for determining the time-scale representation of a given signal. The Choi-Williams distribution, short-time Fourier transform, and Wigner-Ville distribution are similar techniques, and each come with their own set of drawbacks. There has been significant research into developing wavelets for different applications, but here we will focus solely on the Morlet wavelet previously described in § 2.4. Two major benefits to using the Morlet wavelet is the known relationship between scale and frequency, as well as its ability to preserve the phase component of a given signal. Several arbitrarily created sinusoid signals will be investigated here to give the reader some confidence when interpreting the wavelet power spectra for the maneuvering acoustic signals.

A.1 Simple Signals

The first signal investigated is a steady 23 Hz signal spanning one second in time. Each signal is generated with the same frequency resolution as the microphones used in the experiment, and will be plotted on the same frequency and amplitude bounds as used in chapter 4. Further, each signal will have its time series representation displayed beneath the wavelet power spectra. The 23 Hz steady signal is shown in figure A.1a, where the vertical axis is frequency [Hz] and the horizontal axis is time [s]. The contour levels provided on the right hand side of each figure represents the energy magnitude in dB. This figure shows some very important features of the wavelet transform. First, the signal itself is steady, although the wavelet power spectra shows some energy in other frequencies close to the beginning and end of the time series. This energy leakage is due to the cone

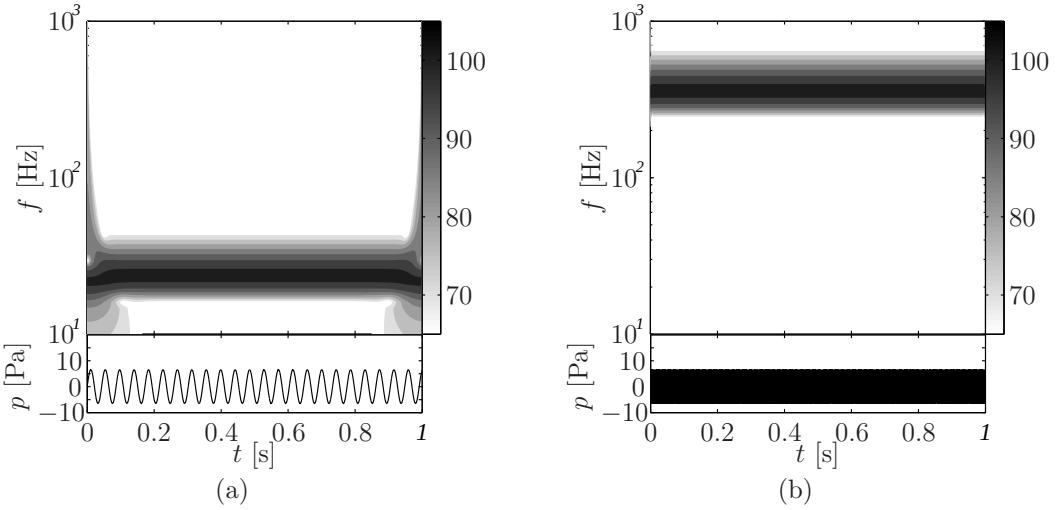

Figure A.1: Steady signal at (a) 23 Hz and (b) 350 Hz.

of influence, related to edge effects of the signal. Lower frequencies are affected deeper into the signal than higher frequencies. For demonstration, a steady 350 Hz signal is provided in figure A.1b, where the edge effects are imperceptible due to its higher frequency content.

The second important feature seen in figure A.1 is the smearing of energy across multiple frequencies. A Fourier transform of the signal would show a strong spike at just the frequency of the signal. Here, however, we can see a spreading of energy to a larger band of frequencies. In order to reduce this spread of energy to other frequencies, the frequency resolution of the wavelet transform would have to be improved. This is possible by modifying the non-dimensional frequency of the Morlet wavelet, described in equation (2.8). However, increasing the non-dimensional frequency would lessen the temporal resolution of the wavelet transform, and so some spectral spreading is inevitable. Furthermore, the wavelet transform's scales, and therefore frequencies, are spaced logarithmically in frequency space, so the spectral spreading width remains fairly constant between the two different signals.

The next signals to be investigated are a linear and quadratic ascending chirp, shown in figure A.2. These signals range from 23 Hz to 350 Hz and show how the wavelet power spectra evolves in time with the signal. Both show similar

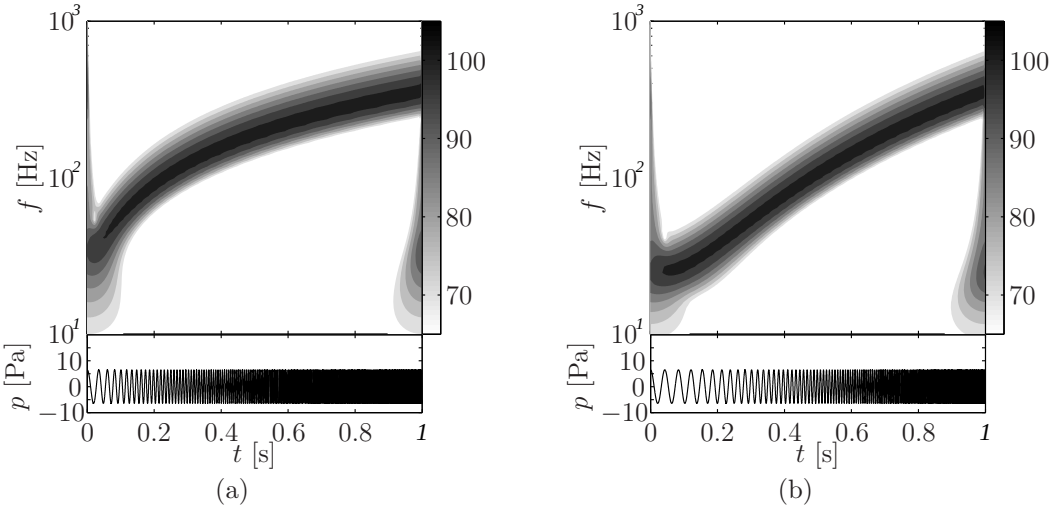

Figure A.2: (a) Linear and (b) quadratic frequency chirp representations.

signs of edge effects and spectral spreading. However, the wavelet power spectra matches well with the frequency varying signal.

A.2 Complex Signals

Now that some simple signals have been investigated, examples of more complex signals are provided. Figure A.3 shows a steady signal at 23 Hz, with

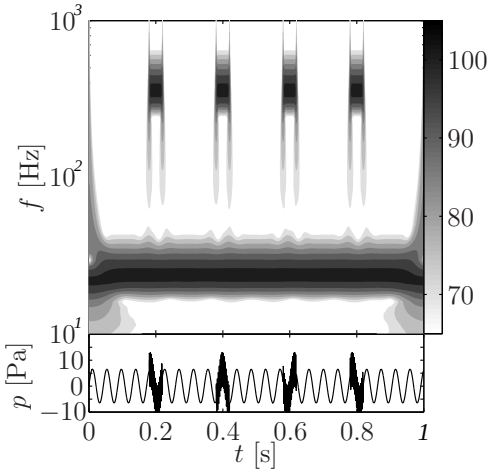

Figure A.3: Steady 23 Hz signal with a transient 350 Hz signal mimicking the main rotor harmonic and blade vortex interaction signature.

a transient component at 350 Hz. This mimics the main rotor harmonic with a

transient blade vortex interaction signal occurring. Notice the signals are superimposed in the time series and the wavelet power spectra adapts to the intermittent 350 Hz signal. The edge effects seen are the exact same as those from the 23 Hz steady signal in figure A.1a.

The transient 350 Hz signal shows frequency spikes at the beginning and ending of each episode. These delta function type spikes are a result of the superposition of both signals resulting in a step response at each transient event initiation and conclusion. Enforcing a smooth pressure transition at each transient phenomenon would remove these spikes.

Finally, the first 3 main rotor harmonics and first 2 tail rotor harmonics are simulated as steady signals, with the transient blade vortex interaction simulated as a transient 350 Hz signal as before. Each harmonic is simulated as half the strength of the previous harmonic, while the first tail rotor harmonic starts at half the strength of the first main rotor harmonic. So the 3 main rotor harmonics in non-dimensional strength are 1, 1/2 and 1/4, while the two tail rotor harmonics are 1/2 and 1/4. The blade vortex interaction signal is simulated at full strength.

The wavelet power spectra of this combined signal is shown in figure A.4. On the left side of the figure are the same columns used in chapter 4 showing the main rotor harmonics, tail rotor harmonics, and combinations of the two. The time series representation is shown below the wavelet power spectra. The time series representation does not appear similar to those seen in the actual acoustic signals, due to the sinusoidal representation of each signature used here.

It can be seen in figure A.4 that the simulated main rotor harmonic and the intermittent blade vortex interaction signals are both identifiable. Finally, the tail rotor and main rotor higher harmonics blend together and become hard to distinguish in the wavelet power spectra.

Some interesting characteristics can be seen in the power spectra, including the cone of influence effects on the border, and a pulsing nature from the interaction of the second and third main rotor harmonic with the first tail rotor harmonic. The delta type frequency spikes associated with the execution of each

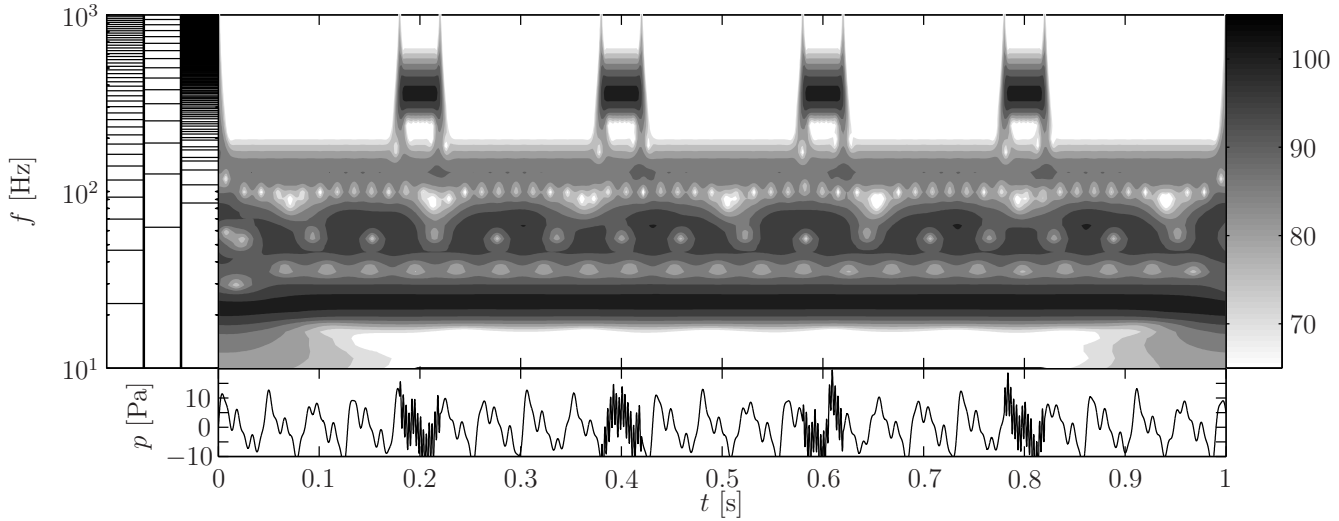

Figure A.4: Simulated sinusoidal representation of the first 3 main rotor harmonics, first 2 tail rotor harmonics, and an intermittent blade vortex interaction event.

transient phenomenon are still present, and can be seen to affect the signal of the second tail rotor harmonic. Overall this should provide the reader some confidence in interpreting the wavelet power spectra seen in chapter 4.

Appendix B

Sensitivity Analysis

Sensitivity analysis provided for various microphones throughout each maneuver. Both the ΔBVISPL and ΔRSPL metrics previously discussed in § 5.2 are evaluated. Within each figure are three windows, representing various times. From left to right, each window starts at 1s, 2s, and 4s of the maneuver *path of interest*.

B.1 Steady Level Flight

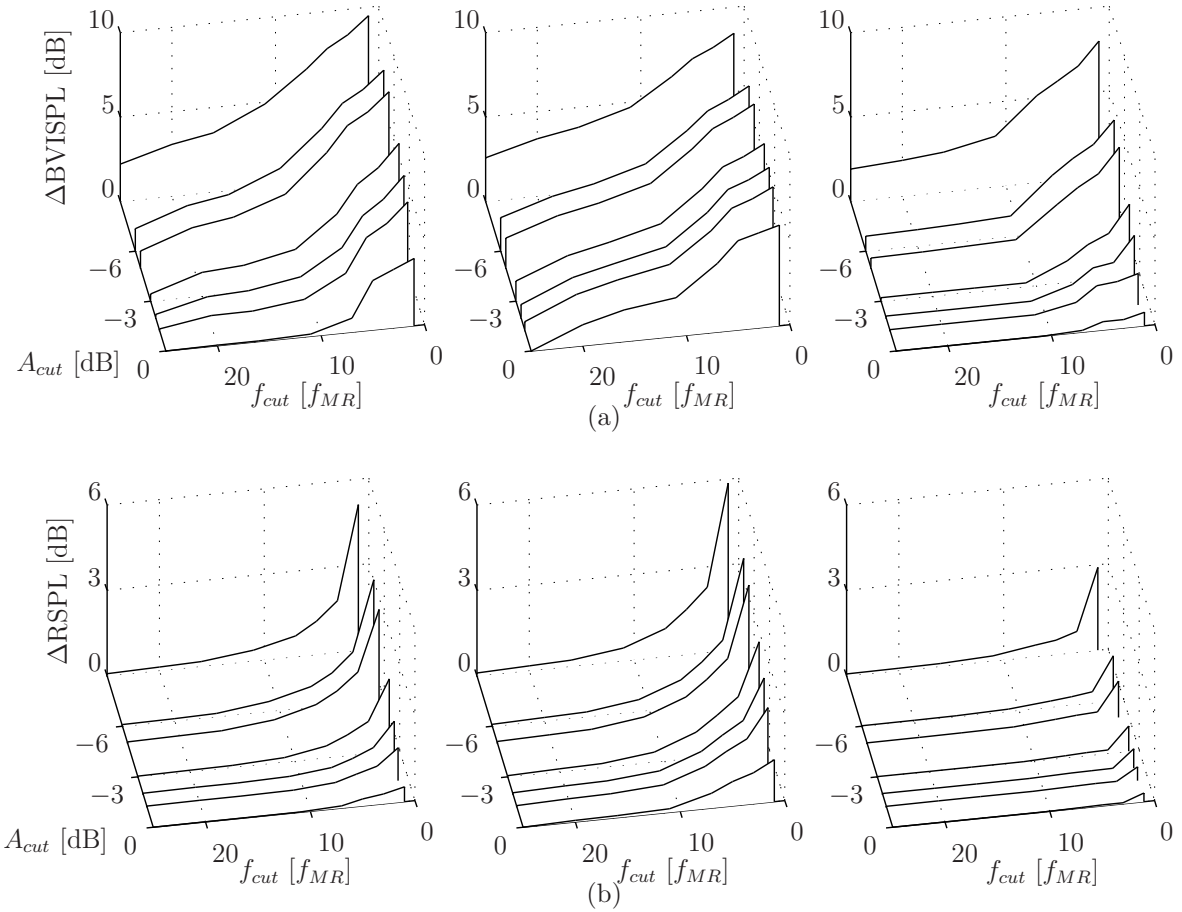

Figure B.1: Steady Level Flight sensitivity analysis from microphone 5 of the (a) blade-vortex interaction and (b) residual averaged sound pressure levels.

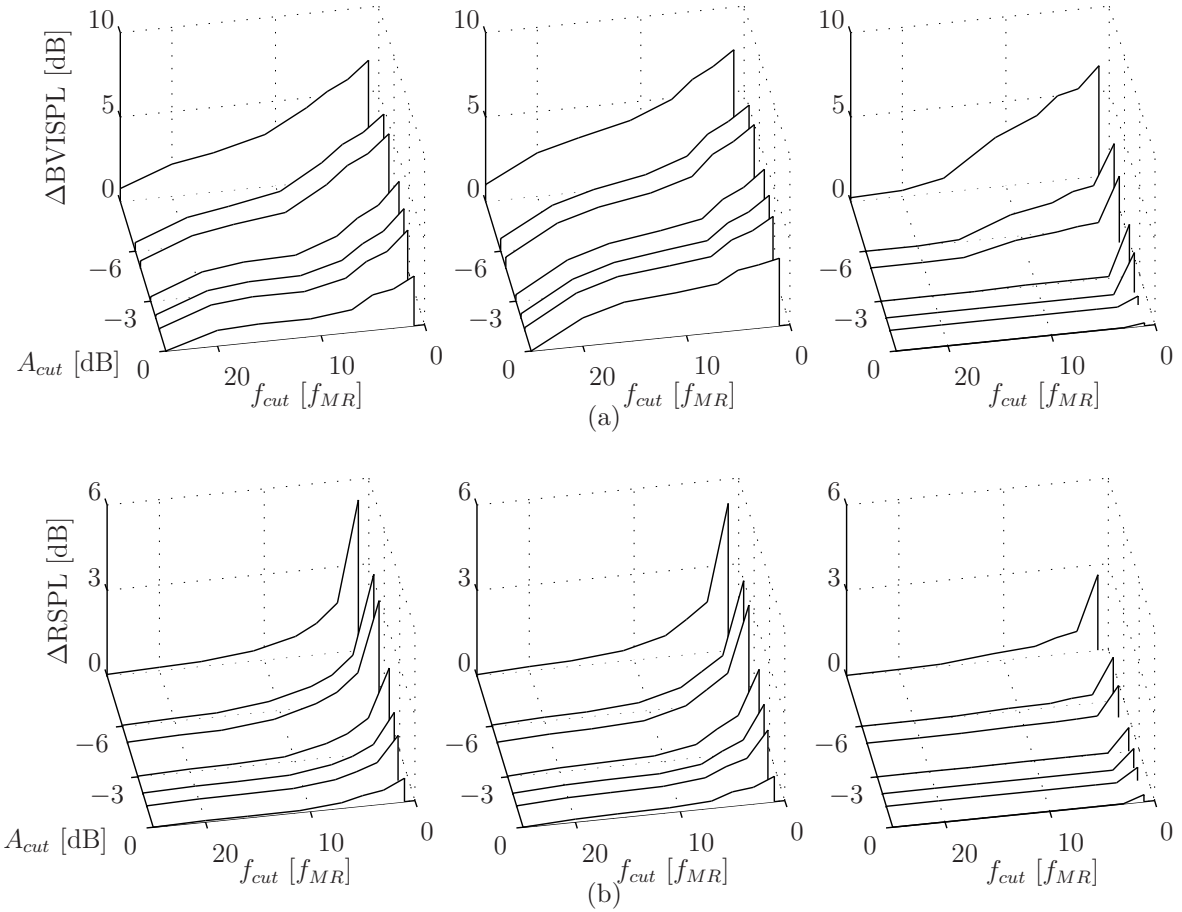

Figure B.2: Steady Level Flight sensitivity analysis from microphone 6 of the (a) blade-vortex interaction and (b) residual averaged sound pressure levels.

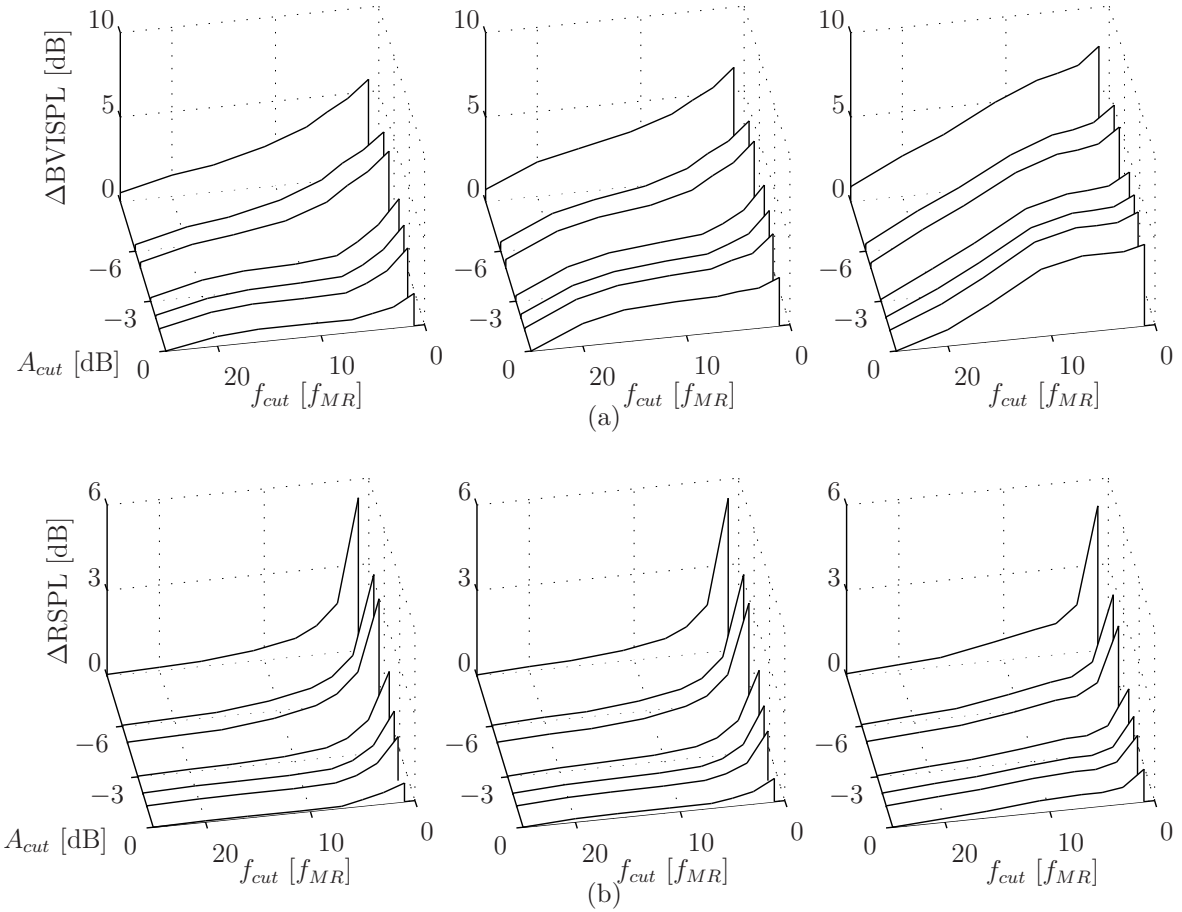

Figure B.3: Steady Level Flight sensitivity analysis from microphone 7 of the (a) blade-vortex interaction and (b) residual averaged sound pressure levels.

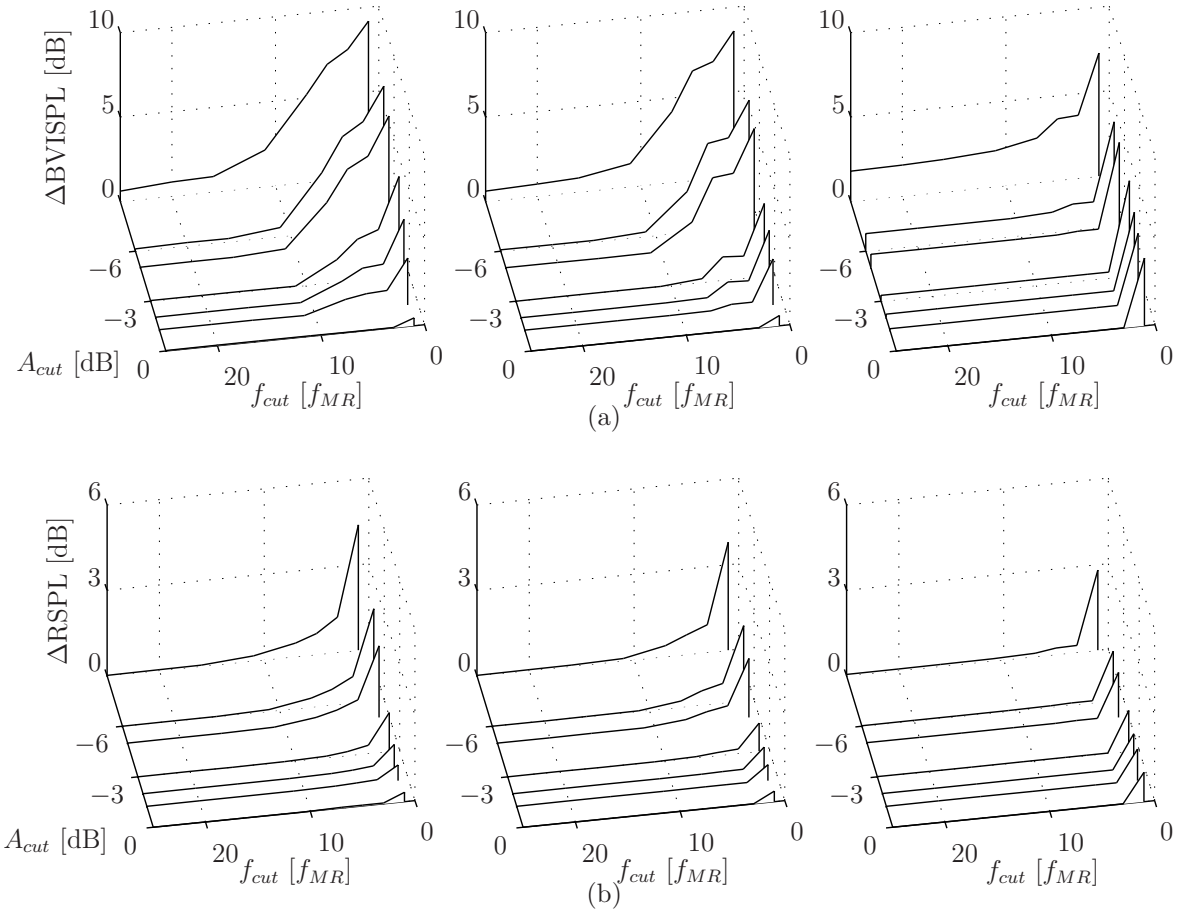

Figure B.4: Steady Level Flight sensitivity analysis from microphone 8 of the (a) blade-vortex interaction and (b) residual averaged sound pressure levels.

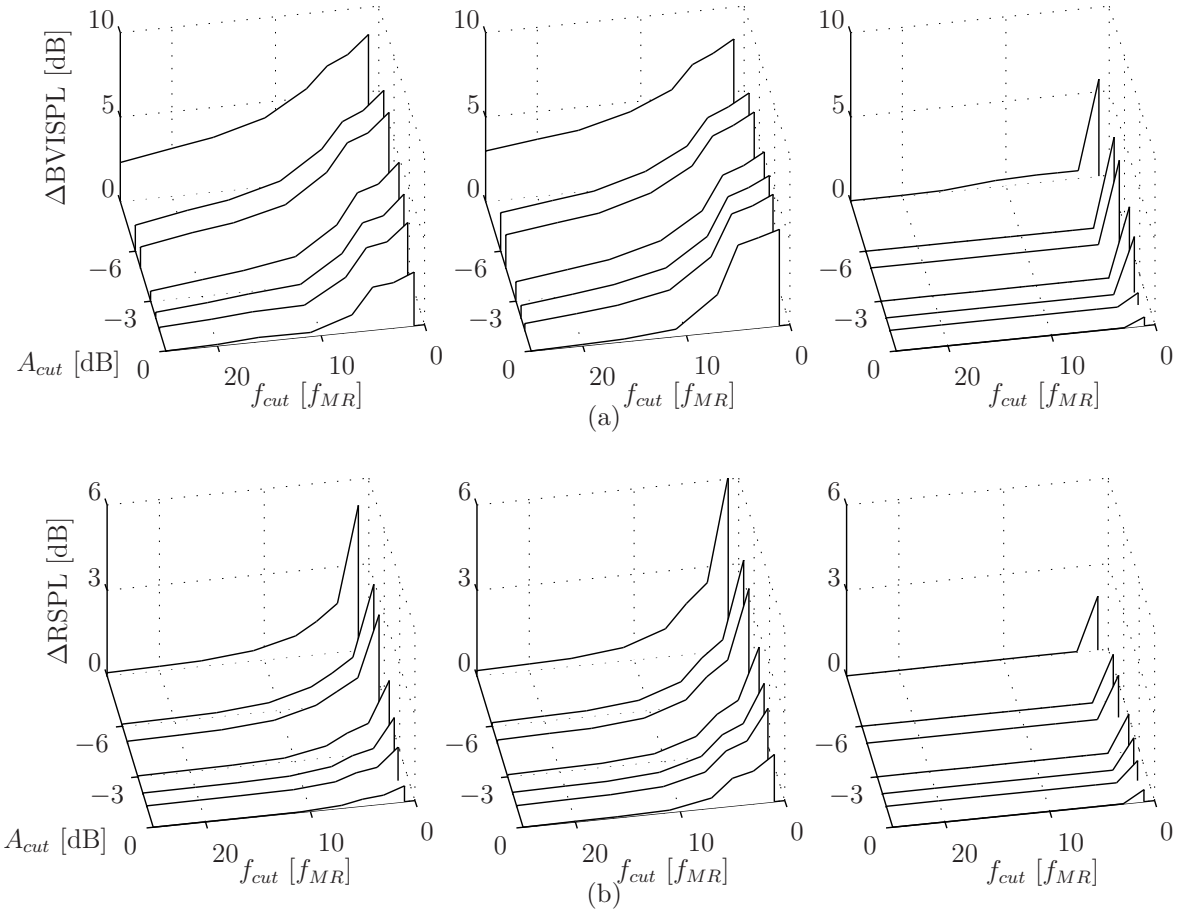

Figure B.5: Steady Level Flight sensitivity analysis from microphone 9 of the (a) blade-vortex interaction and (b) residual averaged sound pressure levels.

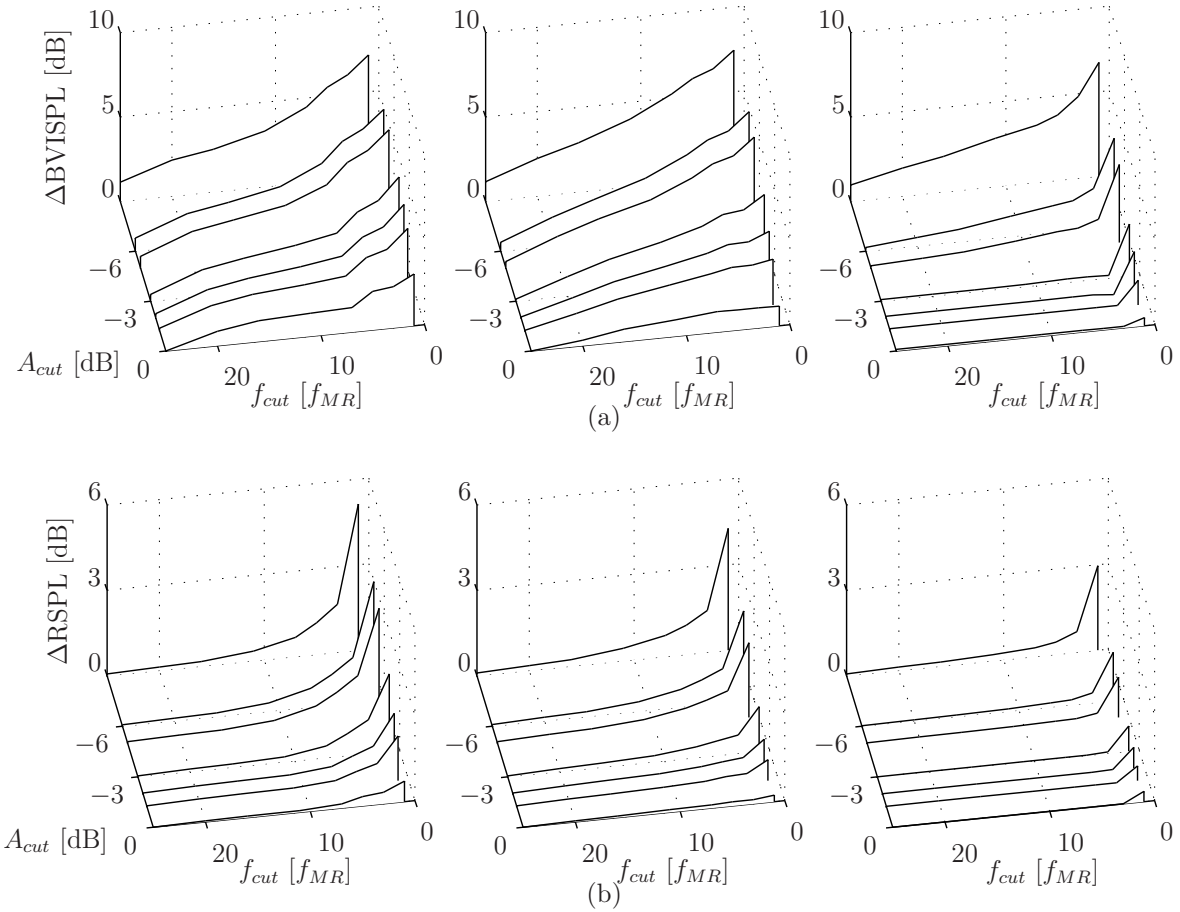

Figure B.6: Steady Level Flight sensitivity analysis from microphone 10 of the (a) blade-vortex interaction and (b) residual averaged sound pressure levels.

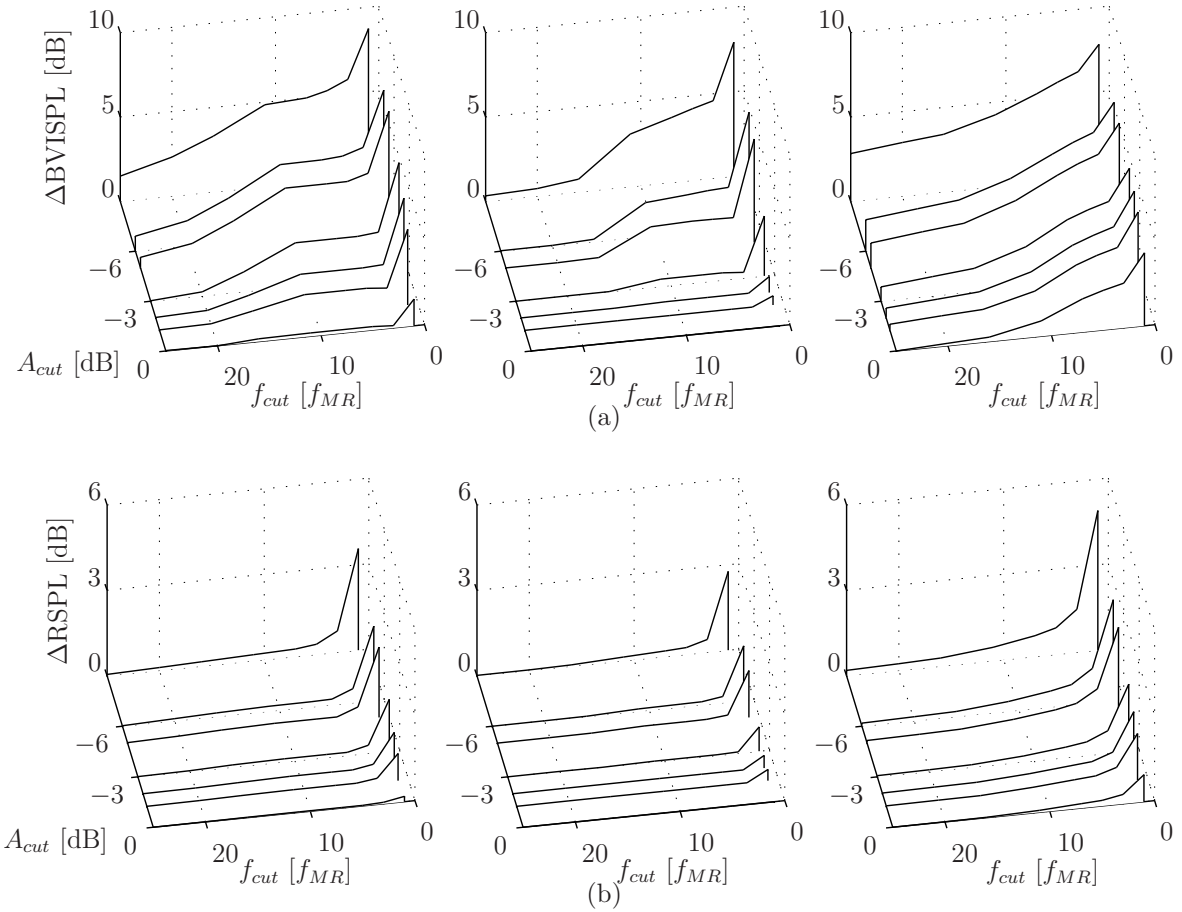

Figure B.7: Steady Level Flight sensitivity analysis from microphone 11 of the (a) blade-vortex interaction and (b) residual averaged sound pressure levels.

B.2 Fast Advancing Side Roll

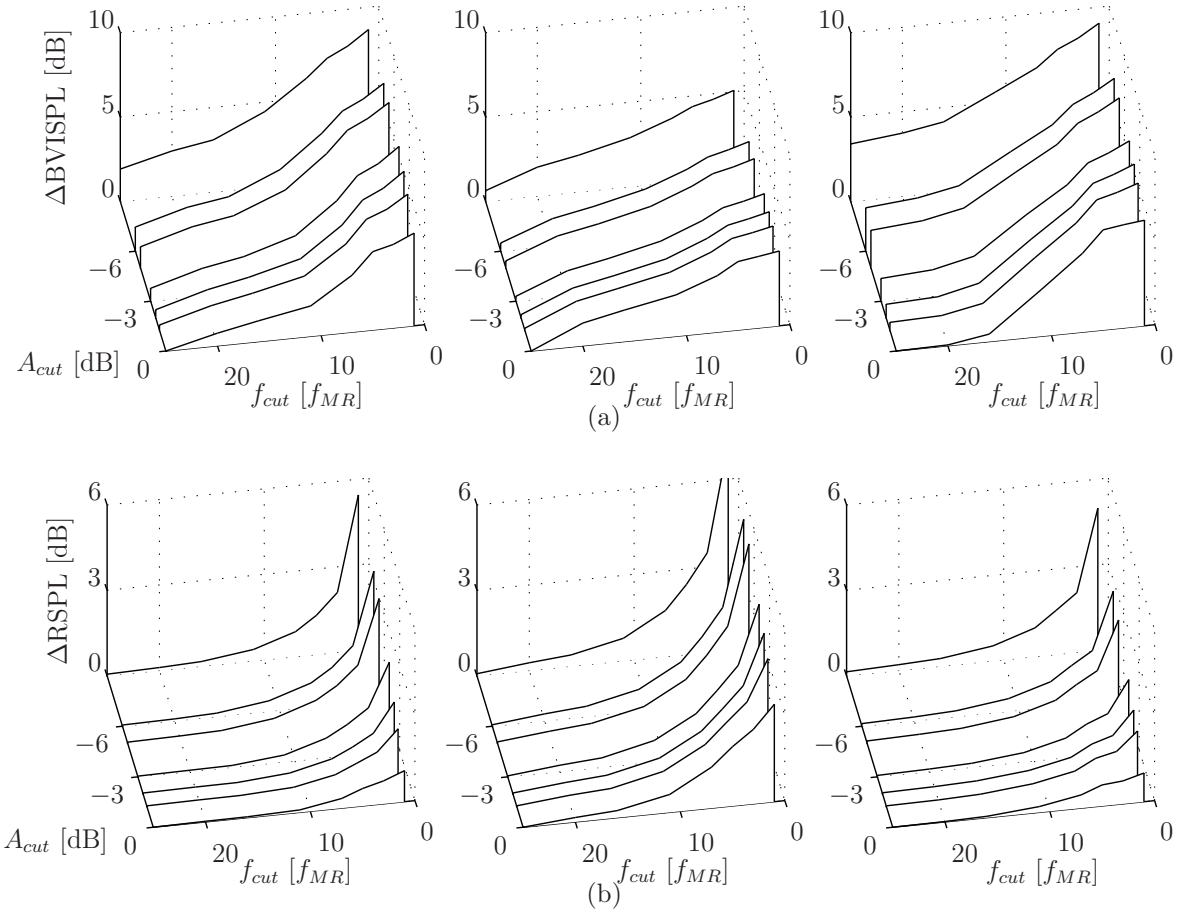

Figure B.8: Fast Advancing Side Roll sensitivity analysis from microphone 5 of the (a) blade-vortex interaction and (b) residual averaged sound pressure levels.

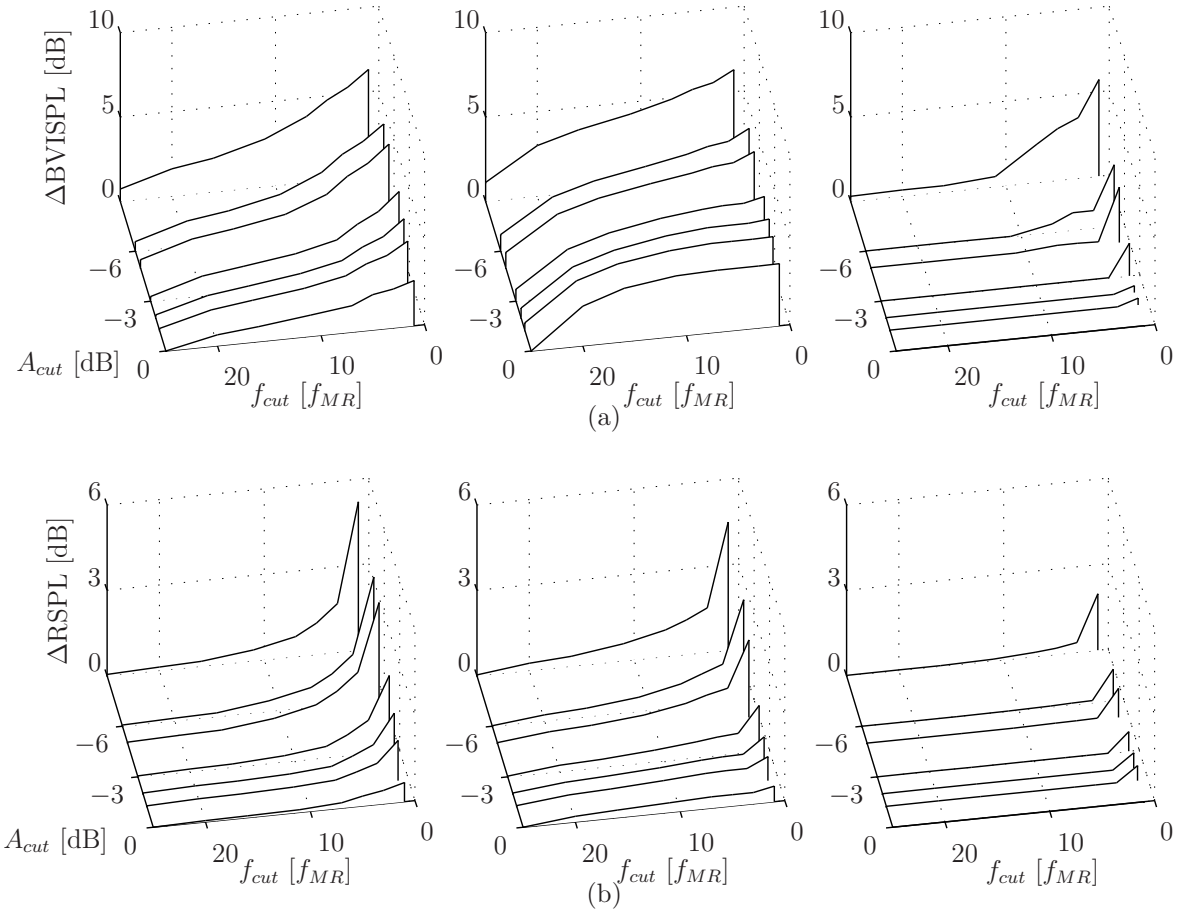

Figure B.9: Fast Advancing Side Roll sensitivity analysis from microphone 6 of the (a) blade-vortex interaction and (b) residual averaged sound pressure levels.

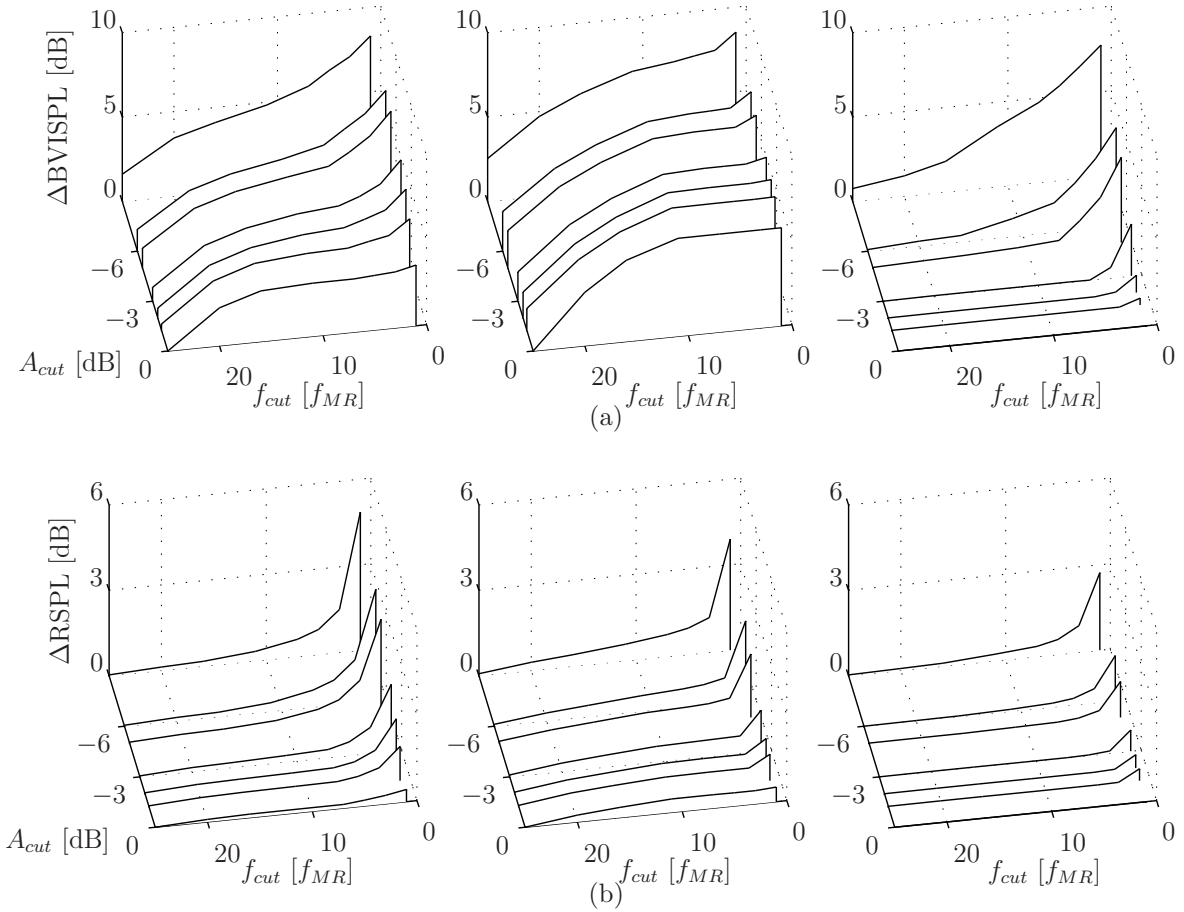

Figure B.10: Fast Advancing Side Roll sensitivity analysis from microphone 7 of the (a) blade-vortex interaction and (b) residual averaged sound pressure levels.

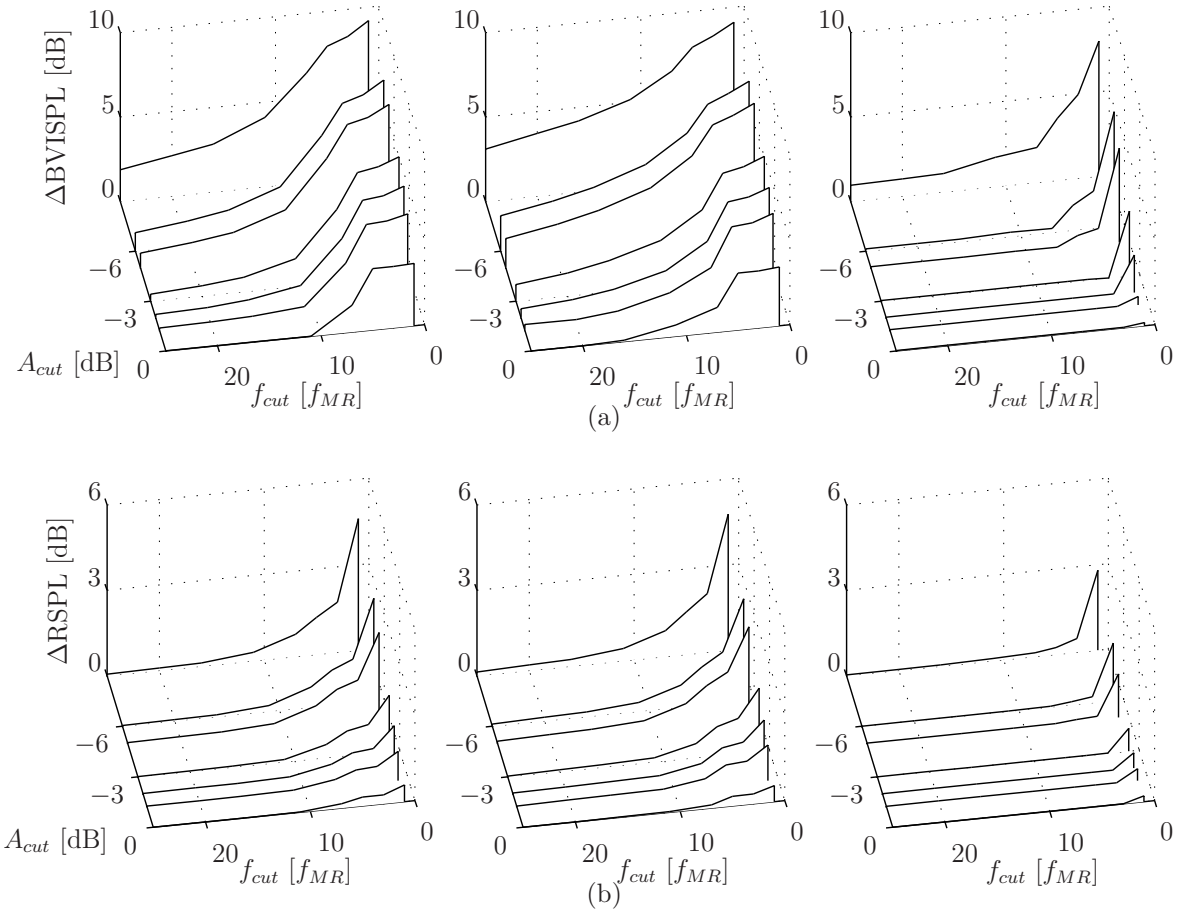

Figure B.11: Fast Advancing Side Roll sensitivity analysis from microphone 8 of the (a) blade-vortex interaction and (b) residual averaged sound pressure levels.

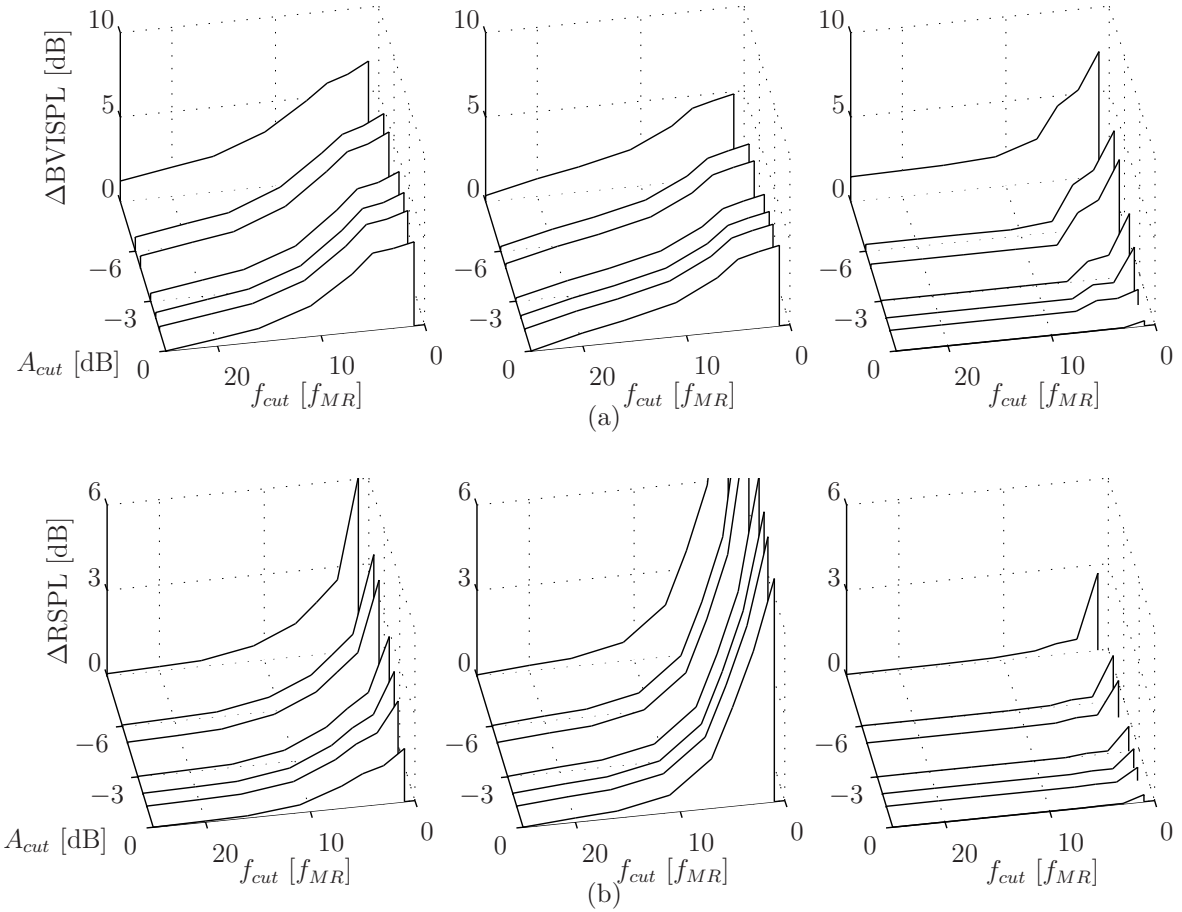

Figure B.12: Fast Advancing Side Roll sensitivity analysis from microphone 9 of the (a) blade-vortex interaction and (b) residual averaged sound pressure levels.

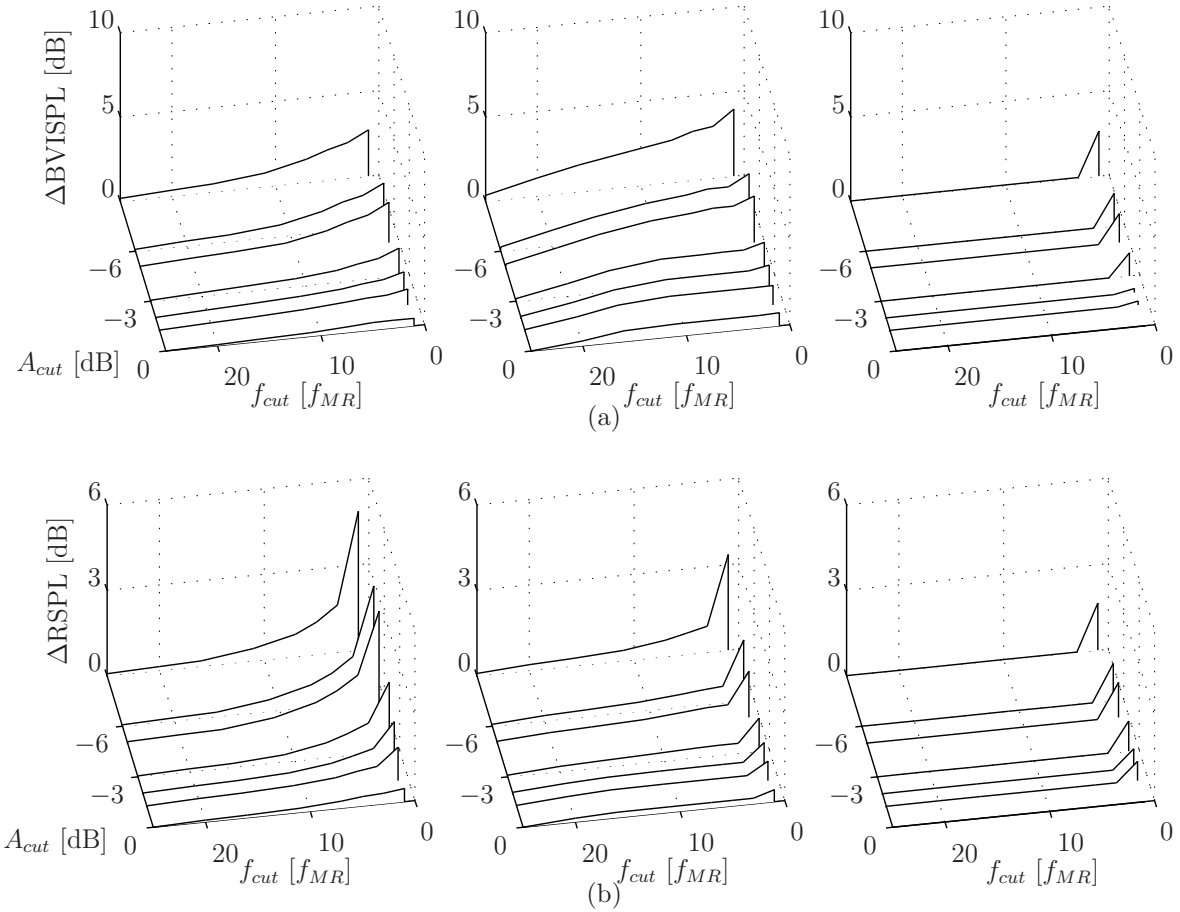

Figure B.13: Fast Advancing Side Roll sensitivity analysis from microphone 10 of the (a) blade-vortex interaction and (b) residual averaged sound pressure levels.

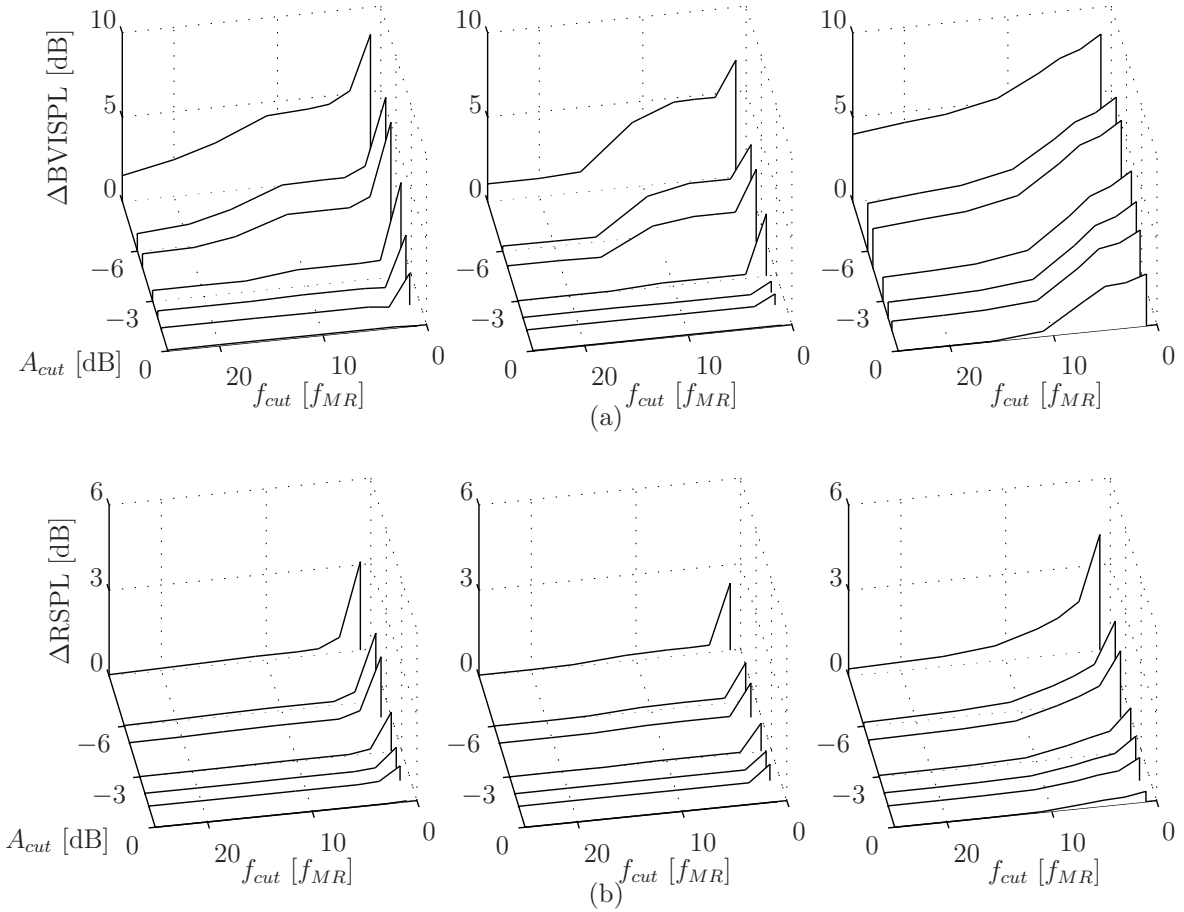

Figure B.14: Fast Advancing Side Roll sensitivity analysis from microphone 11 of the (a) blade-vortex interaction and (b) residual averaged sound pressure levels.

B.3 Medium Advancing Side Roll

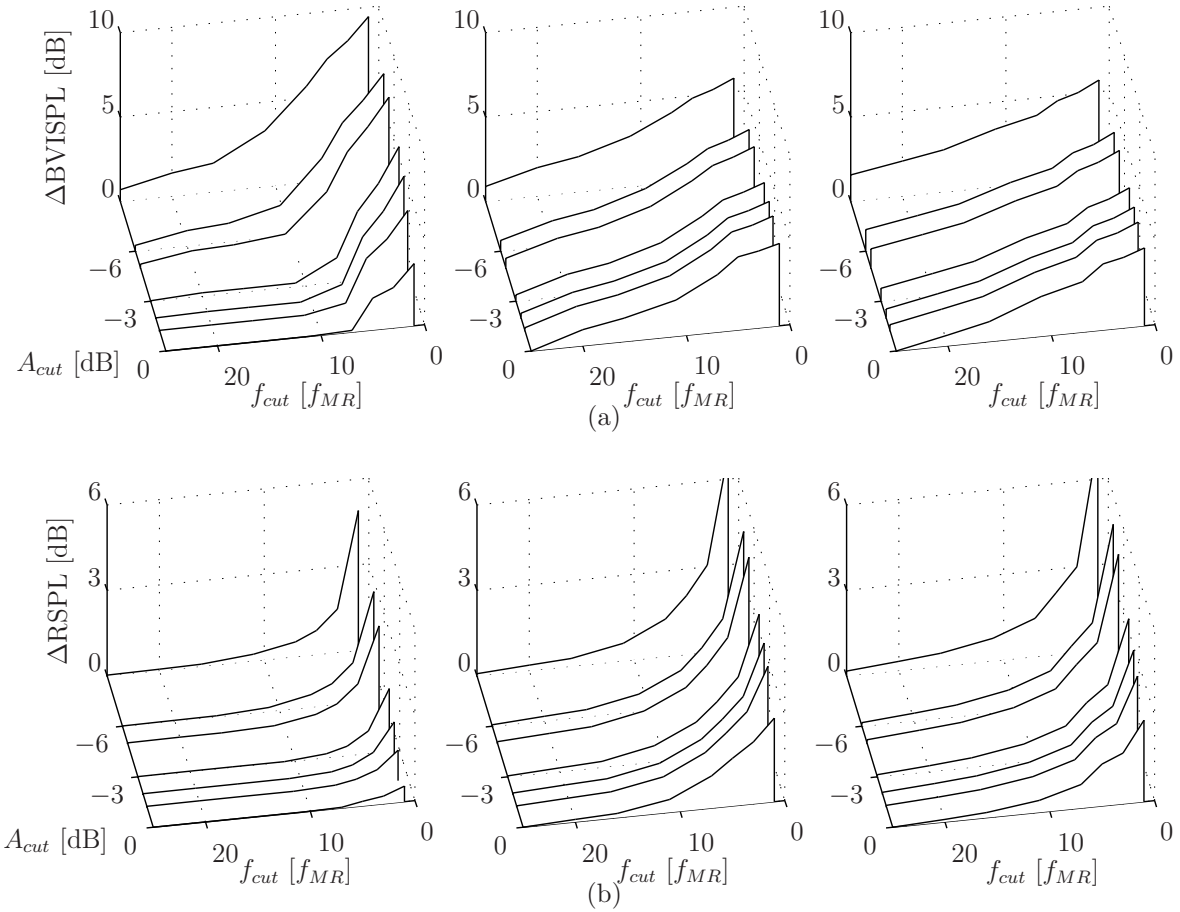

Figure B.15: Medium Advancing Side Roll sensitivity analysis from microphone 5 of the (a) blade-vortex interaction and (b) residual averaged sound pressure levels.

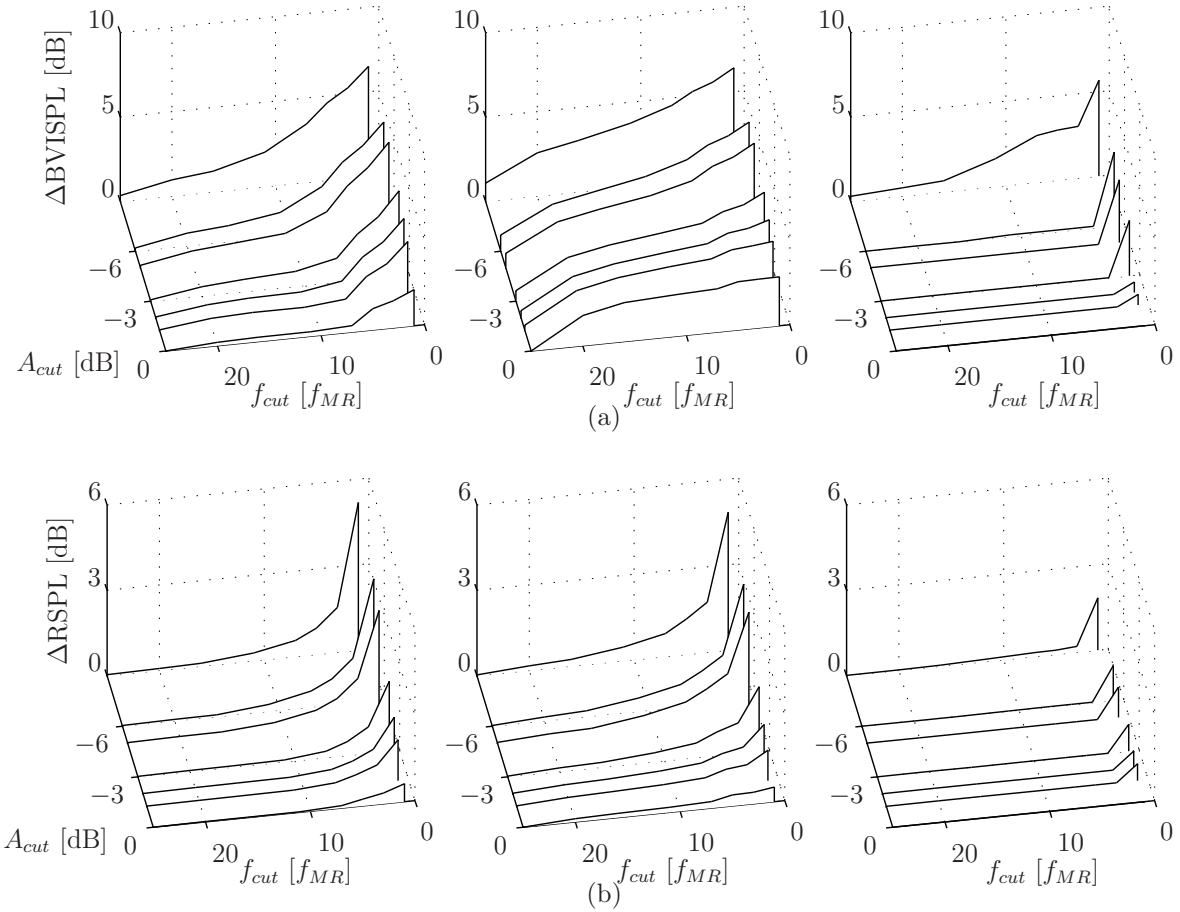

Figure B.16: Medium Advancing Side Roll sensitivity analysis from microphone 6 of the (a) blade-vortex interaction and (b) residual averaged sound pressure levels.

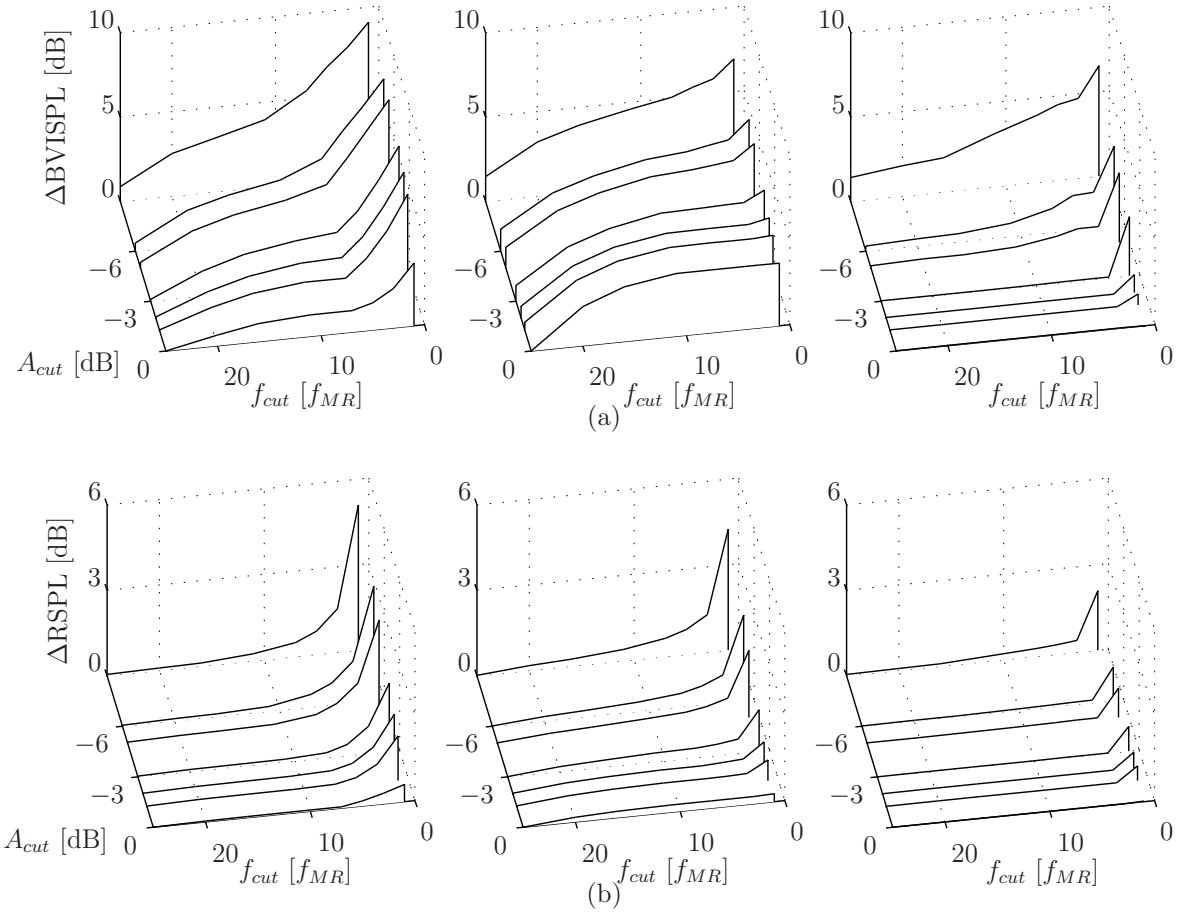

Figure B.17: Medium Advancing Side Roll sensitivity analysis from microphone 7 of the (a) blade-vortex interaction and (b) residual averaged sound pressure levels.

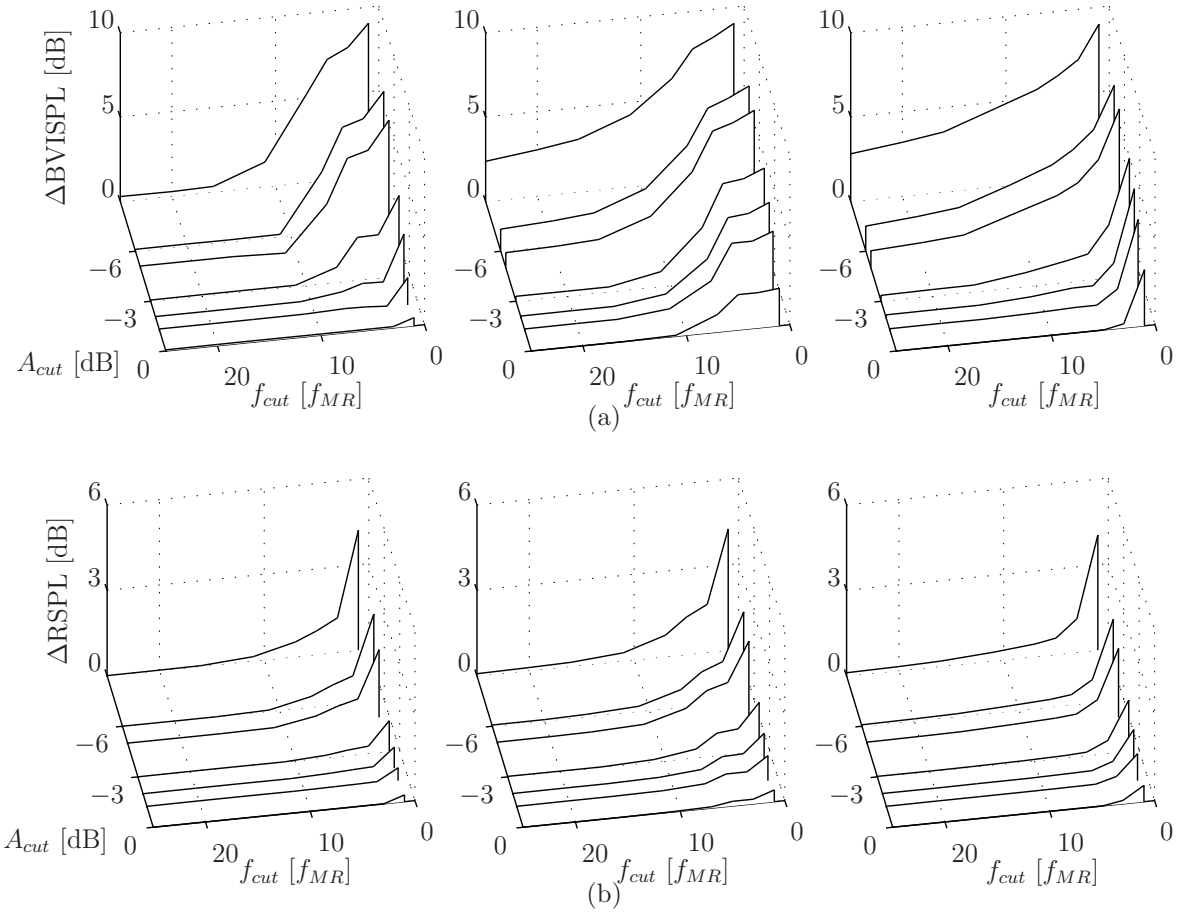

Figure B.18: Medium Advancing Side Roll sensitivity analysis from microphone 8 of the (a) blade-vortex interaction and (b) residual averaged sound pressure levels.

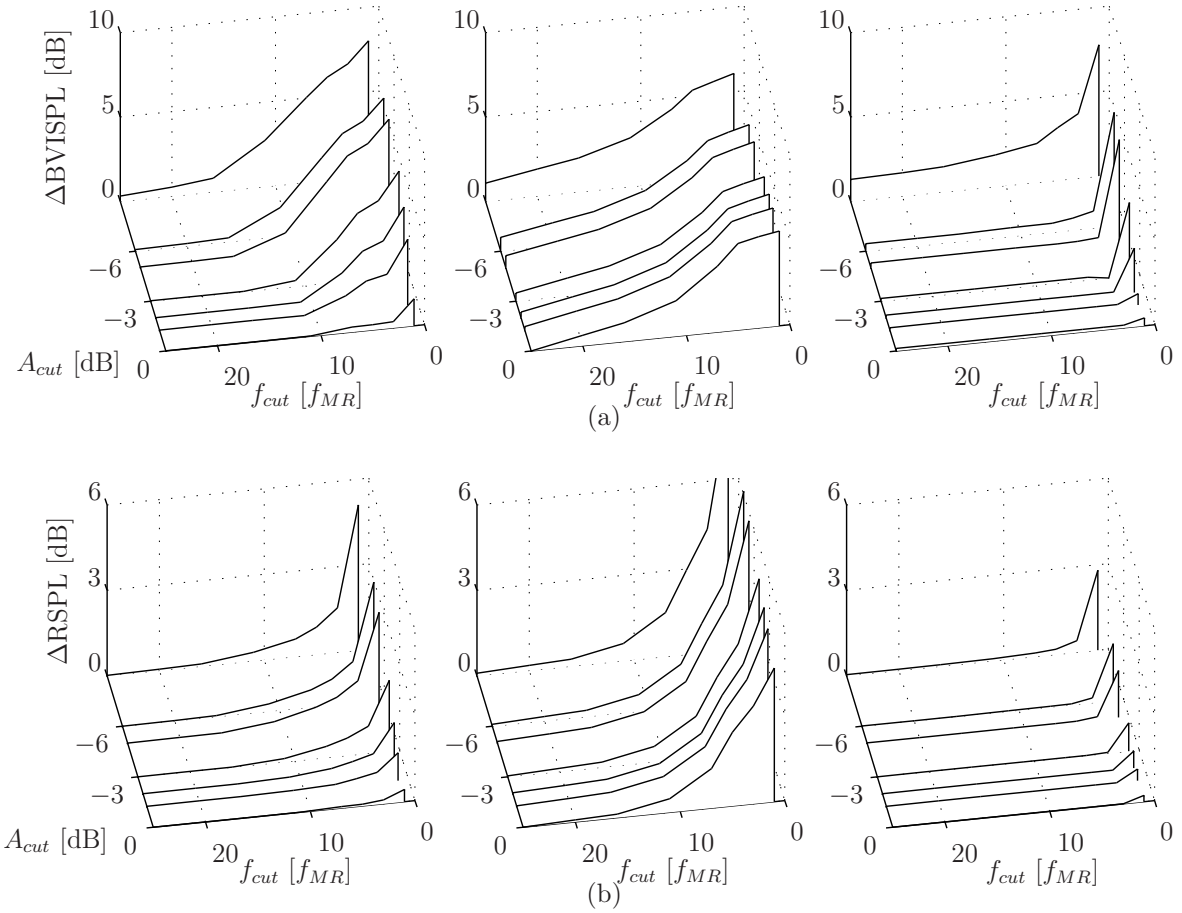

Figure B.19: Medium Advancing Side Roll sensitivity analysis from microphone 9 of the (a) blade-vortex interaction and (b) residual averaged sound pressure levels.

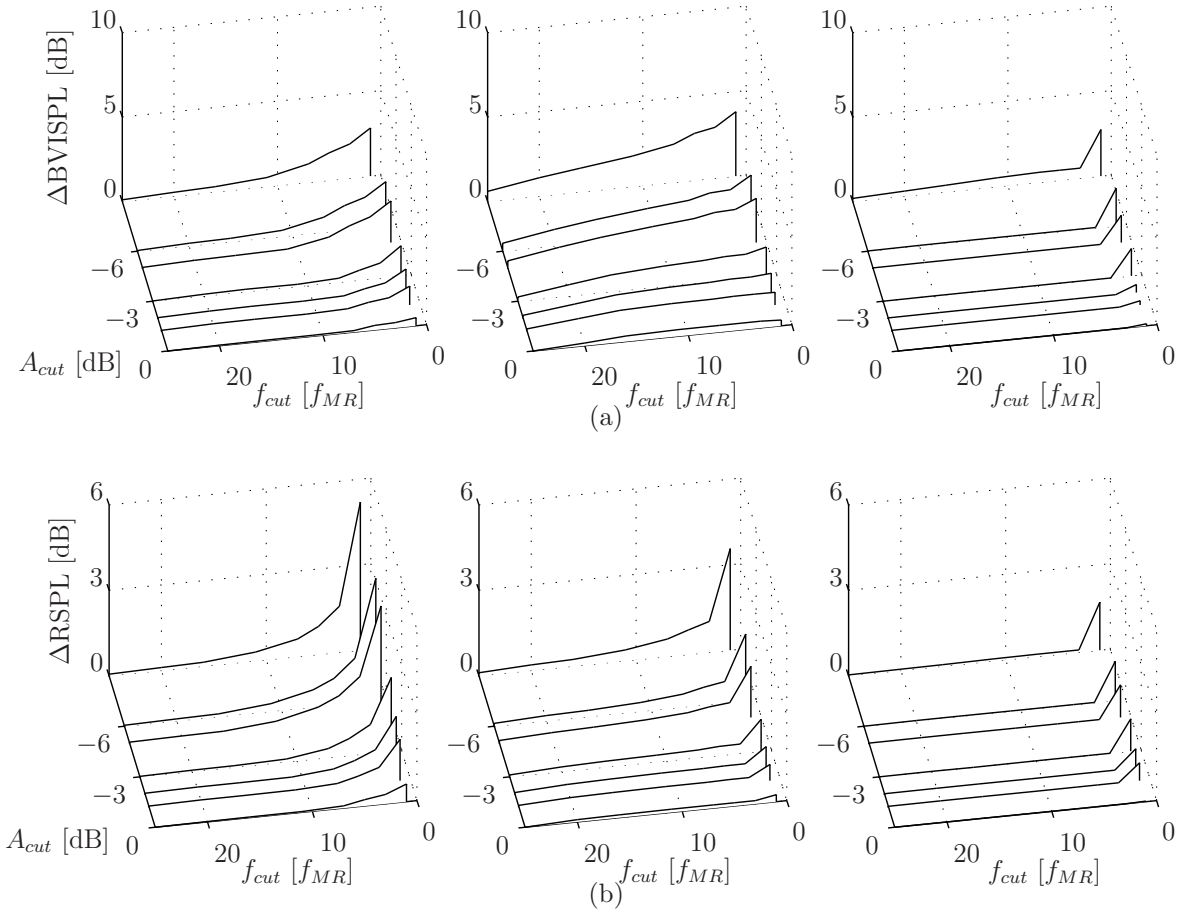

Figure B.20: Medium Advancing Side Roll sensitivity analysis from microphone 10 of the (a) blade-vortex interaction and (b) residual averaged sound pressure levels.

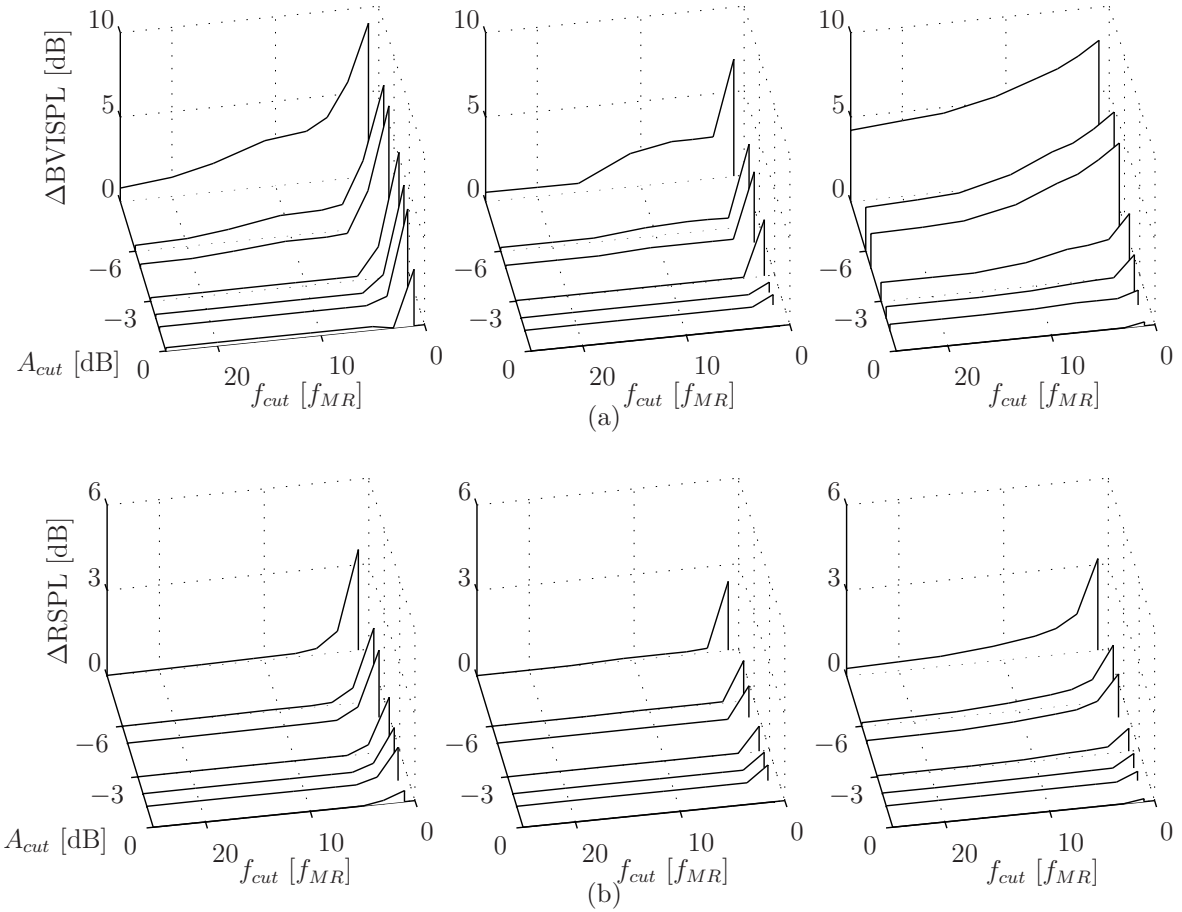

Figure B.21: Medium Advancing Side Roll sensitivity analysis from microphone 11 of the (a) blade-vortex interaction and (b) residual averaged sound pressure levels.

Appendix C

Sensitivity Analysis

Movies comprising the overall sound pressure level, blade vortex interaction sound pressure level, and residual blade pressure level throughout each maneuver is now provided. Each contour plot in the movie is averaged over 0.25 seconds. Movies will function in any PDF viewer that allows GIF encoding, such as Adobe Acrobat Reader.

C.1 Steady Level Flight

Figure C.1: Movie of overall sound pressure level of steady level flight maneuver. Roll (ϕ) and roll rate of change ($\dot{\phi}$) are both identified beneath the contour map.

Figure C.2: Movie of blade-vortex interaction sound pressure level of steady level flight maneuver. Roll (ϕ) and roll rate of change ($\dot{\phi}$) are both identified beneath the contour map.

Figure C.3: Movie of residual sound pressure level of steady level flight maneuver. Roll (ϕ) and roll rate of change ($\dot{\phi}$) are both identified beneath the contour map.

C.2 Fast Advancing Side Roll

Figure C.4: Movie of overall sound pressure level of fast advancing side roll maneuver. Roll (ϕ) and roll rate of change ($\dot{\phi}$) are both identified beneath the contour map.

Figure C.5: Movie of blade-vortex interaction sound pressure level of the fast advancing side roll maneuver. Roll (ϕ) and roll rate of change ($\dot{\phi}$) are both identified beneath the contour map.

Figure C.6: Movie of residual sound pressure level of the fast advancing side roll maneuver. Roll (ϕ) and roll rate of change ($\dot{\phi}$) are both identified beneath the contour map.

C.3 Medium Advancing Side Roll

Figure C.7: Movie of overall sound pressure level of medium advancing side roll maneuver. Roll (ϕ) and roll rate of change ($\dot{\phi}$) are both identified beneath the contour map.

Figure C.8: Movie of blade-vortex interaction sound pressure level of the medium advancing side roll maneuver. Roll (ϕ) and roll rate of change ($\dot{\phi}$) are both identified beneath the contour map.

Figure C.9: Movie of residual sound pressure level of the medium advancing side roll maneuver. Roll (ϕ) and roll rate of change ($\dot{\phi}$) are both identified beneath the contour map.

Bibliography

[1] P. S. Addison. *The illustrated wavelet transform handbook*. Taylor & Francis Group, New York, NY, 2002.

[2] S. Ananthan and J. G. Leishman. Predictions of transient rotor wake aerodynamics in response to time-dependent blade pitch inputs. *American Helicopter Society 59th Annual Forum*, 2003.

[3] W. J. Baars and C. E. Tinney. Transient wall pressure in an over expanded and large area ratio nozzle. *Experiments in Fluids*, 54(2), 2013.

[4] J. D. Baeder. Euler solutions to nonlinear acoustics of non-lifting hovering rotor blades. *NASA*, TM 103837, 1991.

[5] A. Bagai, J. G. Leishman, and J. Park. Aerodynamic analysis of a helicopter in steady maneuvering flight using a free-vortex rotor wake model. *Journal of the American Helicopter Society*, 44(2):109–120, 1999.

[6] T. S. Beddoes. A wake model for high resolution airloads. In *International Conference on Rotorcraft Basic Research, Research Triangle Park, NC, Proceedings*, number 21 in 19, 1985.

[7] G. Bernardini, J. Serafini, M. Gennaretti, and S. Ianniello. Aeroelastic modeling effect in rotor BVI noise prediction. *12th AIAA/CEAS Aeroacoustic Conference*, 1994.

[8] D. T. Blackstock. *Fundamentals of Physical Acoustics*. Wiley-Interscience, 2000.

[9] D. A. Boxwell, F. H. Schmitz, W. R. Splettstoesser, and K. J. Schultz. Helicopter model rotor-blade vortex interaction impulsive noise: Scalability and parametric variations. *Journal of the American Helicopter Society*, 32(1):3–12, January 1987.

[10] D. D. Boyd. HART-II acoustic predictions using a coupled CFD/CSD method. *American Helicopter Society 65th Annual Forum*, 2009.

[11] K. S. Brentner. Prediction of helicopter rotor discrete frequency noise. *NASA*, TM 87721, 1988.

[12] K. S. Brentner. Modeling aerodynamically generated sound: Recent advances in rotor noise prediction. *38th Aerospace Sciences Meeting & Exhibit*, AIAA 2000-0345.

[13] K. S. Brentner, C. L. Burley, and M. A. Marcolini. Sensitivity of acoustic predictions to variation of input parameters. *Journal of the American Helicopter Society*, 39(3):43–52, 1991.

[14] K. S. Brentner and F. Farassat. Helicopter noise prediction: The current status and future direction. *Journal of Sound and Vibration*, 170(1):79–96, 1994.

[15] K. S. Brentner and F. Farassat. Modeling aerodynamically generated sound of helicopter rotors. *Progress in Aerospace Sciences*, 39:83–120, 2003.

[16] K. S. Brentner and H. E. Jones. Noise prediction for maneuvering rotorcraft. *6th AIAA/CEAS Aeroacoustics Conference, 2000*, AIAA 2000-2031.

[17] K. S. Brentner, L. Lopes, H. N. Chen, and J. F. Horn. Near real-time simulation of rotorcraft acoustics and flight dynamics. *American Helicopter Society 59th Annual Forum*, 2003.

[18] K. S. Brentner, G. Perez, G. A. Bres, and H. E. Jones. Toward a better understanding of maneuvering rotorcraft noise. *American Helicopter Society 58th Annual Forum*, 2002.

[19] T. F. Brooks, D. D. Boyd, C. L. Burley, and J. R. Jolly. Aeroacoustic codes for rotor harmonic and BVI noise - CAMRAD.Mod1/HIRES. *Journal of the American Helicopter Society*, 45(2):63–79, 2000.

[20] T. F. Brooks, J. R. Jolly, and M. A. Marcolini. Helicopter main-rotor noise. *NASA*, TP 2825, 1988.

[21] T. F. Brooks, M. A. Marcolini, and D. S. Pope. Main rotor broadband noise study in the DNW. *American Helicopter Society Specialists' Meeting on Aerodynamics and Aeroacoustics*, 1987.

[22] C. L. Burley, T. F. Brooks, M. M. Marcolini, A. G. Brand, and D. A. Conner. Tiltrotor aeroacoustic code (TRAC) predictions and comparison with measurements. *Journal of the American Helicopter Society*, 45(2):80–89, 2000.

[23] F. Caradonna, C. Kitaplioglu, M. McCluer, J. Baeder, J. G. Leishman, C. Berezin, J. Visintainer, J. Bridgeman, C. Burley, R. Epstein, A. Lyrintzis, E. Koutsavdis, G. Rahier, Y. Delrieux, J. Rule, and D Bliss. Methods for the prediction of blade-vortex interaction noise. *Journal of the American Helicopter Society*, 45(4):303–317, October 2000.

[24] R. Celi. Time–frequency visualization of helicopter noise. *Journal of the American Helicopter Society*, 46(4):262–272, 2001.

[25] H. Chen, K. S. Brentner, S. Ananthan, and J. G. Leishman. A computational study of helicopter rotor wakes and noise generated during transient maneuvers. *Journal of the American Helicopter Society*, 53(1):37–55, 2008.

[26] H. Chen, K. S. Brentner, L. V. Lopes, and J. F. Horn. A study of rotorcraft noise prediction in maneuvering flight. *42nd AIAA Aerospace Sciences Meeting and Exhibit*, 2004.

[27] H. Chen, K. S. Brentner, L. V. Lopes, and J. F. Horn. An initial analysis of transient noise in rotorcraft maneuvering flight. *International Journal of Aeroacoustics*, 5(2):109–138, 2006.

[28] H. Chen, K. S. Brentner, and J. S. Shirey. An investigation of transient rotor noise in maneuvering flight. *11th AIAA/CEAS Aeroacoustics Conference*, 2005.

[29] L. Cohen. Time–frequency distributions – a review. *Proceedings of the IEEE*, 77(7):941–981, 1989.

[30] R.R. Coifman and M.V. Wickerhauser. Entropy–based algorithms for best basis selection. *IEEE Transactions on Information Theory*, 38(2):713–718, March 1992.

[31] W. Constantine, C. Pezeshki, R. Bamberger, and M. Mosher. Discrete wavelet analysis of blade vortex interaction noise. *Journal of the Acoustic Society of America*, 97(6):3688–3693, 1995.

[32] C. Dahan and E. Gratieux. Helicopter rotor thickness noise. *Journal of Aircraft*, 18(6):487–494, June 1981.

[33] I. Daubechies. *Ten Lectures on Wavelets*. SIAM Press, 1992.

[34] W. Davis, C. Pezeshki, and M. Mosher. Extracting and characterizing blade–vortex interaction noise with wavelets. *Journal of the American Helicopter Society*, 42(3):264–271, 1997.

[35] I. de Moortel and A. W. Hood. Wavelet analysis: The effect of varying basic wavelet parameters. *Solar Physics*, 222:203–228, 2004.

[36] F. Farassat. Linear acoustic formulas for calculation of rotating blade noise. *AIAA Journal*, 19(9):1122–1130, 1981.

[37] F. Farassat. Derivation of formulas 1 and 1a of Farassat. *NASA*, TM 214853, 2007.

[38] F. Farassat and K. S. Brentner. The influence of quadrupole sources in the boundary layer and wake of a blade on helicopter rotor noise. *International Technical Specialists Meeting Rotorcraft Acoustics and Fluid Dynamics*, 1991.

[39] F. Farassat and K. S. Brentner. The acoustic analogy and the prediction of the noise of a rotating blade. *Theoretical Computational Fluid Dynamics*, 10:155–170, 1998.

[40] F. Farassat and G. P. Succi. The prediction of helicopter rotor discrete frequency noise. *American Helicopter Society 38th Annual Forum*, 1982.

[41] M. Farge. Wavelet transforms and their applications to turbulence. *Annual Review of Fluid Mechanics*, 24:395–457, 1998.

[42] M. Farge, Y. Guezennec, C.M. Ho, and C. Meneveau. Continuous wavelet analysis of coherent structures. *Center for Turbulence Research. Proceedings of the Summer Program*, pages 331–348, 1990.

[43] J. E. Ffowcs Williams and D. L. Hawkings. Sound generated by turbulence and surfaces in arbitrary motion. *Philosophical Transactions of the Royal Society*, A264:321–342, 1969.

[44] T. M. Fletcher, K. Duraisamy, and R. E. Brown. Sensitivity of tail rotor noise to helicopter configuration in forward flight. *American Helicopter Society 65th Annual Forum*, 2009.

[45] I. E. Garrick and C. E. Watkins. A theoretical study of the effect of forward speed on the free–space sound–pressure field around propellers. *NACA*, Report 1198, 1954.

[46] M. Geissbuehler and T. Lasser. How to display data by color schemes compatible with red-green color perception deficiencies. *Optics Express*, 2013.

[47] A. R. George and S. T. Chou. Comparison of broadband noise mechanisms, analyses, and experiments on rotors. *Journal of Aircraft*, 21(8):583–592, August 1984.

[48] M. Gervais, V. Gareton, A. Dummel, and R. Hager. Validation of EC-130 and EC-135 environmental impact assessment using HELENA. *American Helicopter Society 66th Annual Forum*, 2010.

[49] S. A. L. Glegg. Significance of unsteady thickness noise sources. *AIAA Journal*, 25(6):839–844, June 1987.

[50] S. A. L. Glegg. Prediction of blade wake interaction noise based on a turbulent vortex model. *AIAA Journal*, 29(10):1545–1551, 1991.

[51] M. D. Greenberg. *Foundations of Applied Mathematics*. Prentice-Hall, 1978.

[52] D. D. Greenwood. Auditory masking and the critical band. *Journal of Acoustical Society of America*, 33(10), 1961.

[53] E. Greenwood. *Fundamental Rotorcraft Acoustic Modeling from Experiments (FRAME)*. PhD thesis, University of Maryland, 2011.

[54] E. Greenwood. Personal Communication, 2013.

[55] E. Greenwood and F. H. Schmitz. Separation of main and tail rotor noise ground–based acoustic measurements using time–domain de-Dopplerization. *35th European Rotorcraft Forum*, 2009.

[56] E. Greenwood, F. H. Schmitz, and R. D. Sickenberger. A semi-empirical noise modeling method for helicopter maneuvering flight conditions. *American Helicopter Society Annual Forum*, 2012.

[57] L. Gutin. On the sound field of a rotating propeller. *NACA*, TM 1195, 1948.

[58] J. C. Hardin and S. L. Lamkin. Concepts for reduction of blade/vortex interaction noise. *Journal of Aircraft*, 24(2):120–125, 1986.

[59] C. C. Hennes, H. N. Chen, K. S. Brentner, S. Ananthan, and J. G. Leishman. Influence of transient flight maneuvers on rotor wake dynamics and noise radiation. *American Helicopter Society 4^{th} Decennial Specialist's Conference on Aeromechanics*, 2004.

[60] G. F. Homicz and A. R. George. Broadband and discrete frequency radiation from subsonic rotors. *Journal of Sound and Vibration*, 36(2):151–177, 1974.

[61] J. C. Hong and Y. Y. Kim. The optimal selection of mother wavelet shape for the best time-frequency localization of the continuous wavelet transform. *Smart Structures and Materials*, 5049:651–660, 2003.

[62] G. P. Howell, A. J. Bradley, M. A. McCormick, and J. D. Brown. De-dopplerization and acoustic imaging of aircraft flyover noise measurements. *Journal of Sound and Vibration*, 105(1):151–167, 1986.

[63] J. E. Hubbard and K. P. Leighton. Comparison of model helicopter rotor primary and secondary blade/vortex interaction blade slap. *Journal of Aircraft*, 21(5):346–350, 1984.

[64] Y. Inada, C. Yang, N. Iwanaga, and T. Aoyama. Efficient prediction of BVI noise using Euler solver with wake model. *Rotor Korea*, 2007.

[65] W. Johnson. *Helicopter Theory*. Dover, 1994.

[66] K. R. Krothapalli, J. V. R. Prasad, and D. A. Peters. Helicopter rotor dynamic inflow modeling for maneuvering flight. *Journal of the American Helicopter Society*, 46(2):129–139, 2001.

[67] A. J. Landgrebe. The wake geometry of a hovering helicopter rotor and its influence on rotor performance. *Journal of the American Helicopter Society*, 17(4):3–15, 1972.

[68] J. G. Leishman, M. H. Bhagwat, and A. Bagai. Free-vortex filament methods for the analysis of helicopter rotor wakes. *Journal of Aircraft*, 39(5):759–775, 2002.

[69] J. Lewalle, J. Delville, and J. Bonnet. Decomposition of mixing layer turbulence into coherent structures and background fluctuations. *Flow, Turbulence and Combustion*, 64:301–328, 2000.

[70] M. J. Lighthill. On sound generated aerodynamically, I: General theory. *Proceedings of the Royal Society*, A221:564–587, 1952.

[71] J. W. Lim, M. Potsdam, R. Strawn, B. W-C Sim, and T. Nygaard. Blade-vortex interaction airloads prediction using multidisciplinary coupling. *HPCMP Users Group Conference*, 2006.

[72] L. Liu, D. Patt, and P. P. Friedmann. Simultaneous vibration and noise reduction in rotorcraft using aeroelastic simulation. *American Helicopter Society 60th Annual Forum*, 2004.

[73] S. R. Liu and M. A. Marcolini. The acoustic results of a united technologies scale model helicopter rotor tested at DNW. *American Helicopter Society 46th Annual Forum*, 1990.

[74] M. V. Lowson. Focusing on helicopter BVI noise. *Journal of Sound and Vibration*, 190(3):477–494, 1996.

[75] M. J. Lucas and M. A. Marcolini. Rotorcraft Noise Model. *Journal of the Acoustical Society of America*, 101(5), 1997.

[76] A. S. Lyrintzis and A. R. George. Far field noise of transonic blade-vortex interactions. *Journal of the American Helicopter Society*, 34(3):30–39, July 1989.

[77] R. M. Martin and J. C. Hardin. Spectral characteristics of rotor blade/vortex interaction noise. *Journal of Aircraft*, 25(1):62–68, 1988.

[78] A. H. Najmi and J. Sadowsky. The continuous wavelet transform and variable resolution time-frequency analysis. *Johns Hopkins Applied Technical Digest*, 18(1):134–140, 1997.

[79] R. W. Paterson and R. K. Amiet. Noise of a model helicopter rotor due to ingestion of turbulence. *NASA*, CR 3213, 1979.

[80] G. Perez and M. Costes. A new aerodynamic & acoustic computation chain for BVI noise prediction in unsteady flight conditions. *American Helicopter Society 60th Annual Forum*, 2004.

[81] M. Ribera and R. Celi. Simulation modeling of unsteady maneuvers using a time accurate free wake. *American Helicopter Society 60th Annual Forum*, 2004.

[82] F. H. Schmitz, D. A. Boxwell, S. Lewy, and C. Dahan. In-flight far-field measurement of helicopter impulsive noise. *American Helicopter Society 32nd Annual Forum*, 1976.

[83] F. H. Schmitz, D. A. Boxwell, S. Lewy, and C. Dahan. Model- to full-scale comparisons of helicopter blade vortex interaction noise. *American Helicopter Society 38th Annual Forum*, 1982.

[84] F. H. Schmitz, D. A. Boxwell, W. R. Splettstoesser, K. J. Schultz, S. Lewy, and M. Caplot. Model helicopter rotor aerodynamics and acoustics as measured in two anechoic wind tunnels. *J. Aircraft*, 37(2):235–244, 2000.

[85] F. H. Schmitz, G. Gopalan, and B. W-C Sim. Flight-path management/control methodology to reduce helicopter blade-vortex interaction noise. *Journal of Aircraft*, 38(2):193–205, 2002.

[86] F. H. Schmitz, E. Greenwood, R. D. Sickenberger, G. Gopalan, B. W-C Sim, D. Conner, E. Moralez, and W. A. Decker. Measurement and characterization of helicopter noise in steady-state and maneuvering flight. *American Helicopter Society 63rd Annual Forum*, 2007.

[87] F. H. Schmitz and B. W-C Sim. Acoustic phasing, directionality and amplification effects of helicopter blade-vortex interactions. *Journal of the American Helicopter Society*, 46(4):273–282, October 2001.

[88] F. H. Schmitz and Y. H. Yu. Helicopter impulsive noise: Theoretical and experimental status. *NASA*, TM 84390, 1983.

[89] F. H. Schmitz and Y. H. Yu. Helicopter impulsive noise: Theoretical and experimental status. *Journal of Sound and Vibration*, 109(3):361–422, 1986.

[90] K. J. Schultz and W. R. Splettstoesser. Prediction of helicopter rotor impulsive noise using measured blade pressure. *American Helicopter Society 43rd Annual Forum*, 1987.

[91] C. E. Shannon. A mathematical theory of communication. *The Bell System Technical Journal*, 27:379–423, 623–656, July, October 1948.

[92] R. K. Shenoy, F. W. Kohlhepp, and K. P. Leighton. Acoustic characteristics of 1/20-scale model helicopter rotors. *NASA*, CR 177355, 1986.

[93] R. Sickenberger, G. Gopalan, and F. H. Schmitz. Helicopter near-horizon harmonic noise radiation due to cyclic pitch transient control. *American Helicopter Society 67th Annual Forum*, 2011.

[94] R. U. Siegert, C. Nouals, and A. Damongeot. Study of helicopter noise signals using time-frequency analysis methods. *15th AIAA Aeroacoustics Conference*, AIAA-93-4357.

[95] B. W-C Sim and J. W. Lim. Blade-vortex interaction (BVI) noise & airload prediction using loose aerodynamic/structural coupling. *American Helicopter Society 62nd Annual Forum*, 2006.

[96] B. W-C Sim, M. A. Potsdam, D. A. Conner, and M. E. Watts. Direct CFD prediction of low frequency sounds generated by a helicopter main rotor. *American Helicopter Society 66th Annual Forum*, 2010.

[97] B. W-C Sim and F. H. Schmitz. Acoustic phasing and amplification effects of single rotor helicopter blade-vortex interactions. *American Helicopter Society 55th Annual Forum*, 1999.

[98] J. P. Snyder. Map projections: A working manual. *United States Geological Survey Professional Paper 1395*, 1982.

[99] P. Spiegel, H. Buchholz, and M. Pott-Pollenske. Highly instrumented BO-105 and EC135-FHS aeroacoustic flight tests including maneuver flights. *American Helicopter Society 61st Annual Forum*, 2005.

[100] W. R. Splettstoesser, R. Kube, W. Wagner, U. Seelhorst, A. Boutier, F. Micheli, E. Mercker, and K. Pengel. Key results from a higher harmonic

control aeroacoustic rotor test (HART). *Journal of the American Helicopter Society*, 42(1):58–78, 1997.

[101] W. R. Splettstoesser, K. J. Schultz, D. A. Boxwell, and F. H. Schmitz. Helicopter model rotor-blade vortex interaction impulsive noise: Scalability and parametric variations. *NASA*, TM 86007, 1984.

[102] J. H. Stephenson, S. M. Mula, C. E. Tinney, and J. Sirohi. Far wake rotorcraft vortex tumbling. *50^{th} AIAA Aerospace Sciences Meeting including the New Horizons Forum and Aerospace Exposition, Nashville, Tennessee, Jan. 9-12, 2012*, AIAA-2012-425.

[103] J. H. Stephenson and C. E. Tinney. Time frequency analysis of sound from a manuevering rotorcraft. *American Helicopter Society 69^{th} Annual Forum*, 2013.

[104] J. H. Stephenson, C. E. Tinney, E. Greenwood, and M. E. Watts. Time frequency analysis of sound from a manuevering rotorcraft. *In Review*, 2014.

[105] G. P. Succi. Limits on the prediction of helicopter rotor noise using thickness and loading sources: Validation of helicopter noise prediction techniques. *NASA*, CR 166097, 1983.

[106] C. Torrence and G. P. Compo. A practical guide to wavelet analysis. *Bulletin of the American Meteorological Society*, 79(1):61–78, 1998.

[107] B. G. van der Wall. The effect of HHC on the vortex convection in the wake of a helicopter rotor. *Aerospace Science and Technology*, 4(5):321–336, July 2000.

[108] J. A. Visintainer, M. A. Marcolini, C. L. Burley, and S. R. Liu. Acoustic predictions using measured pressures from a model rotor in the DNW. *Journal of the American Helicopter Society*, 38(3):35–44, 1993.

[109] M. E. Watts, E. Greenwood, C. D. Smith, R. Snider, and D. A. Conner. Maneuver acoustic flight test of the Bell 430 helicopter data report. *NASA*, TM In Review, 2014.

[110] M. E. Watts, R. Snider, E. Greenwood, and J. Baden. Maneuver acoustic flight test of the Bell 430 helicopter. *American Helicopter Society 68th Annual Forum*, 2012.

[111] S. Widnall. Helicopter noise due to blade-vortex interaction. *Journal of the Acoustical Society of America*, 50(1):354–365, 1971.

[112] S. E. Widnall and T. L. Wolf. Effect of tip vortex structure on helicopter noise due to blade-vortex interaction. *Journal of Aircraft*, 17(10):705–711, 1980.

[113] Y. H. Yu. Rotor blade-vortex interaction noise. *Progress in Aerospace Sciences*, 36:97–115, 2000.

[114] Y. H. Yu, B. Gmelin, H. Heller, J. J. Philippe, E. Mercker, and J. S. Preisser. HHC aeroacoustic rotor test at the DNW - The Joint German/French/US HART Project -. *20th European Rotorcraft Forum*, 1994.

[115] Y. H. Yu, C. Tung, B. G. van der Wall, H-J. Pausder, Casey Burley, Thomas Brooks, P. Beaumier, Y. Delrieux, E. Mercker, and K. Pengel. The HART-II test: Rotor wakes and aeroacoustics with higher - harmonic pitch control (HHC) inputs - The Joint German/French/Dutch/US Project -. *American Helicopter Society 58th Annual Forum*, 2002.

[116] Q. Zhou and P. F. Joseph. Frequency-domain method for rotor self-noise prediction. *AIAA Journal*, 44(6):1197–1206, June 2006.